Wrocław University of Technology
Centre of Advanced Materials and Nanotechnology

Materials Science
Poland

Vol. 23 • No. 3 • 2005

Oficyna Wydawnicza Politechniki Wrocławskiej

Materials Science is an interdisciplinary journal devoted to experimental and theoretical research into the synthesis, structure, properties and applications of materials.

Among the materials of interest are:

- glasses and ceramics
- sol-gel materials
- photoactive materials (including materials for nonlinear optics)
- laser materials
- photonic crystals
- semiconductor micro- and nanostructures
- piezo-, pyro- and ferroelectric materials
- high-T_c, superconductors
- magnetic materials
- molecular materials (including polymers) for use in electronics and photonics
- novel solid phases
- other novel and unconventional materials

The broad spectrum of the areas of interest reflects the interdisciplinary nature of materials research. Papers covering the modelling of materials, their synthesis and characterisation, physicochemical aspects of their fabrication, properties and applications are welcome. In addition to regular papers, the journal features issues containing conference papers, as well as special issues on key topics in materials science.

Materials Science is published under the auspices of the Centre of Advanced Materials and Nanotechnology of the Wrocław University of Technology, in collaboration with the Institute of Low Temperatures and Structural Research of the Polish Academy of Sciences and the Wroclaw University of Economics.

All accepted papers are placed on the Web page of the journal and are available at the address:
http://MaterialsScience.pwr.wroc.pl

Editorial Office

Karol Langner
Łukasz Maciejewski

Printed in Poland

Drukarnia Oficyny Wydawniczej Politechniki Wrocławskiej
Zam. nr 935/2005.

Contents

Professor Marian Kryszewski 1925-2005 585

R. Sot, K. J. Kurzydłowski, *Ab initio* calculations of elastic properties of Ni_3Al and TiAl under pressure 587

P. Raczyński, S. Pałucha, P. Brol, Z. Gburski, Molecular dynamics of hypoxanthine-3-N-oxide near fullerene "sphere" - a computer simulation 591

P. Raczyński, Z. Gburski, The search for minimum potential energy structures of small atomic clusters. Application of the ant colony algorithm 599

W. Klonowski, E. Olejarczyk, R. Stępień, A new simple fractal method for nanomaterials science and nanosensors 607

J. Sosnowski, Dynamic vortex motion in anisotropic HTc superconductors 613

Ł. Gelczuk, M. Dąbrowska-Szata, G. Jóźwiak, Distinguishing and identifying point and extended defects in DLTS measurements 625

Le Jiang, H. Geisler, E. Zschech, Quantitative mapping of the elastic properties of electron-beam damaged silica-based low-k films 643

K. Nauka, Z. Li, T.I. Kamins, Surface photovoltage in silicon. Novel applications for chemical and biological sensing 653

P. Piszczek, A. Grodzicki, M. Richert, A. Radtke, Thermal properties of multinuclear Ti(IV) and Zr(IV) carboxylate derivatives using thermal analysis and variable temperature MS and IR methods 663

R. Szczęsny, I. Szymańska, P. Piszczek, L. Dobrzańska, E. Szłyk, Chemical vapour deposition (CVD) of metallic layers prepared from silver carboxylates complexes with tertiary phosphines 671

V. S. Vikhnin, T.I. Maksimova, J. Hanuza, Molecular impurity ions as centres with charge transfer degrees of freedom, influence on ferroelectric phase transitions 677

P. Sagar, M. Kumar, R.M. Mehra, Electrical and optical properties of sol-gel derived ZnO:Al thin films 685

J. Plocek, A. Hutlová, D. Nižňansky, J. Buršík, J.-L. Rehspringer, Z. Mička, Preparation of $CuFe_2O_4/SiO_2$ nanocomposite by the sol-gel method 697

S. Mammen, CS. Menon, N.V. Unnikrishnan, Electrical and optical studies on thin films of indium phthalocyanine chloride 707

V. Janickis, R. Maciulevičius, R. Ivanauskas, I. Ancutienė, Study of copper sulfide layers on a polyamide film formed by the use of higher polythionic acids 715

T. Ohmura, W. Mori, T. Takei, T. Ikeda, A. Maeda, Structure and magnetic behaviour of mononuclear and dinuclear Cu(II)/Zn(II) monocarboxylate-pyridine derivatives studied by crystal engineering 729

B. Żurowska, J. Mroziński, Isomeric forms of Cu(quinoline-2-carboxylate)$_2 \cdot H_20$. Spectroscopic and magnetic properties 737

O. Shkurenko, V. Kinzhybalo, T. Lis, Z. Ciunik, M. Mys'kiv, Coordination behaviour of N,N'-diallylpiperazimum(2+) and N-allylhexamemylenetetraminium in their crystalline τ-complexes with ionic copper(I) salts 745

A. B. Burdukov, E.V. Mokina, Y.G. Shvedenkov, V.A. Reznikov, G.I. Roschupkina, G.V. Romanenko, Metal complexes of pyrroline-N-oxide dioxime 757

D. Yoshioka, M. Handa, M. Mikuriya, I. Hiromitsu, K. Kasuga, Polynuclear chain complexes of ruthenium(II, III) pivalate dimers linked by 2,5-dimethyl-*N,N*'-dicyanobenzoquinonediimine, 1,4-benzoquinone and 1,4-naphthoquinone 765

M. Mikuriya, K. Matsunami, Synthesis and structural characterization of a series of transition metal complexes with a tetradentate Schiff-base ligand derived from salicyl aldehyde and 2-(2-aminoethylamino)ethanol 773

V. Sasnauskas, D. Palubinskaitė, The synthesis of hydrosodalite and its use in mortar technology. 793
H. Matysiak, Ł. Ciupiński, A. Olszyna, K J. Kurzydłowski, Multilayer Al_20_3/Mo composites 803
D. Waszak, E. Frąckowiak, The effect of the reactive milling of graphite with boron nitride, tin and antimony on lithium insertion 813
S. N. Kulkami, K. Radhakrishna, Evaluation of metal-mould interfacial heat transfer during the solidification of aluminium- 4.5% copper alloy castings cast in $C0_2$-sand moulds 821
M. Kulczyk, W. Pachla, A. Mazur, R. Diduszko, H. Garbacz, M. Lewandowska, W. Łojkowski, K.J. Kurzydłowski, Microstructure and mechanical properties of nickel deformed by hydrostatic extrusion 839

Professor Marian Kryszewski
1925–2005

Professor Marian Kryszewski, outstanding scientist in the field of physics and physical chemistry of polymers, founder of scientific school of polymers at the Faculty of Chemistry, Technical University of Łódź, and in the Centre of Molecular and Macromolecular Studies, Polish Academy of Sciences in Łódź, passed away on 5th October 2005.

He received MSc. in chemistry under supervision of Professor Antoni Basiński for the analysis of catalytic decomposition of chlorinated olefins at Nicolaus Copernicus University in Toruń. He then worked in the team of Professor Aleksander Jabłoński – a well known specialist in the field of luminescence and molecular optics at the Nicolaus Copernicus University. Determination of absolute rate constant in vinyl bromide photopolymerisation was a basis for his doctoral dissertation, submitted in 1955.

Dr. Kryszewski was a post-doc at Centre de Recherche sur les Macromolécules in Strasbourg with Professor Henri Benoit in 1956–1957, and in 1960–1961 at Brooklyn Polytechnic Institute with Professor Herman Mark. In 1958, he was offered Chair of Physics at the Faculty of Chemistry of the Technical University of Łódź. His scientific achievements paved the way to his professorship and to membership of the Polish Academy of Sciences. Together with Professor Jan Michalski, he was co-founder of the Centre of Molecular and Macromolecular Studies of Polish Academy of Sciences, in 1972. For many years, Professor Kryszewski was Scientific Director and Head of the Polymers Physics Department at the Centre, which was soon recognized for its activity in the domain of polymer physics and chemistry. Simultaneously, Professor Kryszewski continued to be the Head of the Polymers Physics Division at Technical University of Łódź until his retirement in 1995.

Research interests of Professor Kryszewski and his groups at the Centre and at the Technical University covered an exceptionally broad spectrum of problems related to structure and properties of polymers and other organic materials in their condensed phases. A significant accomplishment of Prof. Kryszewski and his co-workers at the

Technical University was development of a new class of conductive materials composed of polymers and organic molecular crystals arranged in a "reticulate-doped" conductive network. Further research, carried out in collaboration with other groups, led to materials characterised by a high anisotropy of electric conductivity, high metallic conductivity and even superconductivity.

His collaborators continued research into dielectrics and high-molecular photoconductors such as thin layers of plasma polymers made of of various heteroorganic monomers. These materials are very important due to their superior dielectric properties, a high thermal and chemical resistance and a capability of modification of their electro-optical properties. Professor Kryszewski was one of pioneers in developing this research frontier in 1960s.

From late 1960s Professor Kryszewski, together with the group, which later continued research at the Centre, was involved in pioneering studies of the morphology of crystalline polymer systems and its correlation with their mechanical, thermal and optical properties. Professor Marian Kryszewski was author and co-author of over 360 original articles and 50 reviews in renowned international journals, 2 monographs, co -editor of 3 books and co-author of 22 inventions patented in Poland and abroad. He was author of the fundamental monograph on electrical properties of polymer systems entitled *Semiconducting Polymers*, first published in Polish in 1968; its enlarged English language edition was co-published by Elsevier and Polish Science Publishers in 1980.

Professor Marian Kryszewski was active member of several scientific societies: member of the Polish Academy of Sciences and its Physics and Chemistry Committees; the Royal Society of Chemistry; the Society of Science Dissemination and Promotion; the European Physical Society. He was active in editorial boards of several journals including the Journal of Applied Polymer Science, Composite Interfaces, Polymers for Advanced Technologies, Polymeric Materials, Polish Journal of Chemistry, Polimery, International Journal of Polymeric Materials, and Materials Science-Poland. He cooperated with many research centres such as the Brooklyn Polytechnic Institute, Claude Bernard University in Lyon, Kyoto University and Max Planck Institute for Polymers Research in Mainz. In recognition of his achievements, he received numerous awards and distinctions including the Maria Curie-Skłodowska Award, the University of Kyoto Medal, the Convallaria Copernicana Distinction. He was also awarded the title of Doctor Honoris Causa by the Technical University of Łódź, and the title of Honorary Professor of the Wrocław University of Technology.

He supervised 45 PhDs, and 12 habilitations were prepared in his scientific school. Many of his former students are now professors at universities or leaders in academic and industrial research centres in Poland and abroad.

The polymer community, to which Professor Kryszewski was always a great authority, has suffered an irretrievable loss.

Andrzej Galeski
Jacek Ulański

Materials Science-Poland, Vol. 23, No. 3, 2005

Ab initio calculations of elastic properties of Ni_3Al and TiAl under pressure*

R. SOT[1, 2**], K. J. KURZYDŁOWSKI[1]

[1]Warsaw University of Technology, Faculty of Materials Science and Engineering, Wołoska 141, 02-507 Warsaw, Poland

[2]Warsaw University, Interdisciplinary Centre for Mathematical and Computational Modelling (ICM), Pawińskiego 5a, 02-106 Warsaw, Poland

The structural parameters and the elastic stiffness coeffcients of Ni_3Al and TiAl under a pressure P were computed by the *ab initio* pseudopotential method with the plane-wave basis set and the generalized gradient approximtion (GGA). The pressure dependence of the elastic constants is an important characteristics for both Ni_3Al and TiAl as these materials are frequently subject to varying pressures during processing. The bulk modulus was also calculated. Stress–strain relationships were used to obtain the elastic constants. The results are in good agreement with the available experimental data.

Key words: *ab initio calculations; density functional calculations*

1. Introduction

In recent years, *ab initio* computations have become one of important tools of modern computational materials science. In the present work, first principles calculations were undertaken for Ni_3Al and TiAl under a pressure P. Ni_3Al compound is known to crystallize in a cubic lattice of Cu_3Au structure type with the space group $Pm\bar{3}m$, while TiAl crystallizes in a tetragonal lattice of AuCu structure type with the space group *P4/mmm*.

2. Computations

For the computations of the crystal structures, ultrasoft pseudopotentials on the assumption of the Gradient Generalized Approximation (GGA) were adopted. The CASTEP [1] program was employed and the computations were carried out at the

---

*The paper presented at E-MRS 2004 Fall Meeting, Warsaw, Poland, 6–10 September, 2004.

**Corresponding author, e-mail: rsot@inmat.pw.edu.pl

ICM of Warsaw University. CASTEP is a DFT pseudopotential total-energy code employing special point integration over the Brillouin zone and a plane-wave basis set for the expansion of the wave functions. The Monkhorst-Pack scheme was used to sample the Brillouin zone. The calculations were considered converged when forces acting on the atoms were less then 0.01 eV/A and the residual bulk stress was smaller than 0.02 GPa. The complete elastic constant tensor from computation of the stresses generated by small deformations of the equilibrium primitive cell [2, 3] was determined. The elastic stiffness tensor $\mathbf{C}$ relates the stress tensor $\boldsymbol{\sigma}$ and the strain $\boldsymbol{\varepsilon}$ by Hooke's law,

$$\sigma_{ij} = C_{ijkl}\,\varepsilon_{kl} \qquad (i,j,k,l = x,y,z) \tag{1}$$

Since the stress and strain tensors are symmetric, the most general elastic stiffness tensor has only 21 non-zero independent components. For cubic crystals, they are reduced to three independent components, $C_{11} \equiv C_{xxxx}$, $C_{12} \equiv C_{xxyy}$, $C_{44} \equiv C_{yzyz}$, (in the Voigt notation). For tetragonal crystals, they are reduced to 6 components.

3. Results

The intermetallic phases, TiAl and Ni_3Al, have been studied by *ab initio* calculations under an applied pressure P. The results for zero-pressure are summarized in Tables 1 and 2 showing the lattice parameters, elastic constants and C_{ij} values calculated *ab initio*, in comparison with experimental data [4–6].

Table 1. Zero-pressure lattice parameters and elastic constants for the Ni_3Al ground-state structure

Method	a [Å]	C_{11} [GPa]	C_{44} [GPa]	C_{12} [GPa]
Ab initio	3.588	230	123	139
Experimental	3.572	230	131	150

Table 2. Zero-pressure lattice parameters and elastic constants for the TiAl ground-state structure

Method	a [Å]	c [Å]	C_{11}[GPa]	C_{33}[GPa]	C_{44}[GPa]	C_{66}[GPa]	C_{12}[GPa]	C_{13}[GPa]
Ab initio	3.989	4.034	170	177	113	73	79	78
Experimental	3.99	4.07	183	178	105	78	74	74

The results of computations under applied pressure P are shown in Figs. 1 and 2 where elastic stiffness C_{ij} is plotted against P.

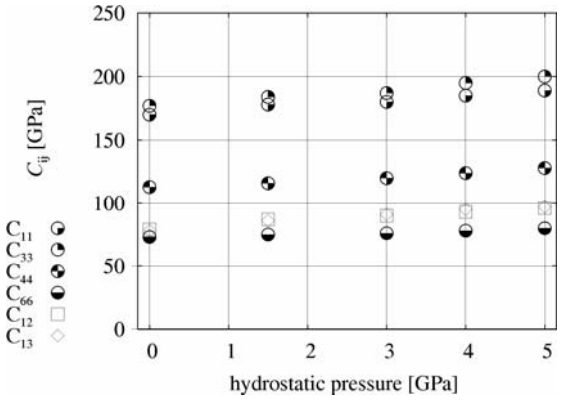

Fig. 1. Elastic stiffness coefficients of TiAl under hydrostatic pressure

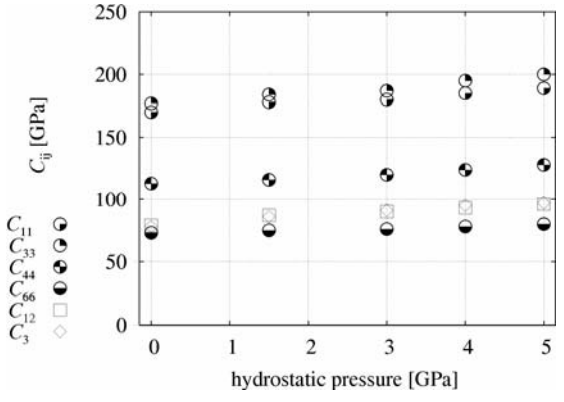

Fig. 2. Elastic stiffness coefficients of Ni_3Al under hydrostatic pressure

These elastic stiffness coefficients satisfy the generalized elastic stability criteria for cubic (Eq. 2) and tetragonal (Eq. 3) crystals under hydrostatic pressure

$$C_{43} > 0, C_{11} > |C_{12}|, C_{11} + 2C_{12} > 0 \tag{2}$$

$$\begin{gathered} C_{11} - C_{12} > 0, \quad \frac{1}{2}(C_{11} - C_{12})C_{33} - C_{12}^2 > 0 \\ C_{11} + C_{12} + C_{33} + \sqrt{(C_{11} + C_{12} - C_{33})^2 + 8C_{13}^2} > 0 \\ C_{44} > 0, C_{66} > 0 \end{gathered} \tag{3}$$

Ab initio computations have been also used to calculate the bulk modulus of the phases *B*, being equal to 109 GPa for TiAl, and 203 for Ni_3Al. Again this is close to the literature value of 108 GPa [5] for TiAl, and 208 GPa [5] for Ni_3Al.

4. Conclusions

Results of *ab initio* calculations for zero pressure are in good agreement with avaiable experimental data (cell constants, elastic constants, bulk moduli). It should be noted that the $C_{ij}(P)$ for Ni_3Al increase linearly with increasing pressure.

Acknowledgements

This study has been supported by the Polish State Committee for Scientific Research, Grant PBZ -KBN-041/T08/2001. The simulations were performed at the Interdisciplinary Centre for Mathematical and Computational Modelling, Pawińskiego 5A, PL-02-106, Warsaw.

References

[1] SEGALL M.D., LINDAN P.L.D., PROBERT M.J., PICKARD C.J., HASNIP P.J., CLARK S.J., PAYNE M.C., *First-principles simulation: ideas, illustrations and the CASTEP code*, J. Phys.: Cond. Matt. 14 (2002), 2717.

[2] KARK B.B. I, STIXRUDE L., CLARK S.J., WARREN M.C., ACKLAND G.J., CRAIN J., Am. Mineral., 82 (1997), 51

[3] WENTZCOVITCH R.M., ROSS N.L., PRIECE G.D., Phys. Earth Planet. Int., 90 (1995), 101.

[4] ICDD 09-0097, J. Met., 9 (1957), 865.

[5] SIMMONS G., WANG H., Single C*rystal Elastic Constans and Calculated Aggregate Properties: A Handbook*, MIT Press, Cambridge, 1971.

[6] *Smithells Metals Reference Book*, 6th Ed., E.A. Brandes (Ed.), Butterworths, London, (1983)

Received 6 September 2004
Revised 4 November 2004

Materials Science-Poland, Vol. 23, No. 3, 2005

Molecular dynamics of hypoxanthine-3-N-oxide near fullerene "sphere" – a computer simulation*

P. RACZYŃSKI**, S. PAŁUCHA, P. BROL, Z. GBURSKI

Institute of Physics, University of Silesia, Uniwersytecka 4, 40-007 Katowice, Poland

A computer simulation (MD method) study is presented for a nanosystem composed of a limited number (n = 15, 25, 35) of hypoxanthine-3-N-oxide (H_3NO) molecules surrounding a single fullerene molecule. The calculations were performed for several temperatures and densities (solid and fluid phases of hypoxanthine-3-N-oxide thin layers). The mean square displacement, diffusion coefficient, linear and angular velocity autocorrelation functions and their Fourier transforms have been obtained for H_3NO.

Key words: *fullerene; hypoxanthine-3-N-oxide; cluster; molecular dynamics*

1. Introduction

The study of bulk samples of fullerene molecules and its compounds is now quite advanced. However, in recent years, one observed vital activity in investigating very small, finite-size fullerene-based systems [1, 2], stimulated by the requirements of bio- and nanotechnology. In this work, an exotic nanosystem, a single fullerene (C_{60}) molecule covered with a number of hypoxanthine-3-N-oxide (H_3NO) molecules was studied *via* the molecular dynamics method (MD) [3]. Amongst other functions [4], (H_3NO) has been identified recently as the putative alarm pheromone of ostariophysan fishes [5].

2. Computational procedure

Use was made of the standard Lennard–Jonnes (LJ) interaction potential V between carbon atoms of buckyball fullerene [1] and the atoms (sites) of hypoxanthine-3-*N*-oxide molecule, as well as between H_3NO and H_3NO sites. Namely,

---

*The paper presented at E-MRS 2004 Fall Meeting, Warsaw, Poland, 6–10 September, 2004.

**Corresponding author, e-mail:praczyns@us.edu.pl

$$V(r_{ij}) = 4\varepsilon\left[\left(\frac{\sigma}{r_{ij}}\right)^{12} - \left(\frac{\sigma}{r_{ij}}\right)^{6}\right]$$

where r_{ij} is the distance between the atoms i and j, ε is the minimum of the potential at a distance $2^{1/6}\sigma$, k_B is the Boltzmann constant. The LJ potential parameters ε and σ are given in table 1 [6]. The L-J potential parameters between unlike atoms are given by the Lorentz–Berthelot rules [3].

Table 1. The Lennard–Jones parameters

Atoms	ε/k_B [K]	σ [Å]	m [10^{-25} kg]
C	58.2	3.851	0.199
O	88.7	2.95	0.26551
N	37.3	3.31	0.11616
H	12.4	2.81	0.016594

The classical equations of motion are integrated up to 5 ns by the predictor-corrector Adams–Moulton algorithm [7]. The integration time step was 0.4 fs which ensures total energy conservation within 0.01%. The initial distribution of molecules was generated by the Monte Carlo (MC) algorithm [3] (10^6 MC steps).

3. Results

In Figure 1, the calculated mean square displacement $\left\langle \left|\Delta\vec{r}(t)\right|^2 \right\rangle$ of the centre of mass of H_3NO is presented for the temperature range of 15–65 K and the concentrations of $C_{60}(H_3NO)_{15}$, $C_{60}(H_3NO)_{25}$ and $C_{60}(H_3NO)_{35}$.

The mean square displacement is definied by $\left\langle \left|\Delta\vec{r}(t)\right|^2 \right\rangle = \left\langle \left|\vec{r}(t) - \vec{r}(0)\right|^2 \right\rangle$, where $\vec{r}$ is the position of the centre of mass of a single molecule [3]. It is known [8] that the slope of $\left\langle \left|\Delta\vec{r}(t)\right|^2 \right\rangle$ is proportional to the translational diffusion coefficient D of a molecule, for the calculated D values of H_3NO, see Fig. 2.

The solid phase appeared at low temperature (T = 15 K) for all concentrations. The nonzero slope of $\left\langle \left|\Delta\vec{r}(t)\right|^2 \right\rangle$ for higher temperatures is the indication of the translational diffusion of hypoxanthine-3-*N*-oxide molecule (liquid phase). The calculated diffusion coefficients of C_{60} and H_3NO molecules in $C_{60}(H_3NO)_{35}$ are compared in Fig. 3.

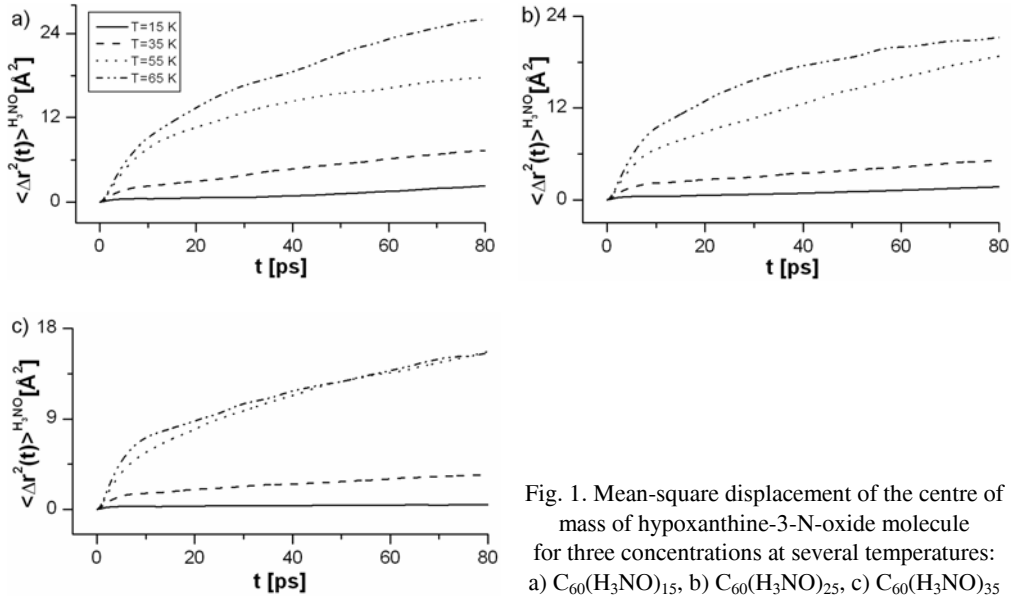

Fig. 1. Mean-square displacement of the centre of mass of hypoxanthine-3-N-oxide molecule for three concentrations at several temperatures: a) $C_{60}(H_3NO)_{15}$, b) $C_{60}(H_3NO)_{25}$, c) $C_{60}(H_3NO)_{35}$

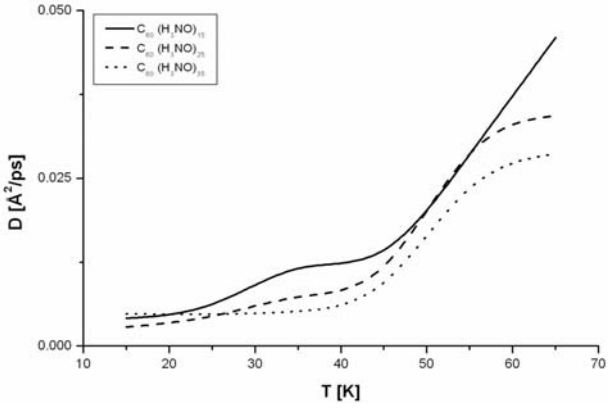

Fig. 2. Translational diffusion coefficient *D* of the centre of mass of hypoxanthine-3-N-oxide molecule for three concentrations at several temperatures

As expected, due to a large difference between the masses of the molecules, the value of *D* for fullerene molecules is much smaller than that for H_3NO and the motion of fullerene during the observed time scale is practically negligible. In Figure 4, one can see the velocity autocorrelation function (VACF)

$$C_{\vec{v}}(t) = \left\langle \vec{v}(t)\vec{v}(0) \right\rangle \left\langle \vec{v}(0)\vec{v}(0) \right\rangle^{-1}$$

where $\vec{v}(t)$ is the translational velocity of the centre of mass of H_3NO molecule, simulated for several temperatures and concentrations.

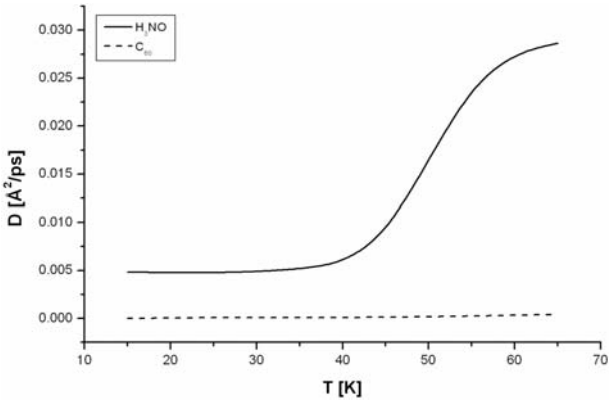

Fig. 3. Calculated diffusion coefficients of C_{60} and H_3NO molecules

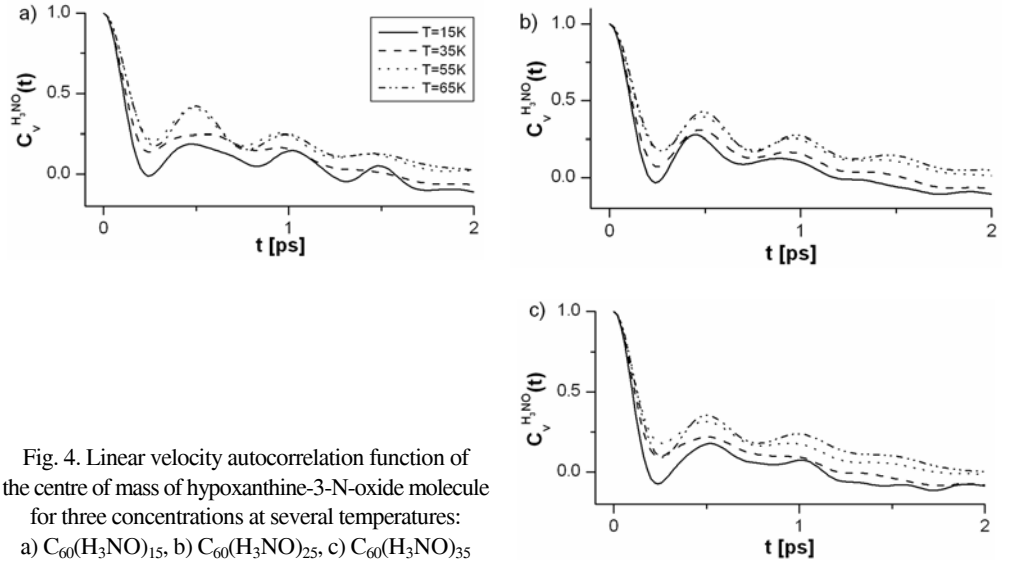

Fig. 4. Linear velocity autocorrelation function of the centre of mass of hypoxanthine-3-N-oxide molecule for three concentrations at several temperatures: a) $C_{60}(H_3NO)_{15}$, b) $C_{60}(H_3NO)_{25}$, c) $C_{60}(H_3NO)_{35}$

The VACF correlation function at the lowest temperature studied, T = 15 K, shows dumped oscillation with the first dip negative – the behaviour attributed to the solid phase. The oscillations of VACF become less pronounced and the first dip never gets negative for higher temperatures (a softer liquid like phase.). Figures 5–7 show the angular velocity correlation functions (AVCF)

$$C_{\vec{\omega}}(t) = \left\langle \vec{\omega}(t)\vec{\omega}(0) \right\rangle \left\langle \vec{\omega}(0)\vec{\omega}(0) \right\rangle^{-1},$$

where $\vec{\omega}(t)$ is the angular velocity of molecule for both C_{60} and H_3NO molecules, as well as their frequency Fourier transforms. In the case of C_{60}, increasing the temperature from T = 15 K to T = 65 K shifts the extrema of AVCFs towards shorter times (faster reorientation, see Fig. 5a).

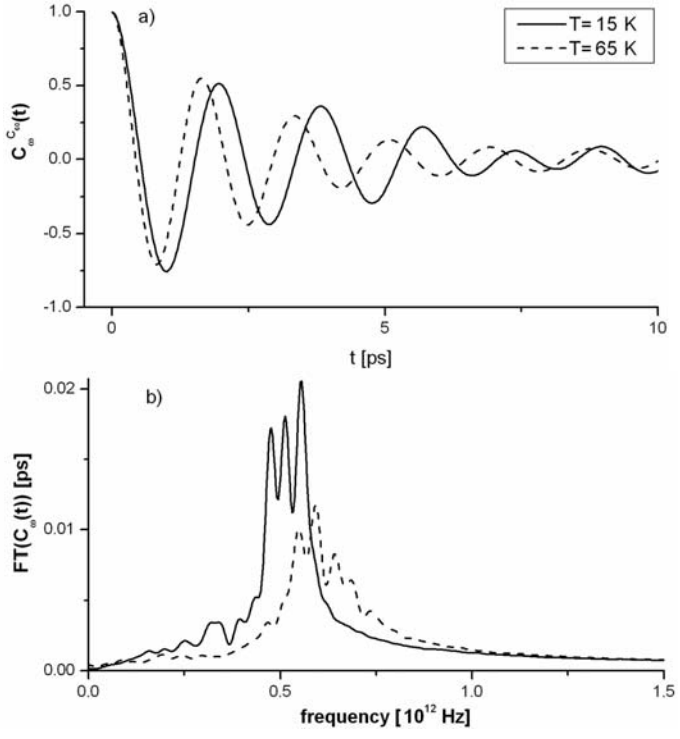

Fig. 5. Angular velocity autocorrelation function of C_{60} molecule in $C_{60}(H_3NO)_{35}$ for several temperatures (a) and the corresponding Fourier transforms (b)

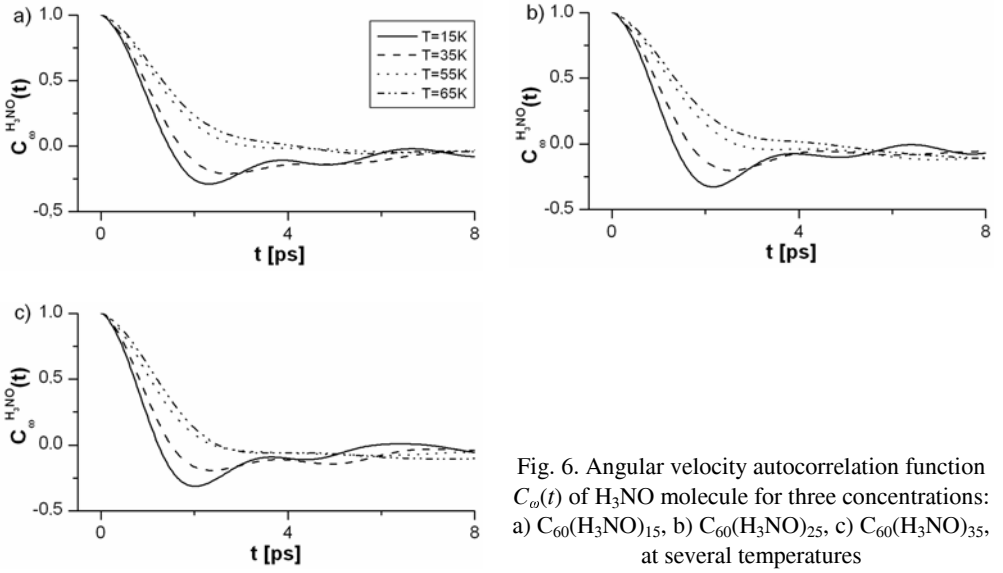

Fig. 6. Angular velocity autocorrelation function $C_{\omega}(t)$ of H_3NO molecule for three concentrations: a) $C_{60}(H_3NO)_{15}$, b) $C_{60}(H_3NO)_{25}$, c) $C_{60}(H_3NO)_{35}$, at several temperatures

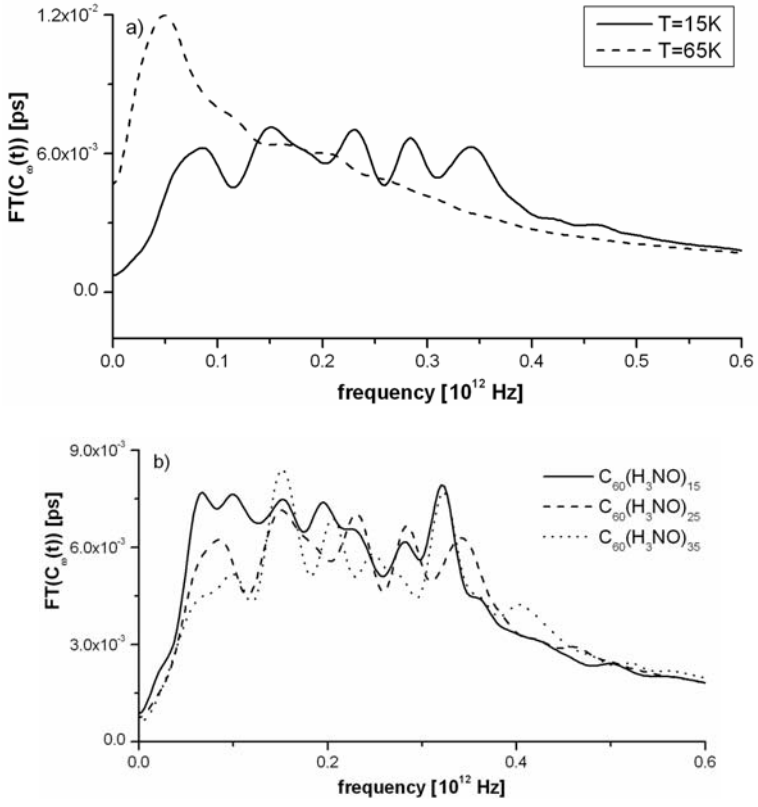

Fig. 7. The Fourier transform of $C_\omega(t)$ of H_3NO molecule in $C_{60}(H_3NO)_n$ cluster: a) $n = 25$, $T = 15$ K and 65 K; b) $n = 15, 25, 35$, $T = 15$ K

The increase of temperature from $T = 15$ K to $T = 65$ K shifts the maxima of the frequency spectrum (Fourier transform) of AVFC from around 5×10^{11} Hz to 6.2×10^{11} Hz. Switching the attention to reorientation of H_3NO molecules one can note, that below $T = 55$ K all AVCF's possess a well defined negative value dip at mid-time (~2 ps) (Fig. 6a–c).

For $T = 55$ K and above AVCFs have the shape similar to the unconstrained rotation [8]. These facts may be an indication of a phase transition around $T = 50$ K. Further support to this conclusion comes from the inspection of Fourier transforms of AVCF (Fig. 7).

Increasing the temperature changes the broad band between $(1–3.5)\times10^{11}$ Hz (solid phase) to the sharp peak around 5×10^{10} Hz after the solid–liquid phase transition (Fig. 7a). The Fourier transform of AVCF in the solid phase ($T = 15$ K) depends only slightly on the number of H_3NO molecules in the layer (Fig. 7b). The Fourier transform plots of VACF and AVCF in the liquid phase ($T = 65$ K) of $C_{60}(H_3NO)_n$ for $n = 15, 25, 35$ are presented in Fig. 8a, b. Here again, the n-dependences of VACF and AVCF are rather weak.

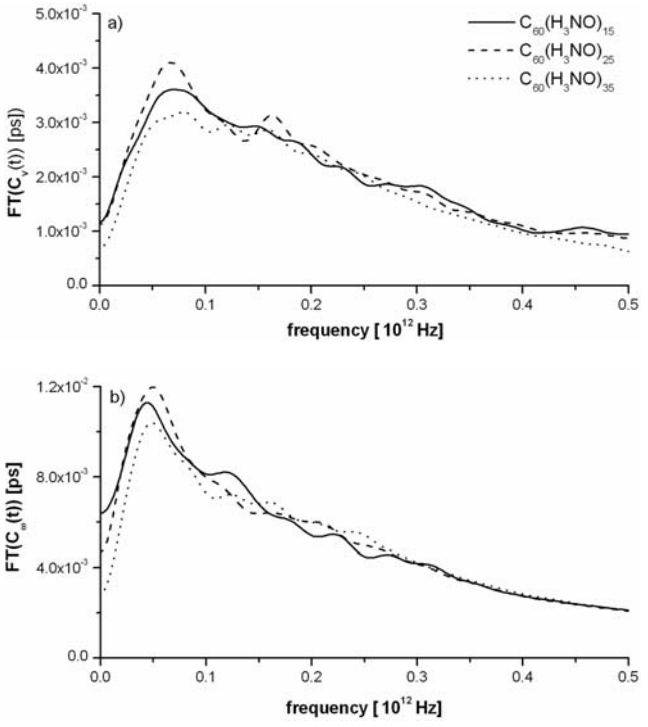

Fig. 8. The Fourier transform of: $C_v(t)$ (a) and $C_\omega(t)$ (b) of H_3NO molecule in $C_{60}(H_3NO)_n$ cluster; n = 15, 25, 35, T = 65 K for both a) and b)

4. Conclusion

In conclusion, it has been shown that well distinguished solid and liquid phases of a spherically shaped hypoxanthine-3-N-oxide layer surrounding fullerene molecule can be observed. The solid–liquid phase transition appears arround T = 50 K. The translational diffusion coefficient of hypoxanthine-3-N-oxide molecule in the liquid phase of the layer has been determined. The mobility (diffusion) of H_3NO molecule in the liquid phase at a given temperature slightly depends on the number of hypoxanthine-3-N-oxide molecules surrounding fullerene (forming the layer). The preliminary MD simulations presented here may encourage some future experimental research in this field.

References

[1] DRESSELHAUS M.S., DRESSELHAUS G., EKLUND P.C., *Science of Fullerenes and Carbon Nanotubes*, Academic Press, New York, 2000.

[2] DAWID A., GBURSKI Z., J. Phys.: Cond. Matter, 15 (2003), 2399.

[3] ALLEN M.P., TILDESLEY D.J., *Computer Simulation of Liquids*, Oxford University Press, Oxford, 1989.
[4] MURARY R., *Harper's Biochemistry*, McGraw-Hill, Maidenhead, Berkshire, 2003.
[5] BROWN G.E., ADRIAN J.C., PATTON T. Jr., CHIVERS D.P., Can. J. Zool., 79 (2001), 2239.
[6] DAWID A., GBURSKI Z., Phys. Rev. A, 68 (2003), 065202.
[7] RAPAPORT D.C., *The Art of Molecular Dynamics Simulation*, Cambridge University Press, Cambridge, 1995.
[8] BARNER A.J.S, ORVILLE-THOMAS W.J., YARWOOD J., *Molecular Liquids*, Reider, Dordecht, 1984.

Received 7 September 2004
Revised 12 October 2004

Materials Science-Poland, *Vol. 23*, *No. 3*, *2005*

The search for minimum potential energy structures of small atomic clusters. Application of the ant colony algorithm*

P. RACZYŃSKI**, Z. GBURSKI

Institute of Physics, University of Silesia, Uniwersytecka 4, 40-007, Katowice, Poland

The ant colony algorithm has been applied to the problem of finding the minimal potential energy configuration of a small physical system (cluster) of atoms interacting via the Lennard–Jones phenomenological potential. The ants were positively motivated if their activity (displacement of atomic positions) leads to a lower total potential energy of the system. Starting from a random spatial distribution of atoms, during the optimalization process, the ants were able to find configurations with energies much lower than the initial ones. The optimized configurations generated by the ant colony algorithm can be used as a good starting point for classical or *ab initio* molecular dynamics (MD) simulations.

Key words: *ant colony algorithm; cluster; potential energy; computer simulations*

1. Introduction

The ant colony algorithm has been widely used to solve more and more problems including the famous Travelling Salesman Problem [1, 2], Vehicle Routing Problems [3], etc. The main idea of this algorithm is to duplicate the way the ants search for food and transport it to the ant-hill (using pheromone traces). In other words, it is an adaptation of the natural search behaviour of ants in an ant colony. Usually, at the beginning, the ants use, or try, many random paths. However, after some time – due to mutual exchange of information in the ant society achieved by chemical tracing (pheromone) – a particular path becomes the most preferred, i.e. there is the highest concentration of pheromone on this chosen track. The application of the ant colony algorithm to the important problem of searching for the minimal potential energy configuration of a physical system of interacting atoms is shown.

---

*The paper presented at E-MRS 2004 Fall Meeting, Warsaw, Poland, 6–10 September, 2004.

**Corresponding author, e-mail: praczyns@us.edu.pl

2. Search procedure

The physical system of interest is a cluster composed of n identical atoms embedded in a cubic box of edge length a. To be more specific, let us consider they are argon (Ar) atoms and $n = 7$. The interaction potential $V(r_{ij})$ between a pair of argon atoms is well described by the Lennard–Jones (LJ) equation [4]

$$V(r_{ij}) = 4\varepsilon \left[\left(\frac{\sigma}{r_{ij}} \right)^{12} - \left(\frac{\sigma}{r_{ij}} \right)^{6} \right]$$

where r_{ij} is the distance between an ith and jth atom. The total potential energy of the system is

$$\varphi = \sum_{i,j=1,j>i}^{n} V(r_{ij})$$

The LJ potential parameters ε and σ for argon are given in Table 1 [5], where k_B is the Boltzmann constant.

Table 1. The Lennard–Jones parameters for argon

Atoms	ε/k_B [K]	σ [Å]	m [10^{-25} kg]
Ar	119.8	3.4	0.664

The number of ants has been chosen as equal to the number of atoms (interacting sites). The initial position $\mathbf{r}_i = (x_i, y_i, z_i)$ of the ith atom has been randomly chosen within the range $[0,a]$ for each component of $\mathbf{r}_i$. In case the positions of neighbouring atoms were too close to each other, the drawing process for these atoms was repeated. This ensures that the system does not explode accidentally. The centre of mass $\mathbf{R}_{CM}$ of the system was calculated. The ants were positively motivated by three factors: pheromone value, drawing the positions of the atoms towards the centre of mass and most importanly, decreasing of the total potential energy. The positions of n atoms can be represented by a graph in three-dimensional space. The vertices of this graph are Ar atoms. Each ant draws one graph's vertex (pick up an atom). Following the ant algorithm procedure [6], the pheromone matrix for this initial configuration must be defined. The pheromone matrix is composed of a pair (i, j) of coefficients characterising the attractiveness of the (i, j) connection (edge) between the ith and jth vertex of the graph. Since at the begining no ant knows more or less than any other, all coefficients of the pheromone matrix are initialized by the same value τ between [0,1].

After establishing the initial conditions, the algorithm described starts. This means the first ant randomly moves the position of one of the $n - 1$ atoms (excluding the atom it is associated with) and the Lennard–Jones potential for this perturbed configu-

ration is calculated and memorized. Then the ant puts the just moved atom to its previous position and randomly moves the next one of the $n - 2$ atoms. The LJ potential for this system is again calculated and memorized. The ant applies the same procedure to the remaining $n - 3$ atoms, etc. The described procedure is repeated by all ants.

Now, each ant knows $n - 1$ potential energies (configurations) corresponding to the random displacements of all vertices of the graph (atoms), except the one where the ant actually remains. To consider next move the ant can use one of two possibilities distinguished by a real number q_0 ($q_0 \in [0...1]$), which is supplied in the set of the starting parameters (see Table 1). The algorithm randomly draws a number between 0 and 1 and compares it to q_0. If this number is smaller than q_0, the first possibility is to find a local best minimum [6] defined by the formula:

$$S(i,j) = \arg\max\{[\tau(i,j)][\eta(i,j)]^{\beta}\}$$

where $\tau(i, j)$ is the pheromone coefficient between the ith and jth vertical (atom), $\eta(i, j) = 1/\varphi$, where φ is the total potential energy of the system in which only the position of (jth) atom has been changed, β is a heuristic parameter which determines the relative importance of the pheromone versus the atomic displacement ($\beta > 0$). The ant will chose the configuration for which the calculated value S(i,j) is the largest, denoted here by argmax. The other possibility (when the randomly drawn number is larger than q_0) is to construct the matrix of probabilities

$$p(i,j) = \frac{[\tau(i,j)][\eta(i,j)]^{\beta}}{\sum[\tau(i,j)][\eta(i,j)]^{\beta}}, \qquad 0 \le p(i,j) \le 1$$

The value of $p(i, j)$ is larger if the LJ potential energy is lower and the pheromone value between the ith and jth vertex is larger. By definition, the sum over j of $p(i, j)$ must be equal to 1 for any fixed i. For fixed $i = i_0$, each $p(i_0, j)$ can be associated with a particular segment from the [0, 1] range. The sum of these segments must be equal to 1 and the whole [0, 1] range is filled. The larger segment of [0, 1] range is associated with the larger $p(i_0, j)$. Then a real number beetwen 0 and 1 is randomly generated, this value falls into one of the segments associated with $p(i_0, j)$, and for that matter with one of the vertices j. If the random number indicates the $p(i_0, j')$ segment of [0,1], the vertex to be chosen is j'.

Before the algorithm step is completed, the local pheromone update is required, i.e. each ant between t, $t + 1$ step, lays a quantity of pheromone on the edge connecting ith and jth vertices (in our case i_0 and j' vertices), following the formula [7]:

$$\Delta\tau_{(i,j)}(t,t+1) = (1-\rho)\tau_{(i,j)}(t) + \rho k \tau_0 \tag{1}$$

where k is the number of ants that visited the same atom (i) and all of them moved another atom (j), ρ is a real number between <0,1> which takes care of the intensity of pheromone [7]. The applied ant algorithm parameters are given in Table 2.

Table 2. The applied algorithm parameters

Parameter symbol	Value
β	5
q_0	0.65
ρ	0.23
τ_0	1

What has been described is one step of the algorithm. The next steps would be essentially similar except that the ant cannot move the vertices already moved in the previous steps. Hence, the total number of steps in the cycle cannot be higher than the number of vertices (atoms) minus one.

At the end of each cycle (composed of maximum $n - 1$ steps), the global pheromone update is performed. This means that the most effective attempt (displacement of atoms) which leads to the lowest LJ potential energy during the cycle, will be marked by an additional amount of pheromone. The formula for global pheromone update is given by [6]:

$$\Delta\tau_{(i,j)}(t,t+z) = (1-\rho')\tau_{(i,j)}(t) + \rho'\tau_{0(i,j)}(t,t+z)$$

where ρ' has the same meaning as ρ in Eq. (1), z is the sum of steps in a cycle. The most effective try will be used as a starting point for a new cycle.

The number of cycles can be very large, the finite number of cycles is called an experiment. For the interpretation we used the average of many experiments.

3. Results

Calculations were performed for a small cluster composed of $n = 7$ argon atoms. Figure 1 shows an example of the initial (randomly chosen) configuration of atoms located in a cubic box (the length of edge $a = 3$ *nm*).

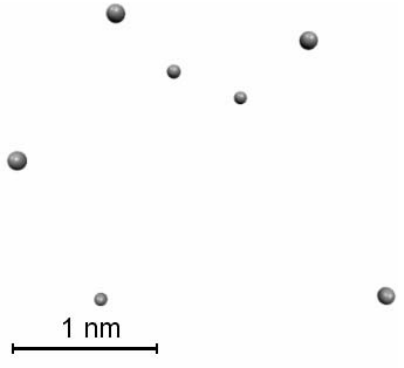

Fig. 1. The snapshot of the starting configuration of Ar_7 cluster (a = 3 nm)

Several values of a have been used for testing the effectiveness of the alghorithm. A natural physical criterion for a stable equilibrium structure is the requirement of minimum potential energy in the system. Guided by this, the ant colony optimalization procedure has been performed. The evolution of potential energy V of the Ar_7 cluster averaged over 10^3 experiments as a function of the number of cycles is given in Fig. 2, for several sizes of the cubic box.

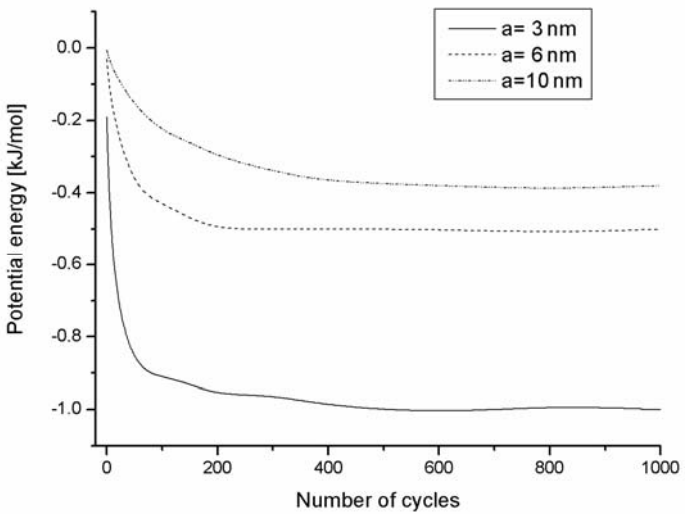

Fig. 2. The average values of the potential energy of Ar_7 cluster (a = 3, 6, 10 nm)

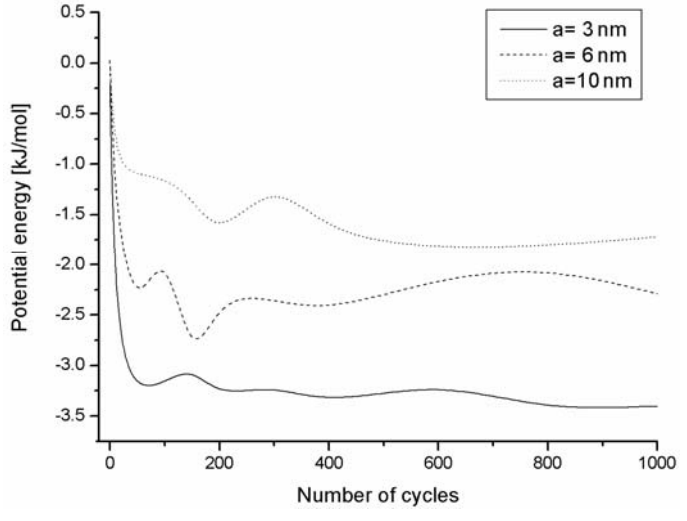

Fig. 3. Examples of potential energy of Ar_7 cluster (a = 3, 6, 10 nm)

The quick relaxation of V towards the required (lower) value can be seen, followed by the saturation. Performing more cycles in the saturation area does not seem

to be effective. The saturated potential energy does depend on the size of the box. The start of optimization procedure in a smaller box leads to a substantially lower energy. Making the box too large generates too many configurations to be checked and the algorithm has the tendency to stop at the local minimum. It is not believed that this type of weakness of the ant algorithm in this context has been reported. Figure 2 shows the average of 10^3 experiments. Figure 3 presents an example of single optimization (non averaged) which is much better as it shows a lower potential energy than the averaged one. The differences between single optimization could be quite substantial and in Fig. 4 the comparison of two extreme optimizations for $a = 3$ *nm* is shown.

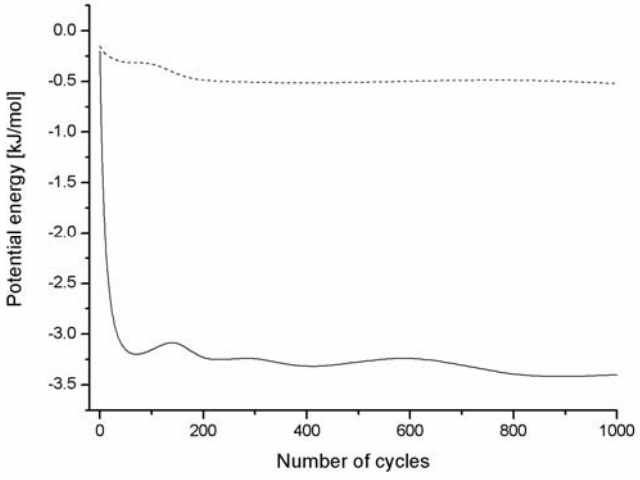

Fig. 4. The comparison of two extreme optimalizations of Ar_7 (a = 3 nm)

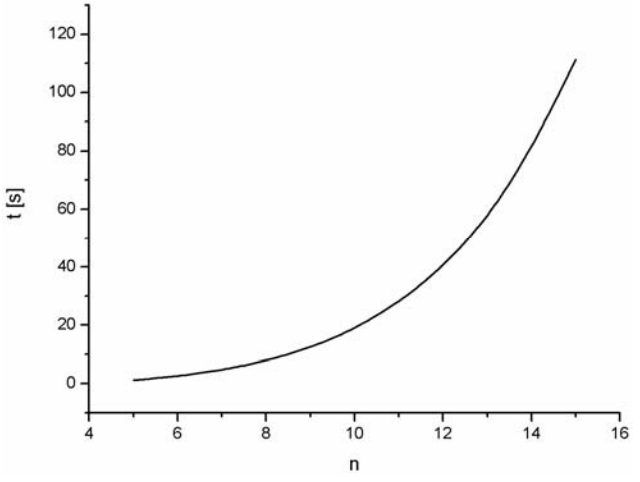

Fig. 5. The calculation time of one cycle of optimalization for Ar_n clusters (n = 5, 7, 10, 13, 15; a = 3 nm; CPU AMD Athlon 2GHz)

It was found that the calculation time t_c required for one cycle was dependent on the number n of atoms in the cluster. This is illustrated in Fig. 5, t_c increases rapidly, non-linearly, with the growing number of atoms.

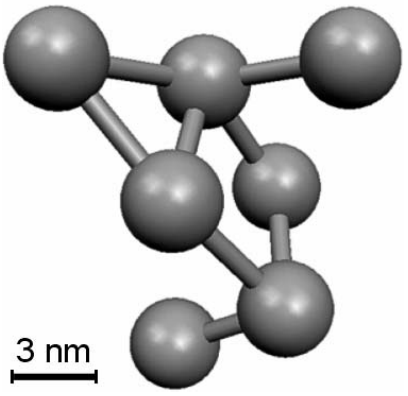

Fig. 6. The snapshot of optimized configuration of Ar_7 cluster (a = 3 nm)

The final cluster's configuration obtained from the initial positions of argon atoms (shown in Fig. 1) is given in Fig. 6.

4. Conclusions

Although the authors cannot guarantee that this is the structure corresponding to the global minimum of potential energy, the increased level of condensation (packing) of the cluster is evident. That was the configuration looked for at the beginning of molecular dynamics or Monte Carlo simulations of the clusters. Starting from this, partially optimized configuration could save computer time for calculations which are solely based on laws of physics (for example molecular dynamics (MD) simulations). This study shows that the ant colony algorithm could be implemented into MD programs as a helpful tool for establishing a reasonable starting configuration. Unfortunately, without additional conditions, one should not expect the ant colony algorithm to guarantee finding the global minimum of potential energy.

References

[1] PALETTA G., Comp. Oper. Res., 29 (2002), 1343.
[2] DORIGO M., GAMBARDELLA L.M., Biosystems, 43 (1997), 73.
[3] CHIANG W., RUSSELL R., Annals of Oper. Res., 63 (1996), 1.
[4] ALLEN M.P., TILDESLEY D.J., *Computer Simulation of Liquids*, Oxford University Press, Oxford, 1989.
[5] DAWID A. GBURSKI Z., J. Phys. Condens. Matter, 15 (2003), 2399.

[6] BONABEAU E., DORIGO M., THERAULAZ G., *From Natural to Artificial Systems*, Oxford University Press, Oxford, 1999.
[7] CORNE D., DORIGO M., GLOVER F., *New Ideas in Optimalization*, Mc Graw-Hill, Maidenhead, Berkshire 2000.

Received 27 September 2004
Revised 1 December 2004

Materials Science-Poland, Vol. 23, No. 3, 2005

A new simple fractal method for nanomaterials science and nanosensors*

W. KLONOWSKI[1,2**], E. OLEJARCZYK[1,2], R. STĘPIEŃ[1,2]

[1]Institute of Biocybernetics and Biomedical Engineering, Polish Academy of Sciences, Warsaw, Poland

[2]GBAF, Medical Research Center, Polish Academy of Sciences, Warsaw, Poland

We proposed a very simple new method of quantitative assessment of surface roughness and texture. We have combined methods that have been used in medicine (histopathology) with methods used in nonlinear time series analysis. A greyscale 2-D image of a 3-D surface is used for calculations of the surface fractal dimension which is a good measure of surface roughness. In the pre-processing step, the image is transformed into 1-D signals ("landscapes") that are subsequently analyzed. The method draws from multiple disciplines and has multidisciplinary applications. One of the possible applications is quality assessment of nanosensors. The same methods of analysis may be used for processing of (bio)signals generated by these nanosensors.

Key words*: fractal dimension; nanosensors; nanomaterials; quality assessment; signal analysis*

1. Introduction

Calculating materials properties from structural models has been one of the most important problems in materials science [1]. There is still a need for relatively simple methods to assess properties of materials, especially surface properties, based on the analysis of experimental data such as microscopic images. Fractal and symbolic methods of image and signal analysis can be very useful for these purposes. The problem is that there exist very different definitions of fractal dimension and very different methods are implemented for their calculations [2]. As scientists become more specialized in narrow disciplines, frequently the methods which need to be applied in their research may have been used in other disciplines for a long time. When we learn this we are often amazed, like Molier's Mr. Jourdain (*Le Bourgeois Gentilhomme*

---

*The paper presented at E-MRS 2004 Fall Meeting, Warsaw, Poland, 6–10 September, 2004.

**Corresponding author, e-mail: wklon@ ibib.waw.pl

II.iv), who says: "Good heaven! For more than forty years I have been speaking prose without knowing it". What is needed is a very multidisciplinary approach to the problems and these methods both, draw from multiple disciplines and have multidisciplinary applications.

These methods may be used for assessing structural properties of materials as well as for quality assessment of nanosensors as their quality depends on surface roughness and texture. Nanotechnologies provide new sensors that enable easy acquisition of biosignals for monitoring of drivers, pilots, etc. and for clinical applications. But before any signal generated by a nanosensor can be used for monitoring or clinical assessment, the signal has to be appropriately processed and visualized. The same data-processing methods, based on fractal and symbolic computational methods, may be used for extraction, fusion, and visualization of multi-modal information from nanosensors for representing and managing signal complexity. These methods are computationally effective and may be applied in real time.

The symbolic method proposed for signal analysis leads to similar results as the fractal dimension method [3, 4], but needs greater sets of data (i.e. longer signals) than those considered here as examples.

2. Methods

The fractal dimension is a good predictor of people's perception of surface roughness [5, 6]. A new method of inferring fractal dimension of a 3-D surface (i.e., of a surface in 3-D physical space) from a 2-D greyscale image of that surface has been developed – the image data are preprocessed to produce 1-D *landscapes*, which are analyzed using signal analysis methods. In this way, the dimensionality of the problem and so its computational complexity is drastically reduced.

A digitized image can be viewed as a surface for which x- and y-coordinates represent position and the z-coordinate represents *grey* level (intensity). The fractal nature of this putative, statistically self-affine surface can then be characterized, both in the spatial domain with fractal dimension, and in the frequency domain with spectral exponent β.

Fractal dimension is invariant with respect to linear scale transformations and it is simply related to power spectrum exponent β. If a fractal Brownian surface embedded in 3-D space has fractal dimension D_s and the power spectrum proportional to f^{β}, its 2-D image shows power spectrum proportional to $f^{2-\beta}$, where $\beta/2 = (3 - D_s)$. Thus, one can use the power spectrum of the image to assess the fractal dimension of the surface. β is also simply related to the Hurst exponent [5, 6]. However, this method of calculation of fractal dimension is much simpler than the spectral or Hurst methods.

Epithelial roughness and texture play a central role in histopatological diagnosis of malignancy. Mattfeldt (1997) preprocessed microscopic 2-D images of tumor cells' epithelium into 1-D signals (*landscapes*) and then embedded these signals in a phase

space, using a 'time-delay' method. He found that the *correlation dimension* differed considerably between benign and malignant mammary gland tumors [7]. Here we propose to use a similar simple method for preprocessing the surface's 2-D image to construct 1-D landscapes, but in the second step to use Higuchi's fractal dimension method [8] for analysis of the landscapes obtained.

A digitized image is a pattern stored as a rectangular data matrix. Grayscale images are matrices where the matrix elements can take on values from 0 to $g_{\max}=(2b-1)$, where b denotes number of bits (for $b = 8 g_{\max} = 255$). The rendering on a video screen is a presentation of the values from white (0) to black ($2b - 1$). Most colour images are overlays of three grayscale images.

Stepping through a grey value image length of N pixels and height of M pixels *row by row* the sum of the grey values in each row, G_m ($m= 1, \ldots, M$), are calculated and the numbers normalized by using the largest of those values G to produce the "horizontal" landscape

$$NGS_m = \frac{G_m}{G}$$

Similarly, stepping through the same image column by column ($n = 1, \ldots, N$) another, "vertical" landscape is produced as shown in. Fig. 1.

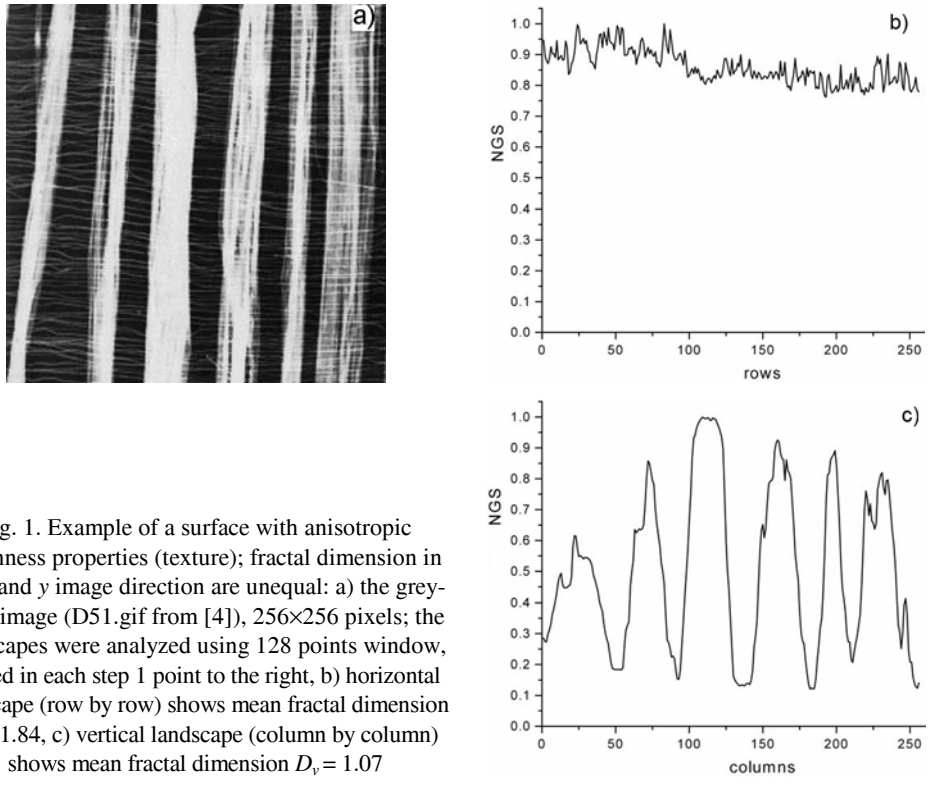

Fig. 1. Example of a surface with anisotropic roughness properties (texture); fractal dimension in the x and y image direction are unequal: a) the grey-scale image (D51.gif from [4]), 256×256 pixels; the landscapes were analyzed using 128 points window, moved in each step 1 point to the right, b) horizontal landscape (row by row) shows mean fractal dimension $D_h = 1.84$, c) vertical landscape (column by column) shows mean fractal dimension $D_v = 1.07$

If necessary, other landscapes may be constructed using a similar counting technique, stepping through the same picture in different directions, e.g. in diagonal directions, or in some rectangular frames. The resulting *NGS* series serve as an input for the subsequent signal analysis using Higuchi's fractal dimension or symbolic dynamics methods.

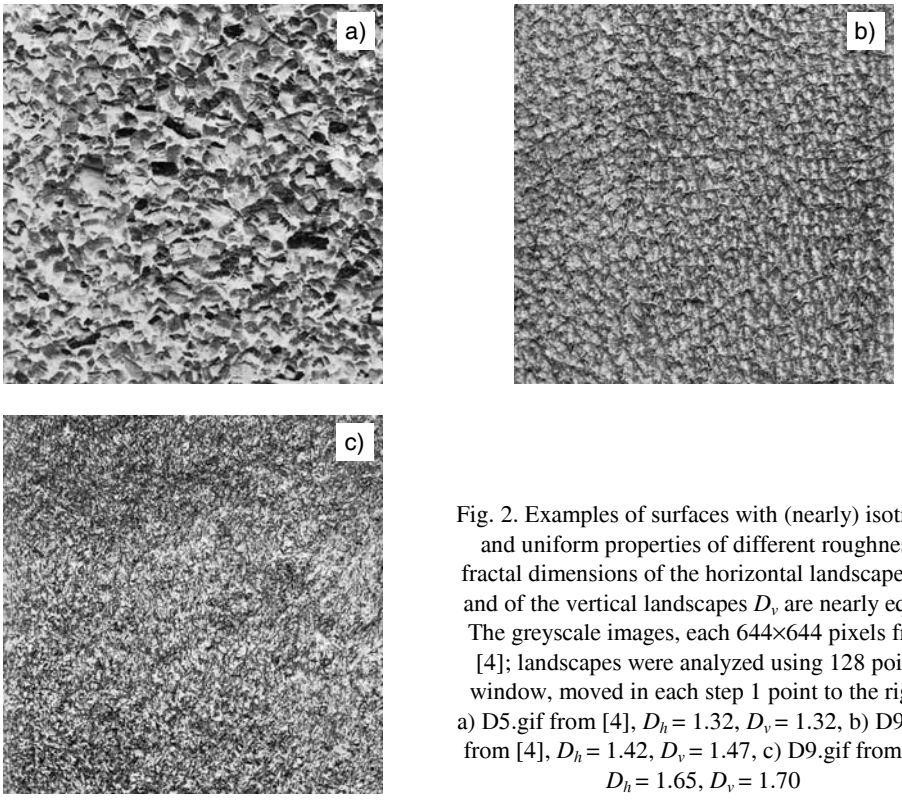

Fig. 2. Examples of surfaces with (nearly) isotropic and uniform properties of different roughness; fractal dimensions of the horizontal landscapes D_h and of the vertical landscapes D_v are nearly equal. The greyscale images, each 644×644 pixels from [4]; landscapes were analyzed using 128 points window, moved in each step 1 point to the right: a) D5.gif from [4], $D_h = 1.32$, $D_v = 1.32$, b) D92.gif from [4], $D_h = 1.42$, $D_v = 1.47$, c) D9.gif from [4], $D_h = 1.65$, $D_v = 1.70$

Higuchi's fractal dimension D is calculated directly from the time series, without embedding the data in a phase space as in the case of e.g., correlation dimension. D_f is, in fact, a fractal dimension of the curve representing the signal under consideration, and so it is always between 1 and 2. Since a simple curve has dimension equal 1 and a plane has dimension equal 2, the fractional part of D_f is a measure of the signal complexity. D_f should not be misled with fractal dimension of an attractor in the system's phase space.

3. Results

As examples we present here analysis of surface images from [9]. If a surface shows anisotropic roughness properties (texture) then fractal dimensions of the hori-

zontal and vertical landscapes differ one from another (Fig. 1). On the other hand, fractal dimensions of landscapes for surfaces that show isotropic roughness properties change appropriately with changes of surface properties – the smaller are unevennesses of the surface, the greater are fractal dimensions of its landscapes (Fig. 2).

4. Discussion

Fractal dimension of a surface is invariant with respect to linear transformation of the data and to transformation of scale. So, the normalization in Eq. (1) is convenient for presentation of the landscapes, but it is not really necessary since it does not change the value of Higuchi's fractal dimension; thus the time necessary for calculations may be even further reduced. Fractal dimension calculated from an image, by virtue of its independence with respect to scale, appears to be nearly independent of the orientation of the surface. If the fractal dimension in the x and y image direction are unequal the surface is anisotropic.

The fractal dimension of a natural surface depends on the dominant process at any particular scale. That is why a surface may need multifractal description [10]. The aim of measuring fractal dimensions is not only to add new structural parameters to already existing ones, possibly describing new structural characteristics but a more important aim is to get a deeper insight into the development of complex structures and the processes that contribute to structure forming.

Fractal methods are becoming increasingly more important in the study of materials characteristics and/or underlying processes' classification [10, 11] as well as in signal analysis [12] and image recognition [13].

5. Conclusions

The proposed method may serve for simple quantitative assessment of surface roughness and texture, in particular for comparative quality assessment of nanosensors. It is also attractive that the same fractal method may be used for processing of (bio)signals generated by nanosensors. Our philosophy is that to be applicable a method should preferably be really simple and easily understandable by non-specialists in the field. The presented fractal method is very simple and it both draws from multiple disciplines and have multidisciplinary application.

Acknowledgements

This work was partially supported by the Polish Ministry of Science and Information Society Technologies (formerly State Committee for Scientific Research (KBN)) grant No. 4 T11F 01 922 and by FP6. Integrated Project SENSATION (IST 507231).

References

[1] KLONOWSKI W., Can. J. Phys., 66 (1989), 1051, 1061; http://hrabia.ibib.waw.pl/~lbaf/PDF_Doc/k32.pdf; http://hrabia.ibib.waw.pl/~lbaf/PDF_Doc/k33.pdf.
[2] KLONOWSKI W., Mach. Graph. Vis., 9 (2000), 403; http://hrabia.ibib.waw.pl/~lbaf/PDF_Doc/gkpo2000.pdf.
[3] KLONOWSKI W., OLEJARCZYK E., STEPIEN R., N*ew Methods of Nonlinear and Symbolic Dynamics in Sleep EEG-Signal Analysis*, [in:] D.D. Feng, E.R. Carson (Eds.), *Modelling and Control in Biomedical System*, IFAC Publications, Elsevier, Oxford, 2003, pp. 241–244.
[4] KLONOWSKI W., OLEJARCZYK E., STEPIEN R., Physica A, 342 (2004), 701.
[5] PENTLAND A.P., IEEE Trans. Patt. Anal. Mach. Intel., 6 (1984), 661.
[6] KUBE P., PENTLAND A., IEEE Trans. Patt. Anal. Mach. Intel.,10 (1988), 704.
[7] MATTFELDT T., *Spatial Pattern Analysis using Chaos Theory: A Nonlinear Deterministic Approach to the Histological Texture of Tumours*, [in:] G.A. Losa, D. Merlini, T.F. Nonnenmacher, E.R. Weibel (Eds.), *Fractals in Biology and Medicine*, Vol. II, Birkhäuser, Basel, 1997, pp. 50–72.
[8] HIGUCHI T., Physica D, 31 (1988), 277.
[9] RANDEN T., Stavanger University College, http://www.ux.his.no/~tranden/brodatz/ or http://www.ux.his.no/sigproc/textures/brodatz/.
[10] STACH S., ROSKOSZ S., CYBO J., CWAJNA J., Mater. Charact., 51 (2003), 87.
[11] STASZCZUK P., MATYJEWICZ M., KOWALSKA E., RADOMSKA J., BYSZEWSKI P., KOZLOWSKI M., Rev. Adv. Mater. Sci., 5 (2003), 471.
[12] KLONOWSKI W., Solitons and Fractals, 14 (2002), 1379.
[13] TANG Y.Y., TAO Y. AND LAM E.C.M., Pattern Recognition, 35 (2002), 1071.

Received 9 September 2004
Revised 22 November 2004

Materials Science-Poland, Vol. 23, No. 3, 2005

Dynamic vortex motion in anisotropic HTc superconductors

J. SOSNOWSKI*

Electrotechnical Institute, Pożaryskiego 28, 04-703 Warsaw, Poland

Dynamic transport properties of layered high-temperature anisotropic oxide superconductors have been investigated. An analysis is performed describing the way resistivity-less transport current flows in these superconductors and how it is limited by the velocity of the vortex motion, creating resistivity determining the critical current. The specific, anisotropic shape of the vortices is considered in connection with the layered crystal structure of the high-temperature oxide superconductors taken into account. The results of numerical calculations of the current–voltage characteristics in such a case are presented, which indicate the influence of anisotropy and inter-plane interaction on the critical current in the nearest neighbours approximation. The elastic energy of the vortex lattice is also included.

Key words: *superconductivity; critical current; ceramic materials*

1. Introduction

Most of high-temperature superconductors discovered so far are planar materials containing CuO_2 planes. Exceptions from this rule are fullerides and magnesium boride, MgB_2, which, in fact, is also a layered material with hexagonal magnesium and boride layers. An example of a tetragonal layered crystal structure of Cu-based high-temperature oxide superconductors of the $YBa_2Cu_3O_{7-x}$ type with a marked antiferromagnetic order of Cu atoms is shown in Fig. 1. The planar structure of these materials influences the magnetic and electric properties of HTc superconductors. The present paper is devoted to an analysis of dynamic transport properties related to the magnetic vortex movement in such anisotropic HTc superconductors. Some basic ideas describing the dynamic vortex motion will be introduced, taking into account vortex pinning on the material inhomogeneities – pinning centres. Individual or collective pinning may then appear. Collective pinning takes place for low pinning centre concentrations, at which many vortices occupy the same pinning centres. Collective pinning is

*E-mail: sosnow@iel.waw.pl

therefore a weak one. In the opposite case of the high pinning centre concentrations, individual pinning dominates, which is especially important for high-temperature superconductors.

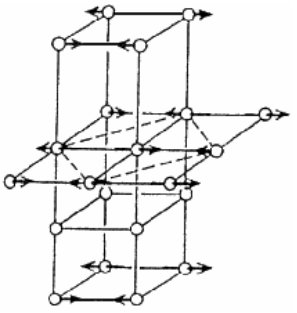

Fig. 1. Antiferromagnetic ordering of Cu atoms
in a YBaCuO unit cell with indicated spins

High-temperature superconducting materials are a very promising tool for investigating this interaction of pancake-shaped vortices created in a perpendicular magnetic field and localized in individual layers. Such thin vortices interact individually with single pinning centres, while for three-dimensional low-temperature superconducting materials the flux lines are captured by many pinning centres. During current flow, the vortices tear themselves off from the pinning centres and start to move. This movement of an array of vortices, realized initially in the flux creep, and for higher currents in the flux flow process, leads to the appearance of resistivity. For low vortex velocities, the Bardeen–Stephen model [1] can be used, in which the resistivity of the flux flow motion is connected with various transition times between the normal and superconducting electrons forming Cooper's pairs, and with the inverse of this process, thus leading to the damping of the movement of vortices and to the appearance of viscosity.

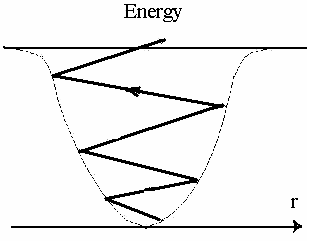

Fig. 2. The Andreev reflections of a quasi-electron
in a vortex core during a rapid flux flow process

For larger currents, the quasi-stationary vortex motion changes into a dynamic one, in which electrons from the vortex core are subjected to frequent Andreev's reflections at the boundary of the core, as presented in Fig. 2. Electrons are then converted into holes, while their energy continuously increases in each reflection process.

Finally, part of the quasiparticles leave the vortex core, which collapses, while its viscosity decreases. This effect, described in the Larkin–Ovchinnikov model [2], leads to the instability of current–voltage characteristics, recently observed experimentally in the Ce-doped $Nd_{2-x}Ce_xCuO_y$ high-temperature superconductor [3].

2. The influence of the pinning interaction on vortex dynamics

Two-dimensional vortices generated in the layered cuprate superconductors in a perpendicular magnetic field are localised in the individual CuO_2 planes, shown in Fig. 1 and are therefore called pancake vortices. The magnetic quantised flux is localized in the base layer, generating circulating currents at distances in the range of the penetration depth. In the surrounding planes, this magnetic flux is screened by induced currents, having therefore opposite direction. This indicates that if the direction of the screening currents is taken into account, pancake vortices in the same plane repel each other, while those in opposite planes attract each other. Therefore, the total electric current flowing in a layered high-temperature superconductor in a perpendicular magnetic field is superposition of the currents generated by individual pancake vortices localized in the surrounding CuO_2 planes.

In the present chapter, the vortex dynamics of high-temperature oxide superconductors is investigated in the framework of the flux creep model, which precedes the flux flow process presented previously. The flux creep effect appears in real HTc superconductors with the inclusion of normal phase precipitations for instance, which act as pinning centres. According to scanning microscopy results and the applied bending strain process, the existence of flat pinning centres has been considered which can arise during the winding procedure of HTc windings from superconducting tapes, in the process of constructing superconducting electromagnets, among others. Micro-cracks, edge dislocations, and other mechanical defects of the flat geometrical shape then appear. They diminish the tape cross-section, which is a dominant effect decreasing the critical current, as well as insert additional pinning centres.

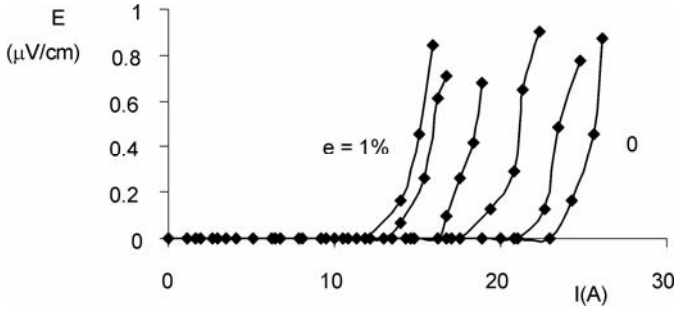

Fig. 3. Experimental results of measurements at 77 K of the current–voltage characteristics for HTc BiSCCO tape versus bending strain *e* in per cents (from the right side *e* = 0, 0.2, 0.4, 0.6, 0.8, 1)

The experimentally observed influence of defects on current–voltage characteristics for HTc superconducting tape is shown in Fig. 3. The figure presents the influence of the bending strain creating mechanical defects on the current–voltage characteristics of BiSrCaCuO tape. Measurements were performed at liquid nitrogen temperature, while the tape was directly immersed into a cryostat filled with liquid nitrogen. The tape-mounting part of an experimental sample holder, which introduces the desired bending strain, is shown in Fig. 4.

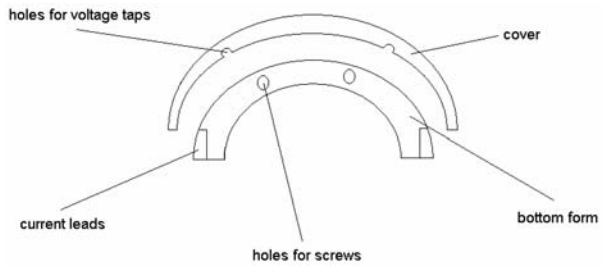

Fig. 4. View of the experimental setup for mounting the sample
for measuring the influence of the bending strain on the critical current

A bending strain, defined as:

$$e = \frac{t}{D} \tag{1}$$

was applied up to 1% by mounting the tape between various dies – upper and bottom ones with changing radii (D/2), while t = 0.27 mm is the tape thickness. The tape width was equal to 3.7 mm. Not too high values of the critical current may be connected with the fact that the measurements (Fig. 3) were performed applying a rectified, non-smoothed current. Complementary investigations performed using a stabilized DC power supply really indicated larger values of the critical current. A decrease in the critical current during the bending procedure is, however, apparent. A certain concentration of defects was introduced into the tape during the technological process, because otherwise the vortex structure could not be anchored and the critical current would disappear. The bending strain inserts additional defects of the micro-crack kind. These defects reduce the superconductor cross-section and, on the other hand, create pinning centres interacting with vortices and thus stimulating current enhancement. In the investigated case, the vortices can be generated both by a weak external magnetic field and as the result of the current magnetic self-induced field. It is assumed in the present paper that in the middle of the regular vortex array a flat pinning centre is placed, whose interaction with the vortices is considered. The anisotropy of this interaction is connected with anisotropic values of the coherence length, determining the vortex core shape in the layered superconductors. The approximation of nearest neighbour interaction between vortices in the layer was assumed. Similar nearest neighbour vortices have been taken into account in the subse-

quent planes. This is a novel approach, since usually current–voltage characteristics are analysed in terms of the power law approximation [4], which is, in fact, a purely technical approach neglecting most of the physical phenomena that occur.

Analysing the nonequilibrium distribution of the vortices, whose gradient is determined by Maxwell's equations, the magnitude of the transport current and the shape of the current–voltage characteristics generated in the flux creep process for a flat geometry of the pinning centres has been elaborated. The initial arrangement of pancake-type vortices was considered in a square lattice in each layer, while with an increase in the transport current the vortices in the lower part of the array are shifted towards each other, decreasing the distance between them, shown by the black points in Fig. 10. The superposition of currents surrounding them, including the induced screening currents from vortices in neighbouring planes, determines the total transport current amplitude. In the calculation, real BiSCCO tape parameters, such as geometrical dimensions, critical temperature, critical magnetic field, coherence length, penetration depth, and others, were used.

3. Theoretical analysis

The influence of magnetic vortex anisotropy and interplane interaction on the current–voltage characteristics and the critical current of HTc oxide superconductors was analytically investigated according to the model presented above. The case of an elliptic vortex core was considered, assuming anisotropic values of the coherence length in a dependence on the direction:

$$y = \pm \xi_b \sqrt{1 - \left(\frac{x}{\xi_a} \right)^2} \tag{2}$$

The enhancement of the free energy of the superconductor in this geometrical approach during the movement captured by the flat pinning centre vortex, at a distance x from the equilibrium position, as shown in Fig. 5, is equal to:

$$U = \frac{\mu_0 H_c^2 \xi_b l}{2\xi_a} \left(x\sqrt{\xi_a^2 - x^2} + \xi_a^2 \arcsin \frac{x}{\xi_a} \right) - \frac{\pi \mu_0 H_c^2 \xi_b \xi_a l}{4} \tag{3}$$

where l is the thickness of the pinning centre, corresponding to the thickness of the CuO_2 layer. The force of the pinning interaction, determined by the gradient of energy as described by Eq. (3), is then given as:

$$F = -\mu_0 H_c^2 \xi_b l \sqrt{1 - \left(\frac{x}{\xi_a} \right)^2} \tag{4}$$

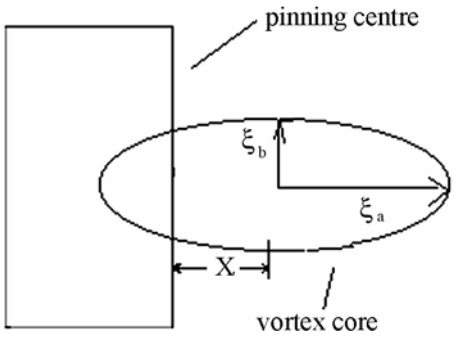

Fig. 5. A view of the investigated geometry of the anisotropic vortex interaction with a pinning centre

The energy barrier is obtained by taking into account the potential related to the Lorentz force:

$$\Delta U(x) = \xi_a \xi_b l \left(\frac{\mu_0 H_c^2}{2\xi_a^2} \left(x\sqrt{\xi_a^2 - x^2} + \xi_a^2 \arcsin\frac{x}{\xi_a} \right) - \pi j B x \right) \tag{5}$$

Vanishing of the derivative from this potential indicates the position x_1, for which the potential barrier is maximal. The potential barrier height is therefore:

$$\Delta U(i) = \xi_a \xi_b l \frac{\mu_0 H_c^2}{2} \left(-\arcsin i - i\sqrt{1-i^2} + \frac{\pi}{2} \right) \tag{6}$$

where the notation $i = j/j_c$ has been introduced. The parameter j_c is defined for individual pinning centres as:

$$j_c = \frac{\mu_0 H_c^2}{B\pi\xi_a} \tag{7}$$

and has the physical meaning of the critical current density, since for $j = j_c$ the energy barrier in Eq. (6) vanishes. Inserting the potential barrier height into the constitutive equation describing the electric field generated in the flux creep process [5], we determine the shape of the current–voltage characteristics for various values of the coherence length anisotropy ξ_a/ξ_b in a fixed magnetic field and temperature. For better visualizing the influence of anisotropy, calculations were performed for a fixed perpendicular cross-section of the vortex core, namely when $\xi_a \times \xi_b$ = const. The results shown in Fig. 6 indicate that anisotropy can lead to a decrease of the critical current. Figure 7, presenting the influence of the anisotropy effects on the dependence of transport current on the potential barrier height, confirms this finding.

Equation (6) describes the case of a fully homogeneous sample, for which the critical current density j_c is constant at each point of the HTc superconductor. As we should expect, however, a real superconductor with pinning centres is characterized

by inhomogeneity, causing the scattering of its cross-section and a local critical current density. This has been taken into account by considering a statistical deviation of the local reduced current density $i = j/j_c$ by a value Δi with respect to the average one. The average value of the potential barrier height ΔU has then been approximated by the relation:

$$\Delta \overset{\frown}{U}(i,\Delta i) = \frac{1}{\Delta i}\int_{i}^{i+\Delta i} \Delta U(i)\,di = \frac{\mu_0 H_c^2 l \xi_a \xi_b}{2\Delta i}\int_{i}^{i+\Delta i}\left(-\arcsin i + \frac{\pi}{2} - i\sqrt{1-i^2}\right)di \quad (8)$$

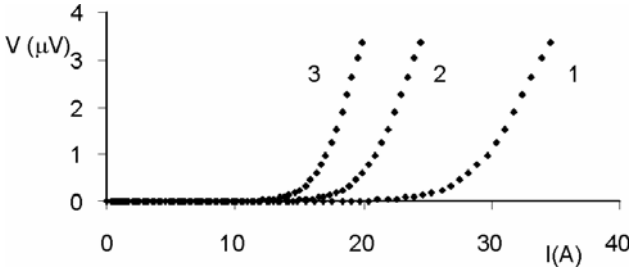

Fig. 6. Influence of the anisotropy of the vortex core shape on the current–voltage characteristics of the HTc superconductors:
1 – $\xi_a/\xi_b = 1$; 2 – $\xi_a/\xi_b = 2$; 3 – $\xi_a/\xi_b = 3$ at $T = 3$ K, $B = 2$ T

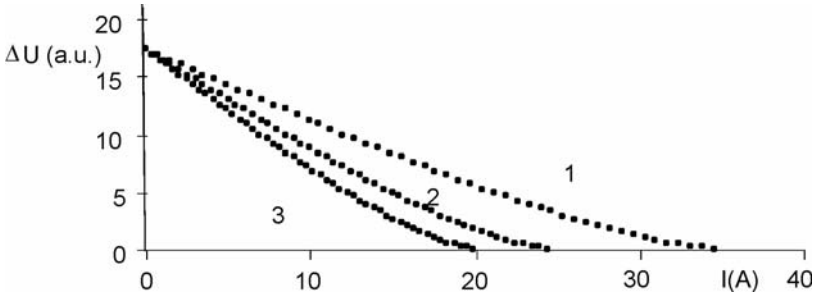

Fig. 7. Influence of the anisotropy of the vortex core shape on the pinning potential barrier of the HTc superconductor in reduced units:
1 – $\xi_a/\xi_b = 1$, 2 – $\xi_a/\xi_b = 2$, 3 – $\xi_a/\xi_b = 3$ at $T = 3$ K, $B = 2$ T

If we use the integral relation:

$$\int \arcsin\frac{x}{a}dx = x\arcsin\frac{x}{a} + \sqrt{a^2 - x^2} \quad (9)$$

then the final expression for the potential barrier height in the presence of sample inhomogeneity is obtained in the form:

$$\Delta\bar{U} = \frac{\mu_0 H_c^2 l \xi_a \xi_b}{2\Delta i}\left(i\arcsin i + \frac{\sqrt{1-i^2}}{3}(2+i^2) - i'\arcsin i' + \frac{\pi\Delta i}{2} - \frac{\sqrt{1-i'^2}}{3}(2+i'^2)\right) \quad (10)$$

where we have introduced the notation: $i' = i + \Delta i$. The parameter Δi in this model is related to the magnitude of the inhomogeneity of material, which for clean materials should be much lower than 1. The results of numerical calculations of the current –voltage characteristics versus magnetic field for $\Delta i = 0.1$ and 0.2 are shown in Fig. 8 for an anisotropy ratio $\xi_a/\xi_b = 2$, indicating the way the sample inhomogeneity influences the *I*–*V* curves. The values of other parameters used in calculations are given in the diagrams. The material inhomogeneity can be connected with the existence of high concentrations of mechanical defects, acting as pinning centres, and thus reducing the superconductor volume of the sample and leading to the decrease of the average total critical current density. Equation 7 describes the critical current density in the case of a single pinning centre, and is later modified by taking into account the decrease of the superconducting tape cross-section connected with the existence of microcracks.

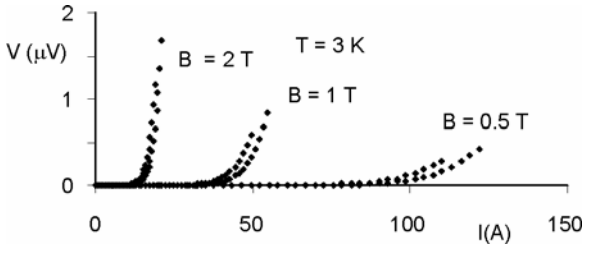

Fig. 8. Influence of the material inhomogeneity, expressed by the parameter $\Delta i = 0.1$ (right) and $\Delta i = 0.2$ (left curve) on the current–voltage characteristics as the function of the magnetic field for HTc superconductor for an anisotropic case $\xi_a/\xi_b = 2$

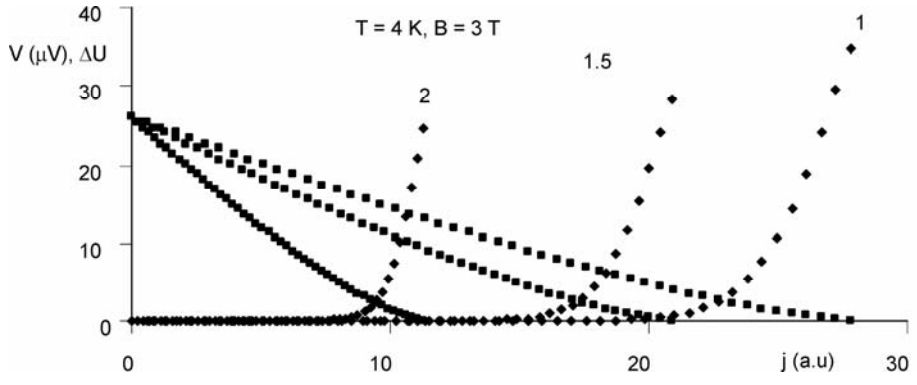

Fig. 9. Influence of the surface pinning centres concentration (in units of 10^{17} m^{-2}) on the current –voltage characteristics and potential barrier height Δ in reduced units for an anisotropic case $\xi_a/\xi_b = 2$

The results of calculations of the influence defects concentration on the current –voltage characteristics and potential barrier height for an anisotropy in the range

$\xi_a/\xi_b = 2$ are shown in Fig. 9. The calculated decrease of the critical current with pinning centre concentration for high defect concentrations, leading to the modification of Eq. (7), is in a good qualitative agreement with the experimental results presented in Fig. 3. From the layered structure of HTc superconductors the surface concentration of pinning centres is determined, giving the number of pinning centres per unit surface of the layer.

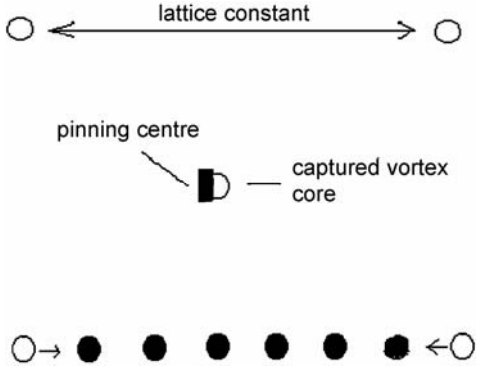

Fig. 10. A schematic view of the vortices movement caused by an increase in the transport current: • indicates the subsequent positions of the nearest vortices around the captured vortex as the function of the current amplitude, the arrows denote direction of motion

The parameter j describes the total current density at the vortex position, which is therefore a superposition of the currents generated by other vortices from the same plane as well as from the surrounding ones. For simplifying the numerical calculations, the nearest neighbour interaction approximation was applied in which it was assumed that the current density at the position of the investigated pinned vortex is a superposition of the screening currents from the nearest vortices. Figure 10 illustrates the geometry mentioned above. An increase in the transport current, according to the Maxwell's equation, leads to the appearance of a magnetic induction gradient, obtained by the shift of vortex positions, and is indicated by the arrows within the nearest neighbouring vortices approximation. The critical current in this model is determined by the condition that the distance between the nearest vortices is in the range of the coherence length, which means that cores occupying two nearest points in the applied partition of the vortex position lattice start to overlap. The same assumption was made for describing the movement of the nearest vortices in the surrounding planes. The flux in the vortices from the surrounding planes generates screening currents in the central plane. The magnitude of these screening currents is inversely proportional to the distance between a given plane and the pinned vortex, while the number of planes interacting in this way is denoted in Figs. 11 and 12 by the symbol k. The expression for the current in pancake vortices was assumed basing on the data for the magnetic induction profile in these vortices [6]:

$$B(r) = \frac{s\Phi_0}{4\pi\lambda^2 r}\exp\left(-\frac{r}{\lambda}\right) \tag{11}$$

Then the current distribution obtained from Maxwell's equation is given by the relation:

$$j_\theta(r) = \frac{s\Phi_0}{4\pi\lambda^2 r}\exp\left(-\frac{r}{\lambda}\right)\left(\frac{1}{r}+\frac{1}{\lambda}\right) \tag{12}$$

where s is the distance between the superconducting layers. The results of calculations of the current–voltage characteristics and potential barrier height versus transport current in a single layer, taking into account interlayer interaction, are shown in Figs. 11 and 12, and indicate the importance of this interaction.

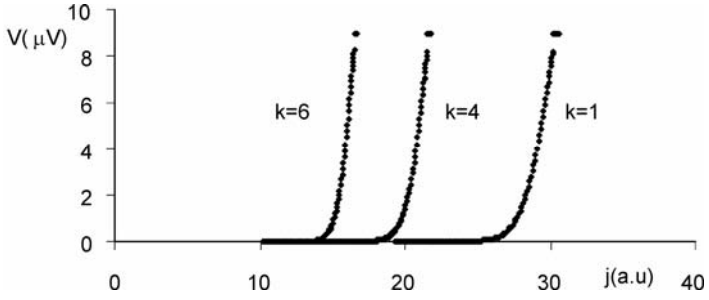

Fig. 11. Influence of the interlayer interaction on the current–voltage characteristics for the HTc superconductor at $T = 40$ K, $B = 0.5$ T. The parameter k determines the number of the interacting CuO_2 planes containing pancake vortices

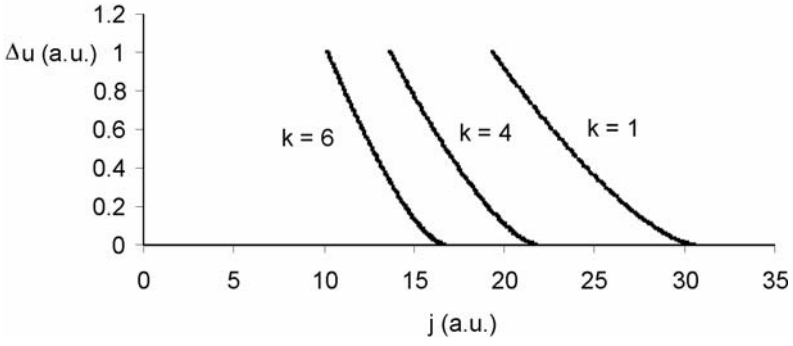

Fig. 12. Influence of the interlayer interaction on the pinning energy barrier for a HTc superconductor at $T = 40$ K, $B = 0.5$ T. The parameter k determines the number of the interacting CuO_2 planes with pancake vortices

In principle, the elastic energy of vortices should also be taken into account in these considerations. From the elastic properties of the vortex lattice the pinning centres acting on the fluxons enhance the energy of the system by moving vortices from

their equilibrium position by a distance x. This leads to an increase in the vortex elastic energy, which is described now by the formula:

$$U_{\mathrm{el}} = \alpha\left(x-\xi_{\alpha}\right)^{2} \tag{13}$$

where the parameter α includes the elasticity shear modulus c_s. The results of calculations of the influence of the parameter α on the critical current density, as a function of the magnetic field, are shown in Fig. 13.

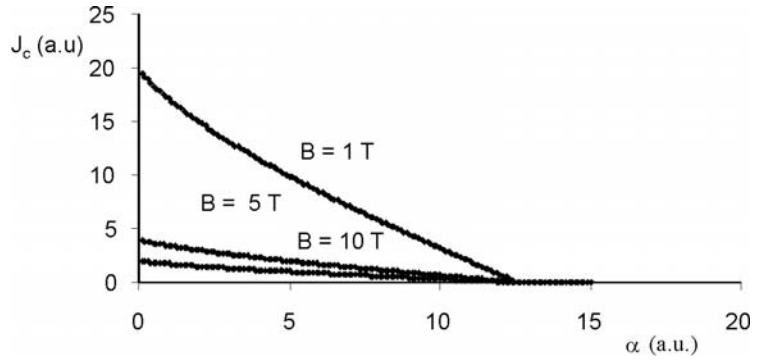

Fig. 13. Influence of the elastic vortex lattice energy described by the parameter α on the local critical current density as the function of the applied magnetic field for $T = 1$ K

4. Final remarks

This paper discusses the dynamics of vortex motion in HTc superconductors. The cases of low and high vortex velocity in the flux flow process have been considered in layered superconductors. The flux creep effect was investigated in the pinned HTc BiSrCaCuO material taking into account the anisotropy of the material parameters and their inhomogeneity, as well as the interaction between vortices in surrounding layers within a nearest-neighbour proximity.

References

[1] BARDEEN J., STEPHEN M.J., Phys. Rev., 140 (1965), A 1197.
[2] LARKIN A.J., OVCHINNIKOV YU.N., Sov. Phys. JETP, 41 (1976), 960.
[3] STOLL O.M., KAISER S., HUEBNER R.P., NAITO M., Phys. Rev Lett., 81 (1998), 2994.
[4] WANG Z., CHEN Z., ZHOU Y., DUAN Z., WANG W., Cryogenics, 40 (2000), 681.
[5] SOSNOWSKI J., J. Tech. Phys., 14 (2004), 21.
[6] BRANDT E.H., Rep. Prog. Phys., 58 (1995), 1465.

Received 6 January 2005
Revised 6 February 2005

Materials Science-Poland, Vol. 23, No. 3, 2005

Distinguishing and identifying point and extended defects in DLTS measurements

Ł. GELCZUK*, M. DĄBROWSKA-SZATA, G. JÓŹWIAK

Faculty of Microsystem Electronics and Photonics, Chair of Advanced Electronic Engineering, Wrocław University of Technology, Janiszewskiego 11/17 St., 50-372 Wrocław, Poland

Convenient and simple criteria are proposed enabling one to distinguish between deep level point and extended defects (e.g. dislocations) in DLTS measurements. The approach is based on earlier reports of several authors and on our own experiences in the field of DLTS data analysis for III–V semiconductors. It consists of standard DLTS measurements widened by line shape and line behaviour analysis, as well as capture kinetics measurements. In the first part, the paper presents a survey of the literature on the analysis of DLTS signals originating from dislocations. In the second part, selected experimental data on distinguishing and identifying deep point and extended defects, in GaAs/GaAs and InGaAs/GaAs heterostructures, are presented.

Key words: *defect identification; deep levels; point defects; extended defects; DLTS*

1. Introduction

One of the reasons why semiconductors find so wide applications in the production of electrical and optical devices is the possibility of modifying their electronic properties by incorporating small fractions of impurities or other defects. Lattice defects are needed for doping the material with shallow, hydrogenic donors and acceptors in order to determine the majority carrier type and concentration. The carrier mobility can usually be controlled as well. For this reason, the ability of controlling defects is immensely important. Therefore, at first it is necessary to master the technological processing of bulk materials with the least number of defects, and then the process of introducing a required number of defects during the growth or after the growth of the semiconductor crystal.

In addition to these so-called desired defects, there are a wide range of undesired defects. In contrast to the hydrogenic, delocalised electron states of dopants, unde-

*Corresponding author, e-mail: lukasz.gelczuk@pwr.wroc.pl

sired lattice defects are characterized by highly localized states, usually situated deep in the band gap, but also, as we know today, even close to the valence or conduction band edges. They are commonly called “deep level defects”. Examples of such deep level point defects are some impurities, vacancies, interstitials, or their clusters. Deep level defects have larger capture cross sections than hydrogenic shallow defects and in most cases determine the minority carrier lifetime. Therefore, these defects play an important role in manufacturing high-speed electronic and optoelectronic devices. Defect investigation and characterization are interesting from the cognitive and practical point of view, because they decide about the effective production of perfect semiconductor devices.

In contrast to deep point defects, spatially extended, many-electron defects form deep lying, closely spaced electronic states in the band gap. Examples of such defects are dislocations, grain boundaries, precipitates, and surface and interface states. Extended defects are known to significantly affect charge-carrier mobility and lifetime. Moreover, they can interact with point defects. By acting as sinks and sources for intrinsic point defects and segregation centres for impurities, they can create detrimental effects in microelectronic devices. The ability of extended defects to sink impurities, however, is utilized in removing impurities from the crystal, a technique known as “gettering of impurities”.

Recently Weber [1] suggested that the proper understanding of defects in semiconductors usually requires the following steps: (i) defect observation and characterization, (ii) defect identification, (iii) defect control, (iv) estimation of the influence of defects on device performance.

The first two steps determine the application area of electrical and optical spectroscopy, such as deep level transient spectroscopy (DLTS), electron beam induced current (EBIC), impedance spectroscopy (IS), and photoluminescence (PL). Structural analysis by X-ray diffraction (XRD), transmission electron microscopy (TEM), and scanning electron microscopy (SEM) are frequently employed as well. These methods are particularly essential in the case of extended defects [1]. The thorough understanding of the nature of a particular defect and its identification usually involve a combination of various methods.

Deep level transient spectroscopy is currently one of the most widely used methods for studying deep level defects in semiconductors [2]. Although the DLTS technique has been primarily developed and well-established for characterizing simple point defects (impurities, vacancies) in semiconductor materials, it can also be applied for studying extended defects such as dislocations, grain boundaries, or precipitates [3].

Over the last two decades, attempts at analysing the DLTS signal coming from dislocations in different semiconductor materials have been made by many authors [3–13]. Today our knowledge on this subject is sufficiently rich for properly examining the odd features of electron emission from dislocations and for distinguishing them from isolated point defects in DLTS measurements. Nevertheless, this requires a careful and accurate analysis, because other phenomena can affect the DLTS signal. In this paper, we discuss possibilities of applying DLTS measurements to characterize

electronic states at dislocations and we propose a simple way to distinguish deep level extended defects (e.g. dislocations) from point defects.

2. Deep level transient spectroscopy – theory

Deep level transient spectroscopy, developed by Lang and co-workers in 1974 [2], is considered to be a powerful and versatile capacitance technique for characterizing deep level defects in semiconductors. It provides all the important defect parameters, such as the thermal activation energy (E_a), electron- and hole-capture cross sections ($\sigma_{n,p}$), and defect concentration (N_T). The DLTS technique relies on temporal capacitance transients (typically exponential in the case of point defects), which occur after a rapid bias change of a Schottky diode or p^+n–n^+p-junction. A reverse bias changes the width of the space-charge region in the diode or junction, and when deep levels are present, they are detected by their contribution to charge redistribution in the depletion region, resulting in a change of capacitance, i.e. capacitance transients [2, 14].

The dynamic process of electron capture and emission by deep traps can be described in terms of a capture cross section σ_n and emission rate e_n. On the basis of the principle of detailed balance, it can be shown that the emission rate is related to the capture cross section by the following equation [2, 14]:

$$e_n = \sigma_n v_{th} N_c \exp\left(-\frac{E_C - E_T}{kT}\right) \tag{1}$$

where v_{th} is the thermal velocity of electrons, N_c is the effective density of states in the conduction band, and $E_C - E_T$ determines the energy level position in the band gap in relation to the conduction band edge (i.e. activation energy). A similar relation can be derived in the case of the emission and capture of holes. The inverse of the emission rate is called the emission time constant (τ_e) of the capacitance transient and it is generally known to satisfy the following relation [15]:

$$C(t) = C_0\left[1 - \frac{n_T(0)}{2N_D}\exp\left(-\frac{t}{\tau_e}\right)\right] \tag{2}$$

where C_0 is the capacitance of the original reverse bias, $n_T(0)$ is the original number of electrons per unit volume occupying the trap level during the transient, N_D is the doping concentration, and t is the time. It follows that if the doping concentration is known, $n_T(0)$ can be obtained, and that for a sufficiently long filling pulse time it describes the trap concentration N_T.

By analysing emission kinetics as a function of temperature, the activation energy of deep traps can be obtained from DLTS measurements. In practice, different constant rate windows (or lock-in frequencies) are used, which change the DLTS peak positions on the temperature scale and allows e_n to be evaluated. Temperature scans

taken for several rate windows (lock-in frequencies) make it possible to construct Arrhenius plots, i.e. plots of the emission rates divided by the temperature squared (e_n/T^2) versus the reciprocal of temperature ($1/T$), for each of the peaks. Finally, the values of activation energy and capture cross section (frequently called "apparent") can be easily evaluated from the slope of the Arrhenius plot and its intersection with the emission rate axis, respectively.

The DLTS technique allows us to study the electric field dependence of the emission rate, thermally activated capture cross section, and concentration distribution profiles of the deep traps as well.

The activation energy is composed of a change in enthalpy and entropy [7, 14]. The entropy term, however, is frequently neglected and the ionisation enthalpy is assumed to be a good approximation to the ionisation energy. The ionisation energy of traps can be lowered in strong electric fields, for example by the Poole–Frenkel effect [14]. Therefore, the electric field dependence of the emission rate has to be taken into account, because neglecting this effect may lead to serious misinterpretations in the determination of deep level parameters. On the other hand, it can yield a lot of useful information on the nature of deep traps. In DLTS measurements, the influence of the electric field on the emission rate manifests itself by a shift of the DLTS peak maximum towards lower temperatures on increasing the value of the electric field. The value of the electric field is established by selecting two filling pulse heights (U_1, U_2) in so-called double correlation DLTS (DDLTS) [16].

When the capture process is temperature dependent for deep levels, the capture cross section can be expressed in terms of a capture barrier [14, 17]:

$$\sigma_n = \sigma_{n\infty} \exp\left(-\frac{E_B}{kT}\right) \tag{3}$$

where $\sigma_{n\infty}$ is the capture cross section at infinite temperature ($T \to \infty$) and E_B is the height of the capture barrier, which has to be overcome by free carriers in order to be captured by a trap. A thermally activated capture cross section can be investigated by measuring the DLTS peak amplitude for different widths of filling time pulses t_p at a constant temperature. The capture cross sections at different temperatures can be extracted from a specific fitting procedure [18].

The depth distribution of deep level concentration can also be measured by DDLTS, using two filling pulses with the same widths and different amplitudes, at a given rate window and constant temperature corresponding to the maximum of the DLTS peak of a selected level. The spatial resolution of the depth profile measurements is set by the constant value of $\Delta U = U_1 - U_2$, and their range by the value of the reverse bias U_R.

In spite of the DLTS possibilities mentioned above, this method requires some caution when analysing results. Occasionally, some phenomena can disturb or even forcibly change the DLTS signal coming from deep traps. This reservation is especially connected with the study of extended defects (e.g. dislocations) by means of the

DLTS technique. In the next sections, we discuss some peculiar features of the DLTS signal coming from dislocations, such as a change in the DLTS line shape, DLTS line behaviour, as well as non-exponential capacitance transients. The impact of other frequently observed features of contemporary semiconductor crystals, generally known as distorting factors of the classical DLTS behaviour, will also be discussed.

3. DLTS line amplitude shape analysis

A frequently observed feature of DLTS lines is a difference in the shape of peaks corresponding to particular deep level defects. This difference arises from the fact that in the case of isolated point defects one can usually observe narrow and symmetric peaks, while the DLTS line peaks associated with extended defects always show symmetric or asymmetric broadening. For these reasons, DLTS data for extended defects cannot be interpreted unambiguously.

The features mentioned above are due to the fact that in a conventional DLTS analysis simple point defects are known to provide exponential capacitance transients, corresponding to electron emission from traps. On the other hand, specific non-exponential capacitance transients are often observed for some deep levels. The origin of non-exponential transients is mainly attributed to the formation of dislocations or dislocation-related defects in semiconductor materials as a result of the repulsive Coulombic barriers associated with such defects (see Sec. 5).

Kimerling and Patel [4] were the first to find asymmetrically broadened DLTS lines, which were associated with dislocations in plastically deformed (PD) n-type and p-type Si that survived annealing at high temperatures. Very similar results were later obtained by Kveder et al. [5] in the case of both n- and p-type silicon, also subjected to the plastic deformation. They noticed several overlapping DLTS lines in preliminarily deformed, but not annealed samples, which were much broader than those typically observed for point defects. They concluded that the traps may be associated to the dislocation core or point defects surrounding the dislocation. After annealing, only one distinctly broadened line remains in the DLTS spectra, and its amplitude shows an anomalous logarithmic dependence on the duration of the refilling pulses (see Sec. 5) [5]. The authors explained these observed changes by the reconstruction of most of the dangling bonds in the dislocation core. Anomalous symmetrical line broadening was also studied by Omling et al. [6] for a deep electron trap in $GaAs_{1-x}P_x$ ternary compound alloys, labelled as the well known EL2-level. This effect was attributed to the dispersion of energy level positions of the defect in the band gap, as a result of varying alloy composition in the crystal. In the proposed model of broadened deep levels, the Gaussian distribution function was used, with the standard deviation of the distribution considered as the broadening parameter. In this model, it was shown that the thermal emission rates and mean values of activation energies can be obtained in a similar way as in conventional DLTS analysis, although the transients are strongly non-exponential. This causes the distortion of DLTS peaks. Moreover, the energy

distribution and corrected deep trap concentration can be calculated from the DLTS spectra observed experimentally [6]. This approach was also predicted to be useful, even when the defect levels are broadened for reasons different than varying alloy composition, such as inhomogeneous strain field distribution in crystals or defect interaction.

This model has also been successfully applied to analysing dislocation-related DLTS peaks in plastically deformed silicon for which symmetrical line broadening was also observed [7]. The DLTS spectra observed in PD silicon were ascribed by Kisielowski et al. [19] to the deformation-induced disorder on the energy level and capture cross section of point defect clouds surrounding dislocations. A few years later, these results were confirmed by Cavalcoli et al. [20] for the same traps observed in PD silicon. The authors paid particular attention to the broadened DLTS peak, labelled C. With regard to its peculiar features, such as shape dependence on the deformation procedure, an increase of concentration with dislocation density, and domination at high deformation temperature, etc., they concluded this trap to be most probably localized at dislocations, while other traps to be mainly due to deformation-induced point defects surrounding dislocations or left behind dislocations during their motion [20].

In n-type GaAs exposed to plastic deformation, Wosiński [8] has also detected a broadened asymmetric DLTS peak, evoked by an electron trap labelled ED1. It is worth noticing that, unlike previously observed deep traps in plastically deformed Si [7], generally attributed to point defect clouds around the dislocation line, the trap in GaAs was considered to be closely related to the core states of 60°-dislocations [8].

The broadened DLTS peaks associated with dislocations are typically observed in SiGe heterostructures [21–23] and ternary compound systems like InGaAs [24–26] and GaAsSb [27, 28]. They are caused by a lattice mismatch between the substrate and epitaxial layer. This leads to the formation of misfit dislocations at the interface, accompanied by threading dislocations [29,30]. Broad DLTS peaks were also recently observed in quaternary compound heterostructures like InGaAsN [31], and were associated either with continuous distributions of states, typical of extended defects, or with groups of closely spaced discrete energy levels.

Unfortunately, there is a wide set of other phenomena that cause significant distortions in conventional DLTS spectra and thereby add complexity to the DLTS formalism. Non-exponential capacitance transients are known to arise in the case of (i) high trap concentrations compared to shallow level doping [32], (ii) closely spaced, multiple deep levels with comparable emission rates [33], (iii) strong electric fields that influence trap emission [34], (iv) capture from free-carrier tails in a depletion region [18], and (v) inhomogeneous carrier concentrations [35]. A superposition of some peaks related to specific clusters of point defects is also one of the observed reasons for the broadening and anomalous behaviour of so-called U-shaped peaks [36]. Therefore, deep level transient spectroscopy requires a careful analysis when broadened spectra are observed.

A common problem appearing when deep impurity levels are studied in compound semiconductors by means of DLTS is the so-called alloy broadening. Semiconductor alloys such as $GaAs_xSb_{1-x}$, $GaAs_xP_{1-x}$, and $Al_xGa_{1-x}As$, and other disordered structures, are substitutionally disordered systems in which the main reason for disorder is the presence of composition fluctuations due to a random distribution of group V atoms in the corresponding sublattice. In such cases, the DLTS spectrum may be broadened and the corresponding capacitance transients may be non-exponential, because of deep level energy spectrum broadening [37]. Broadened DLTS spectra connected with alloy composition fluctuations have already been studied in GaAsP [6, 38], GaAsSb [39, 40], and other disordered systems such as moderately doped GaAs [41].

4. DLTS line amplitude behaviour analysis – "localized" and "bandlike" states

Spatially extended defects, owing to their many-electron character, are associated with a large number of electronic states in the band gap. They form deep-lying one -dimensional energy bands rather than isolated energy levels, typically attributed to point defects. The nature of DLTS lines in the case of extended defects can be investigated within the model developed by Schröter et al. [10–13]. This model (Fig. 1) has revealed that extended defects may be associated with [12]: (i) a density of states $N_d(E)$ that leads to DLTS line broadening, (ii) a capture barrier δE_C, which changes with the defect charge and modifies the capture rate, (iii) an internal equilibration time Γ_i (i.e., the time needed to attain an internal electronic equilibrium of the defect), which affects the filling pulse dependence of the line shape.

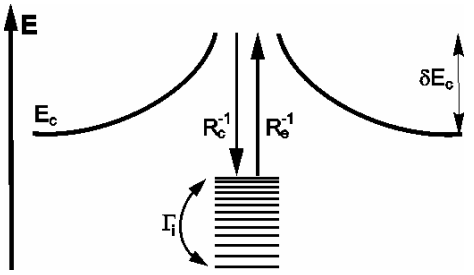

Fig. 1. Band diagram of electronic states at an extended defect [12]. The capture barrier δE_C, the internal equilibration time Γ_i, inverse rates of carrier emission and capture, R_e^{-1} and R_c^{-1}, respectively, are shown in the figure

Considering the internal equilibration time Γ_i, some authors [10–13] have demonstrated that deep-lying electronic states at extended defects can be classified as "localized" or "band-like". By comparing the time Γ_i with the inverse carrier emission rate R_e^{-1} and the inverse of the carrier capture rate defects R_c^{-1} (the time needed to reach

equilibrium with conduction and valence bands), the distinction between ''localized'' and "bandlike" density of states can be made. When $\Gamma_i >> R_e^{-1}, R_c^{-1}$, i.e. the internal electron exchange rate is small, the states are named "localized", whereas in the case of a large internal electron exchange rate, namely when $\Gamma_i << R_e^{-1}, R_c^{-1}$, states are "bandlike".

In the area of DLTS measurements, the criteria designed for distinguishing between these two types of states have been established [10, 11]. They concern the variation of the DLTS line maximum and its shape with the filling-pulse duration t_p. For "localized" states, while changing the filling-pulse duration: (i) the maximum of the DLTS line amplitude stays almost constant, (ii) the high-temperature side of DLTS lines generally coincide after normalizing, (iii) the DLTS line amplitude exhibits a linear dependence on the logarithm of the filling time (Sec. 5). On the contrary, in the case of "bandlike" states, the variation of the filling-pulse time length leads to the following: (i) the maximum of the DLTS line amplitude shifts to lower temperatures on increasing the duration, (ii) the high-temperature side of DLTS – lines coincide, (iii) the DLTS line amplitude exhibits a linear dependence on the logarithm of the filling time (Sec. 5). It is important that in both cases the DLTS line amplitudes are broadened, a typical feature in the case of extended defects (Sec. 3).

Applying the above criteria, "localized" deep electronic states have already been revealed in the case of 60° dislocations in plastically deformed silicon [10], whereas electronic states at dislocation rings bounding nanoscale $NiSi_2$ precipitates in silicon [12] have been related to the "band-like" class of states. A behaviour similar to the "localized" case was experimentally observed by Panepinto and Yastrubchak for the same electron trap in lattice-mismatched InGaAs/GaAs heterostructures grown by MOVPE [24] and MBE [42]. These traps were attributed to narrow clouds of point defects around dislocations and threading dislocations in the layer, respectively. "Bandlike" states have also been observed in the same heterostructures, for a deep hole trap associated with misfit dislocations at the InGaAs/GaAs interface [42].

A conventional analysis of the DLTS spectra for extended defects allows us to determine the apparent values of activation energy and capture cross section, but the interpretation of the obtained parameters is not as obvious as for isolated point defects. While point traps may produce distinct peaks for every trap, a distribution of energetically close traps may produce a single broadened peak [2, 7, 21]. Its thermal emission rate is a weighted average value of the emission rates of all the traps contributing to the peak at a given temperature. According to Grillot et al. [22], the lowest energy states make a dominant contribution to the high-temperature edge of the DLTS peak, whereas the highest-energy states make a dominant contribution to the low-temperature edge of the DLTS peak. Furthermore, for short filling-pulse times, the lowest-energy states are filled first, causing a broadening of the DLTS peak on its low-temperature side with increasing filling-pulse duration. Furthermore, the Arrhenius plots for extended defects differ significantly for different filling-pulse times. Hedemann et al. [11] have shown that apparent activation energies and capture cross sections obtained from Arrhenius plot analyses cannot be treated as average values for

the distribution of levels. The determined parameters should be reported together with the measurement parameters, especially with the filling-pulse length.

It should be noticed that the behaviour of the DLTS signal in the case of isolated point defects can also be taken into account, but less forcibly, mainly as a factor discriminating them from spatially extended effects. Namely, the DLTS signal originating from deep levels and associated with point traps does not show any changes in its peak positions on increasing the filling-pulse duration, while the observed DLTS peak shape is typically narrow and symmetric.

5. Capture kinetics analysis

The main specific feature of DLTS lines, usually considered to be the fingerprint of extended defects, particularly dislocations, is the so-called logarithmic capture law, i.e., a logarithmic dependence of the kinetics for majority charge carriers captured in trap states. Such a law was observed experimentally for the first time by Figielski in plastically deformed Ge and Si [43]. In this paper, it is shown that the steady-state photoconductivity increases linearly with the logarithm of the light intensity over a wide range of illumination. It was also noticed that photoconductivity decayed logarithmically in time after illumination by a rectangular light pulse. The observed phenomena were explained in terms of a barrier model of recombination processes via dislocations. In this model, the capture rate of free charge carriers, limited by a Coulombic barrier of the repulsive electrostatic potential built up at the defect, is proportional to the number of electrons already captured at the dislocation line [8, 43]. Such a dependence can occur when the trap levels are arranged in a linear array, interacting between themselves, and not randomly distributed in the whole crystal.

Furthermore, it turned out that the mentioned phenomena can be successfully observed by the DLTS technique [8]. Today this is exploited in DLTS measurements as a principal argument for discriminating between isolated points and extended traps, which can be expressed as a linear dependence of the DLTS peak amplitude on the logarithm of the filling-pulse duration [8]. This effect has already been observed for dislocations in plastically deformed Si [7, 9, 20] and GaAs [8]. It is also observed in the case of lattice-mismatched heterostructures, like SiGe [21–23], InGaAs [24–26, 42, 44], and GaAsSb [27, 28].

On the contrary, isolated point defects or impurities typically reveal exponential capture kinetics (the exponential capture law). This dependence can also be investigated by DLTS. In this case, a characteristic distinct saturation of the DLTS peak amplitude for long filling-pulse durations is observed [45]. Such a behaviour is typical of noninteracting point defects. As the DLTS amplitude is proportional to the defect concentration, the time at which saturation is reached describes the situation when no more free charge carriers are captured in defect states. Therefore, it determines the trap concentration N_T.

In capture kinetics measurements it is difficult to avoid experimental problems leading to incorrect results. The free-carrier tail effect during the capture process, the

so-called capture in the Debye tail, is a commonly appearing problem. This effect causes the non-exponential character of the capacitance transients. A detailed analysis of capture kinetics measurements was carried out by Pons [18], according to whom capture in the Debye tail contributes slightly to the fast exponential kinetics, changing with the logarithm of the filling-pulse duration. As a result of this contribution, no distinct saturation of the DLTS amplitude with increasing filling time is observed. In order to extract the exponential capture kinetics from the total kinetics, namely getting rid of the capture in the Debye tail and obtaining a correct estimation of the capture rate, a novel fitting model has been proposed [18]. This model was successfully used in measurements of thermally activated capture cross sections [45].

Furthermore, non-exponential thermal emission and capture kinetics are also generally observed in the case of donor-related defects – so-called DX centres – present in many III–V compound semiconductors. Systematic studies of such anomalous emission and capture transients on DX centres have shown that they may be due to various effects, such as a random distribution of atoms in the crystal lattice (alloy broadening) [46, 47], concentrations of DX centres equal to shallow impurity doping [48], or large lattice relaxation [14]. Therefore, a possible existence of DX centres in the investigated heterostructure has also be taken into account when analysing DLTS signals.

It should also be noticed that low-dimensional systems in semiconductor heterostructures, such as quantum wells (QW) and quantum dots (QD), can also evoke some non-classical effects in the emission and capture of charge carriers. These are typically expected to be viewed as spatially extended defects and thereby characterized by the DLTS technique. It is generally known that in DLTS measurements a single quantum well (SQW) acts electrically as a deep level trap, a so-called “giant trap”, because it can capture and emit free carriers from well regions in the same way as a deep trap [49, 50]. Quantum dots (QDs), as quasi-zero-dimensional structures, should behave even more like a classical point defect than quantum wells. The quantisation of energy levels, however, should be taken into account in such low dimensional systems. Thus, the presence of QWs and QDs in compound semiconductors may produce effects that significantly affect the DLTS formalism. Similarly to extended defects, they show symmetrically or asymmetrically broadened DLTS peaks or the non-exponential capture and emission characteristics of free carriers [49–52].

6. Summary – setting up the criteria

We have already presented some crucial results and remarks brought up in a large number of papers. They involved investigations and analyses of peculiar features in DLTS signals originating from deep level traps, associated with both point and extended defects in semiconductor materials. We would like to gather all the mentioned information in order to outline a compact scheme of criteria, making it possible, in

a simple way, to distinguish between isolated point defects and extended defects in DLTS measurements.

In the case of point defects, one can usually observe:

- narrow and symmetric peaks (Sec. 3),
- stability of the DLTS peak maximum with increasing filling pulse duration (Sec. 4),
- exponential capture kinetics (the exponential capture law) (Sec. 5).

For extended defects, a DLTS signal reveals completely opposite features:

- symmetrically or asymmetrically broadened peaks (Sec. 3),
- dependence of the DLTS peak maximum on increasing duration and on the type of electronic state at the extended defect (Sec. 4):
- for "localized" states, the DLTS line maximum stays almost constant and its high-temperature side coincides after normalizing,
- for "bandlike" states, the DLTS line maximum shifts to lower temperatures and, simultaneously, its high-temperature side coincides,
- logarithmic capture kinetics (the logarithmic capture law) (Sec. 5).

In our opinion, the presented facts can be successfully exploited for studying all types of extended defects, including all kinds of dislocations as the most commonly encountered representatives of that "species" of defects. Therefore, the conventional analysis of DLTS data, which makes it possible to obtain all deep level parameters (i.e., thermal emission rates, activation energies, capture cross sections, and concentrations) and to describe their dependencies on the electric field or temperature, can be extended by a more detailed analysis of the nature of the deep level defects observed in semiconductors. The comparison of DLTS data analysis and conclusions drawn from previous reports of dislocation-related deep level states is also indispensable. It is crucial, however, to exclude other numerous phenomena that can affect the DLTS signal coming from samples and cause serious misinterpretations in the analyses of spectra.

7. Experimental identification of extended defects in $A^{III}B^{V}$ semiconductors

DLTS investigations of two kinds of samples, lattice-matched n-GaAs/GaAs (sample A) and lattice-mismatched n-$In_{0.085}Ga_{0.915}As$/GaAs (sample B), were performed. The samples were grown by the MOVPE method. In order to make the DLTS measurements possible, Schottky contacts were prepared by a standard lift-off technique on top of the samples, and ohmic contacts on their back sides. All the technological details concerning sample preparation are given elsewhere [53, 54]. The quality of the Schottky barriers was checked by *I–V* and *C–V* measurements, which indicated good rectifying characteristics. The DLTS measurements were performed

by means of a lock-in type spectrometer DLS-82E, manufactured by Semitrap, Hungary [55]. Conventional DLTS [2] as well as double correlation DLTS methods [16] were applied in our investigations.

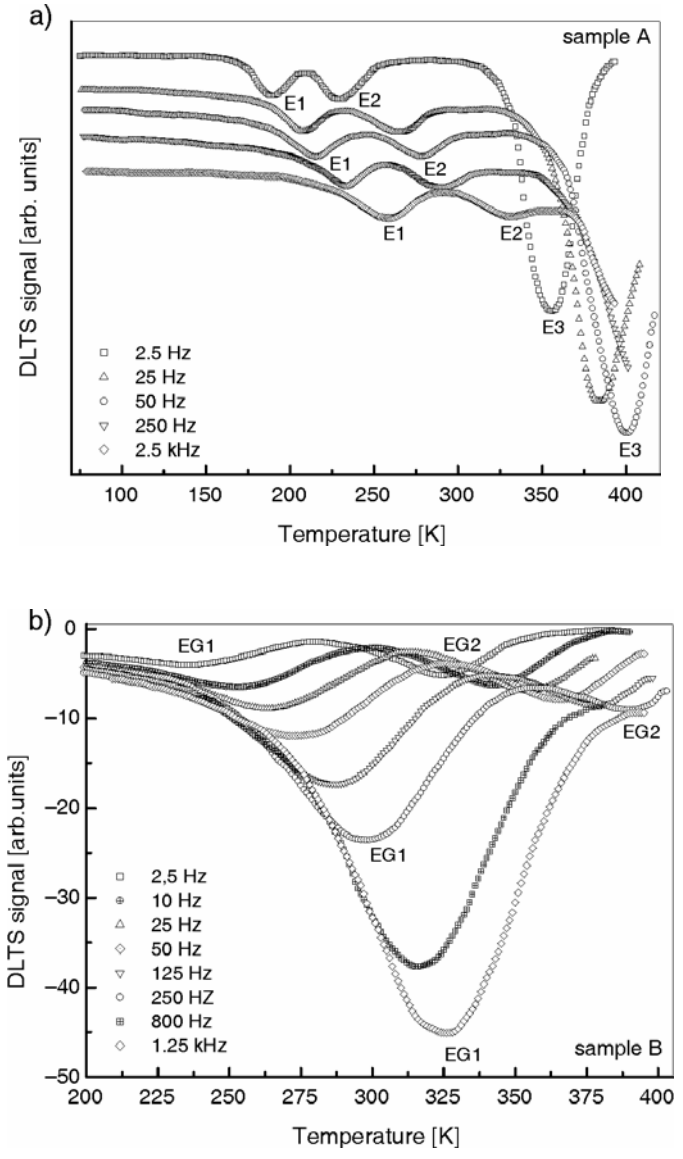

Fig. 2. DLTS temperature spectra of: a) a GaAs/GaAs structure for several lock-in frequencies measured in the conventional DLTS mode in the 77–410 K temperature range; reverse bias was $U_R = -3$ V, filling pulse height $U_1 = -0.5$V, and the width of the pulse 20 μs; scans were vertically moved between themselves for clarity, b) a $In_{0.085}Ga_{0.915}As/GaAs$ system for several lock-in frequencies, measured in the DDLTS mode in the 200–400 K temperature range; reverse bias was $U_R = -1$ V, filling pulse heights $U_1 = 0$ V and $U_2 = -0.5$ V, and the widths of the pulses 20 μs

Example DLTS temperature spectra of the two samples, for several different lock-in frequencies, are given in Fig. 2. Three deep electron traps, labelled E1, E2, and E3, are present in the GaAs/GaAs sample (Fig. 2a), and two electron traps, labelled EG1, EG2, in $In_{0.085}Ga_{0.915}As$/GaAs sample (Fig. 2b). The latter sample was grown in lattice mismatch conditions between the epitaxial layer and substrate. The calculated lattice misfit parameter amounted to about 0.6%, resulting in the generation of a network of two-dimensional 60° misfit dislocations, typically lying along two orthogonal ⟨110⟩ directions at the (001) interface [44]. The DLTS lines of the EG1 trap (Fig. 2b) are distinctly broadened, as opposed to all the other traps presented in both samples. In accordance with the previous information, non-exponential transients connected with the electronic states of dislocations can bring about such as broadening. For sample A, all the DLTS peaks are narrow and symmetric, because only isolated point defects, and no dislocations, were expected to appear in such a structure.

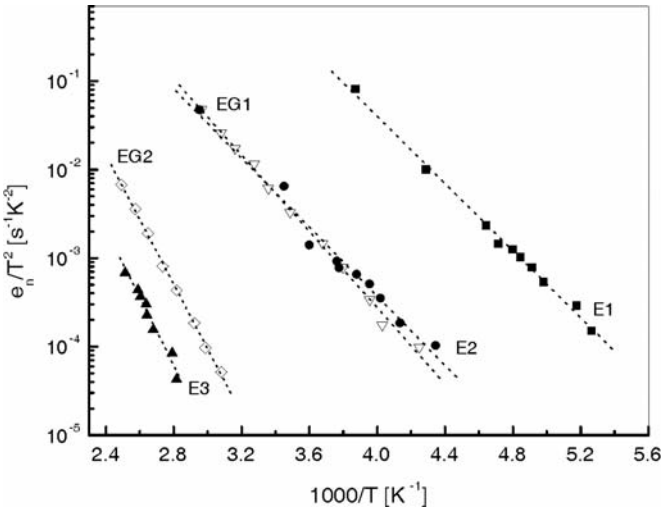

Fig. 3. Temperature dependence of the thermal emission rates (Arrhenius plots) for all the electron traps revealed in GaAs/GaAs (solid symbols) and $In_{0.085}Ga_{0.915}As$/GaAs (open symbols). The dotted lines show the best least-squares fit to the experimental data

Taking the temperature scans from Fig. 2, Arrhenius plots can be constructed, i.e. temperature dependences of the emission rates for each trap in both samples (Fig. 3). The activation energies E_a and capture cross sections σ_n, obtained by means of the standard least-squares fitting procedure, are given in Table 1.

The DLTS line of the trap EG1 is broadened and no saturation is observed up to the longest filling-pulse time used in the experiment (Fig. 4). Such behaviour (the logarithmic capture law), as mentioned in previous sections, is the most characteristic feature of extended defects due to carrier capture being limited by an occupation-dependent barrier [43]. Indeed, after carrying out capture kinetics measurements it turned out that the amplitude of the dominant EG1 line in sample B exhibits a linear

dependence on the logarithm of the filling time, as presented in Fig. 5. Furthermore, no distinct shift of the EG1 peak was observed and a normalized plot of the peak revealed that its high temperature sides match to each other (Fig. 4). This enables us to attribute the EG1 trap to "localized" states at the dislocation core or very close to it.

Table 1. Activation energies E_a and capture cross sections σ_n for traps revealed in samples A and B, determined from Arrhenius plots (Fig. 3) using a filling pulse duration of $t_p = 20$ μs

Sample	Trap	E_a [eV]	σ_n [cm^2]	Identification
A	E1	0.38	9.1×10^{-15}	point defect (EL5)
	E2	0.41	2.6×10^{-16}	point defect (EI1)
	E3	0.76	1.5×10^{-14}	native point defect (EL2)
B	EG1	0.43	5.73×10^{-16} *	misfit dislocation (ED1)
	EG2	0.72	4.22×10^{-14}	native point defect (EL2)

*The value changes with time.

The dislocation trap, labelled EG4, associated with localized states at dislocations, was previously observed in MOVPE grown GaAs/InGaAs/GaAs single-quantum wells by Panepinto et al. [24], who ascribed this trap to misfit dislocations close to the interface in the GaAs buffer layer. The trap was identified by the authors as ED1, and was found for the first time in plastically deformed GaAs by Wosiński [8], then in GaAsSb/GaAs [27], and recently in InGaAs/GaAs [26, 42] lattice-mismatched heterostructures. The activation energy of the trap ED1, equal to 0.68 eV, is much higher than our results for the trap EG1 shown in Table 1 (0.43 eV). We believe our trap has a similar origin as ED1. The difference in activation energies may result from the fact that, as mentioned in Section 4, the measured activation energies (Arrhenius plot) differ significantly for various fixed filling-pulse durations. In this paper, all the activation energies were measured with a filling-pulse time of $t_p = 20$ μs, but the value of t_p used by Wosiński is not known. Furthermore, there are other reasons, such as different growth techniques or indium content, etc. In order to clearly identify the origin of the EG1 trap, further investigations are needed.

On the contrary, it can be seen in Figs. 4 and 5 that the DLTS line of the second electron trap EG2 in sample B shows a distinct saturation for long filling times, characteristic of non-interacting isolated point defects (the exponential capture law). Identical behaviour was also observed for sample A in the case of the dominant trap labelled E3. Moreover, these two traps, E3 and EG2, were identified on the basis of their parameters obtained from Arrhenius plots (Fig. 3). These parameters (Table 1) are very similar to those of the trap EL2 [56] – the dominant native defect in GaAs, identified as an As-antisite defect (As_{Ga}). For the traps E1 and E2, capture kinetics measurements have not been performed, because they revealed saturation already for very short filling-pulse times. From the emission characteristics of the two traps, it

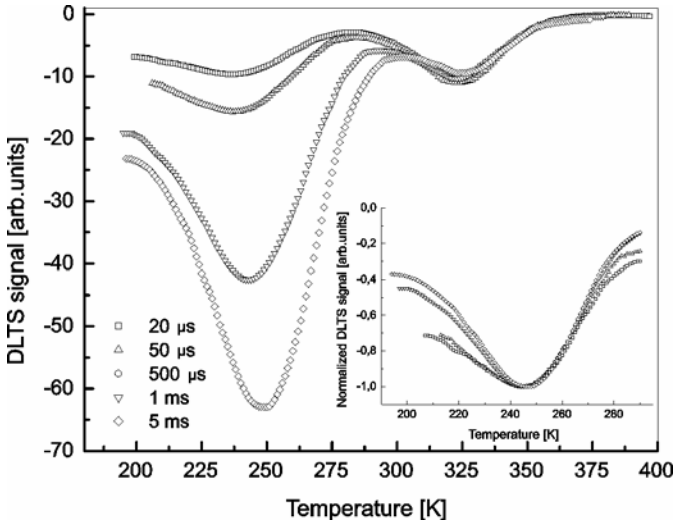

Fig. 4. DLTS temperature spectra of the $In_{0.085}Ga_{0.915}As/GaAs$ heterostructure for different filling pulse times. Reverse bias was $U_R = -1$ V, filling pulses heights $U_1 = 0$ V and $U_2 = -0.5$ V, and the lock-in frequency constant at 2.5 Hz. The inset shows the plot of the normalized DLTS peak amplitude of the trap EG1

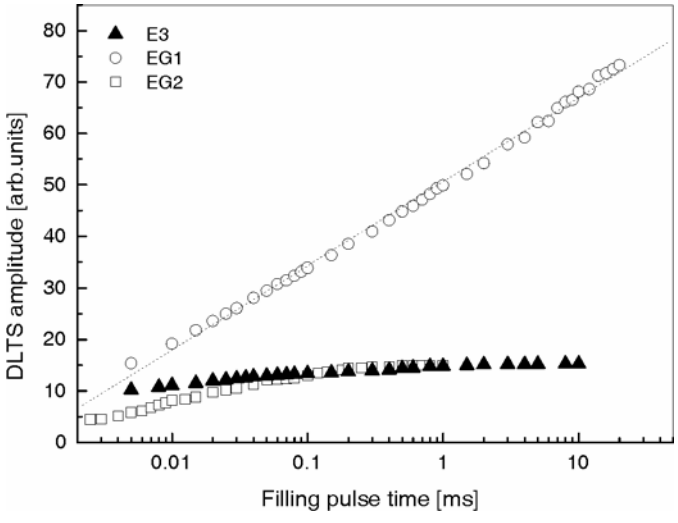

Fig. 5. DLTS peaks amplitudes of the trap E3 (solid symbols) in GaAs/GaAs, and EG1 and EG2 (open symbols) in $In_{0.085}Ga_{0.915}As/GaAs$ as functions of the filling-pulse time

was possible to identify them as the traps EL5 [56] and EI1 [16], respectively. All the deep level parameters determined for each trap in both samples are summarized in Table 1. It is worth noticing that the carrier capture cross section evaluated for the dislocation trap EG1 (Table 1) changes with time. This results from the fact that, by

definition, the capture cross section of an extended defect changes with time – as the charge builds up, the defect becomes less attractive.

8. Conclusions

In conclusion, criteria concerning distinguishing between point and extended defects, especially dislocations, in DLTS experiments have been presented. Criteria containing DLTS line shape and behaviour analysis, as well as capture kinetics measurements, allow us to clearly differentiate between these two types of defects. These exceptional features of point and extended defects encountered in DLTS measurements have been exploited in the analysis and identification of deep level defects in lattice-matched n-GaAs/GaAs and lattice-mismatched n-$In_{0.085}Ga_{0.915}As$/GaAs heterostructures. All deep levels have been identified on the basis of their parameters and the odd features of their DLTS line spectra. The possible association of the trap EG1, revealed in this work in lattice-mismatched samples, with the dislocation trap labelled ED1 in literature, is not obvious and requires further investigations.

References

[1] WEBER E.R., Physica B, 340–342 (2003), 1.
[2] LANG D.V., J. Appl. Phys., 45 (1974), 3023.
[3] FIGIELSKI T., Phys. Stat. Sol. (a), 121 (1990), 187.
[4] KIMERLING L.C., PATEL J.R., Appl. Phys. Lett., 34 (1979), 73.
[5] KVEDER V.V., OSIPYAN YU.A., SCHÖTER W., ZOTH G., Phys. Stat. Sol. (a), 72 (1982), 701.
[6] OMLING P., SAMUELSON L., GRIMMEISS H.G., J. Appl. Phys., 54 (1983), 5117.
[7] OMLING P., WEBER E.R., MONTELIUS L., ALEXANDER H., MICHEL J., Phys. Rev. B, 32 (1985), 6571.
[8] WOSIŃSKI T., J. Appl. Phys., 65 (1989), 1566.
[9] SCHRÖTER W., QUEISSER I., KRONEWITZ J., Inst. Phys. Conf. Ser., 104 (1989), 75.
[10] SCHRÖTER W., KRONEWITZ J., GNAUERT U., RIEDEL F., SEIBT M., Phys. Rev. B, 52 (1995), 13726.
[11] HEDEMANN H., SCHRÖTER W., J. Phys. III France, 7 (1997), 1389.
[12] RIEDEL F., SCHRÖTER W., Phys. Rev. B, 62 (2000), 7150.
[13] SCHRÖTER W., HEDEMANN H., KVEDER V., RIEDEL F., J. Phys. Condens. Matter., 14 (2002), 13047.
[14] SCHUBERT E.F., *Doping in III–V Semiconductors*, Cambridge Univ. Press, 1993.
[15] SCHRODER D.K., *Semiconductor Material and Device Characterization*, Wiley, New York, 1990.
[16] LEFEVRE H., SCHULZ M., Appl. Phys., 12 (1977), 45.
[17] HENRY C.H., LANG D.V., Phys. Rev. B, 15 (1977), 989.
[18] PONS D., J. Appl. Phys., 55 (1984), 3644.
[19] KISIELOWSKI C., WEBER E.R., Phys. Rev. B, 44 (1991), 1600.
[20] CAVALCOLI D., CAVALLINI A., GOMBIA E., J. Phys. III France, 7 (1997), 1399.
[21] GRILLOT P.N., RINGEL S.A., FITZGERALD E.A., WATSON G.P., XIE Y.H., J. Appl. Phys., 77 (1995), 676.
[22] GRILLOT P.N., RINGEL S.A., FITZGERALD E.A., WATSON G.P., XIE Y.H., J. Appl. Phys., 77 (1995), 3248.
[23] CHRETIEN O., APETZ R., VESCAN L., Semicond. Sci. Technol., 11 (1996), 1838.
[24] PANEPINTO L., ZEIMER U., SEIFERT W., SEIBT M., BUGGE F., WEYERS M., SCHRÖTER W., Mater. Sci. Eng. B, 42 (1996), 77.
[25] PAL D., GOMBIA E., MOSCA R., BOSACCHI A., FRANCHI S., J. Appl. Phys., 84 (1998), 2965.

[26] WOSIŃSKI T., YASTRUBCHAK O., MĄKOSA A., FIGIELSKI T., J. Phys.: Condens. Matter, 12 (2000), 10153.
[27] WOSIŃSKI T., MĄKOSA A., FIGIELSKI T., RACZYŃSKA J., Appl. Phys. Lett., 67 (1995), 1131.
[28] PŁACZEK-POPKO E., SZATKOWSKI J., HAJDUSIANEK A., RADOJEWSKA B., Proc. SPIE, 2780 (1996), 153.
[29] TE NIJENHUIS J., VAN DER WEL P.J., VAN ECK E.R.H., GILING L.J., J. Phys. D: Appl. Phys., 29 (1996), 2961.
[30] LIU X.W., HOPGOOD A.A., USHER B.F., WANG H., BRAITHWAITE N.ST.J., Semicond. Sci. Technol., 14 (1999), 1154.
[31] KAPLAR R.J., RINGEL S.A., KURTZ S.R., KLEM J.F., ALLERMAN A.A., Appl. Phys. Lett., 80 (2002), 4777.
[32] STIEVENARD D., LANNOO M., BOURGOIN J.C., Solid-State Electron., 28 (1985), 485.
[33] IKOSSI-ANASTASIOU K, ROENKER K.P., J. Appl. Phys., 61 (1987), 182
[34] SAH C.T., Solid-State Electron., 19 (1976), 975.
[35] ITO A., TOKUDA Y., Solid-State Electron., 46 (2002), 1307.
[36] BRUDNYI V.N., PESHEV V.V., Semiconductors, 37 (2003), 140.
[37] DAS A., SINGH V.A., LANG D.V., Semicond. Sci. Technol., 3 (1988), 1177.
[38] KANIEWSKA M., KANIEWSKI J., Solid State Commun., 53 (1985), 485.
[39] DIWAN A., SINGH V.A., ARORA B.M., MURAWALA P.A., J. Phys C: Solid State Phys., 20 (1987), 3603.
[40] WOSIŃSKI T., MĄKOSA A., RACZYŃSKA J., Acta Phys. Polon. A, 79 (1995), 369.
[41] HARDALOV CH., YANCHEV I., GERMANOVA K., IVANOV TZV., SAMURKOVA L., KIRKOV K., NIGOHOSIAN A., J. Appl. Phys., 71 (1992), 2270.
[42] YASTRUBCHAK O., WOSIŃSKI T., MĄKOSA A., FIGIELSKI T., TÓTH A.L., Physica B, 308-310 (2001), 757.
[43] FIGIELSKI T., Solid State Electron., 21 (1978), 1403.
[44] WATSON G.P., AST D.G., ANDERSON T.J., PATHANGEY B., HAYAKAWA Y., J. Appl. Phys., 71 (1992), 3399.
[45] SZATKOWSKI J., PŁACZEK-POPKO E., SIERAŃSKI K., HANSEN O.P., J. Appl. Phys., 86 (1999), 1433.
[46] CALLEJA E., MOONEY P.M., WRIGHT S.L., HEIBLUM M., Appl. Phys. Lett., 49 (1986), 657.
[47] MOONEY P.M., CASWELL N.S., WRIGHT S.L., J. Appl. Phys., 62 (1987), 4786.
[48] BOURGOIN J.C., FENG S.L., BARDELEBEN H.J., Appl. Phys. Lett., 53 (1988), 1841.
[49] WANG A.Z., ERSEN W.A., Solid-State Electronics, 38 (1995), 673.
[50] YOON S.F., LUI P.Y., ZHENG H.Q., J. Cryst. Growth, 212 (2000), 49.
[51] WALTHER C., BOLLMANN J., KISIEL H., KRIMSE H., NEUMANN W., MASSELINK W.T., Physica B, 273-274 (1999), 971.
[52] GOMBIA E., MOSCA R., FRIGERI P., FRANCHI S., AMIGHETTI S., GHEZZI C., Mat. Sci. Eng. B, 91 (2002), 393.
[53] GELCZUK Ł., DĄBROWSKA-SZATA M., Elektronika, 10 (2003), 3.
[54] GELCZUK Ł., DĄBROWSKA-SZATA M., JÓŹWIAK G., RADZIEWICZ D., Acta Phys. Polon. A, 106 (2003), 265.
[55] FERENCZI G., KISS J., Acta Phys. Acad. Sci. Hung., 50 (1981), 285.
[56] MARTIN G.M., MITONNEAU A., MIRCEA A., Electron. Lett., 13 (1977), 191.

Received 10 May 2005
Revised 27 July 2005

Materials Science-Poland, Vol. 23, No. 3, 2005

Quantitative mapping of the elastic properties of electron-beam damaged silica-based low-*k* films

LE JIANG[1], H. GEISLER[2], E. ZSCHECH[2*]

[1]Gesellschaft für Wissens- und Technologietransfer der TU Dresden mbH, Chemnitzer Strasse 48 b, D-01187 Dresden, Germany

[2]AMD Saxony LLC & Co. KG, Materials Analysis Department, Wilschdorfer Landstrasse 101, D-01109 Dresden, Germany

A quantitative technique for mapping the elastic modulus, performed on organosilicate glass (OSG) thin films with different surface conditions, is described. This modulus mapping technique provides highly valuable information about the elastic properties at the near-surface region of the films. The results show that low-*k* films can be modified by electron beams, yielding a near-surface region with increased stiffness. Compared to quasi-static nanoindentation, the modulus mapping technique is more surface sensitive, and therefore has a better capability to detect slight differences in elastic properties between ultra-thin films of different thicknesses on top of OSG films.

Key words: *modulus mapping; nanoindentation; low-*k*; electron-beam damage; surface*

1. Introduction

Low-*k* dielectric materials for insulating thin films are needed to diminish power consumption and minimize the cross talk between on-chip metal interconnects in leading-edge microelectronic products [1, 2]. Electron treatments can be applied for the local densification of OSG materials in order to increase the stiffness of the backend-of-line (BEoL) layer stack. The local change of the chemical bonding of the interlayer dielectric (ILD) material, however, increases the effective permittivity (*k* value), and consequently the electrical performance of the Cu/low-*k* structure is influenced. It is an extremely challenging task to change the local electronic polarisability and the chemical bonding of the ILD material in such a way that the stiffness of the material is increased significantly and the effective *k* value is increased only slightly. In addition, the adhesion between the etch stop layer and low-*k* material should be improved. As the interconnect line spacing of ultra large scale integrated circuits continues to

*Corresponding author, e-mail: ehrenfried.zschech@amd.com

shrink, optimising the electrical performance of Cu/low-*k* structures and mechanical properties of BEoL layer stacks becomes increasingly important for the integration of low-*k* materials.

For the optimisation of ILD material properties, considering both the integral thin -film material and in particular the near-surface regions, with a typical extension of 10–100 nm, it is necessary to understand the relationship between changed electronic polarisability and chemical bonding, as well as between permittivity and modulus [3]. Particularly, the extent of damage has to be studied quantitatively. An additional argument for the need to understand electron–material interaction is the fact that the imaging of patterned OSG structures is challenging for electron microscopy since the structures are damaged during examination and shrinkage is observed. The analysis of several individual damage processes results in the conclusion that the radiation damage depends on the electron energy, and that it is proportional to the energy dose deposited in the sample for a certain electron energy [4]. The goal of this paper is to propose a methodology for evaluating and quantifying the extent of electron-induced modification in OSG thin films, based on changed nanomechanical properties. Near-surface mechanical properties are examined quantitatively by an elastic modulus mapping technique. This technique allows one to distinguish between ultra-thin layers of different thicknesses with a high surface sensitivity.

2. Experimental

In this study, a carbon-doped oxide dielectric material comprised of Si, C, O, and H (OSG, also called SiCOH), deposited on a blanket wafer using plasma-enhanced chemical vapour deposition (PECVD), was locally modified by the electron beam of a scanning electron microscope (SEM). The modified areas of the OSG film were investigated by applying the modulus mapping technique [5], implemented in a Tribo-Indenter nanomechanical testing instrument with in-situ scanning probe microscopy (SPM) imaging capability (Hysitron, Inc., Minneapolis, MN). A scheme of the Hysitron TriboIndenter measuring system is shown in Fig. 1. During the mapping process, the dynamic test is performed by oscillating the indenter tip with small forces while monitoring the resultant displacement and phase lag due to the material response. Simultaneously, SPM imaging allows the indenter tip to scan across the material surface. The system continuously monitors the stiffness of the sample and provides a plot of the stiffness as a function of the position on the sample. The stiffness is given at each pixel of the image, and the modulus can be calculated if the geometry of the probe tip is known. The complex modulus information obtained by this modulus mapping technique includes the real and imaginary parts, $E = E' + iE''$, and provides the storage (E') and loss (E'') characteristics of a material. The E' and E'' values are given by [6]

$$E' = \frac{k_s \sqrt{\pi}}{2\sqrt{A_c}} \tag{1a}$$

$$E'' = \frac{\omega C_s \sqrt{\pi}}{2\sqrt{A_c}} \tag{1b}$$

respectively, where k_s is the storage stiffness proportional to the ratio of the force and displacement, C_s is the loss stiffness proportional to the phase lag, ω is the frequency, and A_c represents the contact area calculated based on the radius of curvature of the probe tip.

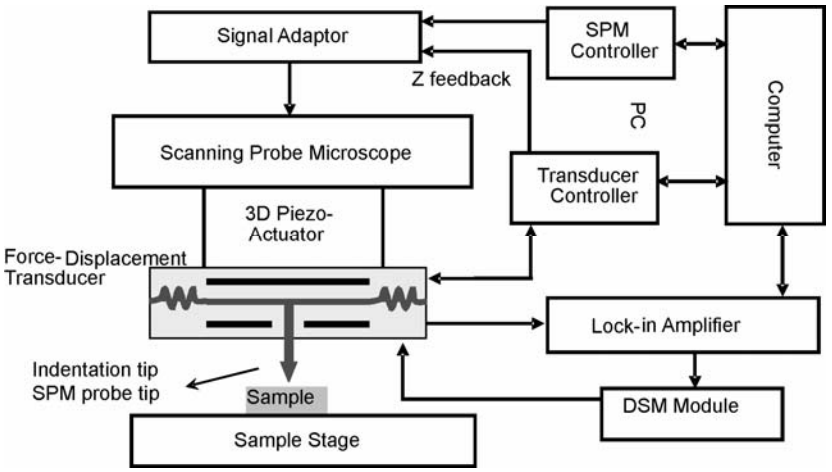

Fig. 1. Schematic diagram of the Hysitron TriboIndenter combined with the nanoDMA and SPM techniques. The DSM module provides the alternation of the signal configurations, necessary for quasi-static or dynamic testing

The results of such a modulus mapping are equivalent to a dynamic indentation test performed at each pixel in a 256 × 256 image. Areas with the size of about 9 μm × 7 μm in an unpatterned low-*k* OSG film with a thickness of about 1000 nm – the original value of *k* was 2.7 – were exposed to an electron beam in an SEM, applying electron beam energies of 1, 3, and 5 keV for the same exposure time. Using the modulus mapping technique, 15 μm × 15 μm areas were scanned with a Berkovich diamond tip mounted on the nanoindentation tool. The measuring parameters (e.g., the oscillation frequency of the ac-force – 200 Hz, dc-force – 2 μN, and amplitude of the ac-force – 1.5 μN) were identical for the as-deposited and electron-beam treated regions of the sample.

Quasi-static nanoindentation was carried out on the same samples for comparison with the modulus mapping technique. A schematic representation of load vs. displacement data for an indentation experiment is shown in Fig. 2 [7, 8]. As the indenter is first driven into the film, both elastic and plastic deformation occurs. After the indenter is withdrawn, the elastic displacements are recovered, and an analysis of the

elastic unloading data can then be used to experimentally relate the measured quantities to the projected contact area and elastic modulus. For any axisymmetric indenter, the relationship is

$$S = \frac{dP}{dh} = \frac{2}{\sqrt{\pi}} E_r \sqrt{A_c} \tag{2}$$

Here, $S = dP/dh$ is the experimentally measured stiffness of the upper portion of the unloading data and E_r is the reduced modulus given by

$$\frac{1}{E_r} = \frac{1-\nu^2}{E} + \frac{1-\nu_i^2}{E_i} \tag{3}$$

where E and v are Young's modulus and Poisson's ratio for the specimen, respectively, and E_i and v_i are the same quantities for the indenter.

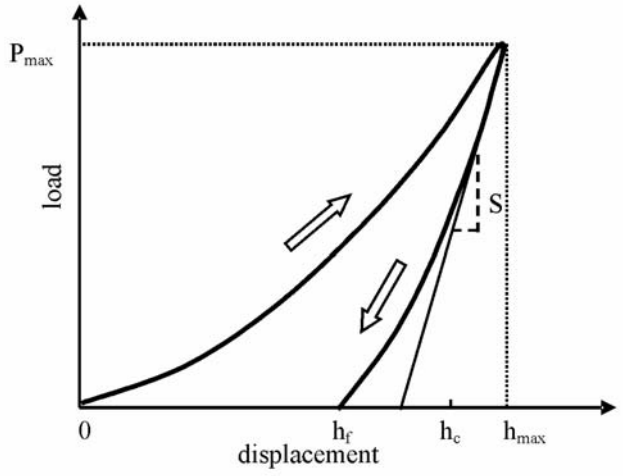

Fig. 2. A schematic representation of load vs. displacement data for an indentation experiment: P_{max} – the peak indentation load, h_{max} – the displacement at peak load, h_f – the final depth of the contact impression after unloading, h_c – the contact depth, S – the initial unloading stiffness

To evaluate the contact area at peak load during the nanoindentation of a thin film, special procedures are used to estimate the contact depth h_c from the load –displacement data, and the contact area is determined by evaluating the area function at this depth, i.e. $A_c = f(h_c)$. The most common procedure determines h_c as

$$h_c = h_{max} - 0.75 \frac{P_{max}}{S} \tag{4}$$

3. Results

For comparison of the modulus mapping technique with the quasi-static nanoindentation technique, OSG thin films 500 nm thick were capped with ultra-thin Ta films. The Ta film thickness varied between 10 and 30 nm. The elastic properties of these ultra-thin films, measured quantitatively by applying the modulus mapping technique, were compared with the data from measurements performed on identical samples applying the quasi-static depth-sensing nanoindentation technique with a normal force F_n ranging from 5 μN to 80 μN.

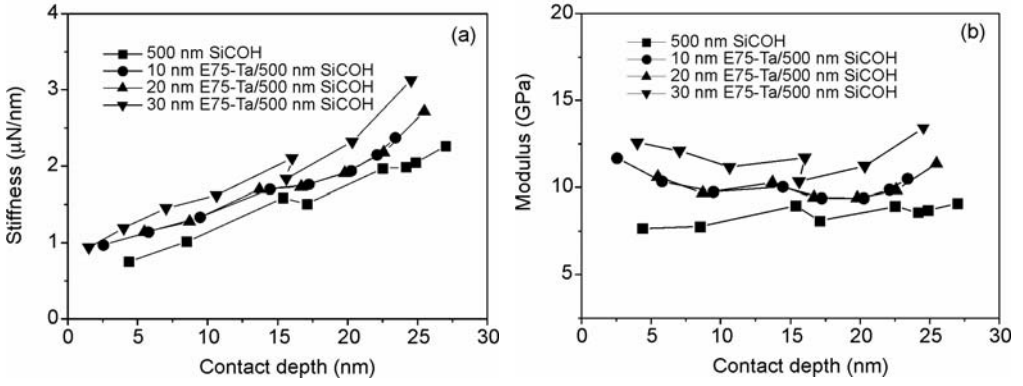

Fig. 3. Stiffness (a) and elastic modulus (b) vs. contact depth from quasi-static indents made on a pure OSG film and on ultra-thin Ta films with different thicknesses on top of OSG films

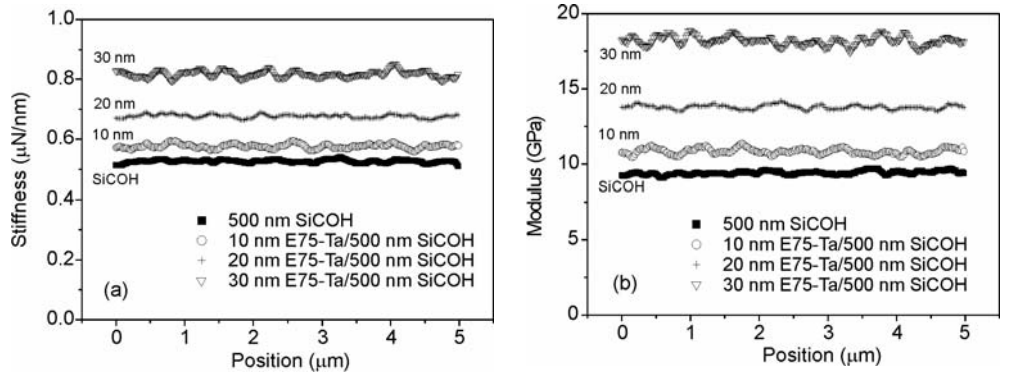

Fig. 4. Stiffness (a) and elastic modulus (b) cross-sectional data from stiffness and modulus maps of a pure OSG film and of ultra-thin Ta films with different thicknesses on top of OSG films

These forces cause shallow indents compared to the film thickness. The storage modulus is used to compare with the quasi-static nanoindentation results for a loss modulus of nearly zero, since the material shows small or negligible viscoelastic properties. As shorthand, the term modulus is used in what follows instead of reduced elastic modulus, which is usually measured by nanoindentation. As expected, both the

stiffness and modulus, obtained with quasi-static indentation and modulus mapping, are increased for the OSG/Ta thin film samples as compared to the bare OSG films. Both the indentation experiment and modulus mapping show an increase of the mechanical stiffness of the samples with increasing Ta film thickness (see Fig. 3 and 4). There is no significant difference between the stiffness and elastic modulus, however, for samples with 10 and 20 nm thick Ta films as seen by the quasi-static indentation technique, whereas a line-section analysis of the quantitative maps shows a clear difference in the stiffness and modulus of these two samples. Extracted from Fig. 4, the mean values of stiffness for a bare OSG film and for OSG films with 10 nm, 20 nm, and 30 nm ultra-thin Ta films on top are 0.53, 0.58, 0.68, and 0.82 μN/nm, and the respective values of elastic modulus are 9.5, 11, 14, and 18 GPa. These results are in agreement with the quasi-static indentation results calculated by extrapolating quasi-static indentation curves down to a contact depth of 1 or 2 nm.

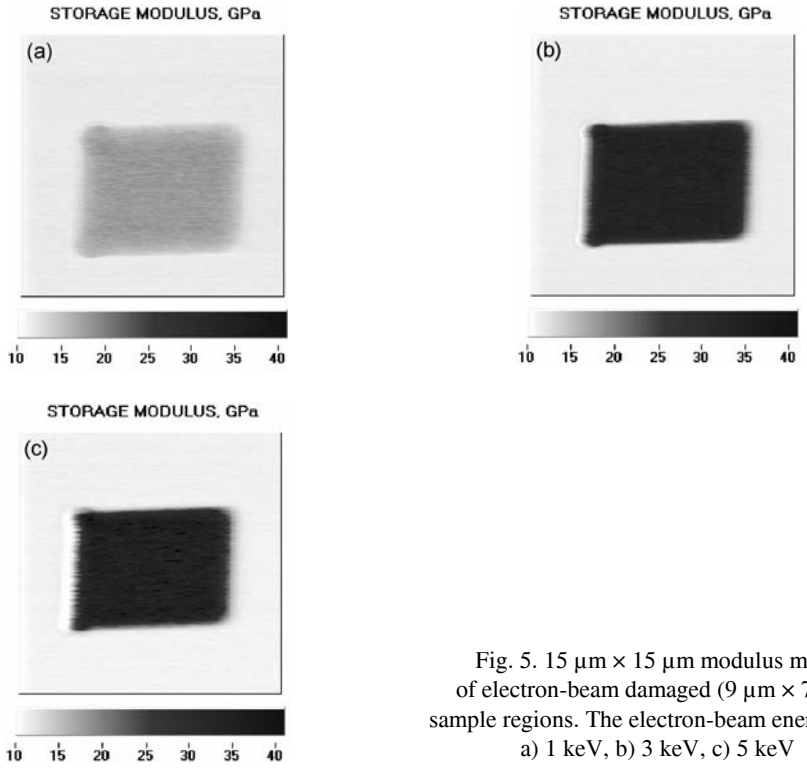

Fig. 5. 15 μm × 15 μm modulus maps of electron-beam damaged (9 μm × 7 μm) sample regions. The electron-beam energy was: a) 1 keV, b) 3 keV, c) 5 keV

Due to the local exposure of the surface to an electron beam, a shrinkage of the OSG thin film was observed. This shrinkage depends on the applied electron energy. Higher electron energies caused more serious damage, leading to deeper craters in the OSG film. Different image contrasts between the damaged region and as-deposited area are shown on quantitative modulus maps in Fig. 5.

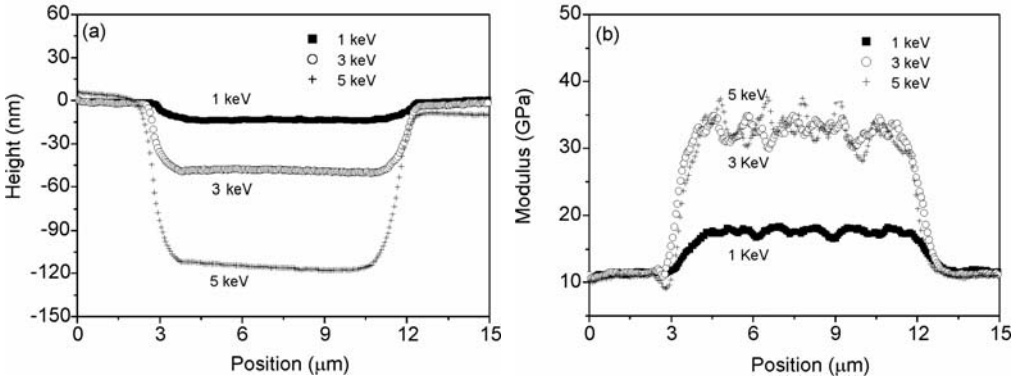

Fig. 6. Cross-sectional data from topography and modulus maps: a) the crater profile caused by the electron beam, b) cross-section profiles of the modulus maps in Fig. 5

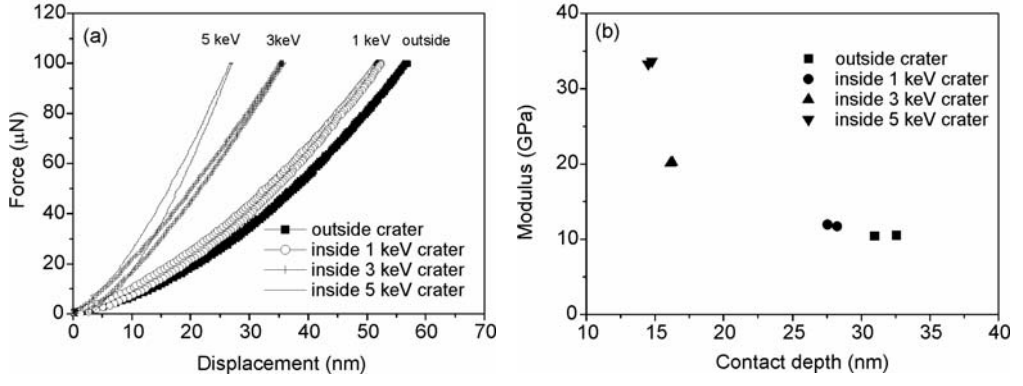

Fig. 7. Quasi-static indentation data for the electron-beam damaged regions of the OSG sample: a) force-displacement curves of samples locally exposed to electron beams of different energies (exposure time for all samples – 25 s), b) the calculated elastic modulus for the sample regions corresponding to the curves shown for in (a)

The crater depth was determined directly from line-section profiles of topography maps as represented in Fig. 6a. The mean values of the storage modulus, determined from a line-section analysis of the modulus maps, are 11, 17, 32, and 35 GPa for 0, 1, 3, and 5 keV electron beam energies used in the surface treatment, respectively (Fig. 6b). The more damaged OSG film regions are characterized by steeper force-displacement curves, and thus, by higher modulus values. This result is confirmed by the quasi-static indentation data shown in Fig. 7a. The modulus values of OSG films are 10.5 GPa, 12 GPa, 20 Gpa, and 33 GPa in the case without damage and with damage with 1 keV, 3 keV, and 5 keV electron beam energies, respectively (Fig. 7b). The mapping data for the as-deposited film and for the area with 5 keV electron beam treatment are comparable with the quasi-static indentation data but those for areas damaged with 1 keV and 3 keV electron beams are higher than the values obtained from indents made on the same sample.

4. Discussion

It is necessary to note that the elastic modulus obtained from quasi-static indentation depends on the stiffness of the material which is determined by the slope of the unloading curve, using a power-law fit to the initial unloading data, and by the area function of the indentation probe based on Pharr–Oliver theory [7]. At very shallow penetration depths, the accuracy of the tip area function becomes more critical for the calculation of the elastic modulus. Using the currently defined area function at very small contact depths (less than 10 nm), the modulus decreases with increasing contact depth. This decrease probably results from the indentation size and the strain gradient plasticity effect [9, 10], which is a near-surface effect. After reaching a minimum value, the modulus increases with increasing depth due to the constraint of the stiffer substrate. Considering that the maximum penetration depth of the tip is about 3.5 nm for the modulus mapping method and that the contact depth is even lower in this case, it is reasonable that the mapping technique results in higher modulus and lower stiffness values, approaching values from low-depth quasi-static indentations.

As expected, the OSG film was modified to different degrees when exposed locally to electron beams for the same exposure time with different energies. The larger the electron beam energy, the more serious the damage on the OSG material, i.e., the deeper were the craters. Since the degree of damage varies with depth for a single crater, higher modulus mapping results for 1 keV and 3 keV electron-beam damaged samples as compared to quasi-static indentation results for the same samples can be explained by the different information depths and surface sensitivities of these techniques. Only the very near-surface region is analysed with the modulus mapping technique, while the quasi-static indentation method measures film properties over a larger depth range. For example, the maximum penetration depth for quasi-static indentation in a crater formed by a 1 keV electron beam is 50 nm, whereas the maximum penetration depth of modulus mapping is only about 3.5 nm. This difference in depth sensitivity explains the different modulus values. In the case of the crater formed by a 5 keV electron beam, the depth of the crater is about 120 nm, and both methods provide similar results. A supposed explanation for this result is that the damage is nearly the same at positions 25 nm and 3.5 nm deep for a material damaged with a 5 keV electron beam energy.

Since the modulus mapping technique is more surface sensitive than quasi-static indentation, it is possible to detect slight differences in the elastic properties of ultrathin layers on top of OSG films. It should also be noted that with the quasi-static indentation method the data from very shallow indents could be significantly affected by measuring noise, drift, or tip area function, which all cause errors. Therefore, the modulus mapping technique should be applied for determining the elastic properties of thin films and near-surface regions.

5. Conclusion

In summary, we have shown that modulus mapping is a valid method for assessing the process-induced modification of dielectric materials, such as OSG damage caused by electron-beam treatment. The modulus mapping technique implemented in a nano-indentation tool with in-situ SPM imaging capability allows a mapping of the stiffness and elastic modulus quantitatively on the scale of a few micrometers on low-*k* films with a very high surface sensitivity. Consequently, the extent of damage caused by a specific process step can be quantified with high spatial resolution. Small areas on low-*k* films, which were locally exposed to an electron beam in a SEM, showed distinct image contrast, the electron-beam treated regions being stiffer than the regions not treated. Different electron energies and/or exposure times lead to quantitatively different modulus maps. The modulus values resulting from the maps agree well with low-load quasi-static nanoindentation data. Small changes in the modulus can be resolved, as shown for different surface treatments of OSG films. Our results show that modulus mapping is more surface sensitive than quasi-static indentation. Modified near-surface regions of low-*k* films can be characterized, and ultra-thin layers can be distinguished quantitatively.

Acknowledgements

Valuable discussions with Dmytro Chumakov and sample preparation performed by Petra Hofmann, both with AMD Saxony, Dresden, Germany, are gratefully acknowledged. The authors would like to thank Reinhard Sturm and Henry Urban, GWT Dresden, Germany, for supporting this study.

References

[1] MAEX K., BAKLANOV M.R., SHAMIRYAN D., IACOPI F., BRONGERSMA S.H., YANOVITSKAYA Z.S., J. Appl. Phys., 93 (2003), 8793.
[2] HO P.S., [in:] *Materials for Information Technology*, E. Zschech, C. Whelan, T. Mikolajick (Eds.), Springer, Berlin, in press (2005).
[3] IACOPI F., TRAVALY Y., STUCCHI M., STRUYF H., PEETERS S., JONCKHEERE R., LEUNISSEN L.H.A., TOKEI ZS., SUTCLIFFE V., RICHARD O., VAN HOVE M., MAEX K., Mat. Res. Soc. Symp. Proc., Warrendale/PA, 812 (2004), 19.
[4] EGERTON R.F., LI P., MALAC M., Micron, 35 (2004), 399.
[5] WARREN O.L, WYROBEK T.J., Meas. Sci. Technol., 16 (2005), 100.
[6] Hysitron Incorporated, *NanoDMA for Viscoelastic Materials*, available online at: http://www.hysitron.com/Products/Sellsheets/new_nanoDMA.htm
[7] OLIVER W.C., PHARR G.M., J. Mater. Res.. 7 (1992), 1564.
[8] PHARR G.M., OLIVER W.C., MRS Bulletin, 17 (1992), 28.
[9] NIX W.D, GAO H., J. Mech. Phys. Solids, 46 (1998), 411.
[10] SAHA R., XUE Z.Y.,.HUANG Y, NIX W.D., J. Mech. Phys. Solids, 49 (2001), 1997.

Received 11 June 2005
Revised 4 August 2005

Materials Science-Poland, Vol. 23, No. 3, 2005

Surface photovoltage in silicon. Novel applications for chemical and biological sensing

K. NAUKA*, Z. LI, T.I. KAMINS

Hewlett-Packard Laboratories, 1501 Page Mill Road, Palo Alto, California 94304, USA

The Surface Photovoltage technique has been recently employed for chemical and biological sensing. Selected chemical and biological species deposited on the crystalline silicon surface introduced surface barrier changes that were detected using the non-contact Surface Photovoltage mode. The magnitude of the surface barrier modifications provided a unique signature of the sensed species. The simplicity and sensitivity of this technique offer an exciting opportunity for a new type of low-cost sensing devices.

Key words: *Surface Photovoltage technique; chemical and biological sensing; crystalline silicon; surface barrier*

1. Introduction

The Surface Photovoltage (SPV) technique monitors semiconductor surface barrier changes introduced by illumination. Since the steady-state semiconductor surface barrier and its illumination induced modifications are related to the surface and bulk properties of the measured material, the technique offers the possibility for simple determination of some fundamental properties of the semiconductor material [1, 2]. SPV measurements can be tailored according to specific needs, for example: sub-bandgap illumination is used to study surface states [3, 4], low intensity above-bandgap illumination is employed to determine minority carrier lifetime [5], light modulation frequency is varied in order to differentiate between the slow surface states and bulk recombination processes [6], and non-contact measurements are selected when the measurement of undisturbed surface properties is desired [6, 7].

The SPV technique has found particularly important applications in the monitoring of silicon wafer properties [7, 8]. Commercial SPV-based monitoring tools were incorporated into silicon integrated circuit (IC) manufacturing processes, facilitating detection in real-time of faulty silicon wafers. These tools were designed specifically for the monitoring of silicon wafers by limiting the measurement parameters (e.g.,

*Corresponding author, e-mail: chris.nauka@hp.com

excitation wavelength, photon flux density) to values appropriate for measuring the silicon electronic properties, while at the same time employing additional features to enhance the measurement capabilities (e.g., multiple probes for detecting the SPV signal, additional illumination, heating stage, corona discharge source).

These applications have led to a better understanding of the Surface Photovoltage phenomena in high quality silicon material and have demonstrated potential applications of the SPV technique beyond silicon IC devices, particularly in the area of nanoscale structures and molecular sensing [9–11]. The last application reflects the growing interest in low-cost sensors for chemical and biological monitoring. The use of the silicon surface as a binding platform for a variety of chemical and biological compounds [12, 13] could lead to SPV sensors that offer the advantages of low manufacturing cost, a device design allowing easy integration with an electronic control platform, sensitivity, the ability to detect multiple species, speed, and reusability. Silicon surface barrier measurements have been previously proposed for sensing small quantities of selected gases [14–16]. Recent reports [17] expanded the technique further to aqueous solutions of a variety of inorganic chemicals, selected organic compounds, and biological DNA species. This paper reviews recent advances in novel SPV applications.

2. Experiment

The SPV technique employed in this work is based on previously described [6] silicon surface charge measurements. The SPV signal Ψ_{SPV} is obtained by illuminating the front side of the silicon wafer with a monochromatic photon flux (λ = 800 nm), while the backside of the wafer is not illuminated (Fig. 1). Photons are absorbed mostly within the region adjacent to the surface and generate excess carriers, decreasing the silicon surface barrier. The potential difference created by the changing surface barrier at the illuminated front side with reference to the unchanged dark back side barrier is the measured SPV signal. At high photon flux, the front surface barrier is reduced to nearly zero, and the SPV signal corresponds to the equilibrium silicon surface barrier.

Since the equilibrium surface barrier height is related to the density and energy spectrum of the surface charges, standard space-charge expressions [1, 2] can be used to calculate the average surface charge density. Intrinsic silicon surface charges are due to bonds terminating at the surface, although the density of broken surface bonds can be reduced by surface reconstruction. In most cases, however, the majority of the silicon surface charges are due to either intentional or unintentional reactions between the silicon surface atoms and the environment. Chemisorbed and physisorbed chemical species change the surface charge density and modify the surface barrier [12, 13, 18]. While monitoring the effect of the surface species, it is important that the measurement does not perturb the surface. Therefore, the present SPV measurements were conducted in a “contactless” mode, without the need for additional silicon processing, and used commercially available SPV measuring equipment [19].

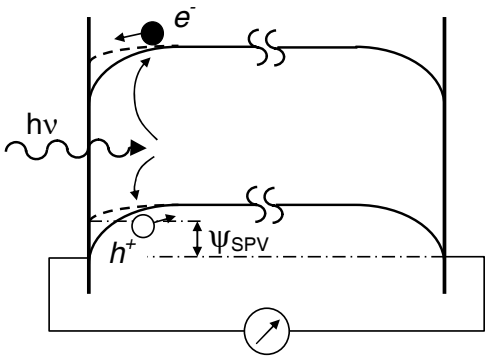

Fig. 1. SPV principle. Illumination with photons with energies higher than the silicon bandgap ($h\nu > E_g$) causes a decrease of the front (illuminated) surface barrier. Under high illumination intensity the surface barrier disappears and the SPV signal corresponds directly to the surface charges

SPV measurements require that the surface be free of defects pinning the Fermi level**;** therefore, only high quality 150 mm diameter silicon wafers were used. They were n-type and p-type, with resistivities between 1 Ω·cm and 25 Ω·cm. Since surface atomic arrangement depends on the surface orientation, only wafers with exact (001) and (111) orientations (±0.5°) or wafers misoriented by 4° from the (111) plane towards [011] were used. The initial uniform surface termination was achieved by annealing the wafers in hydrogen ambient as previously described [9]. Previous reports demonstrated that such a heat treatment can provide a well-organized surface with uniform hydrogen coverage [9, 10].

In order to investigate the effect of chemical species on the silicon surface barrier**,** freshly prepared wafers still maintaining the original H_2 termination were dipped into aqueous solutions of selected inorganic bases and acids. The sensitivity of the technique was tested by varying the chemical concentration and time during which the silicon wafer was exposed to chemicals. The acid pH varied from 1 to 6, and base pH varied from 8 to 13. Corresponding tests were also conducted for constant pH, but with varying chemical species. SPV measurements of the silicon surface barrier were conducted within less than 2 minutes after sample removal from the chemical bath and air drying in order to minimize the reaction between the treated silicon surface and air [9]. Only dry Si surfaces were measured. Occasionally, the surface was blown off with nitrogen after chemical exposure, but before measurements, in order to accelerate the drying of the silicon surface.

In addition, silicon wafers were exposed to a few selected organic compounds belonging to the same family. Wafers were dipped into hot alkanes (pentane, hexane, and octane) for 15 min, and then immediately measured. Either pure alkanes or their solutions in an inert hydrocarbon (xylene) were used. The silicon surface in contact with hot alkanes underwent thermally induced hydrosilylation, providing at least partial, stable monolayer termination [20].

The use of SPV detection was also investigated in a genomic experiment using a single strand, 12-mer DNA probe terminated with an acrylate linker group anchored to a silicon surface functionalised with 3-mercaptopropyl-trimethoxysilane (for a detailed description of sample preparation, see Ref. [11]). The silicon surface barrier

height was then measured and correlated with the presence of the DNA group on the silicon surface. The SPV signal was measured for the single strand DNA probe and also for samples exposed to the completely matched and one-pair mismatched DNA molecules.

3. Results and discussion

The surface band bending, and therefore the measured SPV signal, corresponds to electrical charges residing either on the silicon surface or in its vicinity. Many chemical and biological species are capable of modifying the surface barrier by electrical charge transfer while forming chemical bonds with the silicon surface (chemisorption) or by electrostatic interactions with the silicon surface states (physisorption). In the case of chemisorbed species, the binding energy is usually larger than 0.1 eV. Various processes contributing to physisorption (van der Waals interactions, dipole formation, image forces, etc.) are characterized by binding energies below 0.1 eV [21]. For a given species, the magnitude of the surface photovoltage varies monotonically with the concentration, allowing limited quantification of the concentration. At a fixed concentration, the magnitude of the surface barrier modification is often specific for the molecules reacting with the silicon surface, which offers an opportunity for limited qualitative analysis.

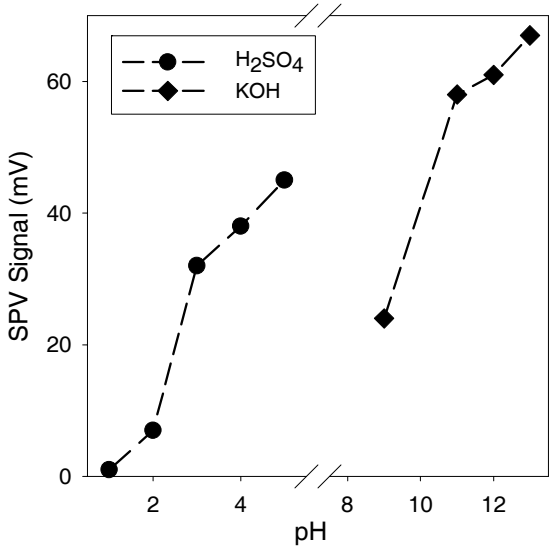

Fig. 2. Correlation between the SPV signal and ionic concentration for selected inorganic base and acid

Exposure of the silicon surface to inorganic bases or acids results primarily in chemisorption of OH^- and H^+ ions, modifying the silicon surface barrier [10, 12, 13].

This process is limited by the number of available ions. The number of ions undergoing reaction with silicon is determined by the base or acid concentration. Figure 2 shows the correlation between the SPV signal and the ionic concentration. The modification of the silicon surface barrier is also related to the type of chemical species. The application of solutions with the same pH, but containing different acids or bases produces different SPV values (Fig. 3). This difference could be related to different counter ions present in the solution (Na and K^+ in the case of bases, and SO_4^- and Cl^- in the case of acids). These counter ions might affect the reaction on the silicon surface or may partially screen the silicon surface charges.

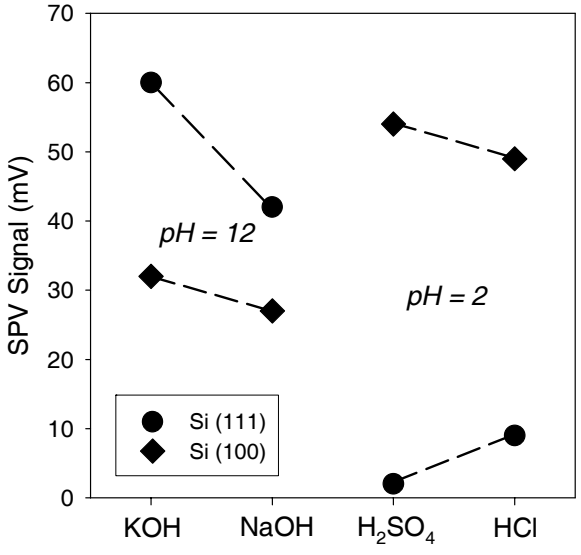

Fig. 3. The SPV signal for different chemical species
with the same pH (shown separately for selected acids and bases).
SPV detection limit was under 0.2 mV

The surface barrier modification usually occurred within the first 10–20 seconds of chemical exposure, reaching for most chemicals steady state after this period (Fig. 4). Long-term change of the Si surface barrier when exposed to KOH is possibly due to a slow etching of the Si surface. The modifications of the silicon surface charges were completely reversible, as shown in Fig. 5. In this case, Si samples were dipped into the acid, dried, then measured, dipped into base, dried, measured again, and the cycle was repeated. Thus, the binding energies of OH^- and H^+ ions cannot be large. Similar observations were previously reported for the ions deposited on silicon surfaces from a gaseous ambient [9]. The ability to respond to small changes in the ionic concentration in a relatively short time, different SPV signals for the same concentration of ions from different chemical species, and signal reversibility makes SPV a potentially valuable technique for low cost chemical sensors.

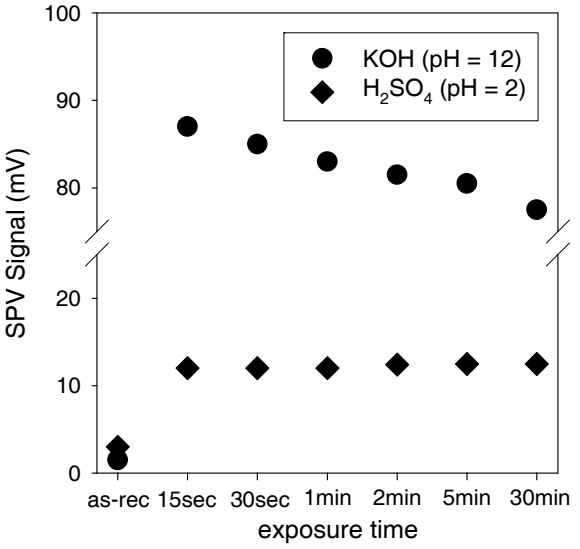

Fig. 4. SPV signal as a function of exposure time for selected acids and bases

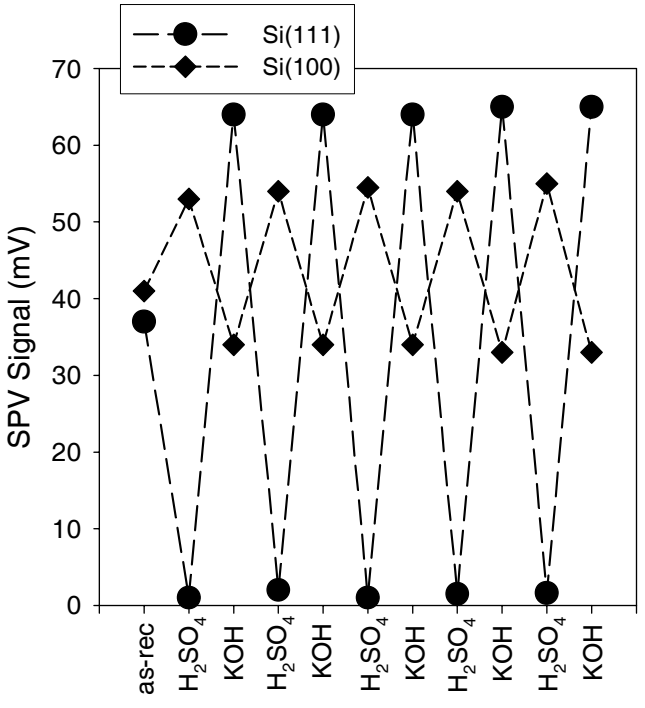

Fig. 5. Change of the SPV signal after sequential acid and base treatments

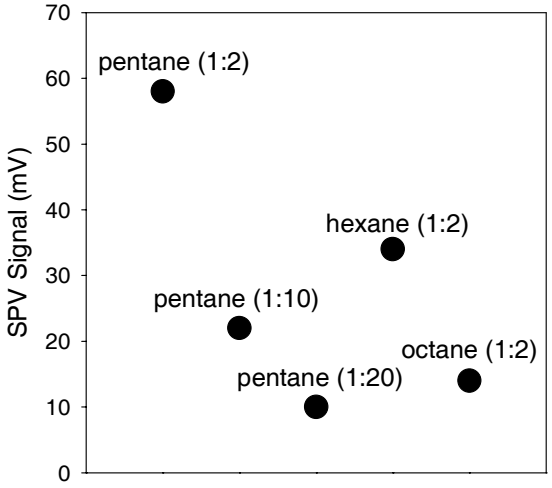

Fig. 6. Changes of the SPV signal induced by exposure to selected alkanes mixed with xylene. Numbers in brackets describe the alkane/xylene ratio. Without any organic species, the SPV signal was 21 mV

Figure 6 shows the response of the silicon surface barrier to the presence of organic species. The goal of this experiment was to investigate the sensitivity of the SPV measurement to an increasing length of the alkane chain. The attachment of alkane molecules can cause partial rearrangement of silicon surface atoms, therefore changing the silicon surface barrier [23, 24]. The degree of this rearrangement is expected to depend on the structure of molecules. The SPV measurement showed correlation between the molecular weight and the extent of silicon surface barrier change. The variation of the SPV signal with changing alkane concentration reflects decreasing surface coverage when the ratio of alkane-to-solvent was decreased.

The measurement of a genomic sample was the first attempt to employ SPV in the area of biological sensing [11]. Assuming DNA density of 3×10^5 12-mer nucleotides per μm^2 from the footprint of a densely packed monolayer [11], we can estimate from the SPV measurement (Fig. 7) that the attachment of a single-strand oligonucleotide to the silicon surface changes the potential barrier by approximately 31.5 meV. This value is in good agreement with an independent experimental result [25] of 30 meV surface potential change when 3×10^5 DNA strands per μm^2 are present.

The hybridisation of the DNA target strands with complementary DNA probe strands reduced the surface barrier by 3 meV. Assuming the same effective charge for the probe and target DNA strands, this change corresponds to a 10% efficiency of hybridization, which is a commonly accepted number. In the control sample, the application of the one-pair mismatched DNA target caused no change in the SPV signal (Fig. 7e), showing that no significant binding between the mismatched target and the probe DNA strands took place.

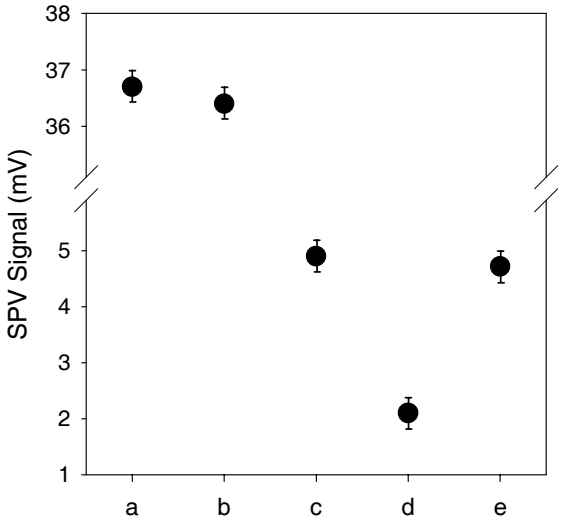

Fig. 7. Genomic experiment – SPV signal corresponding to:
a) silicon substrate terminated with –OH groups,
b) silicon surface functionalised with 3-mercaptopropyl-trimethoxysilane,
c) silicon surface with single strand 12-mer probe DNA attached,
d) sample c) exposed to complementary target DNA, e) sample
c) exposed to non-complementary target DNA (one-pair mismatch)

In conclusion, recent experiments have demonstrated the potential of the Surface Photovoltage technique for chemical and biological sensing. Further work is needed to extend this characterization technique to new chemical and biological applications and to develop a better understanding of the mechanisms behind the observed semiconductor surface barrier changes. Early results, however, indicate that SPV might offer a combination of versatility, low cost, sensitivity, specificity, and sensing speed complementing other chemical and biological characterization techniques.

Acknowledgement

This work was partially supported by the U. S. Defence Advanced Research Projects Agency. Sample preparation by Xuema Li is acknowledged.

References

[1] SCHRODER D.K., Meas. Sci. Technol., 12 (2001), R16.
[2] KRONIG L., SHAPIRA Y., Surf. Sci. Reports, 37 (1999), 1.
[3] GATOS H.C., LAGOWSKI J., J. Vac. Sci. Technol., 10 (1973), 130.
[4] SZARO L., REBISZ J., MISIEWICZ J., Appl. Phys. A, 69 (1999), 409.
[5] LAGOWSKI J., EDELMAN P., DEXTER M., HENLEY W., Semicond. Sci. Technol., 7 (1992), A185.
[6] LAGOWSKI J., EDELMAN P., [in:] Proc. 7th Intern. Conf. *Defects Recognition and Image Processing in Semiconductors* (DRIP VII), Templin, Germany, September 1997.

[7] NAUKA K., [in:] *Semiconductor Characterization: Present Status and Future Needs*, AIP Press, 1996, p. 231–236.
[8] NAUKA K., Microelectron. Eng., 36 (1997), 351.
[9] NAUKA K., KAMINS T.I., J. Electrochem. Soc., 146 (1999), 292.
[10] KAMINS T.I., NAUKA K., WILLIAMS R.S., Appl. Phys. A, 73 (2001), 1.
[11] LI Z., CHEN Y., LI X., KAMINS T.I., NAUKA K., WILLIAMS R.S., NanoLett., 4 (2004), 245.
[12] BURIAN J.M., Chem. Rev., 102 (2002), 1271.
[13] ASHKENASY G., CAHEN D., COHEN R., SHANZER A., VILAN A., Acc. Chem. Res., 35 (2002), 121.
[14] ADAMOWICZ B., MICZEK M., BRUN C., GRUZZA B., HASEGAWA H., Thin Solid Films, 436 (2003), 101.
[15] NICOLAS D., SOUTEYRAND E., MARTIN J.R., Sensors Act. B, 44 (1997), 507.
[16] ZHOU H-S., YAMADA T., ASAI K., HONMA I., UCHIDA H., KATSUBE T., Jpn. J. Appl. Phys., 40 (2001), 7098.
[17] NAUKA K., LI Z., KAMINS T.I., Proc. 27th Intern. Conf. *Physics of Semiconductors* (ICPS-27), Flagstaff, Arizona, July 2004, AIP Press 2005, pp. 1577–1578.
[18] KAMINS T.I., NAUKA K., Electrochem. Sol. St. Lett., 1 (1998), 100.
[19] SPV system, model CMS-III A/R; Semiconductor Diagnostics, Inc., Tampa, FL.
[20] SUNG M.M., KLUHT J., YAUW O.W., Langmuir, 13 (1997), 6164.
[21] MONCH W., [in:] *Semiconductor Surface and Interfaces*, Springer-Verlag, 1996.
[22] SEKER F., MEEKER K., KUECH T.F., ELLIS A.B., Chem. Rev., 100 (2000), 2505.
[23] SIEVAL A.B., DEMIREL A.L., NISSINK J.W.M., LINFORD M.R., VAN DER MAAS J.H., DE JEU W.H., ZUILHOF H., SUNDHOLTER E.J., Langmuir, 14 (1998), 1759.
[24] ZHANG L., WESLEY K., JIANG S., Langmuir, 17 (2001), 6275.
[25] FRITZ J., COOPER E.B., GAUDET S., SORGER P.K., MANALIS S.R., Proc. Natl. Acad. Sci. U.S.A., 99 (2002), 14142.

Received 20 June 2005
Revised 8 July 2005

Materials Science-Poland, Vol. 23, No. 3, 2005

Thermal properties of multinuclear Ti(IV) and Zr(IV) carboxylate derivatives characterized using thermal analysis and variable temperature MS and IR methods

P. PISZCZEK*, A. GRODZICKI, M. RICHERT, A. RADTKE

Faculty of Chemistry, Nicolaus Copernicus University, ul. Gagarina 7, 87-100 Toruń, Poland

Studies of the thermal properties of multinuclear Ti(IV) and Zr(IV) carboxylates with general formulas $[Ti_8O_8(O_2CBu^t)_{16}]$ and $[Zr_6O_4(OH)_4(O_2CBu^t)_{12}]$ which can be used as potential source compounds in producing TiO_2 and ZrO_2 thin layers, were carried out. Thermogravimetric methods (TG/DTG/DTA), mass spectrometry (MS-EI), and variable temperature infrared spectroscopy (VT-IR) were used to determine the thermal decomposition pathway, identify volatile titanium and zirconium species in vapours, and determine their thermal stability. The applications of Ti(IV) and Zr(IV) compounds in MOCVD experiments as potential metal oxide precursors are discussed.

Key words: *Ti(IV) carboxylates; Zr(IV) carboxylates; thermal decomposition; IR spectroscopy; mass spectrometry*

1. Introduction

The substitution of alkoxy groups in Ti(IV) and Zr(IV) alkoxides ($M(OR)_4$, R = Et, Pr^i, Bu^n) by bidendate carboxylate ligands (O_2CR', R′ = MC, Bu^t, CH_2Bu^t) is used to moderate the reactivity of alkoxides in sol-gel processing [1–4] and to introduce organic functionalities [5]. Several multinuclear Ti(IV) and Zr(IV) oxo carboxylates and their complexes with alkoxides can be isolated from stoichiometric reactions of $M(OR)_4$ with carboxylic acids [3, 4, 6, 7]. The source of oxo ligands are water molecules produced during the esterification process of excess acid with liberated alcohol.

In our previous works, we have focused on the structural and spectral characterization of titanium(IV) compounds [6, 7]. Analysis of these data suggests that selected

* Corresponding author, e-mail: piszczek@chem.uni.torun.pl

multinuclear oxo complexes show promising properties as sources of volatile titanium species for the deposition of TiO_2 layers by CVD techniques [6, 10]. Therefore, such problems as: (a) the volatility of titanium and zirconium compounds, (b) their thermolysis pathway, (c) the composition of the gas phase, and (d) the stability of volatile metallic species transported in vapours, should be investigated in detail.

In the presented report, the results of thermal analysis and temperature variable mass spectrometry (MS) and IR studies for Ti(IV) and Zr(IV) compounds of general formulas $[Ti_8O_8(OOCBu^t)_{16}]$ (1) and $[Zr_6O_4(OH)_4(O_2CBu^t)_{12}]$ (2) are described. Moreover, the results of CVD experiments are discussed.

2. Experimental

Syntheses of **1** and **2** were carried out under argon atmosphere using standard Schlenk line and glovebox techniques as reported in literature [4, 7]. Microanalysis, ^{13}C NMR, ^{1}H NMR, and infrared (IR) methods were used to confirm their structure. Both compounds were stored at room temperature under argon atmosphere.

IR spectra were recorded with an FT-IR SPECTRUM 2000 spectrometer. Variable temperature IR spectroscopic studies in the solid phase were carried out with a SPECAC temperature variable cell. IR spectra of vapours transported with the carrier gas (Ar) were studied in a specially constructed reactor, presented in Fig. 1. Thermogravimetric analysis (TGA) was carried out using SDT 2960 TA Instruments, in nitrogen atmosphere from 298 to 773 K and at the ramp rate of 3 $K \cdot min^{-1}$. Mass spectra were measured with an MS AMD-604, MASPEC system using the EI method.

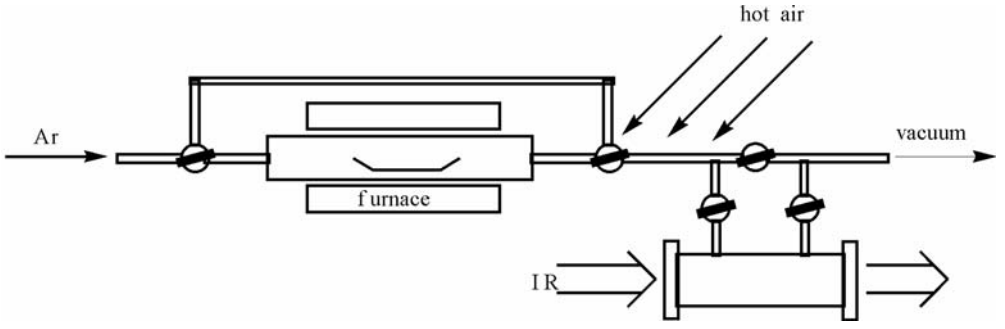

Fig. 1. Schematic diagram of the reactor used for variable temperature IR experiments

Deposition experiments were carried out using a horizontal "cold-wall" CVD reactor with the volume of 10 dm^3, heated substrate electrode on top, 56 mm in size, a gas input shower from a distance of 15 mm and with a gas flow of 60 $cm^3 \cdot min^{-1}$. The morphology of the metal oxide films was studied with a scanning electron microscopy (JSM 5500LV) and EDXS system.

3. Results and discussion

The colourless crystals of $[Ti_8O_8(OOCBu^t)_{16}]$ (**1**) and $[Zr_6O_4(OH)_4(O_2CBu^t)_{12}]$ (**2**) were synthesized by slow evaporation (glovebox) from a 1 : 2 mixture of $M(OPr^1)_4$ (M = Ti(IV) and Zr(IV)) and $HOOCBu^t$ in toluene and *n*-hexane for **1** and **2**, respectively. Crystallographic and spectral studies [4, 7] revealed that the structures of these compounds consist of $\{Ti_8(\mu_2\text{–}O)_8\}$ and $\{Zr_6(\mu_3\text{–}O)_4(\mu_3\text{–}OH)_4\}$ clusters stabilized by carboxylate ligands. Multinuclear titanium(IV) or zirconium(IV) oxo carboxylate molecules are associated through a network of weak van der Waals inter-molecular interactions. This is a promising feature in terms of volatility and suitability as a CVD precursor.

The thermal decomposition of the above compounds was studied using thermogravimetric and differential thermal analysis (TG/DTA/DTG) methods over the temperature range of 298–873 K with a heating rate of 3 K/min under the nitrogen atmosphere. The TGA/DTA/DTG data of **1** have shown that thermal decomposition proceeds in three endothermic stages: 298–589 K, 589–658 K, and 658–738 K, with a weight loss of 73.4%. According to our structural reports [7], the endothermic effect between 298 and 589 K can be explained by the detachment of solvent molecules (toluene) from the crystalline lattice of this compound. During the decomposition process, **1** undergoes a complete conversion to TiO_2 (above 589 K), as was confirmed by X-ray powder diffraction studies. According to thermogravimetric studies, crystals of **2** are stable in N_2 up to 433 K. The multi-step thermal decomposition of this compound proceeds in four endothermic stages: 433–533 K, 623–693 K, 693–757 K, and 757–803 K (weight loss: 60.9%). The final product of decomposition was ZrO_2, and its presence in solid residue was confirmed by X-ray powder diffraction.

The composition of vapours formed during the thermolysis of Ti(IV) and Zr(IV) oxo carboxylate derivatives, and the thermal stability of volatile metallic species were assessed on the basis of MS-EI spectra recorded between 423 and 623 K. According to these data, the following characteristic peaks were found in the spectra of **1**: at m/z = 2027 ($[Ti_8O_8(O_2CBu^t)_{15}]^+$) and m/z = 1554 ($[Ti_8O_8(O_2CBu^t)_{10}]^+$), and in the spectra of **2**: m/z = 1913 ($[Zr_6(OH)_8(O_2CBu^t)_{11}(O_2CC_3H_3)_2])^+$), m/z = 1757 ($[Zr_6O_3(OH)_3(O_2CBu^t)_{11}]^+$), and m/z = 1573 ($[Zr_6O_2(OH)_4(O_2CBu^t)_9]^+$). The stability of multinuclear oxo species has been studied on the basis of the temperature dependence of peak intensity (Fig. 2).

In the case of **1**, the intensity of peaks assigned to titanium-containing fragments was very low below 423 K, which indicates the thermal stability of titanium oxide clusters (Fig. 2a). At the threshold temperature, about 423 K, an increase in the intensity of the m/z = 2027 ($[Ti_8O_8(O_2CBu^t)_{15}]^+$) peak and a simultaneous decrease in the decomposition product peaks (m/z = 1554, $[Ti_8O_8(O_2CBu^t)_{10}]$) are observed. According to these data, the concentration of multinuclear Ti(IV) oxo carboxylate derivatives in vapours is the highest between 513 and 533 K. The thermal stability of these species is low, and their rapid decomposition above 533 K is observed. Similar effects are noticed in thee variable temperature MS spectra of **2** (Fig. 2b). Between 543 and

573 K, however, the decomposition products containing volatile multinuclear zirconium fragments are formed at higher temperatures. Also in this case the thermal stability of these patterns is low, and their decomposition is noticed above 573 K.

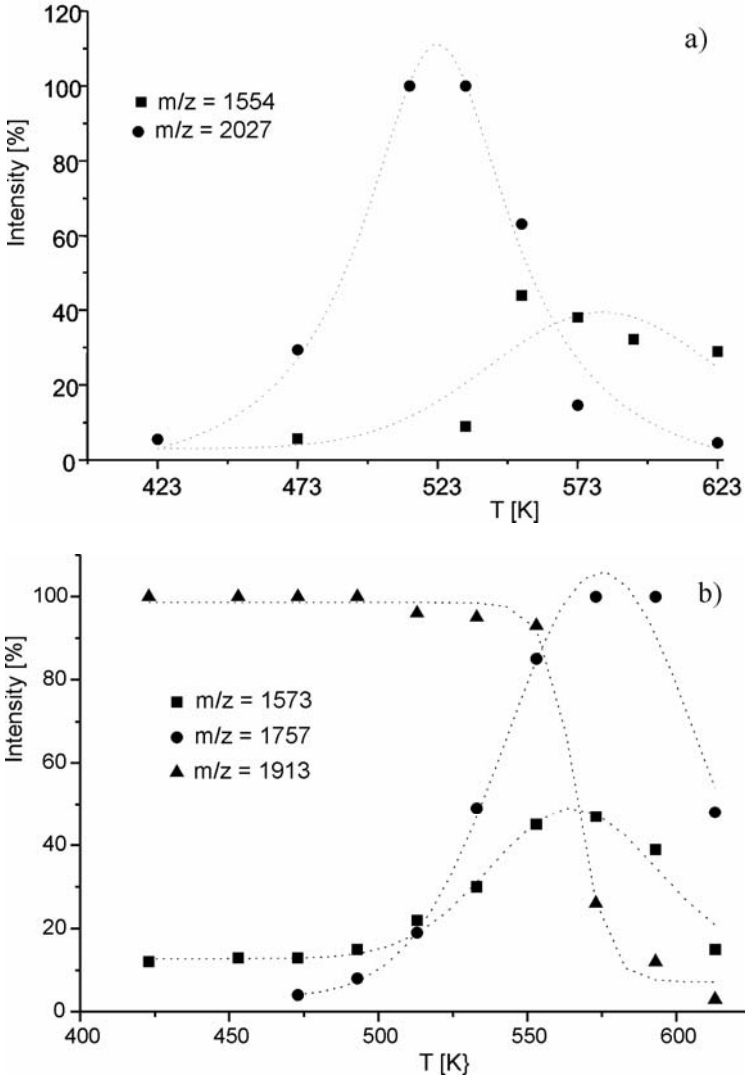

Fig. 2. Results of MS-EI investigations for a) $[Ti_8O_8(O_2CBu^t)_{16}]$ (**1**) and b) $[Zr_6O_8(O_2CBu^t)_{12}]$ (**2**). Variations in the intensity of selected peaks with temperature (m/z = 1554 for $[Ti_8O_8(O_2CBu^t)_{15}]^+$, m/z = 2027 for $[Ti_8O_8(O_2CBu^t)_{10}]^+$, m/z = 1573 for $([Zr_6O_2(OH)_4(O_2CBu^t)_9]^+)$, m/z = 1757 for $([Zr_6O_3(OH)_3(O_2CBu^t)_{11}]^+)$, and m/z = 1913 for $([Zr_6(OH)_8(O_2CBu^t)_{11}(O_2CC_3H_3)_2])^+$)

In order to find another way of characterizing the thermal decomposition pathway of the studied compounds, we have applied variable temperature IR spectroscopy (VT-IR) to the vapours evolved during the above process. The thermal analyser was

connected with the FT-IR instrument and the vapours were transported to the spectrometer chamber, providing the spectra of gaseous products (Fig. 1). The appearance of bands attributed to the vibrations of coordinated carboxylate groups (ν_{as}(COO) = 1520–1600 cm^{-1}) and metal-oxide bridges (ν_{as}(MOM) = 600–800 cm^{-1}) has been used to identify volatile metal-containing species. The temperature variable IR spectra of **1** and **2** are presented in Figs. 3 and 4.

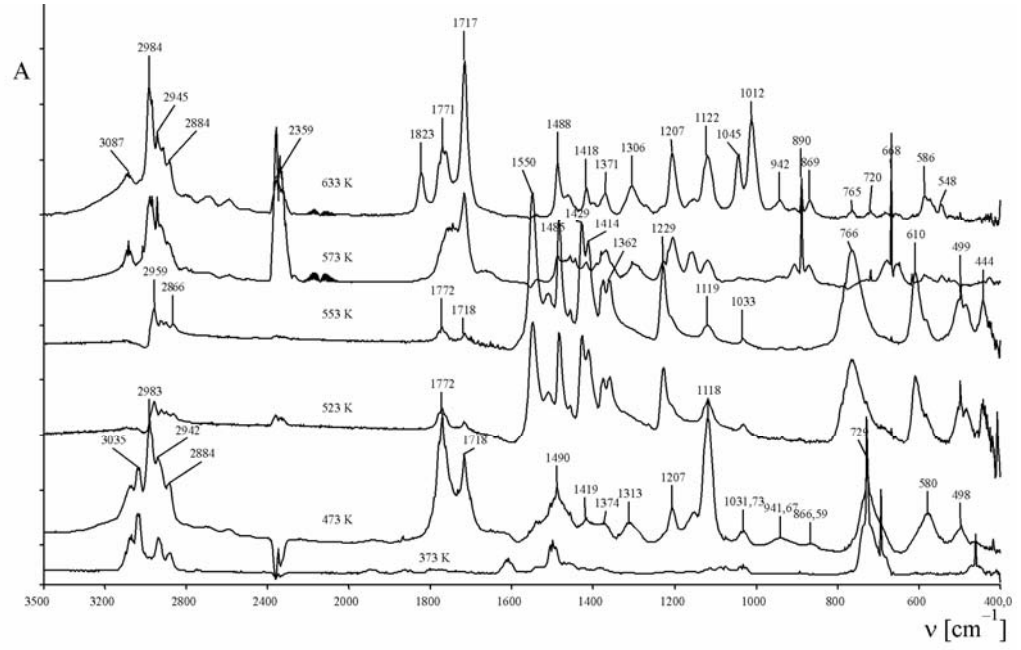

Fig. 3. Variable temperature IR spectra of vapours formed during the thermal decomposition of **1**

An analysis of the VT-IR spectra of **1** (Fig. 3) revealed that three types of volatile species are formed during the three decomposition stages, which confirms the results of thermogravimetric studies [7]. The appearance of absorption bands at 3035, 1610, 1490, and 729 cm^{-1} in spectra recorded below 523 K proves that toluene molecules are detached from the crystal lattice in the first stage of the thermal decomposition of **1**. Simultaneously, the partial decomposition of these compounds accompanies an increase of the intensity of bands at 1772, 1718, 1118, 580, and 498 cm^{-1} in the temperature range of 373–523 K. Stable volatile titanium species, containing multinuclear oxo clusters and stabilized by carboxylate ligands, were detected between 523 and 553 K (with bands at 1550 and 1429 cm^{-1} assigned to the vibration of carboxylate bridges, and at 766 cm^{-1} to the vibration of Ti–O–Ti bridges). The characteristic bands attributed to CO_2 (2359, 668 cm^{-1}), CO (2169, 2105 cm^{-1}), $(RCO)_2O$ (1823, 1771 cm^{-1}), and RCOOR′ (1717 cm^{-1}) were observed in the high-temperature IR spec-

tra. This indicates a higher degree of decomposition, which occurs at temperatures above 553 K.

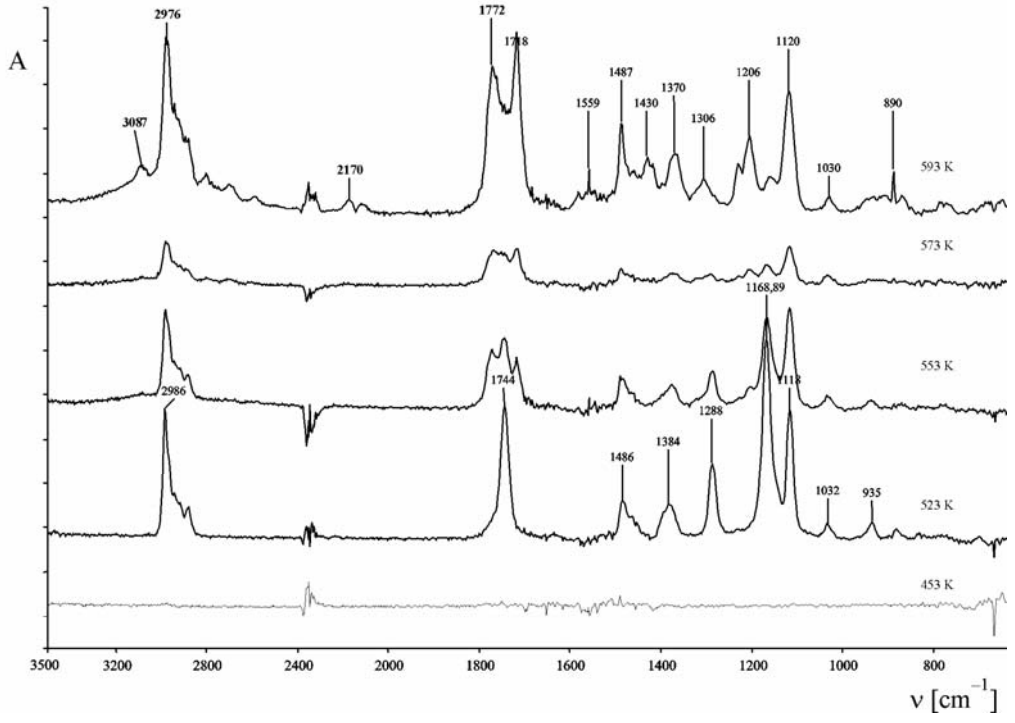

Fig. 4. Variable temperature IR spectra of vapours formed during the thermal decomposition of **2**

VT-IR studies of **2** (Fig. 4) indicate the high thermal stability of this compound between 453 and 593 K. Only bands assigned to volatile organic products, formed during the thermal decomposition of this compound, were observed between 523 and 593 K. Absorption bands, which could be the evidence of the presence of volatile zirconium-containing fragments (e.g. attributed to the vibrations of Zr–O–Zr or coordinated COO groups), were not detected in the IR spectra of the vapours.

Despite the lack of strong intermolecular association of metal-oxide clusters in the crystal lattice, variable temperature MS and IR experiments show that **1** and **2** are characterized by a high thermal stability under the studied conditions. This is a negative feature in terms of the volatility and suitability of CVD precursors. However, the formation of volatile and stable multinuclear titanium oxo clusters in the narrow temperature range of 523–553 K in the case of **1** is possible. Therefore, *cold-wall* CVD experiments using $[Ti_8O_8(O_2CBu^t)_{16}]$ as a TiO_2 precursor were carried out. Thin TiO_2 films (the thickness of layers was below 100 nm) were deposited on Si(111) substrates in the temperature range of 873–923 K, under a total reactor pressure of 2 mbar (vaporization temperature T_V was 523 K). Scanning electron microscopy (SEM) studies of film morphologies show dense and smooth textures for films grown from this com-

pound between 673 and 923 K (Fig. 5). The composition of this film was established by the EDXS analysis. The films are composed mainly of titanium and oxygen atoms. X-ray diffraction (XRD) studies revealed that amorphic films of TiO_2 are formed.

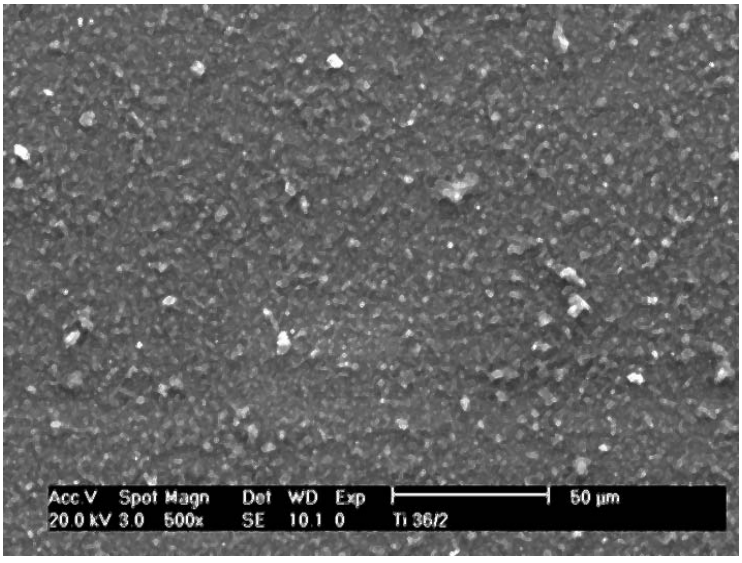

Fig. 5. SEM microphotograph of the film deposited from **1** using the "cold-wall" CVD method

4. Conclusions

Studies of $[Ti_8O_8(O_2CBu^t)_{16}]$ (**1**) and $[Zr_6O_4(OH)_4(O_2CBu^t)_{12}]$ (**2**) proved high thermal stability of these compounds. Thermal decomposition proceeds by the conversion of **1** and **2** to TiO_2 and ZrO_2, which was confirmed by XRD methods for the solid residue. An analysis of the variable temperature IR spectra of vapours revealed that esterification and decarboxylation products are the main gas phase components. However, the volatile and stable multinuclear titanium oxo clusters can also be formed during the thermal decomposition of **1** between 523 and 553 K. The thermal stability of these fragments is suitable for their transport in the gas phase, which is a positive feature for the application of **1** as a CVD precursor. The results of "cold -wall" CVD experiments showed that the deposition of thin (< 100 nm) amorphic TiO_2 films is possible.

Acknowledgements

This work was financially supported by the Polish Committee for Scientific Research, grant No. 4T09A 152 23. The authors wish to acknowledge Dr. A. Leonhard and Dr. C. Taeschner from the Leibniz Institute for Solid State and Materials Research in Dresden (Germany) for their cooperation in CVD experiments.

References

[1] SANCHEZ C., IN M., J. Non-Cryst. Solids, 147/148 (1992), 1.
[2] VARMA I.D., MEHROTRA R.C., J. Prakt. Chemie, 4 (1959), 235.
[3] DOEUFF S., HENRY M., SANCHEZ C., Mater. Res. Bull., 25 (1990), 1519.
[4] KICKELBICK G., SCHUBERT U., Chem. Ber., 130 (1997), 473.
[5] SCHUBERT U., HÜSING N., LORENZ N., Chem. Mater., 7 (1995), 2010.
[6] PISZCZEK P., GRODZICKI A., RICHERT M., WOJTCZAK A., Inorg. Chim. Acta, 357 (2004), 2769.
[7] PISZCZEK P., GRODZICKI A., RICHERT M., GŁOWIAK T., WOJTCZAK A., Polyhedron (2005), in press.
[8] BOYLE T.J., ALAM T.M., TAFOYA C.J., Inorg. Chem., 37 (1998), 5588.
[9] PAPIERNIK R., HUBERT-PFALZGRAF L.G., VAISSERMANN J., HENRIQUES B., GONÇALVES M.C., J. Chem. Soc. Dalton Trans., (1998) 2285.
[10] PISZCZEK P., RICHERT M., GRODZICKI A., BAŁA W., BARTKIEWICZ K., J. Slovak. Meatallography, 10 (2004), 595.

Received 16 December 2004
Revised 31 March 2005

Materials Science-Poland, Vol. 23, No. 3, 2005

Chemical Vapour Deposition (CVD) of metallic layers prepared from silver carboxylates complexes with tertiary phosphines

R. SZCZĘSNY, I. SZYMAŃSKA, P. PISZCZEK, L. DOBRZAŃSKA, E. SZŁYK*

Faculty of Chemistry, Nicolaus Copernicus University, ul. Gagarina 7, 87-100 Toruń, Poland

Silver fluorocarboxylate tertiary phosphine complexes $[Ag(O_2CR)(PR'_3)]$ (where R = CF_3, C_2F_5, Me_3SiCH_2; R′ = Me, Et) have been used as precursors in the *hot-wall* Chemical Vapour Deposition (CVD) of silver films. The pyrolysis of Ag(I) compounds and the thermal stability of metallic species transported in the gas phase were characterized by temperature variable IR (VT-IR) and MS (MS-EI) methods. Metallic films were produced between 403 and 423 K under the deposition pressure of 0.8–2.0 mbar, under an Ar atmosphere and on Si(111) substrates. They were characterized by X-ray diffraction (XRD) and scanning electron microscopy (SEM) integrated with EDX equipment.

Key words: *silver carboxylate; tertiary phosphine; silver films; chemical vapour deposition*

1. Introduction

Low resistivity and high thermal conductivity of silver result in numerous applications of Ag films, including ultra-fast optical switches [1], components of high-temperature superconducting materials [2], and infrared sensors [3, 4]. Chemical vapour deposition (CVD) has been widely used in the fabrication of ultra-thin metallic films at relatively low temperatures, when the appropriate precursors are available. Good silver CVD precursors should exhibit low vaporization and deposition temperatures, and provide high-purity metallic layers. Several inorganic and organometallic species, including AgF, $[Ag(C_4F_7)]_n$, fluorinated Ag(I) β-diketonates and their complexes [Ag(β-diketonate)L] where L is PR_3 (R is Me, Et), silanes (e.g., vinyltrimethylsilane, VTES) or diamines (e.g., tetramethylethylenediamine), have been used as CVD precursors [5–8]. In our studies, we focus on silver carboxylate complexes with tertiary phosphines ($[Ag(O_2CR)(L)]$, where R is a fluorinated, nonfluorinated or silylated

* Corresponding author, e-mail: eszlyk@chem.uni.torun.pl

alkyl, and L is a tertiary phosphine), which could be a new group of CVD precursors. In the present paper, the synthesis, mass spectra (MS) and variable temperature IR studies of volatile species and silver films obtained from $[Ag(O_2CCF_3)(PEt_3)]$ (**1**), $[Ag(O_2CC_2F_5)(PEt_3)]$ (**2**), $[Ag(O_2CCH_2SiMe_3)(PMe_3)]$ (**3**), and $[Ag(O_2CCH_2SiMe_3)(PEt_3)]$ (**4**) are described.

2. Experimental

The synthesis of complexes was performed in an argon atmosphere using standard Schlenk techniques. Trimethylphosphine (1.0 M soln. in THF) (Aldrich) and triethylphosphine (1.0 M soln. in THF) (Aldrich) were used without further purification. Silver (trimethylsilyl)acetate, and precursors (**1**) and (**2**) were synthesized as reported elsewhere [9–12]. Complexes (**3**) and (**4**) were obtained in the reaction of Me_3SiCH_2COOAg (2.5 mmol) suspended in dry, deoxygenated ethanol (30 cm^3), with 2.5 mmol of PR_3 (R = Me (**3**) or Et (**4**)). The mixture was stirred for 3 hours at room temperature in the dark, then filtered and evaporated on a vacuum line. Since (**4**) decomposes at laboratory conditions, it cannot be used in CVD experiments.

IR spectra were recorded with a FT IR Spectrum 2000 spectrometer (Perkin Elmer). Temperature variable IR (VT-IR) (303–523 K) spectra were measured with a SPECAC variable temperature cell, at the dynamic vacuum of $p = 10^{-2}$ mbar. Mass spectra (MS) were measured with a MS AMD-604, MASPEC using the EI method. Thermal analysis (TA) was conducted with a MOM OD-102 (Paulik and Paulik) Derivatograph in the following conditions: sample mass: 0.050 g, temperature range: 298–773 K, heating rate: 2.5 K/min, atmosphere: N_2, 20 dm^3/h.

The silver films were deposited on Si(111) substrates prepared according to [13], using a horizontal *hot-wall* CVD reactor under Ar atmosphere; vaporization temperature T_v was 303–433 K, decomposition temperatures T_D 403–523 K, reactor pressure p 0.3–2.0 mbar and deposition time t 60–90 min. XRD diffraction data were collected with a Philips X'PERT diffractometer, using CuK_α radiation in the range of 2Θ (30–80)°. The morphology of films was studied using a Scanning Electron Microscope (SEM) LEO 1460V with EDX equipment.

3. Results and discussion

The thermal stability of complexes (**1**)–(**3**) was studied by thermogravimetric analysis (TGA). The decomposition started at: 318 (**3**), 403 (**1**), and 423 (**2**) K being completed at 528 (**2**), 553 (**1**), and 618 (**3**) K, leaving metallic silver, what was evident from XRD studies of the residues.

VT-IR spectra of the gaseous products of (**1**) and (**2**) revealed ν(C–H) bands at 2981 and 2902 cm^{-1}, a $\delta(PCH_2)$ band at 1401 cm^{-1}, and a $\delta_r(PCH_2)$ band at 893 cm^{-1},

confirming that the phosphine species detach in the first step of decomposition (Fig. 1). Above 443 K, however, strong bands between 1000 and 1100 cm^{-1} and at 1803 cm^{-1} (**1**) and 1797 cm^{-1} (**2**) were observed. The former bands can be assigned to C–F group vibrations, but the latter are typical of ester groups. Moreover, bands characteristic of CO_2 and CO were detected between 2350 and 2119 cm^{-1}.

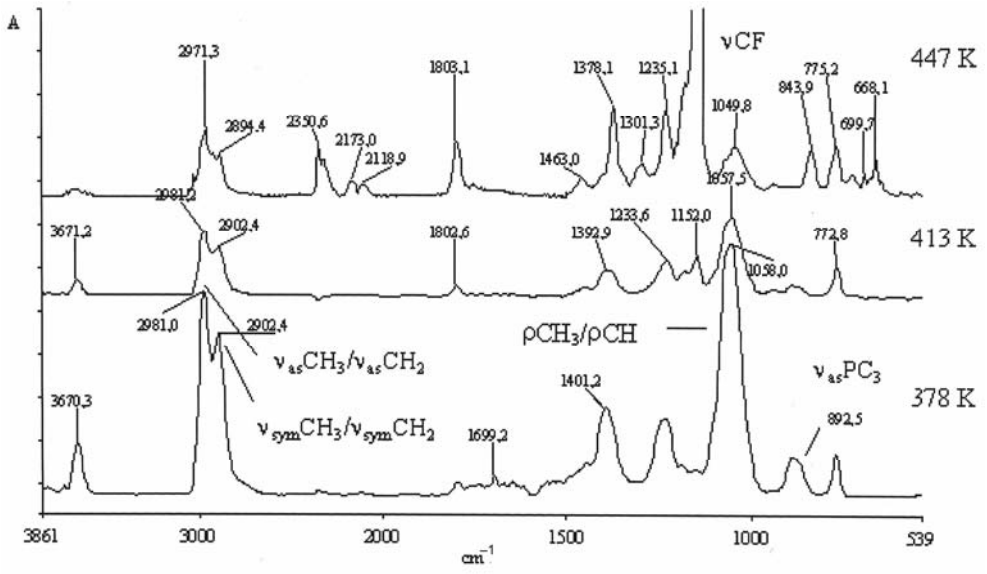

Fig. 1. VT-IR spectra of $[Ag(O_2CCF_3)(PEt_3)]$ (**1**) (gas phase, 318–513 K, KBr)

Mass spectra of volatile metallated species should reveal characteristic signals due to the natural abundance of ^{107}Ag (51.8%) and ^{109}Ag (48.2%), hence fragments that contain one silver atom should display peaks pattern of 1 : 0.93, whereas disilver fragments should give three peaks with 1 : 1.86 : 0.86 relative intensities. The MS (EI, 453 K) of (**1**) and (**2**) exhibited the following fragments: $[PEtH_2]^+$ m/z = 62 (100% for both), $[OPEt_2]^+$ m/z = 106 (**1** – 9%; **2** – 15%), $[PEt_3]^+$ m/z = 118 (**1** – 49%; **2** – 55%), $[Ag(PEt)]^+$ m/z = 167 (**1** – 10%; **2** – 8%), and $[Ag(PEt_3)]^+$ m/z = 225 (**1** – 8%; **2** – 20%). Disilver fragments, $[Ag_2(O_2CCF_3)]^+$ (m/z = 279) and $[Ag_2(O_2CC_2F_5)]^+$ (m/z = 343), were noted as low intensity peaks (1–4%). According to TGA, VT-IR, and MS-EI data, thermal stability can be the main factor influencing the CVD process and the morphology of metallic layers.

In the case of (**3**), MS and VT-IR studies confirmed lack of silver volatile species, which suggests that this compound will not be useful for CVD. The most intensive bands were observed between 393 K and 453 K at 1835 cm^{-1} and 1777 cm^{-1}, clearly indicating that one of the liberated compounds was acid anhydride (Fig. 2). We have nevertheless used (**3**) for *hot-wall* CVD, as it revealed the lowest decomposition onset temperature.

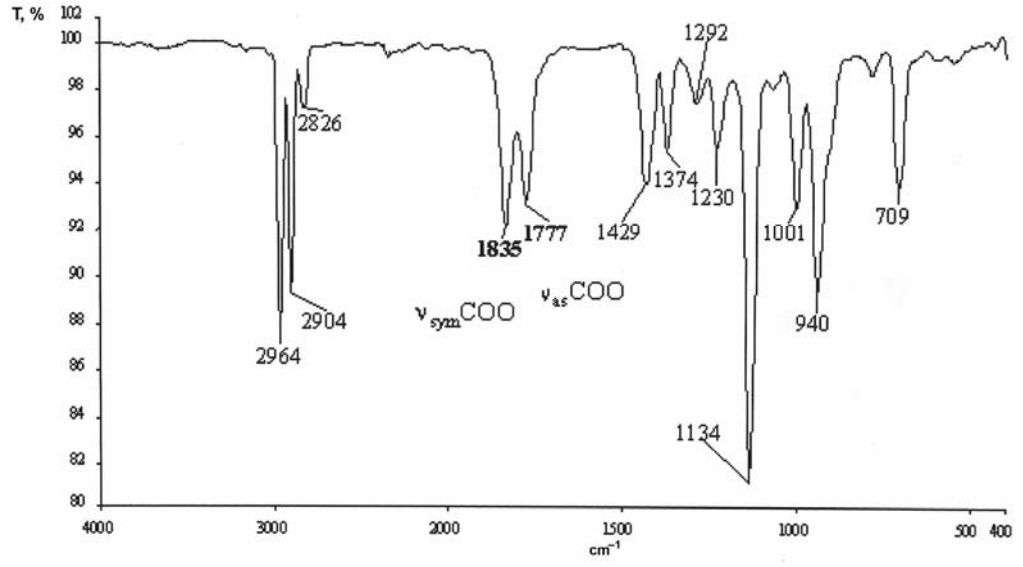

Fig. 2. VT-IR spectra of $[Ag(O_2CCH_2SiMe_3)(PMe_3)]$ (**3**) (gas phase, 453 K, KBr)

Hot-wall CVD experiments were performed using (**1**), (**2**), and (**3**). The silver films obtained from **1** and **2** revealed a cubic structure (Fig. 3), which was evident from XRD measurements (38.2 [111], 44.4 [200], 64.6 [220]).

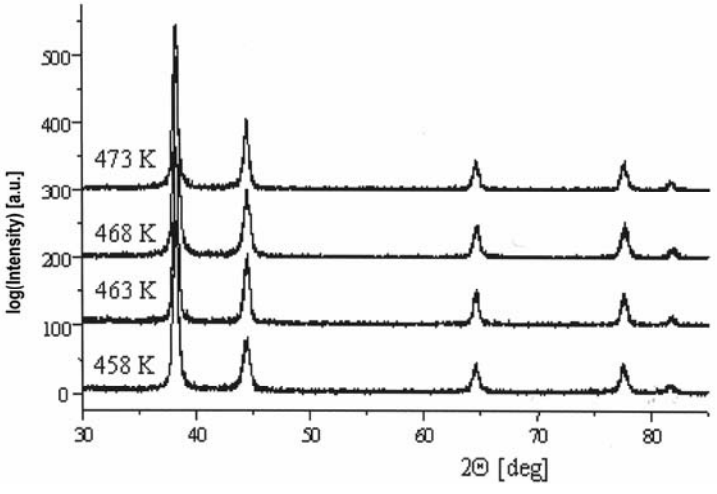

Fig. 3. XRD Θ–2Θ scans of silver films deposited at various temperatures on Si(111) from $[Ag(O_2CC_2F_5)(PEt_3)]$ (**2**)

The SEM micrographs of films produced from (**1**)–(**3**) were studied. The most promising deposition results were obtained for layers deposited from (**2**), where SEM micrographs reveal a rough and cluster structure (Fig. 4) and EDX spectrum are char-

acteristic of metallic silver. It can be noted that films produced from (**1**) demonstrated a lower density and higher non-uniform thickness. The layer morphology of films deposited from (**3**) and the lack of signals in the EDX spectrum that could be assigned to metallic silver suggest that only condensed organic impurities on the substrate surface were present.

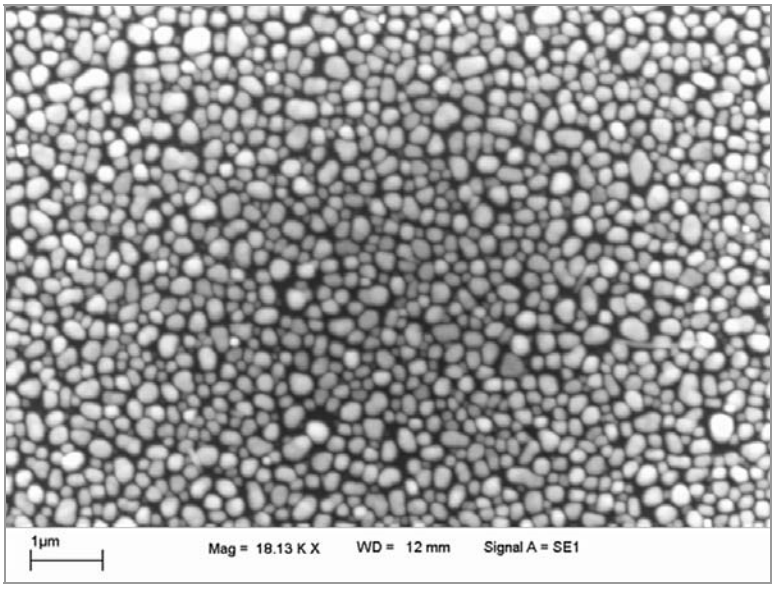

Fig. 4. SEM micrograph of a silver film deposited from (**2**) (Si(111), *hot-wall* CVD, T_v = 433 K, T_D = 523 K)

4. Conclusions

Results of CVD experiments revealed that **1** and **2** are promising precursors for silver films, since both compounds exhibit good volatility and sufficient thermal stability. Variations in the pyrolysis pathway and vapour composition appeared to be the main factors influencing the morphology of the silver films.

Acknowledgements

The authors wish to acknowledge the Polish Committee for Scientific Research for financial support (grant no. 4T08C 039 23).

References

[1] HAYNES C.L., VAN DUYNE R.P., J. Phys. Chem. B, 105 (2001), 5599.
[2] KALYANARAMAN R., OKTYABRSKY S., NARAYAN J., J. Appl. Phys., 85 (1999), 6636.
[3] VAN DUYNE R.P., HULTEEN J.C., TREICHEL D.A., J. Chem. Phys., 99 (1993), 2101.

[4] BAUER S., BAUER-GOGONEA S., BECKER W., FETTIG R., PLOSS B., RUPPEL W., VON MÜNCH W., Sensors Actuat. A–Phys., 37–38 (1993), 497.
[5] YUAN Z., DRYDEN N.H., VITTAL J.J., PUDDEPHATT R.J., Chem. Mater., 7 (1995), 1696.
[6] CHI K.-M., CHEN K.-H., PENG S.-M., LEE G.-H., Organometallics, 15 (1996), 2575.
[7] DEAN L.K.L., BUSCH K.L., Organic Mass Spectrometry, 24 (1989), 733.
[8] LU Y.-F., TAKAI M., NAGATOMO S., KATO K., NAMBA S., Appl. Phys. A, 54 (1992), 51.
[9] SZCZĘSNY R., SZYMAŃSKA I., SZŁYK E., Polish J. Chem., 79 (2005), 627.
[10] SZŁYK E., ŁAKOMSKA I., GRODZICKI A., Polish J. Chem., 68 (1994), 1529.
[11] SZŁYK E., ŁAKOMSKA I., GRODZICKI A., Polish J. Chem., 69 (1995), 1103.
[12] ŁAKOMSKA I., SZŁYK E., GRODZICKI A., Thermochim. Acta, 315 (1998), 121.
[13] SZŁYK E., PISZCZEK P., ŁAKOMSKA I., GRODZICKI A., SZATKOWSKI J., BŁASZCZYK T., Chem. Vap. Deposition, 6 (2000), 105.

Received 16 December 2004
Revised 15 April 2005

Materials Science-Poland, Vol. 23, No. 3, 2005

Molecular impurity ions as centres with charge transfer degrees of freedom. Influence on ferroelectric phase transitions

V.S. VIKHNIN[1], T.I. MAKSIMOVA[1], J. HANUZA[2, 3*]

[1]AF Ioffe Physical-Technical Institute Russian Academy of Sciences, 194021, St.- Petersburg, Russia

[2]Institute for Low Temperature and Structure Research Polish Academy of Sciences, Wroclaw, Poland

[3]Department of Bioorganic Chemistry, Faculty of Engineering and Economics, University of Economics, Wrocław, Poland

The concept of molecular impurity ions (MI) as centres with charge transfer degrees of freedom, interacting (through the order parameter of the phase transition) with local vibrations and non-soft phonons, as well as with light, has been developed. It has been shown that MI can significantly influence a ferroelectric phase transition (FPT) due to a direct interaction of their specific charge transfer degrees of freedom with the ferroelectric order parameter. In this work, we predict a significant increase of the FPT critical temperature when increasing the MI concentration. The MnO_4^- molecular impurity ions embedded in ferroelectric crystals (e.g. molybdates, tungstates, chromates, phosphates) are considered as possible candidates capable of inducing this effect.

Key words: *molecular impurity ions; charge transfer; ferroelectric phase transition; critical temperature*

1. Introduction

The influence of defects on FPT is one of key topics (see, e.g., [1]) research into modern ferroelectric materials. Its possible role in solving the problem of real ferroelectrics is one of the major reasons for this interest. This is important from the point of view of basic sciences as well as applications. In this context, MI doped into ferroelectrics, for example MnO_4^- (as impurity ions) in ferroelectric phosphate, tungstate, molybdate, and chromate crystals, are responsible for a principally new situation arising in the field of FPTs influenced by impurities. Indeed, MIs provide a new possibility for strengthening the influence of defects on FPT due to their specific properties.

*Corresponding author, e-mail: hanuza@int.pan.wroc.pl

Here we deal with a pronounced covalent contribution to ionic-covalent type bonding within MI with significant charge transfer effects. The latter leads to the appearance of new degrees of freedom, characteristic of MI, which directly interact with the ferroelectric order parameter of the matrix. These are charge transfer degrees of freedom connected with fluctuations of charge transfer magnitude relative to its equilibrium value. It is important to note that these charge transfer degrees of freedom $\{q_i\}$ take part in the bi-linear interaction with fluctuations of the soft matrix TO-polarization. This leads to a new origin of the influence of impurities on FPT phenomena. The purpose of the present work is a theoretical consideration of the influence of MI on FPT, taking into account the MI charge transfer degrees of freedom mentioned above. It will be shown that the pronounced increase of FPT temperature can be induced by MIs in this case.

In our first article [2] devoted to the development of the same idea we considered another limiting case of the strong "charge transfer – local lattice vibration" interaction within MI. Such a situation led to a specific resonance increasing the critical temperature of the FPT. This approach takes into consideration the appearance of the well-localized non-Coulomb charge transfer vibronic excitons (see [3, 4] and references therein) in the MI state spectrum. In the present article, we consider an opposite limit, at which the charge transfer–local lattice vibration interaction within MI mentioned above is weak, in agreement with the assumption of the model. This approach seems to be reasonable and necessary for a complete coverage of the problem. Moreover, strong and weak charge transfer–local lattice vibration interaction states can co-exist in real MI as low-lying and higher lying states. Therefore, in reality we deal with both types of states, simultaneously affecting the MI-induced critical temperature increase. The domination of either type of these states depends completely on quantitative values of the parameters. Here we shall consider a situation where the charge transfer fluctuations are purely electronic ones.

MnO_4^- impurity ions doped into the model ferroelectric crystals will be discussed as an example of impurities with well-defined charge transfer degrees of freedom which can directly interact with the soft lattice of the matrix. MnO_4^- impurity ions can replace XO_4^- complexes (X = P, Mo, W, Cr) in the host lattices and manifest a good covalent bonding within molecular ions accompanied by significant equilibrium charge transfer (see [5–9] and references therein).

The results of calculations performed on the basis of the Self Consistent Field X_α-Scattered-Wave method [5, 6] suggest that this is the case for MnO_4^- ions. In this context, we will consider the $M^{I}M'^{I}_2(XO_4)_{1-x}(MnO_4)_x$ crystal (where x is the relative concentration of the MnO_4^- MI). Here we consider the electron-lattice mechanism for the influence of impurities on the ferroelectric phase transition. Note that it is principally different from a pure vibration mechanism, which is much weaker on one hand, and usually leads to a decrease in the critical temperature on the other hand. In our case, the electronic gaps between active initial electronic states are of the order of 1–3 eV, and electron–lattice interaction mixes of these initial electronic states with such gaps. Related lat-

tice variables (soft polarisation P) are slow as compared with the above-mentioned electronic degrees of freedom and take direct part in the phase transition phenomenon. A corresponding scenario develops under adiabatic conditions, namely new terms in the free energy, which are proportional here to P^2, are responsible for the impurity-induced shift of the critical point for the ferroelectric matrix. A similar approach has been successfully used earlier for considering the influence of Jahn–Teller impurities on the ferroelectric phase transition [10, 11].

In spite of the soft critical behaviour of the order-disorder degrees of freedom in the XO_4^- ions-containing crystals, the structure of their order parameters is more complicated than for pure contributions of the order-disorder type. This is the case for improper ferroelectrics [12], in which a soft mode has an order-disorder origin but the resulting polarization is of a displacive-type. Such a phenomenon can be described by the well known pseudo-spin–lattice interaction model (Kobayashi model, [12]). Namely, such a displacive-type polarization mentioned above takes part in the formation of a linear vibronic interaction with the electronic degrees of freedom of MnO_4^- impurity ions in parallel with linear pseudo-spin mode–MnO_4^- electronic degrees of freedom interaction in the framework of our model. Nevertheless, here we take into account also the direct interaction of soft order-disorder type mode with MnO_4^- ion electronic degrees of freedom. It will be shown that the latter circumstance leads to the addition of a positive shift to the FPT critical temperature T_c. Such an effect, related to the order-disorder component of the order parameter of FPT, will only induce an addition increase of T_c with respect to the displacive-type component effect.

The MnO_4^- MI is a very effective optical probe. It is characterized by intense ligand-to-metal charge-transfer absorption bands in the VIS range and well pronounced d–d absorption bands in the red region of the spectrum [7–9, 13]. Also, the multi-phonon resonance Raman spectra and the excitation profiles of Raman scattering of MnO_4^- ions in ionic crystals have been studied thoroughly (see [14] and references therein). Recently, intensive NIR-luminescence has been discovered for MnO_4^- molecular ions embedded in cubic [15, 16] and non-cubic [13, 17] crystal lattices.

Such a set of characteristic properties leads to additional new aspects of the problem under investigation. First, it is related to the possibility of the optical excitation of MI in the ferroelectric matrix. The electronic occupation of excited MI-states can significantly change the properties of MI charge transfer and local distortion of the subsystems. As a result, the MI influence on FPT will be changed by the action of optical pumping. Thus, photo-induced effects in FPT phenomena can be expected. Second, investigations of FPT order parameter behaviour (for instance, its critical temperature dependences) involving optical studies of electronic and vibronic spectra of MI embedded in soft matrices seems fruitful. Let us now consider the effect of MI-induced increase of FPT critical temperature predicted in the present work.

2. Increase of critical temperature induced by the interaction of soft polarization with molecular impurity ions

Let us evaluate the shift (ΔT_C) of the FPT point induced by the interaction between MI charge transfer on the one hand and soft lattice polarization on the other. We shall consider the case of a uniaxial ferroelectric crystal doped with MIs. Here we shall treat the combined phase transition in the crystal as a combined displacive and order -disorder type of behaviour. The displacive-type component is very significant in such mixing [18]. Note that the static behaviour of improper ferroelectrics of the XO_4^- ion -containing type (with the same symmetry for order-disorder and displacive-type order parameters) is identical to that of proper ferroelectrics (for instance displacive type ferroelectrics). We shall consider in this section the case of a dominating displacive -type order parameter (soft polarization) for the interaction with MnO_4^- degrees of freedom. In our approach we also use the mean field approximation, whose validity stems from the long-wave ($k \approx 0$) order parameter. As a result, the MI-induced renormalization of the free energy coefficients for the Landau expansion of the free energy can be considered.

Let us briefly discuss here the arguments for grounding the possibility of inserting MnO_4^- into an XO_4^- ion-containing matrix. First, it is known that MnO_4^- molecular ions exist in the framework of ionic-covalent bonding, with an essential contribution to the covalent part [5–9]. Even in the ionic approach, however, the ionic radii for topical Mn^{5+} and P^{5+}, Mo^{6+} or W^{6+} ions in the four-fold oxygen coordination do not differ strongly from each other (0.47 Å and 0.31 Å, respectively). Such a difference (0.16 Å) is of the order of zero point vibration fluctuations on one hand, and on the other can be compensated by the pronounce pliable behaviour of four oxygen ions in the framework of a real ionic-covalent regime with important covalent contribution. Second, in this context the successful experimental activity of Güdel et al. for the growing different crystals with MnO_4^- impurities should be underlined (see [13, 17] and corresponding references therein) as well as recent positive result of Hanuza and co-workers [19] for growing the ferroelastic crystal $K_3Na(CrO_4)^{2-}$:$(MnO_4)^{2-}$ with MnO_4^- molecular impurity ions.

The topical assumptions regarding MI are the following:

- The main assumption relating to the active O- and Mn-ion charge transfer states of MnO_4^-–MI is the assumption of their good self-localization in the system of host matrix states. Therefore we assume that we are dealing with local or quasi-local electronic states of the MnO_4^- impurity ion, which is an experimental example under discussion.
- The second assumption relating to the active charge transfer states of MI is the assumption of their coherent nature. These are four oxygen ion charge transfer states considered to be coherent states.

• The MnO_4^- impurity ion displays significant covalent O–Mn bonding as mentioned above. Here, the O–Mn covalent bonding coefficient can be estimated as $\gamma_{Mn\text{-}O} \approx 0.44$ and the corresponding equilibrium O–Mn charge transfer value can be high enough (see references [5, 6]). This leads to a decrease of the oxygen ion local negative charge due to O→Mn charge transfer, and to the occurrence of equilibrium oxygen hole states that are well defined within the MnO_4^- MI.

Taking into account these three statements, we deal with a fully-symmetric coherent ground state for oxygen holes (the singlet A state). The excited state here is a triplet T-state (T_x, T_y, T_z) for the four oxygen equilibrium holes in the cubic (T_d) field of the isolated MnO_4^- molecular impurity ion. These A, T_x, T_y, and T_z charge transfer oxygen hole states differ from each other by their different charge distributions among four oxygen ions in accordance with the state symmetry. Thus, the mixing of these states due to an interaction of soft polarization and the order-disorder pseudo-spin related order parameter with such a quartet of oxygen hole states mentioned above corresponds to charge transfer effects.

• The fourth assumption is related to the possibility of using the A, T_x, T_y and T_z charge transfer oxygen hole states mentioned above in the framework of real situations for MnO_4^-–MI embedded in an XO_4^- ion-containing matrix. We shall assume here for simplicity that the splitting of such a triplet of T-states in an uniaxial crystalline field of the matrix is much smaller than the splitting (Δ_{CT}) between T and A charge transfer states in a cubic T_d field for isolated MnO_4^- molecular impurity ions. As a result, such a uniaxial crystalline field of the host lattice could be inessential within our problem analysis with respect to the strong field of molecular origin. Note that the Δ_{CT} value can be of the order of 1 eV (Δ_{CT} = 1 eV in our case). Such a value for Δ_{CT} is typical of oxygen-related energy splitting, for instance for the width of subbands induced by electronic dispersion within the oxygen-related valence bands in oxides. Therefore let us also assume that MnO_4^- impurity ions keep the point group symmetry T_d, which is a good approximation for strong molecular bonding related to the crystalline field effect.

Let us start from a phenomenological consideration of the problem. As regards a pure XO_4^- ion-containing matrix, soft lattice dynamics will be related to the new pseudo-spin soft mode with Cochran-type critical dependence (with the η variable) and the low frequency polarization mode (with the P_z variable), but without critical softening at definite temperature. Such a soft polarization mode subsystem couples with interacting pseudo-spins of the matrix as in the case of KDP (the Kobayashi model [12]). As a result, the free energy of the pure system without MI can be presented in the following form:

$$\delta F_0 = \frac{1}{2}\alpha(T - T^{(0)})(\eta_z)^2 + \frac{\omega_p^2}{2}(P_z)^2 + AP_z\eta_z + \frac{\beta}{4}(\eta_z)^4 + \ldots \qquad (1)$$

where $T^{(0)}$, ω_p, A, β are the critical temperature for soft pseudo-spin mode condensation, the frequency for soft polarization (normalized with respect to the vibration mass coefficient), the coefficient for polarization – pseudo-spin order parameters bi-linear interaction, and the fourth order anharmonicity coefficient of the pseudo-spin order parameter, respectively. Minimization of the free energy equation with respect to P, η allows one to obtain the FPT temperature (T_C) equation, which manifests the increase in T_C induced by bi-linear $P\eta$ interaction:

$$T_C = T^{(0)} + \frac{A^2}{\alpha\omega_p^2} \tag{2}$$

The microscopic origin of the interaction between the MI charge transfer degrees of freedom and the FPT order parameter (soft polarization P_i) is the effect of A-T state mixing by such an order parameter. The corresponding interaction Hamiltonian can be presented in the following form:

$$\hat{H}_{\text{CT-polarization}} = V_i \sigma_x^{(i)} P_i \tag{3}$$

Here, $\sigma_x^{(i)}$ is a Pauli matrix, $\sigma_x^{(i)} = |T_i\rangle\langle A| + |A\rangle\langle T_i|$, V_i is the vibronic parameter for the interaction between charge transfer and soft polarization. Taking into account the second order perturbation theory with respect to the Hamiltonian in (3), we obtain the following, related to the harmonic contribution of P_z (soft polarization along the main axis) to the Landau expansion for free energy:

$$\delta F_P = \frac{\omega_p^2}{2}(P_z)^2 - \frac{nV_z^2}{\Delta_{\text{CT}}}(P_z)^2 \tag{4}$$

where n is the concentration of MI (MnO_4^- ions, for example). Equation (4) remains in its old form after replacing ω_p^2 by $\tilde{\omega}_p^2$ given by

$$\tilde{\omega}_p^2 = \omega_p^2 - \frac{2nV_z^2}{\Delta_{CT}} \tag{5}$$

After substituting Eq. (5) into Eq. (2), we finally get

$$T_C = T^{(0)} + \frac{A^2}{\alpha[\omega_p^2 - 2nV_z^2(\Delta_{\text{CT}})^{-1}]} \tag{6}$$

As can be seen in Eq. (6), the increase of the FPT critical temperature ($\Delta T_C > 0$) induced by increasing concentration has a non-linear character and can be defined for appropriately small concentrations by Eq. (7):

$$\Delta T_C = \frac{2nV_z^2}{\Delta_{CT}\omega_p^2}\left(\frac{A^2}{\alpha\omega_p^2}\right) \tag{7}$$

After substituting into Eq. (7) reasonable values for MnO_4^- impurity ion parameters in order to estimate the effect under consideration ($\Delta_{CT} \approx 1$ eV, $V_z \approx 10$ D, $\omega_p^2 \approx 0.036$, $A^2/\alpha\omega_p^2 \approx 10$ K and the concentration $n \approx 3\times10^{20}$ cm^{-3}), we obtain the critical temperature shift of $\Delta T_C \approx 10$ K. We conclude that the effect predicted in the present paper is large enough to be detected experimentally.

The theoretical considerations presented above describe the effect of molecular impurity ions on a ferroelectric (or ferroelastic) phase transition in crystals built from tetrahedral XO_4^- ions. The pseudo-spin approach is proposed in order to predict the temperature behaviour of these samples. In order to verify these effects, the syntheses of two crystals have been undertaken: KH_2PO_4 and $K_3Na(CrO_4)_2$, both doped with MnO_4^- ions. These two host systems differ substantially from each other. In the KDP crystal, these effects are influenced by hydrogen bonding [20–23]. Other effects could also appear in this crystal, i.e. a considerably different proton affinity of the MnO_4^- and PO_3^{3-} ions. This may lead to nano-regions of reorganized hydrogen bonds. The molecular structure and dielectric properties of the KDP crystal may therefore be changed [23, 24]. Relaxor-type behaviour could influence the phase transition parameters in such cases.

The other host matrix, of the $K_3Na(CrO_4)_2$ type, differs from KDP-like crystals due to smaller differences between the charges of the tetrahedral CrO_4^{2-} ion and doped MnO_4^- ion as well as due to a lack of hydrogen bonds. In spite of the different compositions and structures of these two host systems, we expect that the effect of the impurity ions on their phase transitions will be similar. Our preliminary temperature dependent studies of the shape of the ESR signal in the chromate crystal show that the phase transition temperature agrees well with predictions [19].

Acknowledgements

Authors are grateful to Prof. A.A. Kaplyanskii for attention to this work that was supported partly by RFBR (04-02-17633).

References

[1] STRUKOV B.A., LEVANYUK A.P., *Physical fundamentals of ferroelectric phenomena in crystals* (in Russian), 2nd Ed., Moscow, Nauka, 1995.
[2] VIKHNIN V.S., MAKSIMOVA T.I., Ferroelectrics, 299 (2004), accepted for publication.
[3] VIKHNIN V.S., Solid State Communications, 127 (2003), 283.
[4] VIKHNIN V.S., EGLITIS R.I., KAPPHAN S.E., BORSTEL G., KOTOMIN E.A., Phys. Rev. B 65 (2002), 104304.
[5] JOHNSON K.H., Int. J. Quantum Chem., 5S (1972), 143.
[6] JASINSKI J.P., HOLT S.L., J. Chem. Phys., 63 (1975), 1304.

[7] MARTIN T.P., ONARY S., Phys. Rev. B 15 (1977), 1093.
[8] MAKSIMOVA T.I., MINTAIROV A.M., Phys. Solid State, 29 (1987), 813.
[9] MAKSIMOVA T.I., VOGELSANG, H. STOLZ H., VON DER OSTEN W., Solid State Commun., 92 (1994), 337.
[10] VIKHNIN V.S., Fiz. Tver. Tela, 23 (1981), 2370.
[11] KRISTOFFEL N.N., Fiz. Tver. Tela, 23 (1981), 3267.
[12] BLINC R., ZEKS B., *Soft Modes in Ferroelectrics and Antiferroelectrics*, North-Holland Publ. Comp., Amsterdam, 1974
[13] BRUNOLD T.C., HAZENKAMP M.F., GÜDEL H.U., J. Luminescence, 72–74 (1997), 164.
[14] MAKSIMOVA T., Spectrochim. Acta, Part A, 55 (1999), 1153.
[15] MAKSIMOVA T., HERMANOWICZ K., MACALIK L., HANUZA J., J. Mol. Structure, 563–564 (2001), 353.
[16] MAKSIMOVA T., HANUZA J., HAPPEK U., J. Alloys Comp., 341 (2002), 239.
[17] BRUNOLD T.C., GÜDEL H.U., Inorganic Chemistry, 36 (1997), 1947.
[18] BUSSMANN-HOLDER A., DALAL N., *Fundamental Physics of Ferroelectrics 2001*, Virginia, Williamsburg, 2001, AIP Conf. Proc., H. Krakauer (Ed.), 582, pp. 137–143.
[19] HANUZA J., MACZKA M., HERMANOWICZ K., MAKSIMOVA T., in preparation.
[20] ICHIKAWA M., MOTIDA K., YAMADA N., Phys. Rev. B, 36 (1987), 874.
[21] KATRUSIAK A., Phys. Rev. B, 48 (1993), 2992.
[22] KATRUSIAK A., Phys. Rev. B, 51 (1995), 589.
[23] KATRUSIAK A., SZAFRAŃSKI M., Organic Lett., 5 (2003), 1903.
[24] SZAFRAŃSKI M., KATRUSIAK A., J. Phys. Chem. B, 108 (2004), 15709.

Received 25 November 2004
Revised 10 March 2005

Materials Science-Poland, Vol. 23, No. 3, 2005

Electrical and optical properties of sol-gel derived ZnO:Al thin films

P. SAGAR, M. KUMAR, R.M. MEHRA*

Department of Electronic Science, University of Delhi, South Campus New Delhi, 110021, India

High quality sol-gel derived ZnO and ZnO:Al thin films were deposited on corning (7059) glass substrates by spin coating. The annealed films showed the *c*-axis-preferred orientation. The structural, electrical, and optical properties of the films were investigated as a function of Al concentration from 0 to 3.0 at. %. The maximum conductivity of 18.86 $\Omega^{-1}\cdot cm^{-1}$ with the carrier concentration of 2.2×10^{24} m^{-3} was found for the Al concentration of 0.8 at. %. The conductivity is found to be of the activated type above 375 K, and variable range hopping conduction is observed below room temperature. Various transport parameters, such as the average spacing between donors, effective Bohr radius, donor levels, Debye screening length, and average grain size, have been estimated. The increase in band gap with Al doping is explained in terms of a Burstein Moss shift.

Key words: *sol-gel; ZnO: Al, spin coating; transport parameters*

1. Introduction

Zinc oxide (ZnO) is an interesting wide-band-gap semiconductor material with a direct band gap of 3.36 eV [1] at room temperature and exciton binding energy of 60 meV. It has crystalline structure of the wurtzite type and the unit cell with the constants a = 3.24 Å and c = 5.19 Å. Thin films of undoped and doped ZnO are utilized for a wide variety of electronic and opto-electronic applications, such as surface acoustic wave devices [4], transparent conducting electrodes [2], heat mirrors [3]. Nanoscale porous structures of ZnO with a high surface area find their application in chemical sensors [5] and dye-sensitised solar cells [6]. Various techniques have been used to deposit undoped and doped ZnO films on different substrates, including spray pyrolysis [7], organometallic chemical vapour deposition [8], pulsed laser deposition

*Corresponding author, e-mail: rammehra@netscape.net

[9], sputtering [10], and sol-gel process [11]. Among these, the sol-gel technique is credited with several advantages, such as deposition of high purity, homogeneous, cheaper, large-area films at relatively low temperatures. There are scarcely any reports on the transport parameters of ZnO:Al films prepared by the sol-gel technique.

In this paper, we concentrate on the structural, electrical conductivity and optical properties of sol-gel derived ZnO and ZnO:Al films deposited by spin coating. Estimates of various transport parameters, such as the average spacing between donors (r), effective Bohr radius (a^*), donor levels (E_d), Debye screening length (L_D), and average grain size (l), have been made.

2. Experimental details

The solutions were prepared by dissolving zinc acetate, $Zn(CH_3COO)_2{\cdot}2H_2O$ (purity 99.95%), in anhydrous methanol in increasing Al doping concentrations (98.5% purity $AlCl_3$) ranging from 0 to 3 at. %. The obtained mixture was mixed ultrasonically for about two hours. The solutions became turbid within twenty four hours after preparation. The turbidity was removed using 0.2 micron filters. The substrates were cleaned ultrasonically, first in acetone, and subsequently in methanol for 10 minutes each. They were further cleaned with ion exchanged distilled water for 20 minutes and kept in an oven at 80 °C for 30 minutes. The clear solutions were used for spin coating after 24 hours on corning glass (7059) substrates. The films were first dried at 80 °C and then at 300 °C for 20 minutes each. This process was repeated several times to deposit films of the desired thickness. The films were annealed for half an hour at temperatures from 500 to 600 °C for decomposition and oxidation of the precursors. Diffraction patterns of intensity versus 2θ were recorded with a Philips PW 1830 diffractometer, using a monochromatized X-ray beam with nickel-filtered Cu_kR radiation (λ = 1.5418 Å). A continuous scan mode was used to collect 2θ data from 20 to 60°, with a 0.02 sample pitch and 4 deg·min^{-1} scan rate. The thickness of the films was found to be ≅ 0.14–0.2 μm, as determined by a DEKTECK^{3-ST} surface profilometer. The surface morphology of the films was analysed by Scanning Electron Microscopy (SEM) with a JEOL JSM-6300, and atomic force microscopy (AFM) using an SPI 3700. Optical transmittance measurements were carried out using a Shimatzu UV-260 spectrophotometer. The electrical conductivity (σ) and the Hall coefficient (R_H) were measured by the van der Pauw [12] technique. The sign of the Hall coefficient confirmed the n-type conduction of the films. The carrier concentration (n) and the Hall mobility (μ_H) were determined using the expression $R_H = 1/ne$ and $\mu_H = R_H \times \sigma$, respectively. It should be mentioned that experimental data were reproducible with the accuracy of nearly 1.0%.

3. Results and discussion

3.1. Structural properties

ZnO:Al films were fabricated by the sol-gel technique on Corning glass substrates, and the XRD spectra of the ZnO and ZnO:Al films annealed in the temperature range 525–600 °C were gathered. Figure 1 shows the XRD patterns of ZnO and ZnO:Al films deposited at different Al dopant concentrations and annealed at 575 °C. The films exhibit a dominant peak at $2\theta = 34.34°$ corresponding to the (002) plane of ZnO, and other peaks corresponding to (100) and (101) and indicating the polycrystalline nature of the films. It is seen from the figure that the relative intensity of the (002) peak increases with increasing Al dopant concentration up to a concentration of Al equal to 0.8 at. %, and thereafter it starts to decrease. The increase in peak intensity indicates an improvement in the crystallinity of the films.

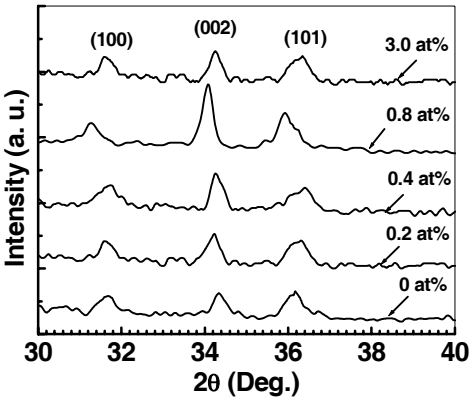

Fig. 1. X-ray diffraction patterns of ZnO and ZnO:Al films with various Al concentrations and annealed at 575 °C in air

Figure 2 shows the variation of the grain size l and texture coefficient TC with Al concentration. The extent of the preferred orientation as compared to other observed orientations is defined by the TC as [13]

$$TC(hkl) = \frac{\dfrac{I(hkl)}{I_0(hkl)}}{\dfrac{1}{N}\sum_N \dfrac{I(hkl)}{I_0(hkl)}} \tag{1}$$

where $I(hkl)$ is the measured relative intensity of the diffraction peak corresponding to hkl and $I_0(hkl)$ is the relative intensity peak corresponding to plane of ZnO powder. The increase in the texture coefficient of the film with an Al concentration of 0.8 at. % indi-

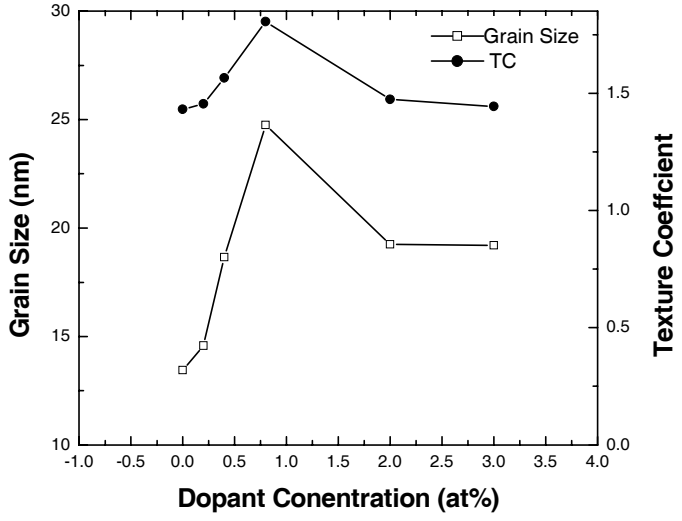

Fig. 2. Variation of the grain size *l* and texture coefficient *TC* with Al dopant concentration

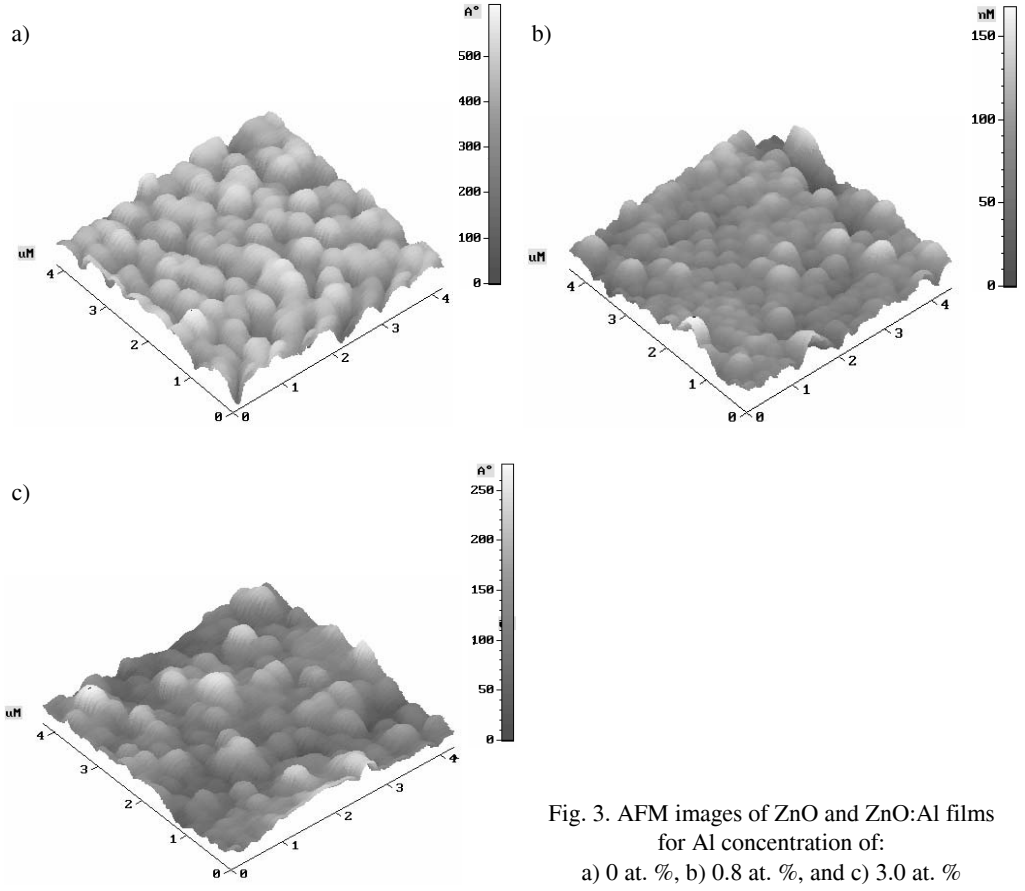

Fig. 3. AFM images of ZnO and ZnO:Al films for Al concentration of:
a) 0 at. %, b) 0.8 at. %, and c) 3.0 at. %

cates that a large number of crystallites are oriented along the *c*-axis. The grain size of the films was estimated from the Scherrer formula [14] using the FWHM of the peak corresponding to (002) plane. The grain size was found to increase from 13 nm (undoped) to a maximum of ~25 nm for an Al concentration of 0.8 at. %. At 3.0 at. % of Al, the grain size was reduced to 19 nm. The scanning electron microphotograph of the film with an Al concentration of 0.8 at. % shows uniformly distributed grains with a smaller number of voids.

Figure 3a–c shows AFM images of ZnO:Al films with an Al dopant concentration of 0.0, 0.8, and 3.0 at. %, respectively. The RMS value of the surface of the undoped ZnO film is 22 nm whereas for the film having 0.8 at. % of Al it is 4.3 nm. At a higher Al dopant concentration (3.0 at. %), the surface was found to be rough (RMS = 86 nm). Thus, this study of structural properties reveals that the film doped with 0.8 at. % of Al is smooth and highly oriented along the *c*-axis oriented with densely packed grains.

3.2. Electrical properties

The values of R_H at different concentrations of Al are given in Table 1. The variations of σ_{RT}, n, and μ_H with Al concentration in ZnO:Al films are shown in Fig. 4. It is seen from this figure that σ_{RT} and μ_H increase with increasing Al concentration. Maximum values of σ_{RT} (18.86 $\Omega^{-1}\cdot cm^{-1}$) and μ_H (52.8 cm^2/Vs) are obtained for 0.8 at. % of Al. With further increase in Al concentration (> 0.8%), σ_{RT} and μ_H are found to decrease. Minami et al. [15] have also reported the value of $\mu_H \cong 45$ cm^2/Vs in Al doped ZnO films.

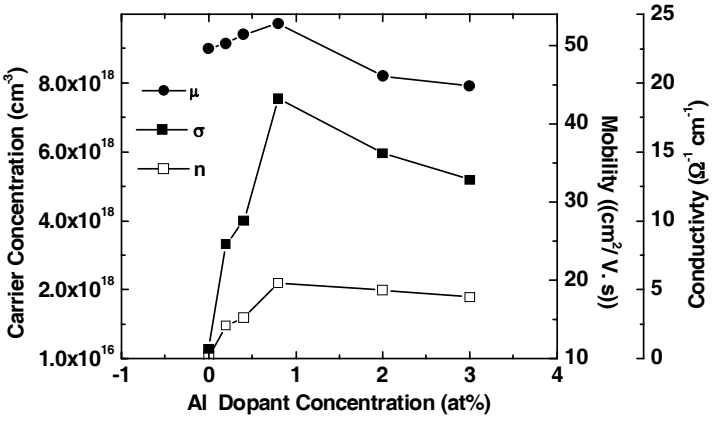

Fig. 4. Carrier concentration n, Hall mobility μ, and resistivity ρ of ZnO:Al films annealed at 575 °C in air as a function of Al concentration

The carrier concentration in the doped ZnO film increases linearly with increasing dopant concentration up to 0.8 at. %. The observed increase in n and μ_H with dopant

concentration up to 0.8 at. % accounts for the increase in conductivity in accordance with the relation $\sigma = ne\mu_H$. The overall variation in n and μ_H can be understood in terms of the position of Al in the ZnO lattice. The ZnO film generally grows as an n-type semiconductor, due to the presence of native defects in the form of zinc interstitials, oxygen vacancies, or both. The observed behaviour at low doping levels (up to 0.8 at. % of Al) is expected to be the result of substitutional doping of Al^{3+} at Zn^{2+} sites, which creates one extra free electron in the conduction band. A decrease in n and μ_H at higher dopant concentrations (> 0.8 at. %) may be due to the interstitial occupancy of Al in the ZnO lattice, which may lead to a distortion of the crystal structure. The presence of Al at interstitial sites and grain boundaries in the form of oxide, besides decreasing grain size, may act as scattering centres and result in a decrease in the observed mobility at dopant concentration > 0.8 at. %. XRD results also suggest the degradation of film structure at higher dopant concentrations.

Table 1. Activation energy at high temperatures E_a, average spacing between donors r, r/a^*, Debye screening length L_D, activation energy of grain boundary limited conductivity E_σ, the change ΔE_g in E_g, and absorption edge shift ΔE^{BM} at different Al dopant concentrations

Dopant conc. (at. %)	E_a (eV)	r (nm)	r/a^* (nm)	L_D (nm)	E_σ (eV)	ΔE_g (eV)	ΔE^{BM} (eV)	R_H (cm^3/C)
0.0	0.94	12	8.3	13.5	0.96	–	–	70.4
0.2	0.82	6.2	4.3	4.0	0.86	0.015	0.011	6.4
0.4	0.66	5.8	4.0	3.6	0.67	0.018	0.013	5.2
0.8	0.43	4.7	3.2	2.7	0.47	0.025	0.020	2.8

Structural surface morphology and electrical studies indicate that films with higher concentrations of Al (> 0.8 at %) are two-phase solids. These films may contain clusters of an Al-rich phase, but not Al^{3+} ions in the interstitials position. Therefore, studies of the temperature variation of electrical conductivity and optical properties are restricted to films containing Al up to 0.8 at %.

The dependence of conductivity ($\ln\sigma$ vs. $10^3/T$) for a ZnO:Al film at high temperatures (375–475 K) is shown in Fig. 5. It is observed that $\ln\sigma$ vs. $1/T$ curves are linear in this temperature range, indicating an activated conduction process following the expression

$$\sigma = \sigma_1 \exp\left(-\frac{E_a}{kT}\right)$$

The activation energies E_a listed in Table 1 are found to decrease with increasing dopant concentration up to 0.8 at. %.

In Figure 5, conductivity variation with temperature in the range of 153–600 K for an undoped ZnO film is also shown as an insert. The data below room temperature

were analysed assuming Mott's variable range hopping conduction process [16]. As shown in Fig. 6, $\ln(\sigma T^{1/2})$ vs. $1/T^{-1/4}$ plots are linear, indicating variable range hopping (VRH) conduction.

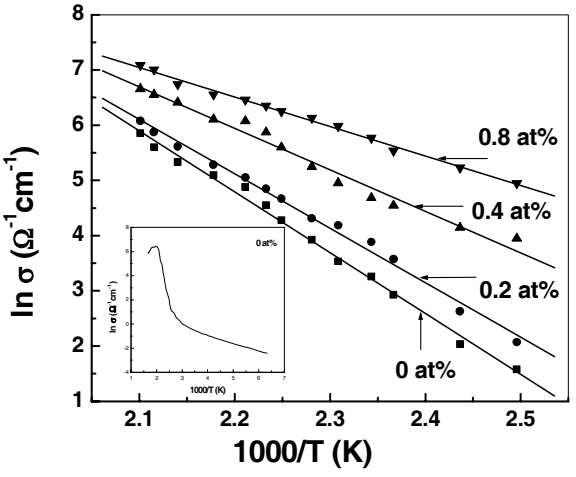

Fig. 5. Arrhenius plot of the DC conductivities σ of ZnO and ZnO:Al films with different Al concentrations

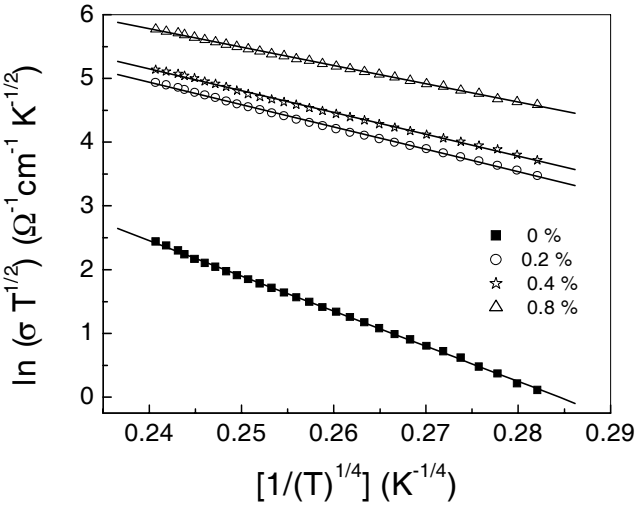

Fig. 6. Plot of $\ln(\sigma T^{1/2})$ versus $T^{-1/4}$ for ZnO and ZnO:Al films with different Al concentrations

Hausmann and Teuerle [17] have classified three types of conduction process in indium-doped single crystals at low temperatures (below 300 K), depending on the ratio of the average spacing between donors r to the effective Bohr radius a^*. The values of r and a^* are given as

$$r = \left(\frac{4\pi N_d}{3} \right)^{-1/3} \tag{2}$$

$$a^* = \frac{a_0 \varepsilon_s m}{m^*} \tag{3}$$

where N_d is the impurity concentration, m is the mass of a free electron, m^* is the effective mass of the electron, ε_s is the relative electric permittivity, and a_0 is the Bohr radius:

$$a_0 = \frac{4\pi\varepsilon_0 \hbar^2}{me^2} = 0.53 \text{ Å}$$

• For $r/a^* > 5$, impurity concentration is low and impurity levels are isolated, while the conduction is explained by charge transport in the conduction band and nearest neighbour hopping between isolated donor levels.

• For $2 < r/a^* < 5$, called the intermediate concentration region, an impurity band is formed by the overlapping wave functions of donors. Therefore, a variable hopping conduction [18] appears between localized states in the impurity band.

• For $r/a^* < 2$, which is the high impurity concentration regime, metallic conduction takes place due to the overlapping of impurity and conduction bands.

The value of r in a doped ZnO film were estimated from Eq. (2), assuming that all donor atoms are ionised and completely contributing their charge carriers to the conduction band at least up to a dopant concentration of 0.8 at. %. The estimated values of r are given in Table 1 and found to decrease from 12.0 nm to 4.7 nm for dopant concentration of 0 and 0.8 at. %, respectively. This decrease in r is attributed to the enhanced substitution of Zn^{2+} by Al^{3+} and increasing concentration of charge carriers in the conduction band. The energy of the donor level of Al in the ZnO lattice E_d can be estimated using the expression

$$E_d = \frac{E_i m^*}{\varepsilon_s{}^2 m} \tag{4}$$

where E_i is the ionisation potential for Al (the energy required to completely remove an electron from the atom). Taking $E_i = 5.984$ eV [19], $m^* = 0.31$ m, and $\varepsilon_s = 8.5$ [19] for ZnO, we obtain the value of $E_d = 25.67$ meV. The values of r, a^* (Eqs. (2) and (3)), and r/a^* are also included in Table 1. It is seen from this table that the ratio r/a^* lies between 2 and 5, which suggests VRH conduction between localized states in the impurity band. The observed value of $E_d = 25.67$ meV for Al in a ZnO lattice also suggests that all impurities will be ionised above RT, and therefore VRH conduction is possible below RT only to the extent observed in the present case.

The effect of grain boundaries on electron transport in the conduction band can be examined by comparing the Debye screening length L_D with the average grain size l. L_D can be expressed as [20]

$$L_D = \left(\frac{\varepsilon_s \varepsilon_0 kT}{e^2 N_d} \right)^{1/2} \tag{5}$$

where ε_s is the relative electric permittivity, ε_0 is the electric permittivity of free space and N_d is the donor concentration. Providing L_D is smaller than $l/2$, a potential barrier around each grain boundary is formed due to band bending. If, however, L_D is larger than $l/2$, the conduction band becomes flat and loses the potential barrier. Electrons are then transported without grain boundary scattering.

L_D for the doped films at 400 K is determined to be in the range 4.0–3.0 nm, while l, as estimated from the FWHM of the XRD peak using the Scherrer formula, lies in the range 13–25 nm (Table 1). It is seen from Table 1 that $L_D < l/2$, which suggests that the effect of the grain-boundary potential barrier on conduction at high temperatures may also be taken into account. The conductivity in this case can be represented as [21]

$$\sigma = \left(\frac{e^2 l N_d}{2\pi m^* kT} \right)^{1/2} \exp\left(-\left(\left(E_C - E_F \right) + e\phi \right) / kT \right) \tag{6}$$

where E_C is the energy of the conduction band minimum, E_F the Fermi level, ϕ the grain boundary potential barrier, and N_d the donor concentration. Assuming

$$E_\sigma = E_C - E_F + e\phi$$

as the activation energy for the grain boundary limited conductivity, the above equation can be written as

$$\sigma T^{1/2} \propto \exp\left(-\frac{E_\sigma}{kT} \right) \tag{7}$$

From the linear plot of ln ($\sigma T^{1/2}$) and T^{-1}, values of E_σ were obtained, and are listed in Table 1. The value of $E_\sigma / E_a \sim 1$ suggests thermionic emission over the grain boundaries at high temperatures in doped ZnO films. Thus, conductivity at higher temperatures depends on the morphology, i.e. the polycrystallinity of films.

3.3. Optical properties

Typical UV transmittances for 0 and 0.8 at % of Al are shown in Fig. 7. It is seen from this figure that the average transmittance T in the visible region is higher than 85% for films having 0.8 at. % of Al.

The optical band gap E_g was calculated using Tauc's plot ($(\alpha h\nu)^2$ vs. $h\nu$), as shown in Fig. 8. The value of α is determined from transmittance spectra. The photon energy at the point where $(\alpha h\nu)^2$ is zero represents E_g, which is determined by extrapolation. An increase in E_g with Al doping up to 0.8 wt% is observed. It should be mentioned

that both the average transmittance and band gap are found to decrease at higher Al doping concentrations. The change ΔE_g in E_g with dopant concentration is also listed in Table 1.

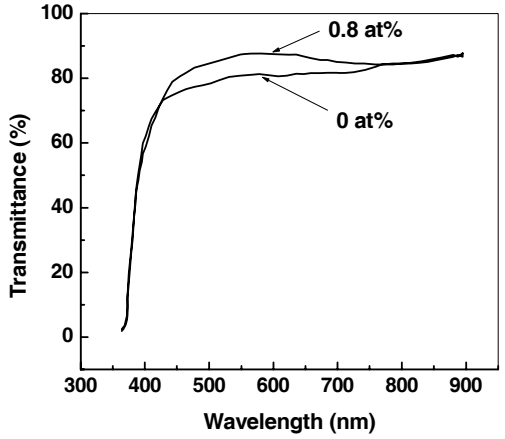

Fig. 7. Variation of transmittance T as a function of Al concentration in the wavelength range of 200–800 nm for ZnO and ZnO:Al films annealed at 575 °C

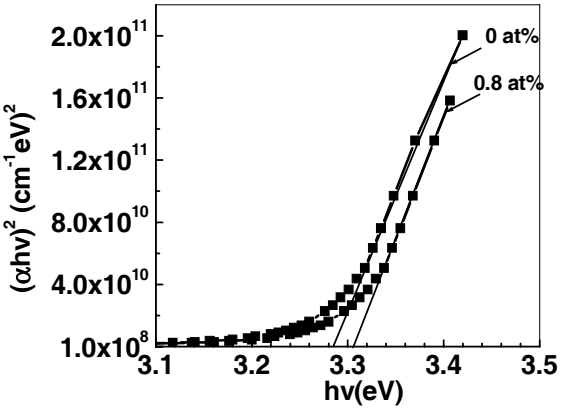

Fig. 8. Band gap E_g estimation for ZnO and ZnO:Al films using Tauc's plot

The dependence of E_g on carrier concentration is analysed considering the Burstein Moss (BM) model [22] for the absorption edge shift ΔE^{BM} in an n-type semiconductor, which is given by

$$\Delta E^{\mathrm{BM}} = \left(3\pi^2 N\right)^{2/3} \frac{\hbar^2}{2m_{vc}^*} \tag{8}$$

where m_{vc}^* is the reduced effective mass [23] given by

$$\frac{1}{m_{vc}^*} = \frac{1}{m_c^*} + \frac{1}{m_v^*} \tag{9}$$

where m_c^* is the effective mass in the conduction band and m_v^* is the effective mass in the valence band. The variation of ΔE_g and ΔE^{BM} with n is shown in Fig. 9, from which it is seen that the BM shift accounts fairly well for the observed change in the band gap.

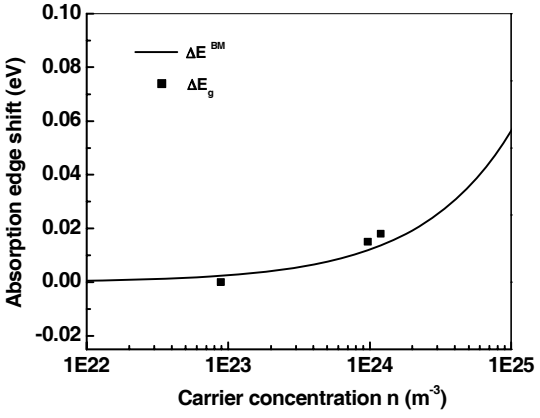

Fig. 9. Absoption edge shift as a function of carrier concentration. The solid line shows the calculated ΔE^{BM}, ■ shows the experimental ΔE_g due to the variation in Al concentration

4. Conclusions

Highly conducting and transparent sol-gel derived ZnO:Al films have been deposited by spin coating. It has been found that the *c*-axis orientation and grain size of the films significantly depend on Al concentration. The analysis of the peak intensity (texture coefficient) and FWHM of the XRD spectra clearly indicate that at the critical dopant concentration (0.8 at. % of Al) the film contains a maximum number of crystallites oriented along the *c*-axis and exhibiting a large grain size. Conductivity data suggest different conduction mechanisms at high and low temperatures. At high temperatures, electrical transport in ZnO:Al films is attributed to the grain boundary potential barrier, which is also confirmed from the estimated Debye screening length and average grain size ($L_D < l/2$). The observed VRH conduction at low temperatures is ascertained from the calculated ratio of the average spacing between donors to the effective Bohr radius ($2 < r/a^* < 5$). The change in band gap due to Al doping is ascertained due to BM shift.

Acknowledgements

The authors wish to acknowledge the financial support of DRDO, Govt. of India, India.

References

[1] BIXIA LIN, ZHUXI FU, YUNBO JIA, Appl. Phys. Lett., 79 (2001), 943.
[2] SRIKANT V., CLARKE D.R., J. Appl. Phys., 81 (1997), 6357.
[3] MINAMI T., NATO H., TAKATA S., Thin Solid Films, 124 (1985), 43.
[4] CHOPRA K.L., MAJOR S., PANDAY D.K., Thin Solid Films, 102 (1983), 1.
[5] WEIBENRIEDER K.S., MULLER J., Thin Solid Films, 300 (1997), 30.
[6] SEOK-SOON KIM, JUN-HO YUM, YUNG-EUN SUNG, Solar Energy Mat. Solar Cells, 79 (2003), 495.
[7] NUNES P., FORTUNADEO E., MARTINS R., Thin Solid Films, 383 (2001), 277.
[8] ROTH A.P., WILLIAMS D.F., J. Appl. Phys., 52 (1981), 6685.
[9] LU Y.F., NI H.Q., MAI Z.H., REN Z.M., J. Appl. Phys., 88 (2000), 498.
[10] JIANG X., WONG F.L., FUNG M.K., LEE S.T., Appl. Phys. Lett., 83 (2003), 1875.
[11] JIMENEZ-GONZALEZ A.E., URUETA J.A.S., SUAREZ-PARRA R., J. Crystal Growth, 192 (1998), 430.
[12] VAN DER PAUW L.J., Philips Res. Repts., 13 (1958), 1.
[13] BARRED C., MASSALSKI T.B., *Structure of Metals*, Pergamon Press, Oxford, 1980, p. 204.
[14] LI B.S., CHU Y.S., SHEN D.Z., LU Y.M., ZHANG J.Y., FAN X.W., J. Appl. Phys., 91 (2002), 501.
[15] MINAMI T., NANTO H., TAKATA S., Thin Solid Films, 124 (1985), 43.
[16] LEE M.J.G., Phys. Rev., 187 (1969), 901.
[17] HAUSMANN A., TEUERLE W., Z. Phys., 257 (1972), 299.
[18] MOTT N.F., J. Non-cryst. Solids, 1 (1968), 1.
[19] KIREEV P.S., *Semiconductor Physics*, Chap. 2, 2nd Ed., Mir Publication, 1975, p. 150.
[20] ORTON J.W., POWELL M.J., Rep. Prog. Phys., 43 (1980), 1263.
[21] SETO J.Y.W., J. Appl Phys. 46 (1975), 5247.
[22] BURSTEIN E., Phys. Rev., 93 (1954), 632.
[23] SINGH A.V., MEHRA R.M., YOSHIDA A., WAKAHARA A., J. Appl. Phys., 95 (2004), 3640.

Received 21 May 2004
Revised 29 June 2005

Materials Science-Poland, Vol. 23, No. 3, 2005

Preparation of $CuFe_2O_4/SiO_2$ nanocomposite by the sol-gel method

J. PLOCEK[1, 2*], A. HUTLOVÁ[1], D. NIŽŇANSKÝ[1, 2],
J. BURŠÍK[1], J.-L. REHSPRINGER[3], Z. MIČKA[2]

[1]Institute of Inorganic Chemistry, ASCR, 25068 Řež u Prahy, Czech Republic

[2]Department of Inorganic Chemistry, Faculty of Science, Charles University of Prague, Albertov 2030, 128 40 Prague 2, Czech Republic

[3]I.P.C.M.S., Groupe des Matériaux Inorganiques, 23 Rue du Loess, F-67037 Strasbourg Cedex, France

This work aims at characterizing the phase relations in the $CuFe_2O_4/SiO_2$ system. Samples were prepared by the sol-gel method. Final heat treatment of the samples was carried out at temperatures in the range of 800–1100 °C. Final products were characterized by HR TEM, X-ray diffraction, magnetic measurements, and Mössbauer spectroscopy. HR TEM revealed nanocrystals with sizes of 7–130 nm, depending on the heat treatment temperature. The spinel structure of $CuFe_2O_4$ in the amorphous silica matrix proved to be stable up to 1100 °C without decomposition to copper silicate and iron (III) oxide. At the same time, the amorphous silica matrix recrystallized to cristobalite at 1100 °C.

Key words: *sol-gel; spinel ferrite; silica matrix; nanocomposite; Mössbauer spectroscopy; transmission electron microscopy; magnetic measurements*

1. Introduction

Nanocomposites have been the subject of many studies in recent years due to the new properties they are expected to exhibit [1]. One of the interesting groups consists of metal oxide compounds in a silica matrix. These materials can have interesting magnetic and magnetooptical properties [2]. One of the ways to prepare nanocomposites with the required properties is the sol-gel method. The advantages of this method are better homogeneity of materials and lower temperatures of treatment. In the case of nanocomposites in a silica matrix, samples with an arbitrary cation to silica ratio can be prepared and the particle size can be controlled by the parameters of heat treatment.

*Corresponding author, e-mail: plocek@ iic.cas.cz

This method was, for example, successful in the preparation of a metastable phase in the Fe_2O_3/SiO_2 system [3–5]. Studies have revealed that the metastable γ-Fe_2O_3 could be present in this nanocomposite up to 800 °C and that the intermediate phase ε-Fe_2O_3 also appears [6]. In the case of ternary oxides with a spinel structure, the situation is more complicated due to the possible formation of silicate. The MFe_2O_4/SiO_2 system is metastable from the theoretical point of view (M^{2+} silicates are formed). Previous studies have revealed, however, that the spinel phase was formed in the silica matrix and that the formation of MFe_2O_4 nanoparticles strongly depends on the type of M^{2+}. Spinel nanocrystals in the silica matrix are stable up to 1100 °C in the case of M = Co, Ni, and Zn [7, 8] and mainly cadmium silicate and iron(III) oxide were found in the final heat treated product in the case of Cd [8].

This work presents the preparation of another MFe_2O_4/SiO_2 system (here M = Cu) and the characterization of the phase relations in this system. It also concerns the ferrite/silica-nanocomposite system prepared by the sol-gel method, which has not yet been studied. This work aims to show the suitability of this method for preparing copper ferrite nanoparticles in the silica matrix. $CuFe_2O_4/SiO_2$ nanocomposites were prepared by the sol-gel method and were heat treated in the temperature range of 800–1100 °C. The final products were studied by X-ray diffraction, HR TEM, magnetic measurements, and Mössbauer spectroscopy.

2. Experimental

Sample preparation. Samples were prepared using the conventional sol-gel method. Copper and iron nitrates were used as spinel precursors. TEOS, HNO_3 as an acid catalyst, formamide as a modifier, and methanol as a solvent were employed for silica matrix preparation. $Fe(NO_3)_3 \cdot 9H_2O$ and $Cu(NO_3)_2 \cdot 3H_2O$ were first dissolved in methanol. The Si/Fe molar ratio was 100/20, which corresponds to a $SiO_2/CuFe_2O_4$ molar ratio of 100/10 (28.5 wt. % of $CuFe_2O_4$). The gelation time was approximately 18 hours at 45 °C and the samples (pellet shape, 5 mm thick and 15 mm in diameter) were left for two days to age. Then they were dried at 40 °C for three days in flowing N_2-atmosphere. After drying, they were first preheated at 300 °C in vacuum for two hours and then heated for four hours at various temperatures (800, 900, 1000, and 1100 °C) in air. The resulting samples were then characterized using powder X-ray diffraction, Mössbauer spectroscopy, HR TEM, and magnetic measurements.

Experimental techniques. A high-resolution transmission electron microscope (Topcon) was used for the direct observation of particle appearance. Particle sizes determination was carried out using Scion Images software. X-ray patterns were measured at ambient temperature using a Siemens D5000 diffractometer. Mössbauer spectra measurements were done in transmission mode with ^{57}Co diffused into a Cr matrix as the source moving with constant acceleration. The spectrometer was calibrated by means of a standard α-Fe foil and the isomer shift was expressed with re-

spect to this standard at 300 K. The fitting of spectra was performed with the help of the NORMOS program. Magnetic measurements were carried out in a vibrating sample magnetometer (VSM) at 298 K.

3. Results

The samples of $CuFe_2O_4/SiO_2$ nanocomposites were obtained by the sol-gel method. Previous studies indicated that vacuum treatment restrains α-Fe_2O_3 (hematite) formation and leads to ferrite formation [7]. For this reason, the samples were first treated at temperatures up to 300 °C under vacuum and then the final heat treatment at 800–1100 took place. Samples annealed at 800 and 900 °C were amorphous, but for those annealed at 1000 °C the crystallization of the silica matrix began. This fact was confirmed by X-ray diffraction, where diffraction peaks of cristobalite appeared at 1000 and 1100 °C. All of the $CuFe_2O_4/SiO_2$ samples heated in the above-mentioned temperature range were dark brown.

3.1. X-ray diffraction measurements and HR TEM observations

All samples were characterized by X-ray diffraction measurements (step 0.1°, time 50 s/step), and the results are shown in Fig. 1. X-ray diffraction patterns of samples

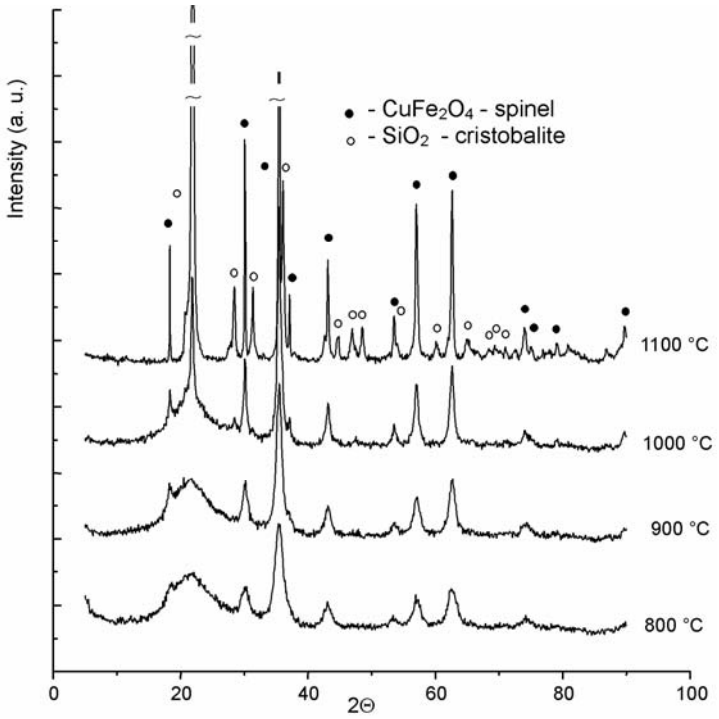

Fig. 1. X-ray diffraction patterns of the $CuFe_2O_4/SiO_2$ samples

heated at 800 °C indicate the presence of amorphous SiO_2, manifested by the characteristic very broad diffraction at 20° (2θ). The recrystallization of the silica matrix into cristobalite starts at 1000 °C and there is no evidence of an amorphous phase (the broad diffraction at 20° is absent) in the sample treated at 1100 °C. The diffraction patterns of phases other than SiO_2 exhibit broad peaks that become sharper with increasing temperature of heat treatment. This corresponds well to the crystal growth. These diffractions were found in all the studied samples annealed at the above-mentioned temperatures and can be well attributed to the ferrite spinel structure. Bulk copper ferrite spinel is slightly distorted due to the Jahn-Teller (JT) effect, therefore it has a tetragonal symmetry.

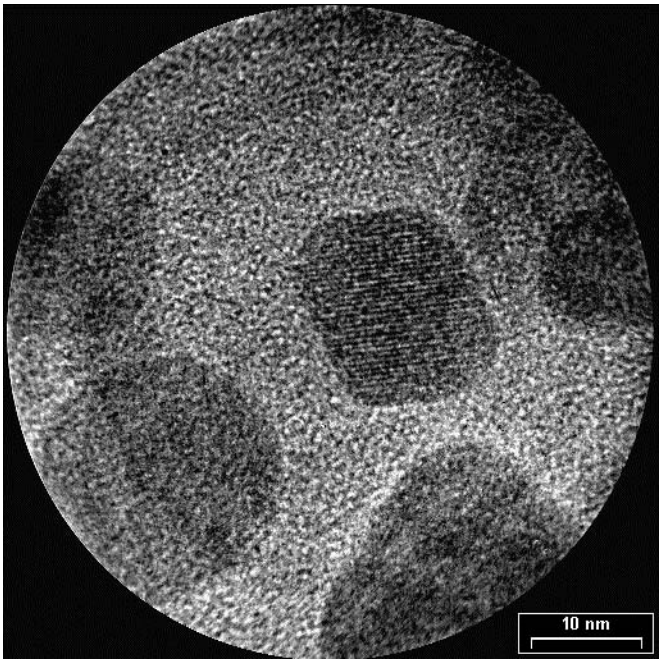

Fig. 2. HRTEM of the $CuFe_2O_4/SiO_2$ sample heated at 1000 °C

Table 1. Average particle size of the $CuFe_2O_4/SiO_2$ composite depending on the annealing temperature

Temperature	800 °C	900 °C	1000 °C	1100 °C
Particle size (nm)	7±2	9±3	15±3	130±17

Direct particle size observation by means of HR TEM confirms the tendency shown by the X-ray diffraction. The mean particle size of the $CuFe_2O_4$ in SiO_2 nanocomposite heated at 800 °C is 7 nm. Particle size rapidly increases with increasing temperature. The sample heated at 1000 °C show a mean particle size of 15 nm

(Fig. 2, Table 1) and the mean particle size of the spinel ferrite particles in the sample heated at 1100 °C is 127 nm. Particles were very well defined and did not exhibit a diffused appearance.

3.2. Mössbauer spectra

X-ray diffraction cannot distinguish between $CuFe_2O_4$ and γ-Fe_2O_3 spinel structures, especially in the case of very small particles, due to very close lattice parameters of both structures. For this reason, the measurements of Mössbauer spectra were carried out. Mössbauer spectra also yield information about the site occupation of the spinel structure and about the number of non-equivalent iron atoms.

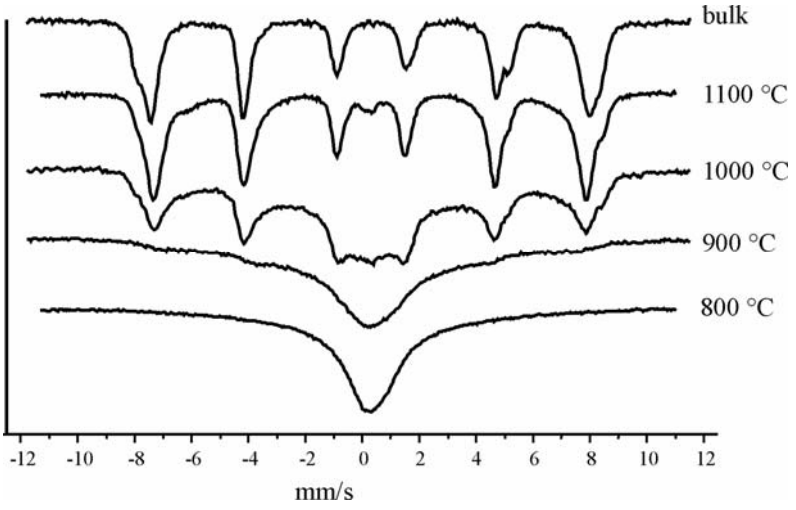

Fig. 3. Room temperature Mössbauer spectra of $CuFe_2O_4/SiO_2$ samples treated at various temperatures in the range of 800–1100 °C, compared to bulk $CuFe_2O_4$

Figure 3 represents spectra obtained at room temperature for samples annealed at 800, 900, 1000, and 1100 °C. The sample treated at 800 °C exhibits a very large

Table 2. Interpretation of the room-temperature Mössbauer spectra of the $CuFe_2O_4/SiO_2$ composite heated at 1100 °C

Subspectrum	Isomer shift δ (mm/s)	Quadrupole splitting E_Q (mm/s)	Hyperfine field B_{hf} (T)	Full line width at half height (mm/s)	Relative area (%)
1	0.361±0.001	–0.065±0.004	50.296±0.012	0.416±0.008	15.6±0.318
2	0.275±0.001	0.014±0.002	47.597±0.012	0.406±0.005	40.0±0.899
3	0.310±0.002	–0.043±0.003	45.779±0.022	0.455±0.007	26.7±0.859
4	0.391±0.006	–0.036±0.013	40.881±0.023	0.813±0.022	14.2±0.395
5	0.225±0.014	0.000±0.825		0.950±0.033	3.4±0.094

singlet, which is characteristic of the superparamagnetic state. In the following spectra (increasing heat treatment temperature) we can see that this band becomes broader and transforms into a sextet, which is well defined for the 1000 °C annealed sample. The 1100 °C heat-treated sample shows a Mössbauer spectrum that can be decomposed into four sextets and one singlet (Fig. 4). The parameters of this fit are given in Table 2. The doublet represents nanoparticles (smaller than the critical size) that are still in the superparamagetic state, but a relative area of 3.4 % suggests that almost all particles are in the ferromagnetic state. For confirming the $CuFe_2O_4$ phase in our nanocomposite, we compared the Mössbauer spectrum of pure bulk $CuFe_2O_4$ (Figure 3, top trace) with the other nanocomposites. The sextet of α-Fe_2O_3 (hematite), which is the most stable phase at these conditions, was not found.

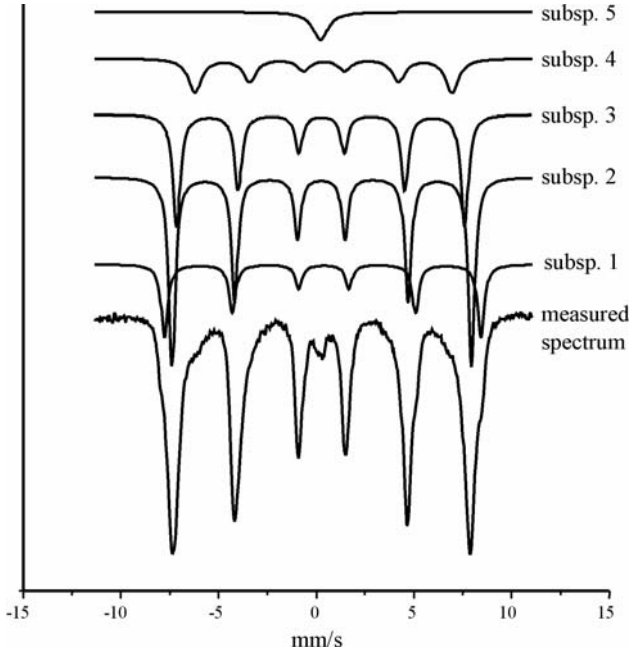

Fig. 4. Room temperature Mössbauer spectrum of $CuFe_2O_4/SiO_2$ samples treated at 1100 °C

3.3. Magnetic measurements

Figure 5 shows a plot of the magnetic moment of our nanocomposites as a function of the applied field (hysteresis curves), measured at room temperature, for all the heat treatment temperatures. We can see from this figure that the saturation magnetization values increase as particle size increases with annealing temperature. The values of saturation magnetization for the prepared samples are listed in Table 3. This Table gives both the values related to the entire nanocomposites and to the ones recalculated for their pure copper ferrite components.

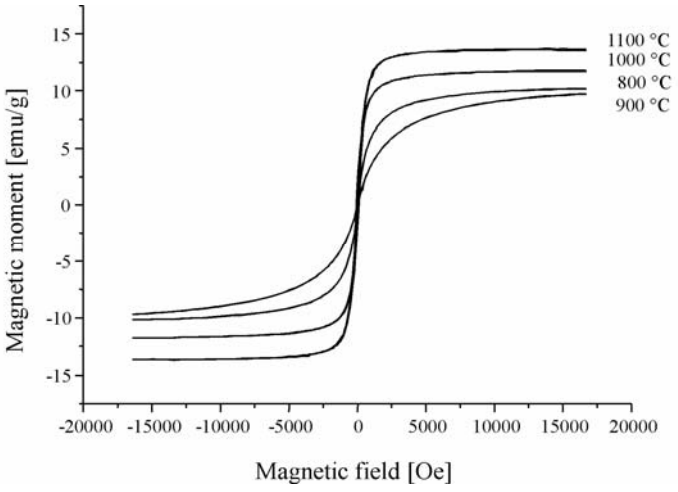

Fig. 5. Magnetic moments of samples heated at 800, 900, 1000, and 1100 °C, measured at 298 K. (Magnetic moments of the entire samples including the SiO_2 matrix)

Table 3. The saturation magnetic moments measured at 298 K of the $CuFe_2O_4/SiO_2$ composite heated at 800, 900, 1000, and 1100 °C

Temperature of treating (°C)	Saturation magnetic moment (emu/g)	
	Composite	Pure $CuFe_2O_4$
800	7.9	27.7
900	9.2	32.3
1000	11.2	39.4
1100	13.4	46.9

4. Discussion

It can be seen from the powder X-ray diffraction data that the spinel phase of $CuFe_2O_4$ is formed in the silica matrix and that it is still stable in the sample annealed at 1100 °C. The presence of iron (III) oxide phases was not proved. There is a theoretical possibility for the presence of γ-Fe_2O_3, because it has the same spinel structure with lattice parameters very close to those of $CuFe_2O_4$. The presence of iron oxide, however, should be accompanied by copper ferrite decomposition and the probable formation of copper silicates. On the other hand, there are no other copper compounds present in the XRD patterns, which can be considered to be indirect evidence supporting our interpretation. In addition, Mössbauer spectroscopy results clearly show that only $CuFe_2O_4$ spinel phase is present. Another finding from XRD is that the spinel phase in the composite has cubic symmetry, while pure stoichiometric $CuFe_2O_4$ is reported to be tetragonal due to the JT effect. This could be caused by the fact that the

diffractions of the spinel phase are broad and therefore we cannot observe the splitting of the diffraction lines due to the JT effect. Nevertheless, there are copper ferrites reported to have cubic symmetry, e.g. cuprospinel, which can be found in the mineral database of powder diffraction files [9]. It is expected that this mineral has neither the stoichiometry of pure copper ferrite nor regular occupation of the cation sites. We probably have a similar situation in our nanocomposite, which means that the structure of our copper ferrite in the silica matrix is not exactly the same same as the structure of inverse spinel. The occupation of tetrahedral and octahedral sites is rather statistical, resulting in a cubic symmetry of spinel structure.

Pure $CuFe_2O_4$ is reported to have a saturation magnetization of about 25 emu/g at room temperature [10]. The ideal inverse spinel structure of $(Fe\downarrow)[Cu\uparrow Fe\uparrow]O_4$ (parenthesis means tetrahedral positions, bracket means octahedral ones) corresponds to the saturation magnetic moment of 1 μ_B. The values of 1.3–2.5 μ_B, however, have been reported in literature [11] corresponding to mixed state of spinel. These various values of μ and thus of saturation magnetization are supposed to be due to different cooling rates during spinel preparation. $CuFe_2O_4$ is known to have cation vacancies, whose amount varies with preparation conditions. This fact must be taken into account for the detailed interpretation of magnetic measurements. In our case, namely the study of the phase relations in the $SiO_2/CuFe_2O_4$ system, we do not take these vacancies into account in the first approach to our interpretation of measurements.

The calculated value of the saturation magnetization of the pure spinel ferrite phase for the 1100 °C heated sample amounts to 46,9 emu/g, which is much higher than the reported value for purely inverse spinel [10]. This can be explained by the mixed character of the spinel structure; some of the copper atoms are located in tetrahedral sites. The formula of our copper ferrite can be written as: $(Fe_{(1-x)}Cu_x)[Fe_{(1+x)}Cu_{(1-x)}]O_4$. From this formula, we can write the equation for the theoretical value of μ as a function of the stoichiometric coefficient x.

$$\mu = 1 + 8x \quad [\mu_B]$$

From our experimental value of M_S (46,9 emu/g), we can calculate the experimental value of 2,01 μ_B per formula unit, which corresponds to $x = 0.13$. Therefore, the formula of our copper ferrite can be written as $(Fe_{0,87}Cu_{0,13})[Fe_{1,13}Cu_{0,87}]O_4$.

The temperature of the Curie point for $CuFe_2O_4$ is 728 K [10], but the coercive field is very low due to a low value of magnetocrystalline anisotropy of copper ferrite. The loops are very compact. Thus, the question whether the corresponding particles in the sample are in the superparamagnetic or ferromagnetic state cannot be answered by magnetization measurements alone. Mössbauer spectra measurements must also be taken into account. From these spectra, we can see that the samples annealed at 800 and 900 °C (with corresponding mean particle size of 7 and 9 nm) are superparamagnetic at room temperature, while the ones annealed at 1000 and 1100 °C (with corresponding mean particle size of 15 and 130 nm, respectively) are predominantly ferrimagnetic.

From HRTEM observations, the sample annealed at 1100 °C contains particles with a mean size of 130 nm, which is a very high value compared to other spinel ferrites in the silica matrix that were prepared in the past [7, 8]. The characteristic values of the particle size for this annealing temperature in the case of Zn, Co, and Ni ferrites are about 10–15 nm. They are probably due to higher diffusion of the Cu^{2+} cation in the silica matrix.

5. Conclusions

$CuFe_2O_4/SiO_2$ nanocomposites were prepared by the sol-gel method and investigated using powder X-ray diffraction, HR TEM, magnetic measurements, and Mössbauer spectroscopy. The $CuFe_2O_4$ spinel phase, which is formed in the studied nanocomposite, is stable up to 1100 °C. The presence of Cu^{2+} cations significantly affects the crystallization of the amorphous silica matrix. Crystallization starts at 1000 °C and leads to a cristobalite phase without any amorphous phase at 1100 °C. Magnetic measurements revealed that the spinel structure of copper ferrite has a mixed-state character. The calculated saturation magnetic moment is consistent with an approximate distribution of Cu and Fe in the tetrahedral and octahedral positions corresponding to the formula $(Fe_{0,87}Cu_{0,13})[Fe_{1,13}Cu_{0,87}]O_4$.

Acknowledgements

This work was prepared with the financial support of a Grant from the Agency of Academy of Science, Czech Republic (KJB4032402) and Research Centrum Project of the AS CR no. LN00A028.

References

[1] TRONC E., Nuovo Cimento, 18 (1996), 163.
[2] NIZNANSKY D., VIART N., REHSPRINGER J.L., J. Sol-Gel Sci. Technol, 8 (1997), 615.
[3] NIZNANSKY D., REHSPRINGER J.L., DRILLON M., IEEE Trans. Magnetics, 30 (1994), 821.
[4] CANNAS C., GATTESCHI D., MUSINU A., CANNAS C., GATTESCHI D., MUSINU A., PICCALUGA G., SANGREGORIO C., J. Phys Chem. B, 102 (1998), 7721.
[5] DELMONTE F., MORALES M.P., LEVY D., DEL MONTE F., MORALES M.P., LEVY D., FERNANDEZ A., OCAÑA M., ROIG A., MOLINS E., O'GRADY K., SERNA C., Langmuir, 13 (1997), 3627.
[6] TRONC E., CHANÉAC C., JOLIVET J.P., J. Solid State Chem., 139 (1998), 93.
[7] HUTLOVA A., NIZNANSKY D., PLOCEK J., BURSIK J., REHSPRINGER J.L., J. Sol-Gel Sci. Technol., 26 (2003), 473.
[8] PLOCEK J., HUTLOVA A., NIZNANSKY D., BURSIK J., REHSPRINGER J.L., MICKA Z., J. Non-Cryst. Solids, 315 (2003), 70.
[9] ICDD-JCPDS #25-0283
[10] SCHIEBER M.M., [in:] *Experimental Magnetochemistry Nonmetallic Magnetic Materials*, E.P. Wolfhart (Ed.), North-Holland Publ., Amsterdam, 1967.
[11] KRUPICKA S., *Fyzika feritu*, Academia, Prague, 1969.

Received 26 January 2005
Revised 23 March 2005

Materials Science-Poland, Vol. 23, No. 3, 2005

Electrical and optical studies on thin films of indium phthalocyanine chloride

S. MAMMEN*, C.S. MENON, N.V. UNNIKRISHNAN

School of Pure and Applied Physics, Mahatma Gandhi University, Kottayam 686 560, Kerala, India

Vacuum evaporated thin films of indium phthalocyanine chloride were prepared at room temperature. Post-evaporation annealing was done at 353, 403, 453, and 503 K. The electrical conductivities and optical absorption spectra of these films were studied. From the optical absorption spectra over a wavelength range of 200–900 nm, the optical energy band gap E_g was calculated. A decrease in E_g is observed with increasing annealing temperature. The thermal activation energy E_a is not notably affected by annealing. It is found that E_a varies with changing thickness of the film.

Key words: *phthalocyanine; activation energy; optical band gap; annealing*

1. Introduction

In the field of organic dyes and pigments, the materials considered to be most important are the phthalocyanines (Pcs). These materials are generally p-type semiconductors and have the advantage of being sufficiently stable towards chemical and thermal treatment. They can easily be vacuum deposited, resulting in high purity thin films without decomposition. Phthalocyanines are of interest in the fabrication of electronic molecular devices such as opto-electronic devices [1], gas sensors [2, 3], static induction transistors [4–6], and photoreceptor devices in laser beam printers and photocopiers [7]. Electrical, optical, and structural properties of phthalocyanine thin films are dependent on various parameters, such as evaporation rate, substrate temperature, and post-deposition annealing [8, 9]. Among various phthalocyanines, indium phthalocyanine chloride (InPcCl) has received considerably less attention. In the present study, we report on the electrical and optical properties of as-deposited and annealed InPcCl thin films.

*Corresponding author, e-mail: masabe@rediffmail.com

2. Experimental

Indium phthalocyanine chloride, procured from Aldrich Chemicals (USA), was purified by the train-sublimation technique using nitrogen gas as the carrier [10] and was used as the source material for thermal evaporation. Thin films of InPcCl were prepared on a glass substrate using a Hind Hivac 12A4 evaporation plant. Glass slides with dimensions of 7.5×2.5×1.3 mm^3 were used as substrates. Evaporation of the material was done at a base pressure of 10^{-5} Torr using a molybdenum boat. The deposition rate was controlled at 10–13 nm per minute. Surface samples 2 mm in breadth were used for the study. InPcCl thin films 230±5 nm thick were annealed in air for 1 h at 353, 403, 453, and 503 K in a furnace with a temperature controlled by a controller with recorder. Vacuum deposited silver, with an inter-electrode distance of 1 cm, was used for the contact electrodes. Electrical conductivity measurements were performed using a programmable Keithley electrometer model No. 617, in the temperature range of 303–548 K. To avoid any possible contamination, measurements were performed in vacuum at 10^{-3} Torr. Since phthalocyanines are photosensitive [11], the measurements were done in darkness. The thickness of the films was measured using Tolansky's multiple beam interference technique [12]. The absorption spectra of InPcCl thin films were recorded using a Shimadzu 160A spectrophotometer.

3. Results and discussion

3.1. Electrical conductivity studies

The electrical conductivity σ can be expressed as:

$$\sigma = \sigma_0 \exp\left(-\frac{E_a}{kT}\right) \tag{1}$$

where σ is the conductivity at temperature T, E_a is the thermal activation energy, k is the Boltzmann constant, and σ_0 is a pre-exponential factor. A plot of $\ln\sigma$ vs. (1000/T) yields a straight line, whose slope can be used to determine the thermal activation energy of the film. Figure 1 gives the plot of ln σ vs. (1000/T) for InPcCl thin films with thicknesses of 880, 595, 304, and 196 nm. There are three linear regions for each graph, corresponding to three activation energies, E_1, E_2, and E_3. Three activation energies for thin films of NiPc, $Eu(Pc)_2$, and H_2Pc have already been reported [13–15]. The thermal activation energy E_1 is associated with an intrinsic generation process, i.e. the resonant energy involved with a short-lived excited state. E_2 and E_3 are associated with impurity conduction, i.e. short-lived charge transfer forms between the impurity molecule and the host in which the supply of energy detaches the electron from the phthalocyanine complex [16].

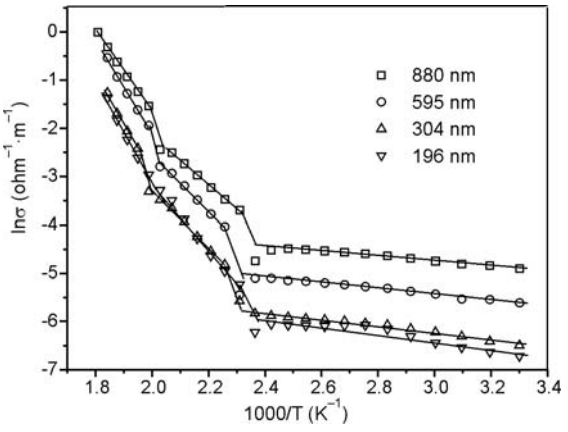

Fig. 1. Plot of $\ln\sigma$ vs. (1000/T) for InPcCl thin films of various thicknesses deposited at room temperature

In some cases, however, impurities can be traps as well. A change in the slope, and hence the activation energy, is interpreted as a change from extrinsic to intrinsic conduction [17], which adds support for the present result. The activation energies E_1, E_2, and E_3 are collected in Table 1. The calculated error in the determination of activation energy is ±0.01eV. It is seen that as thickness increases, the activation energy E_1 decreases. This lowering of activation energy is probably influenced by the structure of the film and therefore by the distribution of electronic tail states. A similar behaviour has been reported for $Eu(Pc)_2$ and H_2Pc thin films [14, 15].

Table1. Activation energy of InPcCl thin films of various thicknesses deposited at room temperature

Thickness	Activation energy (eV)		
	E_1	E_2	E_3
880 nm	0.73	0.44	0.05
595 nm	0.82	0.51	0.05
304 nm	0.92	0.49	0.06
196 nm	0.99	0.59	0.07

Figure 2 shows the plot of ln σ vs. (1000/T) for InPcCl thin films annealed at 353, 403, 453, and 503 K. For each sample there are three activation energies, E_1, E_2, and E_3. The three activation energies for InPcCl thin films annealed at 353, 403, 453, and 503 K are determined and collected in Table 2. It is seen that the intrinsic activation energy E_1 increases with increasing annealing temperature. This can be attributed to better film ordering due to annealing. A similar behaviour of activation energy has been observed for NiPc, MgPc, and CoPc thin films [13, 18, 19]. Variation in the

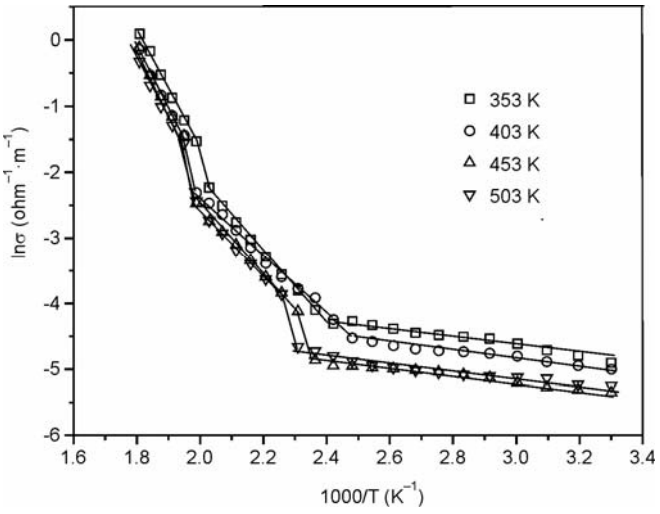

Fig. 2. Plot of $\ln\sigma$ vs. (1000/T) for InPcCl thin films annealed in air at various temperatures

Table 2. Activation energy of InPcCl (of thickness 230±5 nm) thin films annealed at various temperatures

Annealing temperature	Activation energy (eV)		
	E_1	E_2	E_3
353 K	0.76	0.45	0.04
403 K	0.79	0.42	0.05
453 K	0.79	0.46	0.06
503 K	0.81	0.46	0.06

extrinsic activation energies of InPcCl thin films during annealing can be attributed to the distribution of trap levels [20].

3.2. Optical studies

The UV visible spectrum observed for phthalocyanines originates from the molecular orbitals within the aromatic 18π electron system and from overlapping orbitals on the central metal atom [21]. The direct electronic transition from π to π* orbitals in the 300–450 nm range results in an intense band called the Soret band (B-band). The absorption edge of this peak can be related to fundamental absorption from which the energy band gap is obtained [22]. The fundamental absorption edge is analysed within the one electron theory of Bardeen et al. [23], and the absorption coefficient α is calculated from the spectra shown in Fig. 3. The coefficient α is related to the photon energy $h\nu$ by the relation

$$\alpha = \alpha_0 (h\nu - E_g)^{1/2} \tag{2}$$

for direct allowed transitions, E_g being the optical band gap and α_0 a constant.

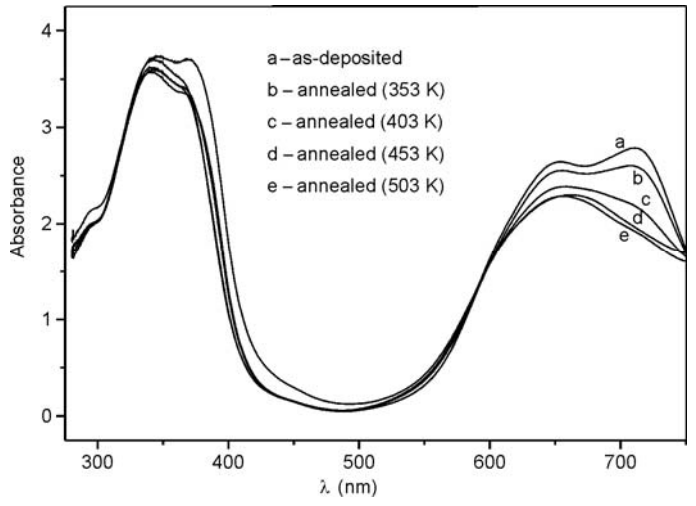

Fig. 3. Optical absorption spectra of InPcCl thin films: as-deposited and annealed in air at various temperatures

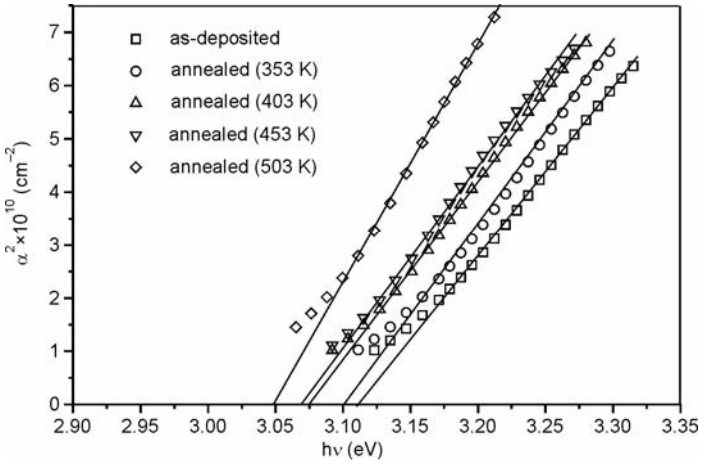

Fig. 4. Plot of α^2 vs. $h\nu$ for InPcCl thin films: as-deposited and annealed in air at different temperatures

Plots of α^2 vs. $h\nu$ near the absorption edge for as-deposited InPcCl thin films and films annealed in air at 353, 403, 453, and 503 K are shown in Fig. 4. A satisfactory straight line fit is obtained for α^2 as a function of $h\nu$, showing the existence of a direct gap. Extrapolation of the straight-line graphs to $\alpha^2 = 0$ gives the value of optical band gap. The band gaps obtained for InPcCl are given in Table 3. Any crystal phase

Table 3. Optical band gap of InPcCl as-deposited thin film and films annealed at different temperatures

Annealing temperature	Optical band gap E_g (eV)
353 K	3.10
403 K	3.08
453 K	3.07
503 K	3.05
As-deposited	3.11

change would affect the gap between the conduction band and valence bands in phthalocyanines, because the orbital overlap between parallel pairs of molecules will be affected [24]. The notable change in the optical band gap E_g for the film annealed at 503 K can be attributed to this.

4. Conclusions

The annealing of InPcCl thin film alters the activation energy for electrical conduction and the optical band gap. Also, by careful monitoring thickness during deposition, films having a desired activation energy can be made, which can help optimise properties of molecular electronic devices fabricated using InPcCl thin films.

Acknowledgments

One of the authors, MS, acknowledges the University Grants commission of India for providing a teacher fellowship under the FIP scheme.

References

[1] GHOSH A.K., MOREL D.L., FENG T., SHAW R.F., ROWE C.A. Jr., J. Appl. Phys., 45 (1974), 230.
[2] HAMANN C., MRWA A., MULLER M., GOPEL W., RAGER M., Sens. Actuat., B4 (1991), 73.
[3] WILSON A., WRIGHT J.D., CHADWICK A.V., Sens. Actuat., B4 (1991), 499.
[4] JOSEPH C.M., MENON C.S., Mater. Lett., 52 (2002), 220.
[5] JOSEPH C.M., NARAYANAN UNNI K.N., MENON C.S., Mater. Lett., 50 (2001), 18.
[6] KUDO K., IIZUKA M., KUNIYOSHI S., TANAKA K., Thin Solid Films, 393 (2001), 362.
[7] BORSENBERGER P.M., WEISS D.S., *Organic Photoreceptors for Imaging Systems*, Marcel Dekker, New York, 1993.
[8] COLLINS R.A., BELGACHI A., Mater. Lett., 9 (1989), 349.
[9] COLLINS R.A., STRICKLAND K.R., JEFFERY M.J., DAVISON K., JONES T.A., Mater. Lett., 10 (1990), 170.
[10] RIAD A.S., Physica B, 270 (1999), 148.
[11] ABDEL-MALIK T.G., ALY A.A., ABDEEN A.M., EL-LABANY H.M., Phys. Status Sol. A, 76 (1983), 651.
[12] MAISSEL L.I., GLANG R., *Handbook of Thin Film Technology*, McGraw-Hill, New York, 1985.
[13] NARAYANAN UNNI K.N., MENON C.S., Mater. Lett., 45 (2000), 326.
[14] NARAYANAN UNNI K.N., MENON C.S., J. Mater. Sci. Lett., 20 (2001), 1203.
[15] NARAYANAN UNNI K.N., MENON C.S., J. Mater. Sci. Lett., 20 (2001), 1207.
[16] GUTMANN F., LYONS L.E., *Organic Semiconductors*, Wiley, New York, 1967, p. 509.

[17] AMBILY S., MENON C.S., Thin Solid Films, 347 (1999), 284.
[18] KRISHNAKUMAR K.P., MENON C.S., Indian J. Pure Appl. Phys., 36 (1998), 342.
[19] AMBILY S., MENON C.S., Indian J. Pure Appl. Phys., 37 (1999), 566.
[20] SUSSMAN A., J. Appl. Phys., 38 (1967), 2748.
[21] OUGH E.A., STILLMAN J.M., Can. J. Chem., 71 (1993), 1891.
[22] COLLINS R.A., KRIER A., ABASS A.K., Thin Solid Films, 229 (1993), 113.
[23] BARDEEN J., SLATT F.J., HALL L.T., *Photoconductivity Conf.*, Wiley, New York, 1965.
[24] HARRISON S. E., ASSOUR J.M., J. Chem. Phys., 40 (1964), 365.

Received 7 March 2005
Revised 28 May 2005

Materials Science-Poland, Vol. 23, No. 3, 2005

Study of copper sulfide layers on a polyamide film formed by the use of higher polythionic acids

V. JANICKIS*, R. MACIULEVIČIUS, R. IVANAUSKAS, I. ANCUTIENĖ

Department of Inorganic Chemistry, Kaunas University of Technology,
Radvilėnų 19, LT-50254 Kaunas-9, Lithuania

Cu_xS layers on polyamide obtained by a sorption-diffusion method have been studied. These layers are formed when ions of higher polythionates and sulfur sorbed into polyamide react with a solution of Cu(I–II) salt. By potentiometric studies it has been determined that x varies in the interval $1 < x < 2$ in electrically conductive or semiconductive copper sulfide layers. The composition of the Cu_xS layer changes more significantly during the first 30 days in the direction of x decreasing. X-ray diffraction studies of the Cu_xS layers revealed six phases: with $x = 2$ (chalcocite), $x = 1.9375$ (djurleite), $x = 1.75$ (anilite), $x = 1.12$ (yarrowite), $x = 1.06$ (talnakhite), and $x = 1$ (covellite). The phase composition of the Cu_xS layer depends on the period of keeping in Cu(I–II) salt solution and on the sulfur concentration in the polyamide.

Key words: *polyamide; polythionic acid; sulfurisation; layer of copper sulfide*

1. Introduction

Semiconductive and electrically conductive composites have been widely studied and used in various fields of modern technology. Polyamides (PAs) with layers of copper sulfides belong to this group of composites. These modified polymers may be used as conductive substrates for the deposition of metal [1–3], as semiconductors [1, 4], gas sensors functioning at temperatures tending to room temperature [5, 6], as polarizers of infrared radiation [7] or solar absorber coatings [8].

Copper sulfide films are formed mainly in two ways: by treating a polymer containing an absorbed sulfurisation agent with a solution of a metal salt or by the sulfurisation of metal compounds absorbed in a polymer. Various solutions can serve as agents for the sulfurisation of polymers, e.g. sodium polysulfide (Na_2S_n, $n = 4.8$) aqueous solutions [9], polythionic acid ($H_2S_nO_6$, $n = 9$–45) aqueous solutions [10]. Hydrophobic polymers adsorb elemental sulfur from Na_2S_n [11] or $H_2S_nO_6$ [10] solu-

*Corresponding author, e-mail: Vitalijus.Janickis@ktu.lt

tions. Hydrophilic and semi-hydrophilic polymers, including PA are capable of absorbing ions of various electrolytes from aqueous solutions [12]. Therefore, PA absorbs polysulfide ions from sodium polysulfide solution [13] and polythionate ions from polythionic acid solution [14]. Unfortunately, a solution of polysulfide is highly alkaline at high concentrations (about 2 mol/dm^3), therefore this agent is suitable only for the sulfurisation of alkali–resistant polymers.

In this study, layers of copper sulfide on PA were obtained by the sorption –diffusion method developed by us [15], using 2 mmol/dm^3 solutions of polythionic acids. Copper sulfide layers on PA are formed via heterogeneous chemical reactions [16]:

$$S_nO_6^{2-} + 2Cu^+ + 2H_2O \rightarrow Cu_2S + (n-3)S + 2H_2SO_4 \quad (1)$$

$$2xCu^+ + 1/8S_8 \rightarrow Cu_xS + xCu^{2+} \quad (2)$$

Molecules of elemental sulfur in PA are formed [14] as a result of the known decomposition [17] of higher polythionic acids:

$$H_2S_nO_6 \rightarrow H_2S_{n-x}O_6 + xS \quad (3)$$

The rate of decomposition at elevated temperatures is significantly higher than at room temperature.

In the first stage of the process, the ions of higher polythionates diffuse into PA when it is kept in a solution of higher polythionic acid ($H_2S_nO_6$, n = 9–45) [14, 16]. In the second stage, sulfurised PA is treated with a solution of Cu(II) sulfate containing hydroquinone as the reducing agent [15, 16].

The usefulness of composites obtained by modifying polymers with layers of copper sulfide is determined by their electrical properties, which vary significantly even when the chemical composition is only slightly changed [9, 18]. The electrical resistance itself increases over 6 times when the value of x in Cu_xS is increased from 1 to 2 [19]. Therefore, electrical measurements enable preliminary information about the composition of the layer to be obtained. The composition can be more precisely determined by X-ray diffraction studies.

The aim of the present work was to study the phase composition of copper sulfide in PA formed by the sorption-diffusion method, using highly sulfurised $H_2S_nO_6$ (n = 21–33), on the basis of potentiometric measurements and X-ray diffraction analysis.

2. Experimental

The layers of copper sulfide were deposited on a PA PK-4 (specification TY 6-05 -1775-76) film 70 μm thick. Samples 15×70 mm^2 in size were used. The samples were boiled before sulfurisation in distilled water for 2 h in order to remove the remainder

of the monomer. Then they were dried using filter paper and subsequently over $CaCl_2$ for 24 h [14].

PA samples were exposed to a solution of polythionic acid. The average number of sulfur atoms n in a molecule of $H_2S_nO_6$ was established by the methods described in Ref. [20]. PA was treated in a thermostatic vessel, using a continually stirred $H_2S_nO_6$ solution. Polythionate ions, $-O_3S-S_n^{2-}-SO_3^-$, i.e. the anionic particles containing the chains of divalent sulfur atoms [21], were incorporated into PA. Then the samples were removed, rinsed with distilled water, dried over $CaCl_2$, analyzed, and then used in further experiments.

Samples of sulfurised PA were treated with the solution of a mixture of univalent and divalent copper salts (Cu(I–II) salt, containing 0.34 mol/dm^3 of Cu(II) salt and 0.06 mol/dm^3 of Cu(I) salt) prepared from crystalline $CuSO_4 \cdot 5H_2O$ and hydroquinone [16, 22]. Then they were rinsed with distilled water and dried over $CaCl_2$. The amount of sulfur in PA samples was determined by the amount of iodine used for the complete oxidation of polythionates diffused into PA [23]. The amount of copper in PA samples was determined by AAS [24].

The electrode potentials of PA films with Cu_xS layers were measured in the acidic solution of cupric sulfate by a universal EB-74 ionometer.

The phase composition of copper sulfide layers was investigated by X-ray diffraction using a DRON-6 diffractometer (CuK_α radiation). X-ray diffractograms of PA samples with layers of Cu_xS were analysed using the programs "Search Match", "ConvX", "Xfit", and "Microsoft Excel" to eliminate the maxima of PA.

3. Results and discussion

In our previous study [16], we found that the physical properties of PA films with deposited layers of Cu_xS, for instance their electrical conductivity, are determined by the concentration of sorbed sulfur in PA and by the treatment conditions of sulfurised PA in the solution of Cu(I–II) salt. Cu_xS is a p-type semiconductor, having hole conductivity. The most conductive sulfide layer is the one with the composition close to CuS [25]. CuS is distinguished among the binary (1:1) metal sulfides due to its mixed-valency and unique structure, which contains both monosulfides and disulfides. In CuS, the formal charge [26] of Cu is +1 and the average charge of S is –1. The Cu^{2+} ion is a relatively strong oxidizer, capable of oxidizing sulfide to a disulfide ion. During this process, the one missing *d*-electron (hole) of the d^9 configuration is transferred to the sulfur. Therefore, Cu is essentially monovalent in copper sulfides. In CuS, the electron deficiency (holes) in S is partially relieved by the formation of S–S bonds (for two-thirds of the S atoms) and partially delocalized through the p-band of S, which gives a formalism of $(Cu^+)_3(S_2^{2-})(S^-)$ or $(Cu^+)_3(S_2^-)(S^{2-})$. Thus, CuS exhibits an ideal metallic behaviour [27].

We have established [16] that at lower sorbed sulfur concentrations in PA, thin copper sulfide layers of low electrical conductance are formed. When the sulfur con-

centration is sufficient and the period of interaction with copper salt is rather short, more conductive layers are obtained, since their composition (according to the data of chemical analysis) differs significantly from that of Cu_2S. After keeping such sulfurised films in a solution of copper salt for a long time, copper ions diffusing into the sulfide layer change not only its thickness, but also its stoichiometric composition [16]. Simultaneously, these ions fill the vacancies in the copper lattice and increase the x value. The composition of layers approaches that of Cu_2S, and its conductivity decreases. Thus, having measured resistance, one can determine the surface layer composition. The approximate composition of copper sulfide layers can be estimated according to their electrode potentials. The aqueous electrochemical method is ideal for studying phase equilibria of binary sulfides, since stable and metastable assemblies can be differentiated and phase fields accurately delineated [28]. It is known [28] that the composition of copper sulfides can be estimated according to their electrode potentials in acidic $CuSO_4$ solution when the following reversible reaction takes place [29]:

$$Cu_xS \leftrightarrow Cu_{x-y}S + yCu^{2+} + 2ye \tag{4}$$

It has been pointed out that the potentials are practically independent of the composition of the electrolyte. The electrode potential was measured in the electrochemical cell Cu|aq. $CuSO_4 + H_2SO_4|Cu_xS$ [28].

When the value of x in copper sulfides increases, the electrode potential against copper over the temperature range of 0–105 °C decreases from 280 mV to 0 mV. The potential for low chalcocite was 0–125 mV, djurleite – 125–145 mV, anilite – 145–165 mV, covellite – 165–280 mV, sulfur – ≥280 mV [28]. The results of experiments [16, 30] show that the sulfide layer composition continued to change after 30 days following its formation.

Copper and sulfur form five solid phases stable at room temperature, two of which are stoichiometric, i.e. CuS (covellite) and Cu_2S (chalcocite), while the remaining three are non-stoichiometric: $Cu_{1.75}S$ (anilite), $Cu_{1.8}S$ (digenite) and $Cu_{1.95}S$ (djurleite). Copper and sulfur form also a number of mixed phases [31]. At 27 °C, the stable phases are CuS, $Cu_{1.75}S$, $Cu_{1.95}S$ and Cu_2S [32]. In the present study, all the measured potential values were less than 280 mV and greater than 0 mV. Consequently, by depositing the sulfide layers using the method of the sorption-diffusion, copper sulfide (Cu_xS) layers with x varying in the interval $1 < x < 2$ were obtained.

The potentials of Cu_xS layers on PA were measured 1 hour and 1, 10, 30, and 60 days after its formation. The results obtained show that the potentials of these layers are higher when PA is sulfurised in a solution of polythionic acid $H_2S_nO_6$ with a higher value of n for a longer time [14, 16] and at higher temperatures. Under these conditions, the polymer structure [30] undergoes the most intensive amorphization, resulting in more favorable conditions for the diffusion of sulfur compounds. In our opinion, there is a possibility of chemisorption of polythionic acids. In aquatic, neutral, and slightly acidic medium, polycaproamide functional groups (–COOH and $–NH_2$) are ionized, i.e. contain protonated amino ($-NH_3^+$) and carboxylic ($–COO^-$)

groups [33]. A variety of new effects become important insofar as the interactions of inorganic sorbates with PA are concerned, i.e. electrostatic interaction of $S_{n-2}(SO_3)^{2-}$ with the sorbent and exchange reactions of these ions with ligands previously bound to the polymer surface or their ionized functional groups.

Ionic strength of the solution and ionic competition also affect the sorption to charged sorbent groups, especially if inorganic ions compete for binding sites. The most probable mechanism for the other interaction involves chemical bonding of the charged sorbate ions $S_{n-2}(SO_3)^{2-}$ to the surface or to some functional groups of the solid phase. A surface reaction forms other sorbed species, different from inorganic ions dissolved in the proximity of the surface. A special role must also be attributed to the interaction of copper ions (Cu^{2+}, Cu^{+}) with the sorbed products. Sulfur, either as a free chalcogenide ion, or covalently bound to the amido group of PA, behaves as a very effective Lewis base towards many transition metals, e.g. iron, copper, zinc and molybdenum [34]. Potentiometer readings showed a decrease in the molar ratio Cu:S; i.e. the composition of Cu_xS changes in the direction of decreasing x with the increase of c_s in the polymer sulfide layer.

The results of our research show that copper ions only slightly diffuse into boiled PA. After 30 min of treatment in a solution of copper salt, the mass of non-sulfurised PA increases by 1–3%. X–ray structural tests of PA show [30] that the acidic medium as well as PA interaction with $S_nO_6^{2-}$ ions drastically changes the crystal structure of PA. Favorable conditions for the fast and easy diffusion of copper ions into PA are formed. This is proved by Cu:S molar ratios (Table 1) calculated after having kept the PA sample in $H_2S_nO_6$ and copper salt solutions. In our opinion, the molar ratios of the amounts of copper and sulfur in PA at the beginning were twice higher due to the adsorption of copper compounds onto the surface of the formed layer. The longer PA is kept in $H_2S_nO_6$ solutions the more the structure of PA changes and more $S_nO_6^{2-}$ ions diffuse, and, consequently, diffusion of copper ions through the sulfide layer is obstructed to a greater extent.

Table 1. Molar ratios of Cu/S in layers of copper sulfide*

Duration of treatment** (min)	4	6	10	15	20	30	60
Cu:S	2.62	2.10	2.10	1.59	1.71	1.46	1.18

*The duration of treatment with the solution of Cu(I–II) salt was 15 min

**With the solution of $H_2S_{21}O_6$

The change in potential with time shows that the composition of the Cu_xS layer changes in the direction of decreasing x. This change is particularly noticeable during the first 30 days, when the surface potentials grow on average by 15 mV. The measurements of the potential after 1, 2, and 3 months show that it does not change (Fig. 1).

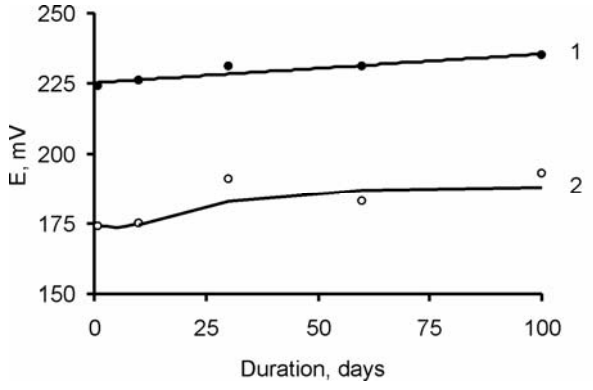

Fig. 1. The time dependences of the electrode potential of copper sulfide layers formed on PA. PA was treated with $H_2S_nO_6$ solution at 50 °C for 30 min. The average number of sulfur atoms in $H_2S_nO_6$ molecules, n: 1 – 33; 2 – 23

In this case, changes in the composition of the Cu_xS layer are caused by factors other than changes in the structure of PA. A small potential of the surface of Cu_xS layer in 1 hour after its formation shows that the composition of layers aproaches $Cu_{1.75}S$. These high values of x can be attributed to the agility of copper ions, slow stirring of copper salt solution, swelling of PA in highly sulfurised $H_2S_nO_6$ solutions, and to its more activated surface. In the course of time, however, due to the interaction of the copper sulfide layer with unreacted elemental sulfur and polythionate ions remaining in the polymer, the phase composition of the outer layer changes; x decreases and the potential increases. The following solid-phase reactions proceed:

$$(x - y)Cu_xS + yS \rightarrow xCu_{x-y}S \quad (5)$$

$$(x - y)Cu_xS + yS_nO_6^{2-} \rightarrow xCu_{x-y}S + yS_{n-1}O_6^{2-} \quad (6)$$

The stoichiometric composition of Cu_xS layers changes more significantly during the first 30 days (Fig. 1). Several phases of copper sulfides are metastable. Consequently, solid-state transformations take place: the metastable forms of copper sulfides may convert to the thermodynamically more stable ones. For example, after a few hours, the high digenite ($Cu_{1.805}S$) inexorably began to convert into the low digenite ($Cu_{1.765}S$), which, in turn, converts to anilite ($Cu_{1.750}S$) [28]. At 41 °C, anilite decomposes into CuS and low digenite, whereas low digenite transforms into high digenite around 82 °C [32].

The potential of the Cu_xS layer on PA depends on the time PA is kept in $H_2S_nO_6$ solution (Fig. 2). Up to 60 minutes in $H_2S_nO_6$ ($n = 33$) solution results in the prevalence of CuS with an average phase composition of $Cu_{1.75}S$. An interval of 60–120 min shows a marked increase in the potential, and the layer phase composition approaches CuS and remains almost stable.The Cu:S molar ratio, however, changes only by 0.03 after 60–120 min. Thus, after 2 hours the destruction of PA is high and the sulfide layer is

uniform enough not to obstruct the diffusion flow. This results in a Cu_xS layer possessing fewer copper-containing phases. Measurements of the potential after 30 days show that they changed more for PA soaked in $H_2S_nO_6$ solution for a shorter time (Fig. 2, curves 2 and 4). The potentials of PA soaked for longer times changed insignificantly. This proves that diffusion processes are faster in PA with a more destructed crystalline structure, due to a slighter blocking effect of the sulfide layer.

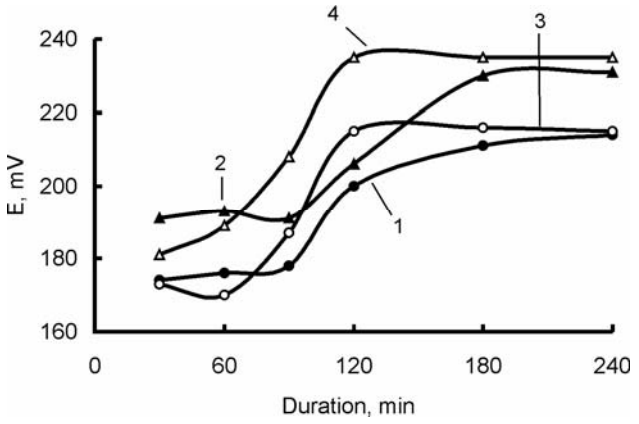

Fig. 2. The dependence of the electrode potential of copper sulfide layers formed on PA on the duration of treatment with a solution of $H_2S_nO_6$ at 50 °C. The average number of sulfur atoms in $H_2S_nO_6$ molecules, *n:* 1, 2 – 21; 3, 4 – 33. The electrode potentials were measured after: 1, 3 – 1 h; 2, 4 – 30 days

The potential of a Cu_xS layer on PA kept in $H_2S_nO_6$ for a shorter time changes in a different manner (Fig. 3).

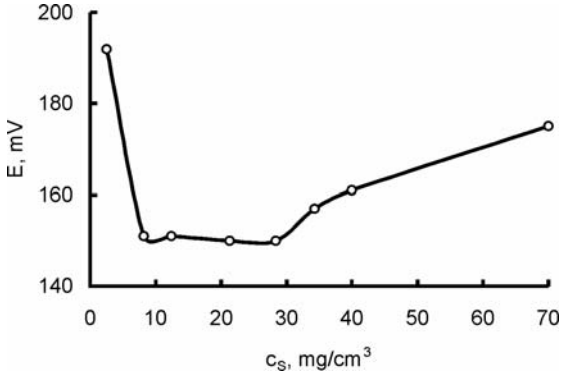

Fig. 3. The dependence of the electrode potential of copper sulfide layers formed on PA on the sulfur concentration in the polymer. PA samples were treated with the solution of $H_2S_{21}O_6$ at 50 °C. The duration of treatment with a solution of Cu (I–II) salt was 15 min

During the first 8 minutes, there is a sudden drop in the potential, followed by the stabilization of a phase for about 20 min. After this, the potential of the Cu_xS layer starts to slowly increase. This indicates that the Cu_xS layer is immediately formed on the polymer surface, its uniformity being higher if PA structure is less destroyed. Further changes in potential are related to changes in the phase composition, due to slow diffusion of copper ions through the sulfide layer as well as by its reaction with sulfur compounds in the deeper layers of a polymer.

While changing the interaction time of PA with copper salt solution, the potential of Cu_xS layers changes as well (Fig. 4). It can be noted that a sulfide layer with a predominant phase close to CuS forms on the polymer surface during the first 5 minutes of interaction with copper salt solution. It has not yet "blocked" the movement of the diffusion stream, therefore it takes 5 minutes of interaction for the uniformity of the layer to start growing and the value of x to reach ~1.75. After 12–15 minutes, a sufficiently compact layer is formed, significantly slowing copper ion diffusion into the bulk of the polymer, and the phase with $x = 1.75–1.95$ becomes predominant.

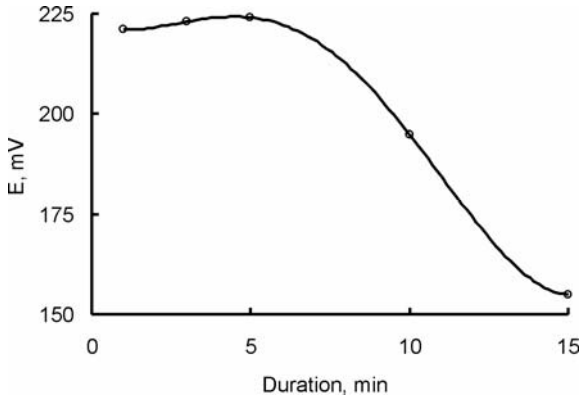

Fig. 4. The dependence of the electrode potential of copper sulfide layers formed on PA on the duration of treatment with a solution of Cu(I–II) salt at 78 °C. PA samples were treated with a solution of $H_2S_{21}O_6$ at of 50 °C. The concentration of sulfur in PA was 70.0 mg/cm^3

An increase of the temperature of $H_2S_nO_6$ solution influences the composition of Cu_xS layers slightly more at temperatures above 40 °C (Fig. 5); it does not depend significantly, however, on the number of sulfur atoms n in $H_2S_nO_6$ molecule.

Potentiometric tests of Cu_xS layers allow only a relative determination of the phase composition of the layer formed on the polymer surface. The value of potential highly depends on the number of copper ions absorbed in PA and on the degree of the polymer swelling resulting from a non-uniform sulfide layer. According to the data in [32], the potential of the $Cu_{2-x}S$ electrode in a solution of cupric salts is nearly always more positive than the potential of the Cu electrode under the same conditions, and the placement of both electrodes in the same cell containing Cu^{2+} ions should give the following reactions:

$$Cu(s) + Cu^{2+}(aq) \rightarrow 2Cu^{+} \quad (7)$$

$$Cu_{2-x}S(s) + 2yCu^{+} \rightarrow Cu_{2-x+y}S(s) + yCu^{2+}(aq) \quad (8)$$

The sulfide electrode should, hence, be continuously reduced and change its composition during an experiment. Therefore, X-ray phase tests were applied to specify the data on the phase composition of the sulfide layer.

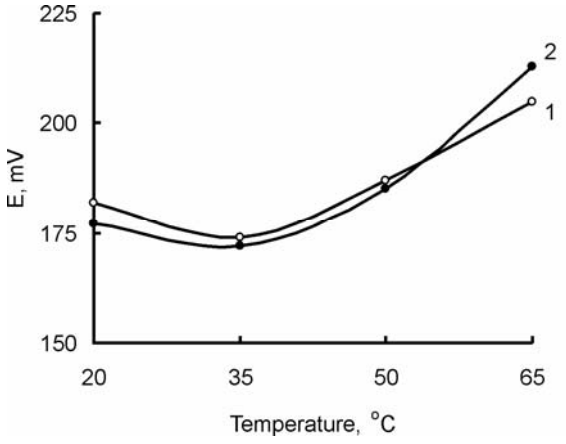

Fig. 5. The dependence of the electrode potential of copper sulfide layers formed on PA on the temperature of the $H_2S_nO_6$ solution. The average number of sulfur atoms in $H_2S_nO_6$ molecules, n: 1 – 21; 2 – 27

The phase composition of the deposited film was established by comparing its X-ray images with those of known minerals [35–37]. The chemical composition and crystal structure of the majority of Cu_xS minerals, such as chalcocite (Cu_2S), djurleite ($Cu_{1.95}S$), yarrowite ($Cu_{1.12}S$), and covellite (CuS) were investigated [38]. The crystal structure of Cu_xS depends on the chemical composition and conditions of synthesis. The composition of Cu_xS deposited by chemical methods has been scarcely investigated.

Structural studies of Cu_2S layers deposited by sorption-diffusion methods are limited by the polycrystallinity of the layers obtained, by the existence of Cu_xS phases with various compositions and structures, and by the crystallinity of the PA film itself. The intensities of its maximum at $\theta < 130°$ exceeds the intensity of copper sulfide maximum a few times. Therefore, the region of $2\theta \geq 26.0°$ was investigated in detail.

When keeping PA samples with the sorptive polythionate anions for different periods of time in copper salt solution at 78 °C, Cu_xS layers of different compositions we obtained. X-ray diffractograms of the layers showed the peaks of not one but various copper sulfide phases (Figs. 6 and 7).

The monoclinic djurleite ($Cu_{1.9375}S$) prevails (peaks at 2θ = 33.96, 35.30, 37.30, 38.41, 40.57, and 48.02°) in the composition of sulfide films on PA, initially sulfurised for 4 min (Fig. 6, curve 1) in $H_2S_{21}O_6$ solution at 50 °C (the time of the sulfurised PA treatment with Cu(I–II) salt solution was 15 min, the temperature of the

Cu(I–II) salt solution was 78 °C). Phases of orthorhombic anilite ($Cu_{1.75}S$) (peaks at $2\theta = 36.30$ and 46.02°) and chalcocite (Cu_2S) (peak at $2\theta = 49.01°$) are also present in the layers. When the time of treatment in the polythionic acid solution is prolonged to 10 min, changes in film composition occur: the intensity increases for the peaks at 2θ = 38.41, 40.57, and 48.02° of monoclinic djurleite and for the peak of orthorhombic anilite at $2\theta = 46.02°$. A new phase in the composition of the sulfide film on PA – a phase of hexagonal yarrowite ($Cu_{1.12}S$, peaks at $2\theta = 43.51$ and 47.12°) also appears. As soon as after 15 minutes of PA treatment in a solution of $H_2S_{21}O_6$, the orthorhombic anilite phase peaks at $2\theta = 34.73$, 36.30, 42.61, 46.02, 49.59, 50.17, and 50.72° predominate in the composition of sulfide layers (Fig. 6, curve 3).

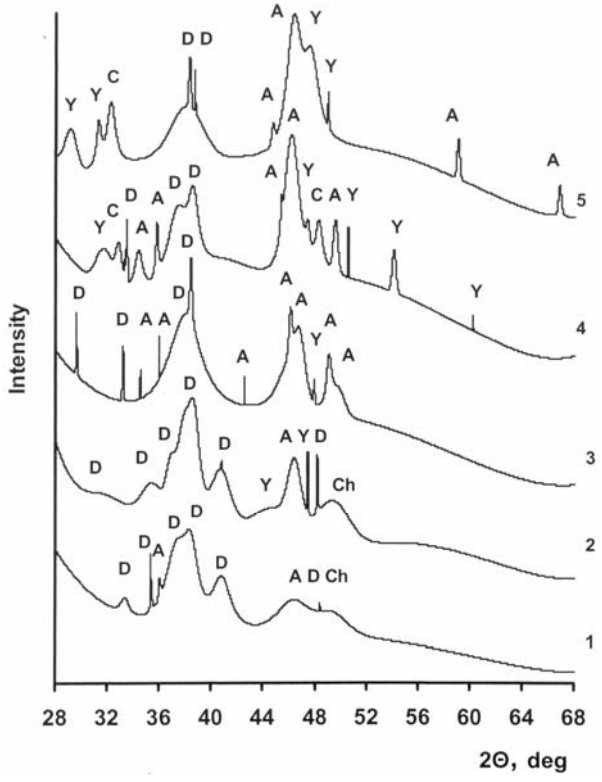

Fig. 6. X-ray diffraction patterns of layers of Cu_xS on PA (peaks of: D – djurleite, A – anilite, Ch – chalcocite, Y – yarrowite, C – covellite). PA was initially treated with a solution of $H_2S_{21}O_6$ at 50 °C for different times (τ_s, min) and subsequently with a Cu(I–II) salt solution for 15 min. The concentration of sulfur in the polymer c_s [mg/cm^3]: 1 – 2.5 ($\tau_s = 4$); 2 – 21.3 ($\tau_s = 10$); 3 – 28.4 ($\tau_s = 15$); 4 – 40.0 ($\tau_s = 30$); 5 – 70.0 ($\tau_s = 60$)

After 30 minutes of initial PA sulfurisation, new peaks at 2θ = 31.10, 50.64, 54.15, and 60.06° for hexagonal yarrowite (Fig. 6, curve 4) and peaks at $2\theta = 32.82$, 44.82, and 47.47° for hexagonal covellite (CuS) appear in the diffractograms. When

the time of treatment in $H_2S_21O_6$ solution is further prolonged, the hexagonal yarrowite and orthorhombic anilite phases become dominating in the sulfide layers on PA.

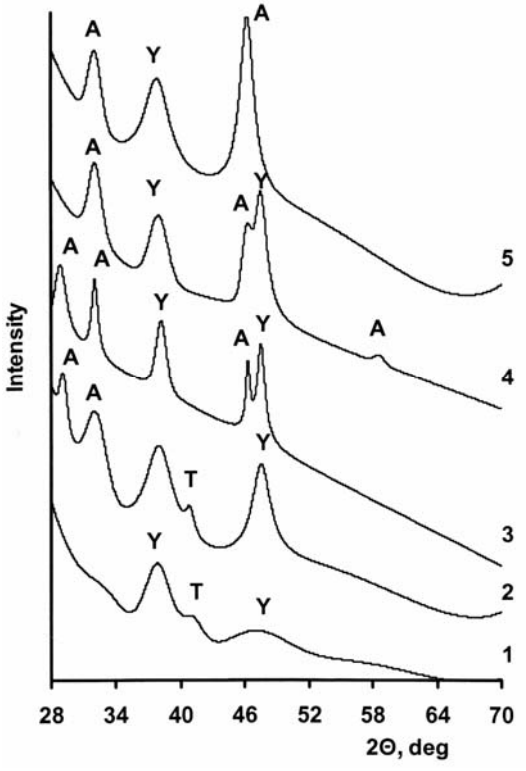

Fig. 7. X-ray diffraction patterns of layers of Cu_xS on PA (peak of: T – talnakhite, Y – yarrowite, A – anilite). The sulfur concentration in PA was 70.0 mg/cm^3. The period of treatment with a Cu(I–II) salt solution at 78 °C: 1 – 1 min; 2 – 3 min; 3 – 5 min; 4 – 10 min; 5 – 20 min

X-ray diffractograms of PA sulfurised under the same conditions ($H_2S_{21}O_6$, 50 °C, sulfur concentration in PA c_s = 70 mg/cm^3) and treated for various periods of time in the solution of Cu(I–II) salt at 78 °C are presented in Fig. 7. After 1-min treatment, peaks at 2θ = 38.4 and 47.7°, due to hexagonal yarrowite, and a negligible peak at 2θ = 40.6°, due to cubic talnakhite ($Cu_{1.06}S$), are noticeable (Fig. 7, curve 1). When the treatment time in the Cu(I–II) salt solution is prolonged (3 and 5 min), the intensities of the peaks of yarrowite increase and new peaks of orthorhombic anilite at 2θ = 29.1, 32.1, and 46.3° appear in the patterns (Fig. 7, curves 2 and 3). On further prolongation of the time of sulfurised PA treatment in Cu(I–II) salt solution (10 and 20 min), the intensities of the anilite peaks increase and those of the yarrowite peaks decrease (Fig. 7, curves 4 and 5). Consequently, when the concentration of sulfur in PA is the same and treatment time in Cu(I–II) salt solution is prolonged, the phase composition of the layer obtained becomes uniform. After 20 minutes, the anilite phase remains the

dominating phase in the sulfide layer. Hence, in the course of sulfurised PA treatment in Cu(I–II) salt solution, the phase composition of Cu_xS films changes in the direction of increasing x.

4. Conclusions

Cu_xS layers on polyamide (PA), obtained by the sorption-diffusion method using highly sulfured polythionic acids ($H_2S_nO_6$, n = 21–33) were studied. These layers are formed when ions of higher polythionates and sulfur sorb into polyamide and react with a solution of copper (I–II) salt. The approximate composition of copper sulfide layers on PA was determined on the basis of potentiometric measurements and X-ray diffraction analysis. It was determined by potentiometric studies that the value of x in the composition of copper sulfide layers varies in the interval $1 < x < 2$. The potential of copper sulfide layers increases with increasing sulfur concentration diffused into the polymer. Due to the interaction of the copper sulfide layer formed with unreacted elemental sulfur remaining in the polymer, the phase composition of the outer layer changes; the value of x decreases, resulting in an increase in the potential of the Cu_xS layer. The composition of Cu_xS layers changes more significantly during the first 30 days in the direction of decreasing x. By the X-ray diffraction studies it was determined that the Cu_xS layers obtained are composed of six phases, comprising monoclinic djurleite ($Cu_{1.9375}S$), orthorhombic anilite ($Cu_{1.75}S$), chalcocite (Cu_2S), cubic talnakhite ($Cu_{1.06}S$), hexagonal yarrowite ($Cu_{1.12}S$), and hexagonal covellite (CuS). The ratio between the concentrations of these phases depends on the duration of polyamide sulfurisation in a solution of polythionic acid and on the time of sulfurised polymer treatment with the copper (I–II) salt solution. Djurleite prevails in the composition of Cu_xS film if PA is sulfurised shortly (a few minutes) in a solution of $H_2S_nO_6$. When the duration of sulfurisation is prolonged, the maxima of djurleite slightly decrease and the maxima of anilite increase. On further prolongation, the phases of anilite and yarrowite become dominating. When polyamide sulfurised under the same conditions is shortly treated (few minutes) in a solution of copper(I–II) salt, the yarrowite, talnakhite, and anilite phases are detected. If treatment in the Cu(I–II) salt solution is prolonged, the formation of a sulfide phase containing more copper, namely anilite, is observed. Thus, in the course of sulfurised polyamide treatment with the solution of Cu(I–II) salt, the phase composition of Cu_xS film changes and x increases.

References

[1] CARDOSO J., GOMEZDAZA O., IXLILCO L., NAIR M.T.S, NAIR P.K., Semicond. Sci. Technol., 16 (2001), 123.
[2] HU H., NAIR P.K., Surface Coat. Technol., 81 (1996), 183.
[3] M*etallizing of Plastics – A Handbook of Theory and Practice*, R. Suchentrunk (Ed.), Finishing Publ., Stevenage, Herts, 1993.

[4] BHATTACHARYA R.N., WIESNER H., BERENS T.A., MATSON R.J., KEANE J., RAMANATHAN K.R., SWARTZLANDER A., MASON A., NOUFI R., J. Electrochem. Soc., 144 (1997), 1376.
[5] GALDIKAS A., MIRONAS A., STRAZDIENĖ V., ŠETKUS A., ANCUTIENĖ I., JANICKIS V., Sensors and Actuators B, 67 (2000), 76.
[6] ŠETKUS A., GALDIKAS A., MIRONAS A., ŠIMKIENĖ I., ANCUTIENĖ I., JANICKIS V., KAČIULIS S., MATTOGNO G., INGO G.M., Thin Solid Films, 391 (2001), 275.
[7] BARANAUSKAS M., ŽEBRAUSKAS A., USSR Patent 1331291 (1986).
[8] HU H., CAMPOS J., NAIR P.K., J. Mater. Res., 11 (1996), 739.
[9] ŽEBRAUSKAS A., Chemistry (Lithuania), 2 (1992), 112 (in Russian).
[10] ANCUTIENĖ I., JANICKIS V., Progr. Colloid. Polym. Sci., 116 (2000), 129.
[11] BARANAUSKAS M., ŽEBRAUSKAS A., ŠALKAUSKAS M.I., PROKOPČIKAS M., Trans. Lithuanian Acad. Sci. Ser B, 2 (1983), 3 (in Russian).
[12] ZAIKOV G.E., YORDANSKIY A.L., MARKIN V.S., *Diffusion Electrolytes into Polymers*, Khimia, Moscow, 1984 (in Russian).
[13] ŽEBRAUSKAS A., BARANAUSKAS M., Zh. Prikl. Khim., 62 (1989), 2773.
[14] MACIULEVIČIUS R., JANICKIS V., IVANAUSKAS R., Chemistry (Lithuania), 11 (2000), 141.
[15] MACIULEVIČIUS R., JANICKIS V., IVANAUSKAS R., Lithuanian Republic Patent LT 4402 B (1998).
[16] JANICKIS V., MACIULEVIČIUS R., IVANAUSKAS R., ANCUTIENĖ I., Colloid. Polym. Sci., 281 (2003), 84.
[17] GREVYS S., JANICKIS V., Proceedings of National Conference: Chemistry and Chemical Technology, Kaunas, 1975. p. 25 (in Lithuanian).
[18] ANCUTIENĖ I., JANICKIS V., Materials Science (Lithuania), 6 (2000), 275.
[19] ŽEBRAUSKAS A., Chemical Technology (Lithuania), 3 (1996), 39 (in Lithuanian).
[20] JANICKIS J., VALANČIŪNAS J., ZELIONKAITĖ V., JANICKIS V., GREVYS S., Trans. Lithuanian Acad. Sci. Ser. B (Lithuania), 88 (1975), 83 (in Russian).
[21] FOSS O., S*tructures of Compounds Containing Chains of Sulfur Atoms*, [in:] H.J. Emeleus and A.G. Sharpe (Eds.), *Advances in Inorganic Chemistry and Radiochemistry*, Academic Press, New York, 1960, p. 237.
[22] ANCUTIENĖ I., .JANICKIS V., GREVYS V., Chemistry (Lithuania), 2 (1997), 3.
[23] NORKUS P.K., ŠIMKEVIČIŪTĖ G.S., Zh. Analit. Khim., 26 (1971), 39 (in Russian).
[24] *Analytical methods for atomic absorption spectrometry Perkin-Elmer* 503, Perkin-Elmer, 1973.
[25] ORMONT B.F., *Compounds of Variable Composition*, Khimia, Leningrad, 1969 (in Russian).
[26] TAKEUCHI K., KUDOH Y., SATO G., Z. Kristallogr., 173 (1985), 119.
[27] ZHANG X., KANATZIDIS M.G., HOGAN T., KANNEWURF C.R., J. Am. Chem. Soc., 118 (1996), 693.
[28] POTTER II R.W., Economic Geology, 72 (1977), 1524.
[29] ŽEBRAUSKAS A., ŠATAITĖ J., BALTĖNIENĖ L., Chemistry (Lithuania), 2 (1991), 134 (in Russian).
[30] IVANAUSKAS R., JANICKIS V., MACIULEVIČIUS R., Chemical Technology (Lithuania), 13 (1999), 71 (in Lithuanian).
[31] JOHANSSON J., KOSTAMO J., KARPPINEN M., NIINSTÖ L., J. Mater. Chem., 12 (2002), 1022.
[32] STØLEN S., GRØNVOLD F., *Thermodynamic Properties of the CuS–Cu_2S system*, [in:] H. Brodowsky and H.J. Schaller (Eds.), *Thermochemistry of Alloys*, Academic Publishers, Kluwer, 1989, p. 213.
[33] DE GRUYTER W., *Concise Encyclopedia Chemistry*, Berlin, New York, 1994.
[34] MASSEY A.G., *Main Group Chemistry*, Wiley, New York, 2000.
[35] ŽEBRAUSKAS A., MIKALAUSKIENĖ A., LATVYS V., Chemistry (Lithuania), 2 (1992), 131 (in Russian).
[36] YAMAMOTO T., KAMIGAKI T., KUBOTA E., Kobunshi Ronbunshu (Japan. J. Polymer Sci. Technol.), 44 (1987), 327 (in Japanese).
[37] NOMURA R., KONAYO K., MATSUDA H., Ind. Eng. Chem. Res., 28 (1989), 877.
[38] GOBLE R., Canad. Mineral., 23 (1985), 61.

Received 7 March 2005
Revised 28 May 2005

Materials Science-Poland, Vol. 23, No. 3, 2005

Structure and magnetic behaviour of mononuclear and dinuclear Cu(II)/Zn(II) monocarboxylate-pyridine derivatives studied by crystal engineering

T. OHMURA, W. MORI*, T. TAKEI, T. IKEDA, A. MAEDA

Department of Chemistry; Faculty of Science, Kanagawa University,
2946 Tsuchiya, Hiratsuka 259-1293, Japan

Metal organic frameworks such as copper(II) monocarboxylate (formate and benzoate) pyridine derivatives and zinc(II) monocarboxylate (*p*-phenyl benzoate and benzoate) pyridine derivatives have been prepared. The complexes were synthesized at room temperature using pyridine or *p*-phenyl pyridine to grow single crystals, which were subsequently analyzed using single-crystal X-ray analysis. These structures are formed by hydrogen bonding and self-assembly by the π-stacking of mononuclear units. The magnetic susceptibilities of the copper(II) complexes obeyed the Curie–Weiss law over the range of 2–300 K. The Weiss constants θ indicated the existence of small antiferromagnetic interactions arising from the hydrogen bonding.

Key words: *mononuclear metal complex; single-crystal X-ray analysis; antiferromagnetic interaction*

1. Introduction

For many years metal organic frameworks were unknown and attempts were made to prepare them by using a variety of combinations of metal ions and organic ligands. In recent years, however, numerous significant advances in the design concepts of metal organic frameworks have been reported.

The transition metal carboxylates species are interesting due to their capabilities for gas storage, ion exchange, catalytic activity, etc. The syntheses and structures of transition metal carboxylates are also critically important for their properties and applications. Previously, we have reported that dinuclear copper(II) dicarboxylates [1], molybdenum(II) dicarboxylates [2], ruthenium(II) or (II, III) dicarboxylates [3], and rhodium(II) tetracarboxylate exhibit gas-occlusion properties and catalytic activity for the hydrogenation of ethylene and propene [4].

*Corresponding author, e-mail: moriw001@kanagawa-u.ac.jp

Recently, we have conducted crystal engineering on mononuclear Cu(II), Ni(II), and Zn(II) carboxylates-pyridine systems in order to obtain porous materials with a large number of cavities [5]. In the present study, we chose three sample mononuclear units: copper(II) formate-*p*-phenyl pyridine (**a**), copper(II) benzoate-pyridine (**b**), zinc(II) *p*-phenyl benzoate-pyridine (**c**), and one sample dinuclear unit, zinc(II) benzoate-pyridine (**d**), and we investigated their crystal structures and magnetic behaviours.

2. Experimental procedure

Materials and methods. Copper(II) formate tetrahydrate, Zn(II) nitrate hexahydrate, and benzoic acid were purchased from Wako Chemical Company. All other organic ligands were purchased from Tokyo Kasei Chemical Company and used as received without further purification. Elemental microanalyses of the complexes were conducted on crystalline samples using a Perkin-Elmer PE 2400 series II CHNS/O analyser. Thermogravimetric analysis was performed using TG8101D and TAS300 with an aluminium pan in an ordinary atmosphere, at the scan rate of 1 °C/min. The temperature dependence of the magnetic susceptibilities of the copper(II) complexes was measured by a Quantum Design MPMS-5S SQUID magnetometer in the temperature range of 2–300 K, at 5000 Oe.

Preparation of complexes. The synthetic methods used for the ligand exchange procedure were similar to those reported previously, obtaining single-crystal samples of the complexes [5]. Forms of mononuclear and dinuclear Cu(II)/Zn(II) monocarboxylate-pyridine derivatives were synthesized as follows.

Copper(II) formate-*p*-phenyl pyridine. A DMSO solution (40.0×10^{-3} dm^3) of *p*-phenyl pyridine (0.2751 g) was added to an aqueous solution (40.0×10^{-3} dm^3) of copper(II) formate tetrahydrate (0.2000 g). The mixture was then allowed to stand for several days at room temperature, after which it yielded deep blue, plate-like single crystals that were formulated as $Cu^{II}(O_2C{-}H)_2(C_6H_5{-}C_5H_4N)_2{\cdot}(H_2O)$ (**a**). Anal. calcd. for $C_{24}H_{22}N_2O_5Cu$: C, 59.81; H, 4.60; N, 5.81%. Found: C, 59.48; H, 4.46; N, 5.73%.

Copper(II) benzoate-pyridine. A pyridine solution (30.0×10^{-3} dm^3) of benzoic acid (0.0905 g) was added to an aqueous solution (10.0×10^{-3} dm^3) of copper(II) nitrate trihydrate (0.1500 g). The mixture was then allowed to stand for several days at room temperature, after which it yielded deep blue, plate-like single crystals that were formulated as $Cu^{II}(O_2C{-}C_6H_5)_2(C_5H_5N)_2{\cdot}(H_2O)$ (**b**). Anal. calcd. for $C_{24}H_{22}N_2O_5Cu$: C, 59.81; H, 4.60; N, 5.81%. Found: C, 60.73; H, 5.12; N, 5.23%.

Zinc(II) *p*-phenyl benzoate-pyridine. An aqueous solution (10.0×10^{-3} dm^3) of zinc(II) nitrate hexahydrate (0.0300 mg) was added to a pyridine solution (10.0×10^{-3} dm^3) of *p*-phenyl benzoic acid (0.0400 mg). The mixture was then allowed to stand for

several days at room temperature, after which it yielded colourless, plate-like single crystals that were formulated as $Zn^{II}(O_2C{-}C_6H_4{-}C_6H_5)_2(C_5H_5N)_2$ (**c**). Anal. calcd. for $C_{36}H_{28}N_2O_4Zn$: C, 69.96; H, 4.57; N, 4.53%. Found: C, 67.85; H, 4.77; N, 4.31%.

Zinc(II) benzoate-pyridine. An aqueous solution (10.0×10^{-3} dm^3) of zinc(II) nitrate hexahydrate (0.5000 mg) was added to a pyridine solution (10.0×10^{-3} dm^3) of benzoic acid (0.4100 mg). The mixture was then allowed to stand for several days at room temperature, after which it yielded colourless, plate-like single crystals that were formulated as $Zn_2^{II}(O_2C{-}C_6H_5)_4(C_5H_5N)_2]$ (**d**). Anal. calcd. for $C_{38}H_{30}N_2O_8Zn_2$: C, 59.01; H, 3.91; N, 3.62%. Found: C, 58.76; H, 3.42; N, 4.51%.

X-ray crystal structure determinations. The crystal structures of **a**, **b**, and **d** were determined by X-ray diffraction using a Rigaku R-AXIS RAPID diffractometer with graphite-monochromated MoK_α radiation. The crystal structure of **c** was determined by X-ray diffraction using a Rigaku CCD Mercury diffractometer with graphite -monochromated MoK_α radiation. The structures of all complexes were solved by a direct method using the program SIR-92 and were refined by full-matrix least -squares iterations. The non-hydrogen atoms (Cu, Zn, C, O, and N) were refined anisotropically. All the H atoms were idealized by using riding models, which were located in a difference Fourier map and then refined isotropically. No disorder was observed in any of the structures.

3. Results and discussion

3.1. X-ray single-crystal analysis

The use of pyridine as a solvent is satisfactory for crystallization. Introducing the concept of crystallization using pyridine and pyridine derivatives is very useful for understanding metal-organic structures. In this work, we have succeeded in the synthesis of mononuclear and dinuclear Cu(II)/Zn(II) monocarboxylate-pyridine derivatives. Crystallographic data and other pertinent information are summarized in Table 1.

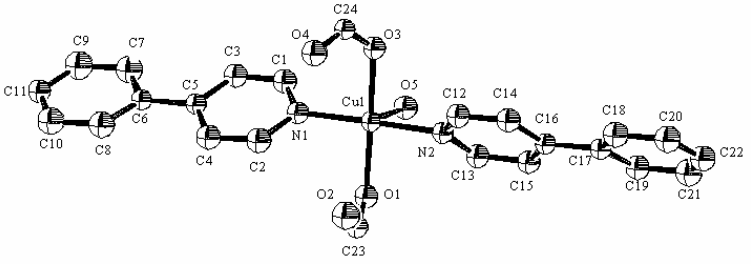

Fig. 1. ORTEP view of **a**, showing the numbering scheme (50% probability). The hydrogen atoms have been omitted for clarity

Table 1. Crystallographic data and structure refinement parameters for complexes **a–d**

Parameter	Compound			
	a	**b**	**c**	**d**
Chemical formula	$C_{24}H_{24}N_2O_5Cu$	$C_{12}H_{10}NO_{2.5}Cu_{0.5}$	$C_{36}H_{28}N_2O_4Zn$	$C_{19}H_{15}NO_4Zn$
Formula mass, Da	459.82	239.99	618.01	386.71
Crystal system	orthorombic	orthorombic	monoclinic	monoclinic
a, Å	5.757	15.651(3)	9.5397(5)	9.663(4)
b, Å	15.165	45.697(7)	10.5192(5)	10.450(3)
c, Å	24.151	5.973(1)	29.201(2)	17.363(6)
α, deg	90	90	90	90
β, deg	90	90	96.4334(7)	98.67(2)
γ, deg	90	90	90	90
V, Å^3	2108.63	4272.1(1)	2911.9(3)	1733.4(1)
ρ_{calcd}, g/cm^3	1.45	1.492	1.410	1.482
T, K	123	143	143	143
R[a]	0.074	0.072	0.040	0.034
Rw	0.213[b]	0.083[b]	0.054[b]	0.040[c]
Z	4	16	4	4
μ, cm^{-1}	10.73	10.618	8.877	14.397

[a] $R = \Sigma||F_0| - |F_C||/\Sigma|F_0|$. [b] $Rw = [\Sigma w(|F_0| - |F_C|)^2/\Sigma wF_0^2]^{1/2}$. [c] $Rw = [\Sigma(w(F_0^2 - F_C^2)^2/\Sigma(F_0^2)^2]^{1/2}$.

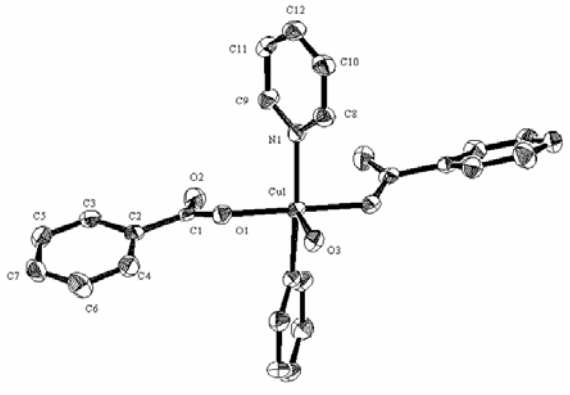

Fig. 2. ORTEP view of **b**, showing the numbering scheme (50% probability). The hydrogen atoms have been omitted for clarity

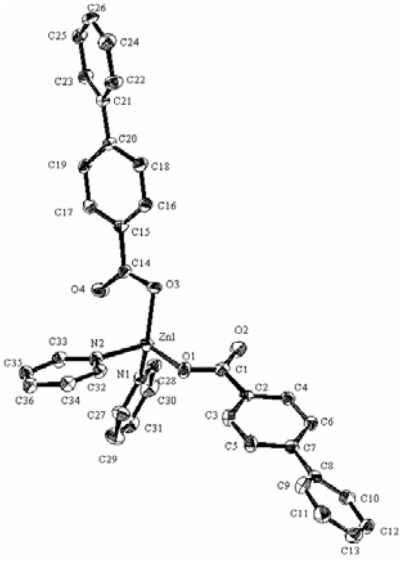

Fig. 3. ORTEP view of **c**, showing the numbering scheme (50% probability). The hydrogen atoms have been omitted for clarity

In Figures 1–4, we present ORTEP drawings of the unit containing Cu and Zn atoms and all attached atoms for each structure. The atomic numbering scheme for the

species is defined in each figure. In the process of crystallization, the intermolecular interaction between the aromatic rings of the ligands (carboxylate or pyridine), the so-called π-π stack, might act as a driving force for the self-assembly of the mononuclear or dinuclear units by suspending no guest molecules.

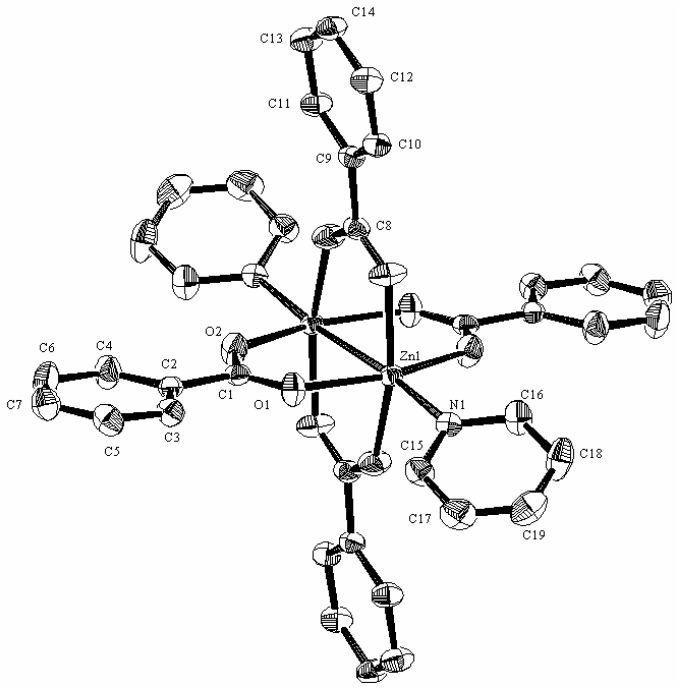

Fig. 4. ORTEP view of **d**, showing the numbering scheme (50% probability)

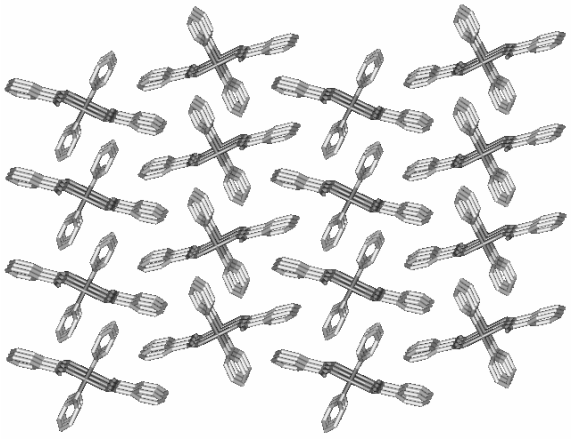

Fig. 5. Structural features of **b** using the Rigaku/MSC program package. The chain complex consisting of hydrogen bonding between Cu(II) ions effectively bridged between the carboxyl substituents and coordinated water molecules, forming a one-dimensional chain. For clarity, the hydrogen atoms have been omitted

Mononuclear copper(II) monocarboxylates have a regular one-dimensional structure with hydrogen bonding, clearly characterized by X-ray crystallography. Hydrogen bonding occurs between one mononuclear unit and adjacent mononuclear units through the O atoms of the carboxylate groups and coordinated water molecules, increasing the structural dimensionality. Figure 5 shows the packing diagram of **b**. These structures are one-dimensional ones, very similar to those of mononuclear copper(II) terephthalate-pyridine derivatives [5].

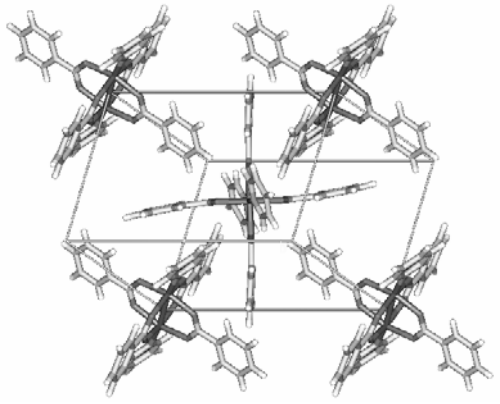

Fig. 6. Packing diagram view of **d**, using the Rigaku/MSC program package. For clarity, the hydrogen atoms have been omitted

In contrast to the copper(II) complexes, the crystal structures of **c** and **d** contain no coordinated water molecules and, thus, no water hydrogen bonding. These structures are simply constructed by the intermolecular interactions between one mononuclear or dinuclear unit and the surrounding mononuclear or dinuclear units, as shown in Fig. 6. In preparation of **d**, the dinuclear Zn(II) complex (but not the mononuclear Zn(II) complex) was nevertheless synthesized by a similar procedure. This result is attributable to a slight difference of pH value in the reaction solvent when using a different organic ligand.

3.2. Stability of complexes

TG-DTA analysis shows that the coordinated solvent is eliminated from the network as temperature rises. When the coordinated solvents are released, the colour of **a** and **b** changes from deep blue to pale blue [5]. Similarly, the colour of **c** and **d** changes from colourless to white. These networks are stable during the initial weight loss of the coordinated solvent, whereas they are not stable during the loss of coordinated molecules (pyridine and/or water) from these frameworks [5].

3.3. Magnetic properties

The magnetic susceptibilities of mononuclear copper(II) carboxylate-pyridine derivatives with linear chains of hydrogen bonds obey the Curie-Weiss law; the obtained Weiss

constants indicate ferromagnetic or antiferromagnetic interactions. We have clarified the paramagnetic properties of the mononuclear copper(II) monocarboxylate-pyridine derivatives by magnetic measurements. The complexes **a** and **b** exhibit small antiferromagnetic interactions ($\theta = -0.74$ K for **a** and $\theta = -0.44$ K for **b**), albeit much weaker. The temperature dependence of the magnetic susceptibility for **b** is shown in Fig. 7. In addition, the magnetic properties for similar systems, mononuclear copper(II) dicarboxylate-pyridines, have been reported – small antiferromagnetic interactions and ferromagnetic interactions through hydrogen-bonded pathways in [Cu(II)(μ-O_2C–C_6H_4–CO_2)(C_5H_5N)$_2$(H_2O)]·py·H_2O ($\theta = -1.4$ K) [5], [Cu(II)(μ-O_2C–C_6H_4–CO_2)(p-C_6H_5–C_5H_4N)$_2$(H_2O)]·2MeOH ($\theta = 5.5$ K) [5], and [Cu(II)(μ-O_2C–C_6H_4–Br)(C_5H_5N)$_2$(H_2O)] ($\theta = 9.0$ K) [6]. In these complexes, in which one copper(II) ion is linked by hydrogen bonding between two bridging carboxylate groups and one coordinated water molecule, two pathways are provided for super exchange interaction between the copper(II) ions.

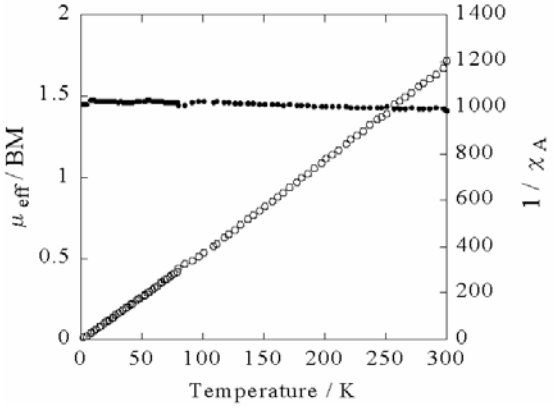

Fig. 7. Temperature dependence of the effective magnetic moment (●) and magnetic susceptibility (○) of **b**

These results suggest that ferromagnetic and antiferromagnetic interactions play an important role in determining bridge geometries and super-exchange interactions between copper(II) ions through Cu–O–C–O–H–O–Cu pathways [5]. In contrast, the magnetic behaviour of mononuclear copper(II) tetracarboxylate-pyridine (CuTCPPpy), in which no hydrogen bonding exists, is scarcely affected by the magnetic interaction between copper(II) ions [7].

4. Conclusions

We have synthesized three samples of mononuclear metal(II) monocarboxylate-pyridine derivatives: copper(II) formate-*p*-phenyl pyridine (**a**), copper(II) benzoate-pyridine (**b**), zinc(II) *p*-phenyl benzoate-pyridine (**c**), and one sample dinuclear zinc(II) monocarboxylate, zinc(II) benzoate-pyridine (**d**). The crystal structures and

magnetic behaviour of these samples were investigated. Copper(II) complexes, which are self-assembled by hydrogen bonding and the π-stacking of mononuclear units, form one-dimensional structures. The use of pyridine as a solvent simplified obtaining single crystals for mononuclear and dinuclear metal(II) carboxylates. Furthermore, we believe that it is possible to control the synthesis of mononuclear and dinuclear units for metal(II) carboxylates using different pH reaction solvents.

We have demonstrated the paramagnetic properties of **a** and **b**, as elucidated by magnetic measurements (SQUID), whereas **c** and **d** were found to be diamagnetic. The magnetic susceptibilities of **a** and **b** obeyed the Curie–Weiss law over the range of 2–300 K ($\theta = -0.74$ K for **a**, and $\theta = -0.44$ K for **b**). The Weiss constants θ indicated the existence of small antiferromagnetic interactions arising from the hydrogen bonding.

Compared to important industrial adsorbents, the system discovered in the present work is the simplest and most advantageous adsorbent for studies in pure and applied chemistry, because mononuclear copper(II) carboxylates-pyridine derivatives can be converted into special absorbents and exhibit large amounts of gas-occlusion properties with axial ligand exchange. That is the subject of further studies [8].

References

[1] MORI W., INOUE F., YOSHIDA K., NAKAYAMA H., TAKAMIZAWA S., KISHITA M., Chem. Lett., (1997), 1219.
[2] TAKAMIZAWA S., MORI W., FURIHATA M., TAKEDA S., YAMAGUCHI K., Inorg. Chim. Acta, 283 (1998), 268.
[3] TAKAMIZAWA S., OHMURA T., YAMAGUCHI K., MORI W., Mol. Cryst. Liq. Cryst., 342 (2000), 199; OHMURA T., MORI W., HIRAGA H., ONO M., NISHIMOTO Y., Chem. Lett., 32 (2003), 468.
[4] SATO T., MORI W., KATO C.N., OHMURA T., SATO T., YOKOYAMA K., TAKAMIZAWA S., NAITO S., Chem. Lett., 32 (2003), 854.
[5] OHMURA T., MORI W., HASEGAWA M., TAKEI T., YOSHIZAWA A., Chem. Lett., 32 (2003), 34; OHMURA T., MORI W., HASEGAWA M., TAKEI T., IKEDA T., HASEGAWA E., Bull. Chem. Soc. Jpn., 76 (2003), 1387.
[6] DEL SESTO R.E., ARIF A.M., MILLER J.S., Inorg. Chem., 39 (2000), 4894.
[7] OHMURA T., MORI W., in preparation.
[8] TAKEI T., MORI W., OHMURA T., KOJIMA N., TADA M., IWASAWA Y., *Syntheses and gas-occlusion properties of microporous coordination polymers of copper(II) dicarboxylates bridged by pillar ligand*, in preparation.

Received 7 March 2005
Revised 28 May 2005

Materials Science-Poland, Vol. 23, No. 3, 2005

Isomeric forms of Cu(quinoline-2-carboxylate)$_2$·H$_2$O Spectroscopic and magnetic properties

B. ŻUROWSKA, J. MROZIŃSKI*

Faculty of Chemistry, University of Wroclaw, F. Joliot-Curie 14, 50-383 Wroclaw, Poland

Spectroscopic and magnetic data for the compound Cu(2-qic)$_2$·H$_2$O (**1**), where 2-qic is quinoline-2-carboxylate, were studied in the light of its known X-ray structure. The geometry of the CuN_2O_3 chromophore shows a very distorted five-coordinated structure, intermediate between tetragonal pyramid and trigonal bipyramid, resulting from the didentate N,O-bonded two chelate ligands and one water molecule. The crystal structure is stabilized by an extended hydrogen-bonding network. Magnetic data reflect the molecular character of the compound with a very weak exchange interaction ($zJ' = -0.23$ cm^{-1}) transmitted through H-bonds. The physico-chemical properties of **1** are compared with those of recently reported isomeric forms of identical stoichiometries, namely Cu(quinoline-2-carboxylate)$_2$·H$_2$O, obtained in an unusual oxidative P-dealkylation reaction. The compound **1** was prepared directly from quinaldinic acid.

Key words: *copper(II) complexes; quinolinecarboxylate; isomerism; magnetism*

1. Introduction

The coordination chemistry of transition-metal complexes containing carboxylates is interesting from the structural and magnetic point of view. Copper(II) carboxylates have been the subject of numerous investigations, especially with nitrogen donor ligands [1, 2]. The literature on complexes of metal(II) with quinoline-2-carboxylate is rather scarce, in fact only some X-ray structures have been reported [3–8]. Their crystal structure shows an N,O-chelating behaviour of the quinoline-2-carboxylate ion. In a recent publication [9], the spectroscopic and magnetic properties of two differently synthesized forms – green (**2**) and blue-green (**3**) quinoline-2-carboxylates with the same formula Cu(2-qca)$_2$·H$_2$O (ligand abbreviated as 2-qca) were presented. Both of these complexes are five-coordinated, involve the same CuN_2O_3 chromophore, and are examples of distortion isomers. It is interesting from the synthetic and

*Corresponding author, e-mail: jmroz@wchuwr.chem.uni.wroc.pl

structural point of view that both forms of $Cu(2\text{-}qca)_2 \cdot H_2O$ (**2** and **3)** have been obtained in an unusual oxidative P-dealkylation reaction [9]. Figure 1 shows the conversion of the starting 2-qmpe to the 2-qca ligand, where 2-qmpe is diethyl 2-quinolylmethylphosphonate ligand.

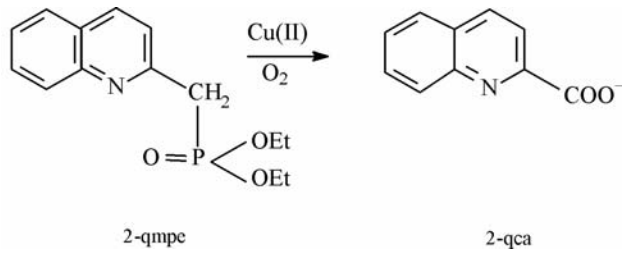

2-qmpe 2-qca

Fig. 1. A schematic drawing of the starting 2-qmpe converted to 2-qca ligand in oxidative P-dealkylation reaction of the 2-qmpe [9]

Unfortunately, we have not succeeded in preparing crystals suitable for X-ray studies for neither compound **2** nor **3**. Therefore, here we describe the results of spectroscopic and magnetic measurements of $Cu(quinoline\text{-}2\text{-}carboxylate)_2 \cdot H_2O$ (**1**), obtained directly from quinaldinic acid of known X-ray structure [3]. The crystal structure of **1,** on the basis of the known structural data, is presented in relation to the spectral and magnetic properties. The physico-chemical properties of the **1**, **2**, and **3** forms of $Cu(quinoline\text{-}2\text{-}carboxylate)_2 \cdot H_2O$ are compared.

2. Experimental

Synthesis of the complex(1): The starting materials and solvents for synthesis were obtained commercially and used as received. $Cu(2\text{-}qic)_2 \cdot H_2O$ was prepared according to the procedure described earlier [3]. Note that, although no problem was encountered in this work, perchlorate salts containing organic ligands are potentially explosive. They should be prepared in small quantities and handled with care. Elemental analysis calculated for $[C_{20}H_{14}CuN_2O_5]$: C, 56.40; H, 3.32; N, 6.58; Cu, 14.92, Found: C, 56.85; H, 3.30; N, 6.34; Cu, 14.53 wt. %.

Physical techniques. Metal content was determined using a Carl Zeiss Jena atomic absorption spectrophotometer, elemental analyses were carried out using a Perkin -Elmer elemental analyser 2400CHN, and solid-state electronic spectra (28 000–4000 cm^{-1}) on a Cary 500 spectrophotometer. Solid-state EPR spectra were recorded at room temperature and at 77K on a Bruker ESP 300E spectrometer operating at X-band, equipped with a Bruker NMR gauss meter ER 0.35 M and a Hewlett Packard microwave frequency counter HP 5350B. Magnetic susceptibility measurements were carried out with a Quantum Design SQUID magnetometer (type MPMSXL-5). Measurements were recorded at a magnetic field of 0.5 T in the temperature range

1.8–300 K. Corrections are based on subtracting the sample holder signal and estimating the contribution χ_D from the Pascal constants [10]. The effective magnetic moment was calculated from $\mu_{eff} = 2.83(\chi_M T)^{1/2}$ using a temperature-independent paramagnetism of 60×10^{-6} cm^3·mol^{-1} for Cu(II) ions [11].

3. Results and discussion

The molecular structure of Cu(2-qic)$_2$·H$_2$O (**1**), described elsewhere [3], is shown in Fig. 2. The quinaldinate ion acts as a didentate ligand bonded through a pyridyl nitrogen and carboxylate oxygen atoms to form a complex involving a five-member stable chelating ring. Water molecule occupies the fifth position. This compound is mononuclear with its coordination geometry around the copper(II) ion five-coordinated, with a configuration intermediate between a trigonal bipyramid and a square-based pyramid. This is consistent with calculations of the degree of distortion for coordination polyhedra, which give a structural index $\tau = 0.44$ (τ distinguishes between square-pyramidal and trigonal-bipyramidal geometries, defined as $\tau = (\beta - \alpha)/60$, where α = 140.3(1)0: O(1)–Cu(1)–O(2) and β = 168.2(1)0: N(1)–Cu(1)-N(2) are the largest coordination angles [12]).

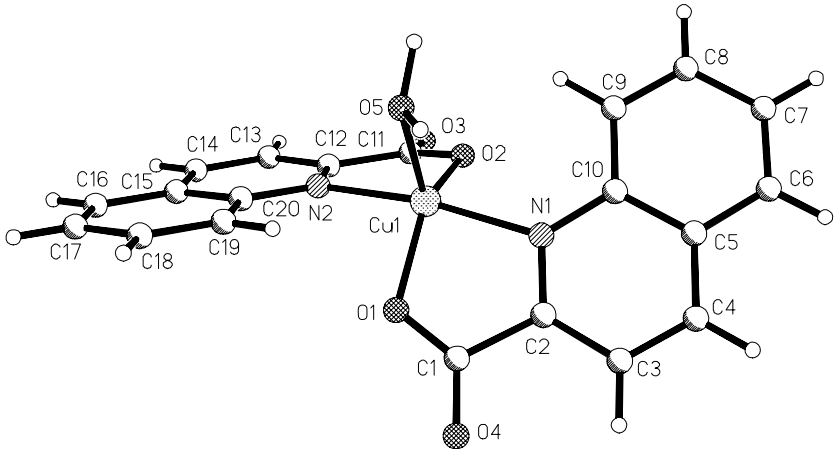

Fig. 2. Molecular structure of Cu(2-qic)$_2$·H$_2$O (**1**) with the atomic numbering [3]

An interesting feature of the crystal structure, not presented earlier, results from the fact that water molecules appear to be involved in two particularly short intermolecular hydrogen bonds with two non-coordinated carboxylic oxygen atoms of a neighbouring molecule (O–H...O: 1.60(5) and 1.80(5) Å), which enhances the crystal-packing stability (Table 1). This gives rise to a two-dimensional (2D) polymer sheet hydrogen-bonded lattice (Fig. 3) with two different Cu...Cu distances: 7.628(3) [x, $y - 1$, z] and 7.756(2) Å [$x - 1$, y, z] (Fig. 2). Additionally, the crystal lattice is stabilized by inter- and intramolecular (C–H…O) hydrogen bonds (Table 1).

Table 1. Hydrogen bonds for $Cu(2\text{-qic})_2 \cdot H_2O$ (**1**)

D–H...A		*d* [Å]			Angle DHA [deg]
		D–H	H...A	D...A	
1	1 O(5)–H(1)...O(4)^{i}	1.05(5)	1.60(5)	2.642(4)	168(5)
2	1 O(5)– H(2)...O(3)^{ii}	0.93(5)	1.80(6)	2.685(4)	158(5)
3	1 C(4)–H(4)...O(3)^{iii}	1.00(6)	2.48(6)	3.412(4)	155(4)
4 Intra	1 C(9)–H(8)...O(2)	0.99(6)	2.57(5)	3.095(5)	113(4)
5 Intra	1 C(19)–H(14)...O(1)	1.00(5)	2.45(6)	3.067(5)	120(4)

Symmetry transformations used to generate equivalent atoms: [*iii*] = 1 – x, –1/2 + *y*, 1/2 – *z*; [*ii*] = –1 + *x*, *y*, *z*; [*i*] = *x*, 1 + *y*, *z*

The infrared spectrum of **1** shows strong carboxylate stretching frequencies, $\nu_{as}(COO)$ at 1635 and $\nu_s(COO)$ at 1377 cm^{-1}, in the range characteristic of copper(II) carboxylate compounds. Separation values ($\Delta\nu$) of 260 cm^{-1} for $\nu(COO^-)$ bands indicate that the coordination of the carboxylate group is monodentate [13, 14].

The distortion of the CuN_2O_3 chromophore causes the appearance of an asymmetric band in d-d reflectance spectra, with a maximum at 13 890 cm^{-1}. There is also evidence of a weak, poorly resolved shoulder on the low-frequency side with almost comparable intensity at about 10 200 cm^{-1}, separated by ca. 4 000 cm^{-1}, which is consistent with the stereochemistries between the tetragonal pyramid and trigonal bipyramid. This splitting indicates a very distorted structure, and these bands can be assigned to the d_{xz}, $d_{yz} \rightarrow d_{x^2-y^2}$ and $d_{z^2} \rightarrow d_{x^2-y^2}$ transitions on the basis of the information reported by Hathaway et al. [15]. A strong bonding of the ν(OH) stretching region, observed at 3294 cm^{-1}, is in good agreement with polymeric intermolecular O–H...O association [16], confirmed by the X-ray crystal structure.

The X-band EPR spectra of polycrystalline solids at room temperature and at 77 K exhibit only one isotropic line, with a small deformation for the *g* value of approximately 2.10. This phenomenon may be due to the exchange coupling and a misalignment of the molecular axes of different molecules in the unit cell [15], and does not to allow for conclusions about the geometry.

In view of the structural data, one should expect that exchange interactions occur between copper ions through a strong hydrogen bond system. Therefore, here we describe the results of magnetic measurements on this compound in the temperature range of 1.8–300 K and analyse the data in order to obtain the precise magnitude of the exchange interaction energy between copper(II) ions from susceptibility measurements at low temperatures.

Magnetic susceptibility results for the polycrystalline sample show that the magnetic moment is close to the normal value for an uncoupled copper(II) system, which may suggest the absence of spin exchange, however the values of $\chi_{Cu}T$ (Fig. 4) slightly decrease with temperature. They are 0.413 $cm^3 \cdot K \cdot mol^{-1}$ ($\mu_{eff} = 1.82\mu_B$) at 300 K and 0.384 $cm^3 \cdot K \cdot mol^{-1}$ ($\mu_{eff} = 1.75\mu_B$) at 4.2 K. The magnetic susceptibility data obey the Curie

–Weiss law within the measured temperature region, with C = 0.42 cm^3·K·mol^{-1} and θ = –0.25 K. A small negative value of θ may suggest the existence of a very weak intermolecular antiferromagnetic exchange between copper ions within the crystal lattice via the hydrogen bond system. Keeping with the crystal structure, the experimental susceptibility was fitted to the expression for the magnetic susceptibility of a magnetic centre of Cu(II) (**1**), in a molecular-field correction, namely Eq. (2) [17]:

$$\chi_{\mathrm{Cu}} = \frac{N\beta^2 g^2}{4kT} \tag{1}$$

$$\chi_{\mathrm{Cu}}^{\mathrm{corr}} = \frac{\chi_{Cu}}{1 - \frac{2zJ'}{N\beta^2 g^2}\chi_{\mathrm{Cu}}} \tag{2}$$

where χ_{Cu} is the magnetic susceptibility of a paramagnetic centre, $\chi_{\mathrm{Cu}}^{\mathrm{corr}}$ is the measured experimental susceptibility, zJ' is the intermolecular exchange parameter, and z is the number of nearest neighbours. Least squares fitting of the experimental susceptibility data to this equation gives zJ' = –0.23 cm^{-1} and g = 2.06 (R = 5.52·10^{-5}).

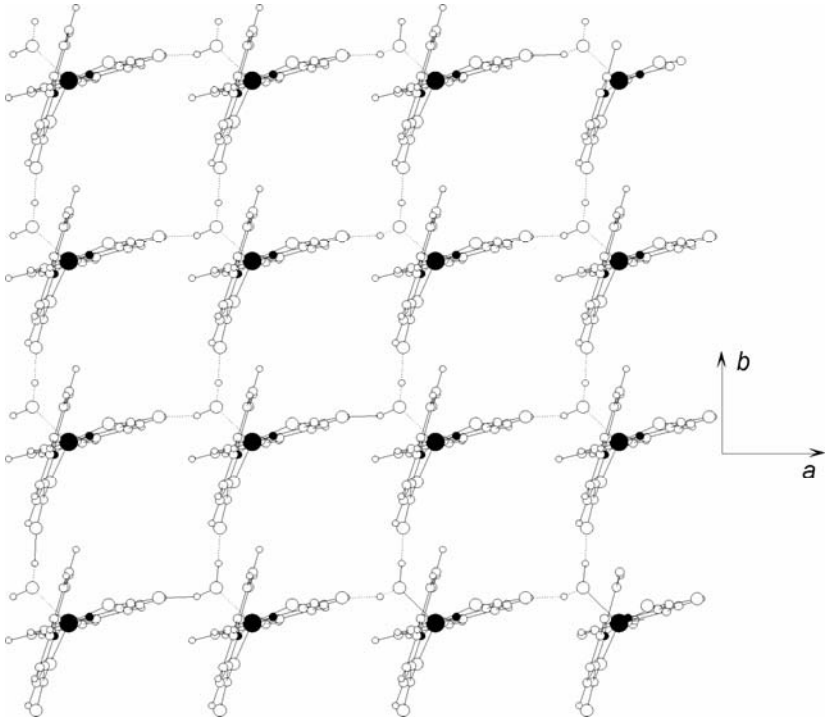

Fig. 3. Projection of the layer of Cu(2-qic)$_2$·H_2O (**1**) along z axis.
Hydrogen bonds are represented as dashed lines

Table 2. Ligand-field infrared spectral data and magnetic parameters (cm^{-1})

Vibration[a]	Compound		
	$Cu(2\text{-qic})_2\cdot H_2O$ (**1**)	$Cu(2\text{-qca})_2\cdot H_2O$[b] (**2**)	$Cu(2\text{-qca})_2\cdot H_2O$[a] (**3**)
	Colour		
	Green	Blue-green	Green
	Reaction		
	$Cu(CH_3COO)_2\cdot H_2O$ + 2-Hqic	$CuCl_2$ + 2-qmpe	$Cu(ClO_4)_2$ + 2-qmpe
$\nu(COO)_{as}$	1630vs	1635vs	1636vs
$\nu(COO)_s$	1370vs	1377vs, 1347s,sh	1377vs, 1346s,sh
$\Delta\nu$	260	258	259
δ(C=N)[c]	406s	406s	405s
ν(OH)	3294vs	3292vs	3294vs
ν(Cu–N)	270m	262m	263m
ν(Cu–O)[d]	351s, 323vs	320m, 285s	320m, 284vs
d-d	13 890s, 10 200s	13950s, 9550s	14 000w, sh 11 950s
Parameters[e]	$zJ' = -0.25\ cm^{-1}$ $g = 2.08$	$zJ' = -0.21\ cm^{-1}$ $g = 2.10$	$zJ' = -0.23\ cm^{-1}$ $g = 2.06$

[a]Denotations: vs – very strong, s – strong, m – medium, sh – shoulder. [b]From Ref. [9]. [c]Out-of-plane ring deformation. [d]From COO^-. [e]Experimental magnetic data **2** and **3** are presented in Ref. [9].

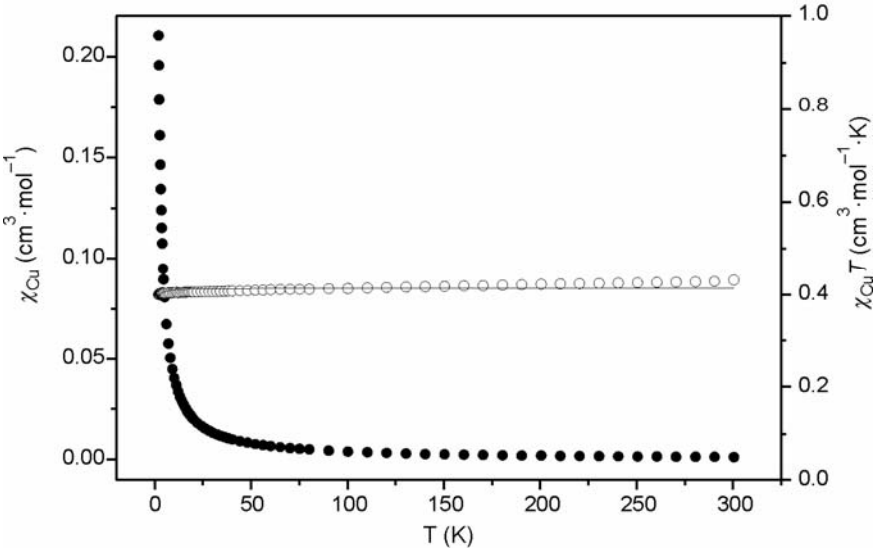

Fig. 4. χ_{Cu} (•) (experimental) and $\chi_{Cu}T$ (o) (calculated) vs. temperature of $Cu(2\text{-qic})_2\cdot H_2O$ (**1**)

For complexes **2** and **3**, experimental magnetic data, presented earlier [9], were analysed using the same model function (2). The fit gives $zJ' = -0.21\ cm^{-1}$, $g = 2.10$, ($R = 5.39\cdot10^{-5}$) for **2**, and $zJ' = -0.22\ cm^{-1}$, $g = 2.08$, ($R = 5.42\cdot10^{-5}$) for **3**.

A small negative value of zJ' for **1**, **2,** and **3** reveals very weak antiferromagnetic interactions between copper(II) ions through a hydrogen bond system in the crystal lattice, which has been confirmed by X-ray data for **1**. The same fitting agreement factor *R*

$$R = \sqrt{\frac{\sum \frac{1}{\chi_i^{\exp}} \left(\chi_i^{\exp} - \chi_i^{\text{calc}}\right)^2}{\sum \frac{1}{\left(\chi_i^{\exp}\right)^2}}}$$

was used throughout the paper.

In this paper, we compare (Table 2) the properties of three forms of Cu(quinoline -2-carboxylate)$_2$·H$_2$O (**1**), presented here with a known crystal structure [3], and differently prepared forms **2** and **3**, which have been recently published [9].

4. Summary

In conjunction with crystal structure and spectral studies, the magnetic properties of a hydrogen bond network polymer of Cu(quinoline-2-carboxylate)·H$_2$O was investigated. The hydrogen bonds generate an extensive network, which is likely to contribute to the stability of the crystal lattice. Structural analysis of the network structure of Cu(2-qic)$_2$·H$_2$O (**1**) demonstrates that water molecules and geometric disposition of the organic ligand plays an important role in the construction of network polymers. In general, it is significant to note that the intermolecular hydrogen bonding interactions are very important, since they enhance the stability of the complexes and are responsible for creating distinct structural features in the crystal structure and realizing the dimensionality of the system [18, 19]. It is also worth noting that the exchange interactions between magnetic centres are a general phenomenon for coordination in bioinorganic chemistry.

Finally, the study presented here suggests that the compound **1** of known crystal structure and compound **2** have stereochemistries between those of the tetragonal pyramid and trigonal bipyramid. Compound **3** has a trigonal-bipyramidal stereochemistry. This may be considered as an example of distortion isomers differing by the degree of distortion of their CuN_2O_3 chromophore.

References

[1] *Magneto-Structural Correlation in Exchange Coupled Systems*, R.D. Willett, D. Gatteschi, O. Khan (Eds.), Reidel, Dordrecht, 1985.

[2] SEGAL D., *Chemical Synthesis of Advanced Ceramic Materials*, Cambridge Univ. Press, Cambridge, 1989.

[3] HAENDLER H.M., Acta Crystallogr., C42 (1986), 147.
[4] GOHER M.A.S., MAUTNER F.A., Polyhedron, 12 (1993), 1863.
[5] HAENDLER H.M., Acta Crystallogr. C52, (1996), 801.
[6] BRAND U., VARHENKAMP H., Inorg. Chem., 34 (1995), 3285.
[7] LI W., OLMSTEAD M.M., MIGGINS D., FISH R.H., Inorg. Chem., 35 (1996), 51.
[8] DOBRZAŃSKA D., DUCZMAL M., JERZYKIEWICZ L.B., WARCHOLSKA J., DRABENT K., Eur. J. Inorg. Chem. (2004), 110.
[9] ŻUROWSKA B., OCHOCKI J., MROZIŃSKI J., CIUNIK. Z., REEDIJK J., Inorg. Chim. Acta, 357 (2004), 755.
[10] KÖNIG E., *Magnetic Properties of Coordination and Organometallic Transition Metal Compound*s, Springer-Verlag, Berlin, 1966.
[11] CARLIN R.L., *Magnetochemistry*, Springer-Verlag, Heidelberg, 1986.
[12] ADDISON A.W., RAO T.N., REEDIJK J., VAN RIJN J., VERSCHOOR G.C., J. Chem. Soc. Dalton Trans. (1984), 1349.
[13] DEACON G.B., PHILLIPS R.J., Coord. Chem. Rev., 33 (1980), 227.
[14] NAKAMOTO K., *Infrared in Raman Spectra of Inorganic and Coordination Compounds*, Wiley, New York, 4th Edn., 1986.
[15] HATHAWAY B.J., BILLING D.E., Coord. Chem. Rev., 5 (1970), 143.
[16] NAKAMOTO K., MARGOSHES M. RUNDLE R.E., J. Am. Chem. Soc., 77 (1985), 6480.
[17] SMART J.S., *Effective Field Theories of Magnetism*, W.B. Saunders Comp., Philadelphia, 1966, p. 24.
[18] FISHER B.E., SIGEL H., J. Am. Chem. Soc., 102 (1980), 299.
[19] JANIAK C., Angew. Chem. Int. Ed. Engl., 36 (1997), 1431.

Received 16 December 2004
Revised 3 March 2005

Materials Science-Poland, Vol. 23, No. 3, 2005

Coordination behaviour of N,N′-diallylpiperazinium(2+) and N-allylhexamethylenetetraminium in their crystalline π-complexes with ionic copper(I) salts

O. SHKURENKO[1], V. KINZHYBALO[1], T. LIS[2], Z. CIUNIK[2], M. MYS'KIV[1*]

[1]Department of Chemistry, Ivan Franko National University, Kyryla and Mefodiya 6, 79005 Lviv, Ukraine

[2]Faculty of Chemistry, University of Wroclaw, F. Joliot-Curie 14, 50-383 Wroclaw, Poland

This brief review discusses the coordination behaviour of π-coordinated copper(I) in the structures of $[Cu_2(\mu\text{-}dapp)(NH_2SO_3)_4]\cdot 2H_2O$ (**1**), $[C_4H_{12}N_2][Cu_2(\mu\text{-}dapp)(NH_2SO_3)_6]\cdot 2H_2O$ (**2**), $[Cu_2(\mu\text{-}dapp)(H_2O)_6](SiF_6)_2\cdot 2H_2O$ (**3**), $[Cu_2(\mu\text{-}dapp)(NO_3)_4(H_2O)_2]\cdot 2H_2O$ (**4**), $[Cu(\mu\text{-}ahmta)(NO_3)(H_2O)](NO_3)\cdot H_2O$ (**5**), and $[Cu(\mu\text{-}ahmta)(H_2O)_2](BF_4)_2\cdot H_2O$ (**6**) complexes (*dapp* = N,N′-diallylpiperazinium(2+), ahmta = N-allyl-hexamethylenetetraminium), obtained as single crystals by means of an alternating current electrochemical technique. The above π-complexes are formed respectively by $CuSO_3NH_2$, Cu_2SiF_6, $CuNO_3$, and $CuBF_4$ salts, unknown in a free state.

Key words: *diallylpiperazinium(2+); N-allylhexamethylenetetraminium; copper(I) π-complexes*

1. Introduction

Crystal engineering is delineated by the nature and structural consequences of intermolecular forces and by the way in which such interactions are utilized for controlling the assembly of molecular building blocks into infinite architectures [1]. The most considerable recent advances in crystal engineering have been achieved within the framework design because it is possible to simplify complex crystalline structural features into easily identifiable network topologies based on the chemical and structural information of the constituent molecular tectons (building blocks) [2, 3]. Although significant progress has been made on the theoretical front of crystal engineering, structure prediction with theoretical tools has met with less success compared to network-based approaches [4, 5]. Since modelling intermolecular forces

*Corresponding author, e-mail: myskiv@franko.lviv.ua

and cooperative effects in order to calculate crystalline lattice energies is a very difficult task, it is impossible to quantify intermolecular forces and atomic charges precisely. One can, however, estimate the directional preferences of molecules through electrostatic interactions [6]. It is obvious that crystal structure, which is not combined from simple tectons, is more difficult to predict and design, because it is still unkown which factors determine the structure formed. Only wider crystal chemistry investigations of organometallic architectures can help in this case.

Supramolecular motifs containing an olefin–copper(I) bond as a bridging spacer have recently attracted much attention [7]. Copper(I)–olefin π-complexes are involved in the preparation and reactions of olefin and alkyne complexes [8–10], as catalytically active species in copper-catalyzed reactions [11, 12], and as agents for selective olefin/paraffin separations [13, 14].

Our previous studies on copper(I) halide complexation with N,N′-diallylpiperazinium(2+) (*dapp*) [15] and N,N,N′,N′-tetraallylpiperazinium(2+) [16] cations revealed unusual coordination behaviour of the ligands: Cu(I)–(C=C) interaction does exist in the presence of Cl atoms and is absent in the case of Br. Such a dissimilarity is not displayed in copper(I) halide complexes with aliphatic olefin derivatives (e.g., copper(I) chloride and bromide form π-complexes with diallylammonium halide [17–20]) or with aromatic heterocyclic derivatives [21, 22].

On the other hand, the dimorphism of copper(I) chloride complexes with N-allylhexamethylenetetraminium (*ahmta*) chloride – [(μ_3-*ahmta*)Cu_2Cl_3] and [(μ-*ahmta*)Cu_2Cl_3] [23] – is a result of the different roles of the ligand: *ahmta* acts as a σ,σ,π- and σ,π-ligand, respectively.

In connection to this, we consider the coordination behaviour of *dapp* and *ahmta* moieties in [Cu_2(μ-*dapp*)$(NH_2SO_3)_4$]·$2H_2O$ (**1**), [$C_4H_{12}N_2$][Cu_2(μ-*dapp*)$(NH_2SO_3)_6$]·$2H_2O$ (**2**) [24], [Cu_2(μ-*dapp*)$(H_2O)_6$]$(SiF_6)_2$·$2H_2O$ (**3**), [Cu_2(μ-*dapp*)$(NO_3)_4(H_2O)_2$]·$2H_2O$ (**4**), [Cu(μ-*ahmta*)$(NO_3)(H_2O)$]·(NO_3)·H_2O (**5**), and [Cu(μ-*ahmta*)$(H_2O)_2$]$(BF_4)_2$·H_2O (**6**) [25] π-complexes, which we have recently obtained and structurally investigated by X-ray diffraction. The ligand moieties are presented in Fig. 1.

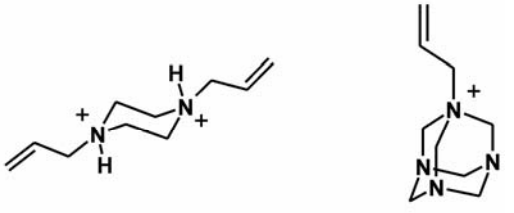

a) b)

Fig. 1. Schematic view of the cations:
a) N,N′-diallylpiperazinium(2+) (*dapp*),
b) N-allylhexamethylenetetraminium (ahmta)

2. Results

Synthetic aspects. Crystalline π-complexes (**1**, **3**–**6**) were obtained by means of an alternating-current electrochemical technique [26]:

$$LX + CuX_2 \cdot nH_2O + Cu^0 \xrightarrow{C_2H_5OH,\ [e]} L_aCu^I{}_bX_c \cdot dH_2O$$

L = *dapp*, *ahmta*; X = $1/2\,SiF_6^{2-}$, NO_3^-, $NH_2SO_3^-$ and BF_4^-. Compound **2** was formed under conditions described in [24].

One may note that although Cu_2SiF_6, $CuNO_3$, $CuNH_2SO_3$, and $CuBF_4$ are unknown in a free state, they can exist in the form of stable complexes due to relatively strong Cu(I)–(C=C) π-interactions. A brief structural survey of the compounds follows.

Structure of $[Cu_2(\mu\text{-}dapp)(NH_2SO_3)_4]\cdot H_2O$ (1). The centrosymmetric cation of diallylpiperazinium(2+) in this structure acts as a bridge (Fig. 2). The C=C bonds of allylic groups are coordinated by copper(I) atoms at a distance of 1.919(4) Å. It is interesting that the C=C bond successfully competes with the nitrogen atoms of two sulfamate anions. Moreover, this bond is elongated to 1.368(6) Å. The oxygen atom of the sulfamate anion is located in the axial position of the trigonal-pyramidal copper(I) coordination environment at a distance of 2.574(3) Å. The deviation of the Cu atom from the equatorial plane (*Δ*) is 0.12 Å. Such a geometry of the coordination centre should be attributed to the effective Cu(I)–(C=C) interaction. The presence of the water molecule, which forms a strong hydrogen bond with the oxygen atoms of sulfamate anions (2.39(4)–2.51(5) Å) and weaker ones with the nitrogen atom of the H–N-group of the piperazine ring (2.750(4) Å), promotes the stabilization of the crystal structure as well as weaker contacts such as N(H)…O(NH_2SO_2) (2.854(5) –2.936(5) Å, 145(4)–178(5)°).

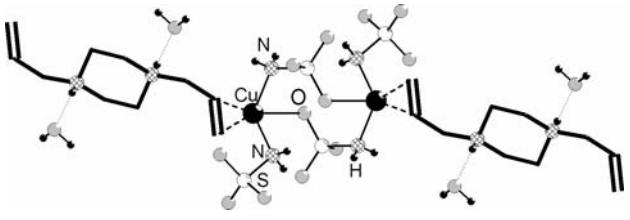

Fig. 2. A fragment of the infinite chain **1**

Structure of $[C_4H_{12}N_2][Cu_2(\mu\text{-}dapp)(NH_2SO_3)_6]\cdot 2H_2O$ (2). The structure of **2** contains centrosymmetric piperazinium(2+) and diallylpiperazinium(2+) cations. As before, the *dapp* cation plays a bridging function and forms dimers (Fig. 3). This is the first crystalline π-complex described where the coordination environment of copper(I) consists of three nitrogen atoms of $NH_2SO_3^-$ anions and a C=C bond. These nitrogen atoms in the tetrahedral coordination polyhedron of Cu(I), however, hinder

effective Cu(I)–(C=C) binding due to steric restrictions (Δ = 0.46 Å). An elongated distance *d*(Cu–*m*) 1.962(9) Å and imaginary abridgement of the coordinated C=C bond up to 1.29(2) Å are caused by a moderate disorder of this double bond.

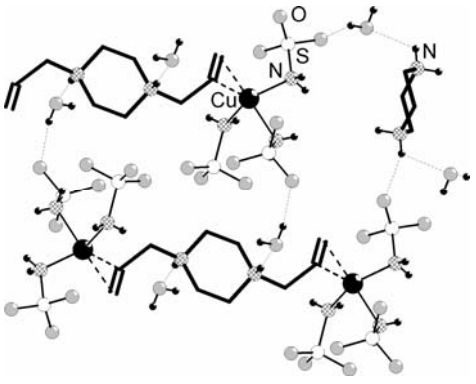

Fig. 3. The packing of $\{(O_3SH_2N)_3Cu(\textit{dapp})Cu(NH_2SO_3)_3\}$ dimers in structure **2** and the system of hydrogen bonds

The hydrogen bonds N–H…O (2.01(9)–2.36(7) Å, 140(8)–160(8)°) play a decisive role in the structure formation and withdraw electron density from the N atoms of sulfamat moieties. The latter circumstance allows Cu–(C=C) π-interactions to be realized even in the presence of three donor N atoms of sulfamate anions. The crystallization water molecule in this structure forms hydrogen bonds with both the oxygen atoms of sulfamate anions ((O_w)H...O 1.92(9)–2.12(6)Å, 155(8) –156(6)°) and with the H atoms of the piperazine(2+) core ((N)H...O_w 1.69(8) Å, 156(7)°).

Structure of $[Cu_2(\mu\text{-}\textit{dapp})(H_2O)_6](SiF_6)_2\cdot 2H_2O$ (3). The crystal structure of **3** contains only one independent Cu(I) atom. Its trigonal pyramidal coordination environment consists of three oxygen atoms (from H_2O molecules) and a double C=C bond of the ligand (see Table 1). The SiF_6^{2-} anion possesses an octahedral geometry (Si–F distances 1.652(9)–1.690(9) Å) and is involved only in the formation of hydrogen bonds. The small size of oxygen atoms as well as the stabilizing influence of strong H-bonds create conditions for very effective Cu–(C=C) π,σ-interaction. In reality, the Cu–*m* (*m* is the midpoint of a double C=C bond) distance is equal to 1.89(1) Å and the Cu atom is removed from the plane of equatorial ligands by only Δ = 0.17 Å. The length of the coordinated double bond equals 1.32(2) Å. Strong O–H...F hydrogen bonds (with distances *d*(H…F) 1.9(1)–2.3(1) Å and angles O–H...F 145(8)–162(9)°) withdraw excess electron density from the copper(I) atom and thus reduce a π-dative contribution. Due to the bridging function of the diallylpiperazinium(2+) cation (Fig. 4), the dimers $\{(H_2O)_3Cu(\textit{dapp})Cu(H_2O)_3\}$ are displayed in (3). They are combined into a three-dimensional framework by a branching network of

C–H...F and O–H...F hydrogen bonds. It is necessary to note that the molecule of crystallization water is held in the crystal structure by an effective N–H...O_{aq} hydrogen bond (the nitrogen atom belongs to the piperazine ring, *d*(H...O) is 1.8(2) Å, and the N–H...O_{aq} angle is 171(9)°).

Table 1. Selected distances and angles in the structures of **1–6** (*d*, Å and *ω*, °)

Structure	Parameter	Value	Structure	Parameter	Value
1	Cu–N2	2.030(4)	**4**	Cu–O_{aq}1	1.956(2)
	Cu–N3	2.040(3)		Cu–O2	1.991(1)
	Cu–O1	2.574(3)		Cu–O5	2.531(2)
	Cu–*m*1,2	1.919(4)		Cu–*m*4,5	1.884(2)
	C1–Cu–C2	39.2(1)		C4–Cu–C5	40.19(8)
	C1=C2	1.368(6)		C(4)=C(5)	1.379(3)
2	Cu–N3	2.101(6)	**5**	Cu–O11	2.033(2)
	Cu–N4	2.082(7)		Cu–N3	2.052(3)
	Cu–N5	2.295(6)		Cu–Ow1	2.241(3)
	Cu–*m*1,2	1.962(9)		Cu–*m*(1,2)	1.917(3)
	C1–Cu–C2	36.4(4)		C1–Cu–C2	39.7(1)
	C1=C2	1.29(2)		C1=C2	1.368(5)
3	Cu–O2	2.37(2)	**6**	Cu–O1	2.174(3)
	Cu–O3	1.989(9)		Cu–O2	2.032(2)
	Cu–O4	2.000(9)		Cu–N1	2.066(3)
	Cu–*m*1,5	1.89(1)		Cu–*m*1,2	1.921(4)
	C1–Cu–C5	38.5(5)		C1–Cu–C2	39.5(1)
	C1=C5	1.32(2)		C1=C2	1.374(5)

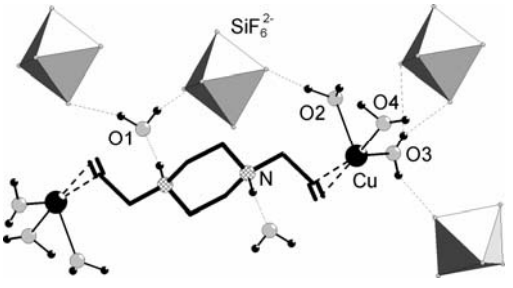

Fig. 4. {$(H_2O)_3Cu$(*dapp*)$Cu(H_2O)_3$} dimers and SiF_6^{2-} (octahedra) anions in the outer coordination sphere of crystal structure **3**

Structure of [Cu_2(μ-*dapp*)$(NO_3)_4(H_2O)_2$]·$2H_2O$ (4). The coordination polyhedron of the Cu(I) atom in π-complex **4** is a trigonal pyramid that contains a double C=C bond, a water molecule, an oxygen atom from a nitrate anion in the equatorial position, and one more oxygen atom of NO_3^- in the apical position (Table 1). Such ligands in the metal coordination environment promote an efficient Cu(I)–(C=C) interaction. A short copper–*m* distance of 1.884(4) Å is caused by the considerable axial

deformation of the coordination polyhedron (Cu–O5 2.531(2) Å), by the hard Lewis base in the apical position, and by the absence of steric restrictions. Although one of the hydrogen bonds (C5–H52...O3, 2.58(3) Å, 142(3)°) rotates the coordinated C=C group by an angle of 9.8°, this bond is elongated up to 1.379(3) Å nevertheless, which is evidence for significant π-dative interaction. The unusual small deviation of the Cu(I) atom from the plane of equatorial ligands (Δ = 0.05 Å) confirms a conclusion about the effective Cu(I)–(C=C) π-interaction, which one could explain by a specific unification of steric and electron factors in the formation of the copper(I) coordination sphere.

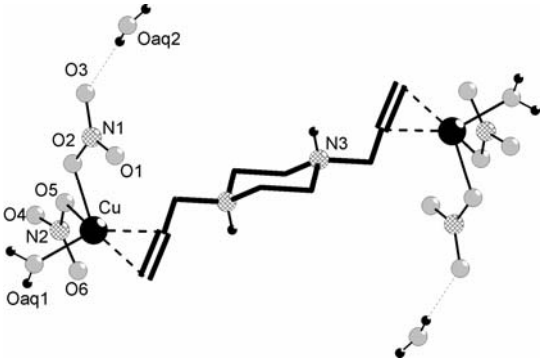

Fig. 5. The bridging function of *dapp* moiety in **4**

As a result of the bridging function of the diallylpiperazinium(2+) cation, structure **4** consists of {$(NO_3)_2(H_2O)Cu(\mu$-*dapp*$)Cu(H_2O)(NO_3)_2$} dimers (Fig. 5), which are integrated into a three-dimensional framework by a branching system of hydrogen bonds. In contrast to **1–3**, the crystallization water molecule here is held in the structure due to the hydrogen contacts of O_{aq}–H...O(–NO_2) and O_{aq}–H...O_{aq} (1.93(3) –2.22(3) Å, 154(3)–176(3)°). The H atom of the N–H-group takes part in a strong H-bond with the oxygen atom of the NO_3^- moiety (1.97(2) Å, 174(2)°). This hydrogen bond causes a lengthening of the N(2)–O(4) distance in the anion to 1.261(2) Å.

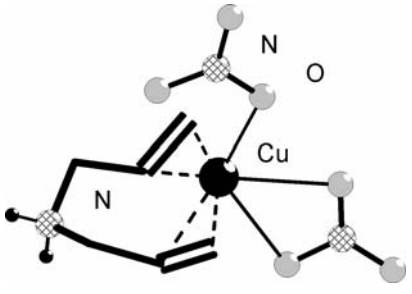

Fig. 6. The monodentate and bidentate functions of nitrate anions in the complex [$Cu((C_3H_5)_2NH_2)(NO_3)_2$]

Contrary to the above complex, in the case of dyallylammonium copper(I) dinitrate [27], NO_3^- moieties demonstrate a different coordination behaviour: one NO_3^- anion is monodentate, whereas the two oxygen atoms of the other nitrate anion are coordinated to the Cu(I) atom (Fig. 6).

Structure of [Cu(μ-ahtma)(NO_3)(H_2O)](NO_3)·H_2O (5). The Cu atom possesses a trigonal-pyramidal environment, formed by the oxygen atom of the nitrate anion, a nitrogen atom, and a C=C bond of adjacent *ahmta* cations in the equatorial plane. The apical position is occupied by the oxygen atom of the water moiety, so that *ahmta* acts as a bidentate bridging π,σ-ligand and connects Cu atoms into metal-organic chains lying along the [001] direction (Fig. 7). Water and nitrate moieties of the outer coordination sphere take part in the formation of a well-developed branched system of strong H-bonds (O_{aq}–H...O(–NO_2) 1.751(5)–2.051(5) Å, 157.3(1)–169.9(1)°; O_{aq}–H...O_{aq} 1.926(6) Å, 173.8(2)°). The latter unite metal-organic chains into a 3-D network. The pyramidal distortion of the coordination sphere, being rather moderate (Δ = 0.33 Å), corresponds to a slightly elongated Cu–Ow1 apical bond (2.241(3) Å) as compared to the ideal Cu^I–O distance of 1.99 Å [28].

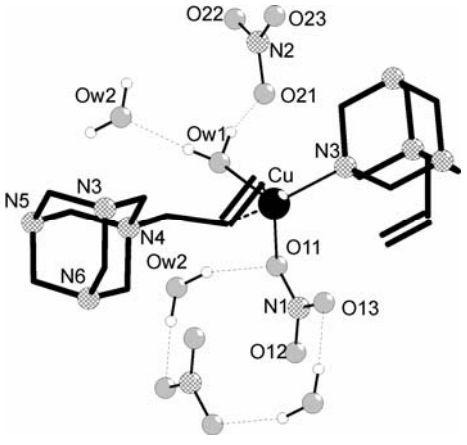

Fig. 7. The hydrogen bond system the structure **5**

It should be pointed out that one nitrate and one water moiety are situated in the inner coordination sphere and two others in the outer one.

Structure of [Cu(μ-ahtma)(H_2O)$_2$](BF_4)$_2$·H_2O (6). In this structure, one crystallographycally independent Cu atom possesses a reasonably deformed (Δ = 0.25Å) trigonal-pyramidal environment, formed by the oxygen atom of a water moiety, a nitrogen atom, and the C=C bond of adjacent *ahmta* cations in the equatorial plane. The apical position is occupied by the oxygen atom of another water moiety (Fig. 8). Similar to **5**, here *ahtma* also acts as a bidentate bridging π,σ-ligand that connects Cu atoms into metal-organic chains. Contrary to **5**, all anion moieties are in the outer coordination sphere, forming a branched network of strong H-bonds with

water molecules (O_{aq}–H...F 1.633(2)–2.026(4) Å, 142.3(2)–159.4(3)°). Tetrahedral BF_4^- are slightly disordered, because they are involved in weak interactions – van der Waals and F…H–O bonds.

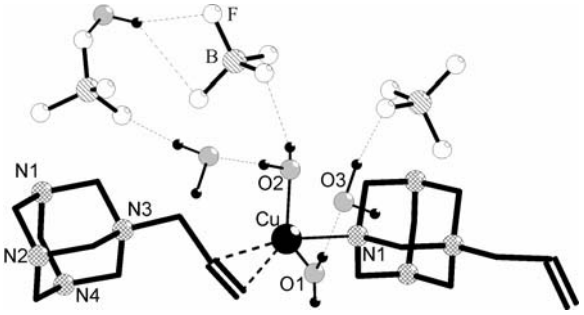

Fig. 8. The hydrogen bond system in structure **6**

3. Discussion

The diallylpiperazinium(2+) cation realizes all the coordination abilities in structures **1–4** as a bidentate π,π-ligand. This is not surprising, because the presence of two flexible allylic groups and the small size of the piperazine ring allow steric restrictions to be avoided at the stage when molecular building blocks assemble into

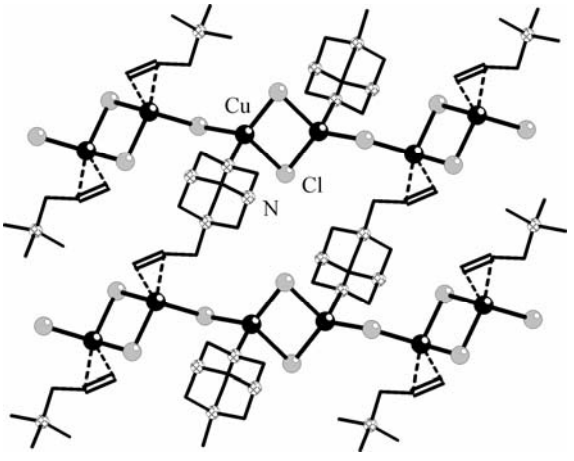

Fig. 9. A fragment of the structure of [(μ_3-*ahmta*)Cu_2Cl_3]

infinite architectures. Therefore, *dapp* plays a bridging role and forms either infinite chains (if some other ligands in the coordination environment are also bridging, as in complexes **1** and [Cu_2(μ-*dapp*)Cl_4] [15]) or X_3Cu–*dapp*–CuX_3 dimers (if X serves as a terminal ligand, as in structures **2–4**). In turn, the chloride anion acts as bridge

ligand and/or as a terminal one. Contrary to this, only two symmetrically related allylic groups of the N,N,N′,N′-tetraallylpiperazinium(2+) cation are coordinated to Cu atoms in the complex $[(C_3H_5)_2N(CH_2)_4N(C_3H_5)][Cu_2Cl_4]$ [16].

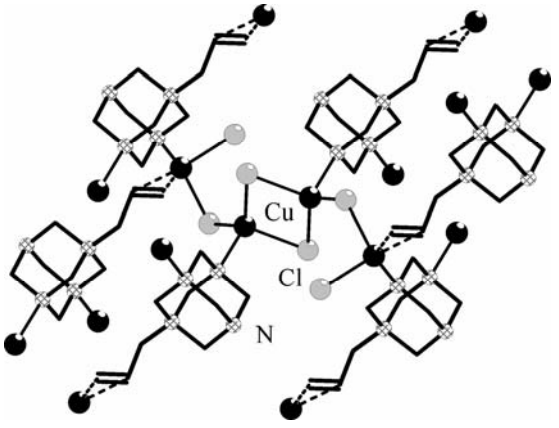

Fig. 10. Flattened layers in the crystal structure of [(μ-*ahmta*)Cu_2Cl_3]

Concerning the coordination behaviour of N-allylhexamethylenetetraminium (*ahmta*), it should be emphasized that the presence of only one allylic group, free electron pairs of three nitrogen atoms, and the significant size and rigidity of the ligand all decide about its spatial properties in the structures. In copper(I) chloride complexes [23], *ahmta* connects CuCl fragments into different topologies depending on the role of the ligand. In the case of μ_3-*ahmta*, which acts as a π,σ,σ-ligand, the structure of a 3D-network is observed (Fig. 9). If its role changes to μ-*ahmta* (π,σ-ligand), infinite inorganic $[Cu_2Cl_3]_\infty$ chains, connected by bridging $[(CH_2)_6N_4(C_3H_5)]^+$ moieties into flattered layers, occur (Fig. 10). If *ahmta* dentation decreases up to one (σ-ligand), the structure consists of only isolated *ahmta*$CuCl_2$ fragments (Fig. 11).

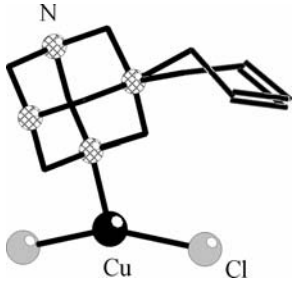

Fig. 11. An isolated *ahmta*$CuCl_2$ fragment
in the structure of [(*ahmta*)$CuCl_2$]

SiF_6^{2-} and BF_4^- anions are harder bases than the soft Lewis acid copper(I) atom. That is why these anions lie in the outer coordination sphere in structures **3** and **6**.

Due to significant "electron-withdrawing" ability, all fluorine atoms of the anions form a system of hydrogen bonds. The shortest contacts in **3** are caused by larger negative charge on the hexafluorosilicate anion as compared to the tetrafluoroborate moiety.

In **4** and **5**, some N–O bonds in NO_3^- anions differ in their lengths (1.233(4) –1.282(4) Å). An elongation of N–O2, N–O4, and N–O5 in **4**, and N–O11 and N–O21 bonds in **5** is caused by their role in the structure: O2, O5, and O11 are coordinated to Cu, whereas O4 and O21 take part in the formation of strong H-bonds; though the reason is different, the effect is nearly the same. The stereochemical peculiarities of the nitrate anion have been confirmed by earlier observations [27]. In structures **4** and **5**, Cu–O–N angles and Cu–O–N–O torsion angles are close to 120° and 0°, respectively, showing the directionality of copper(I)–ONO_2^- interactions via the free electron pairs of oxygen atoms.

The H(N)-atoms of the piperazine ring participate in strong hydrogen bonds. Crystallization water molecules are present in structures **1–3** due to these contacts, and are involved in structures **4–6** by H-bonds with anions and other water molecules.

Thus, the presence of strong (O–)H…O and O–H…F bonds in the construction of ionic copper(I) π-complexes creates additional possibilities in the structures of these ionic compounds as compared to copper(I) chloride complexes, in which only relatively weak (C–)H...Cl and sometimes (N–)H…Cl contacts are present.

Water moieties in the coordination sphere of Cu play an important role: they transfer some charge via H-bonds to the anion in the outer coordination sphere, providing an ionic character of the compounds.

Table 2. Geometric characteristics of the copper(I) coordination environment in the π-complexes under consideration

Compound	Cu–*m* [Å]	$l_{C=C}$ [Å]	Δ [Å]	Cu–L_{ap} [Å]	Angle C–Cu–C [deg]
1	1.919(4)	1.368(6)	0.12	2.574(3)	39.2(1)
2	1.962(9)	1.29(2)	0.46	2.295(6)	36.4(4)
3	1.89(1)	1.32(2)	0.17	2.37(2)	38.5(5)
4	1.884(2)	1.379(3)	0.05	2.531(2)	40.19(8)
5	1.917(3)	1.368(5)	0.33	2.241(3)	39.7(1)
6	1.921(4)	1.374(5)	0.25	2.174(3)	39.5(1)

It is possible to draw some conclusions about the contribution of both the σ-component, which depends on the magnitude of the Cu–*m* distance, and π-back donation component, which is connected with the elongation value of coordinated C=C bonds ($l_{C=C}$) (Table 2). This is not obligatory, hence strengthening of the σ–component (shortening Cu–*m*) intensifies the π-back donation component (increasing of $l_{C=C}$ value) of π-interactions. The magnitude C–Cu–C angle appears to be a convenient measure of Cu(I)–(C=C) interaction strength, because it depends on

either Cu–*m* distance or elongation of multiple C=C bond. Axial lengthening depends on the hybridization state of the copper atom, steric factors, and the basicity of the apical ligand. Therefore it cannot be a convenient parameter for our aim. The Δ value is the only evidence of copper(I) transfer from the sp^3- to the dsp^2-hybridization state (in the last case $\Delta = 0$) and, according to the oxidative addition concept [29], it is also a measure of the Cu(I)–(C=C) interaction effectiveness (see [29] for more details about the electron effects in copper(I) olefinic π-complexes). Figure 12 demonstrates the good convergence dependence of copper atom deviation from the *rms*-plane of equatorial ligands on the C–Cu–C angle for complexes **1–4**. Such linearity for complexes **1–4** is interpreted by the absence of any drastic effects in the Cu(I) coordination sphere, contrary to **5**, **6**, in which N donor atoms of the onium form of quasiaromatic hexamethylenetetramine are present in copper(I) surrounding of the complexes.

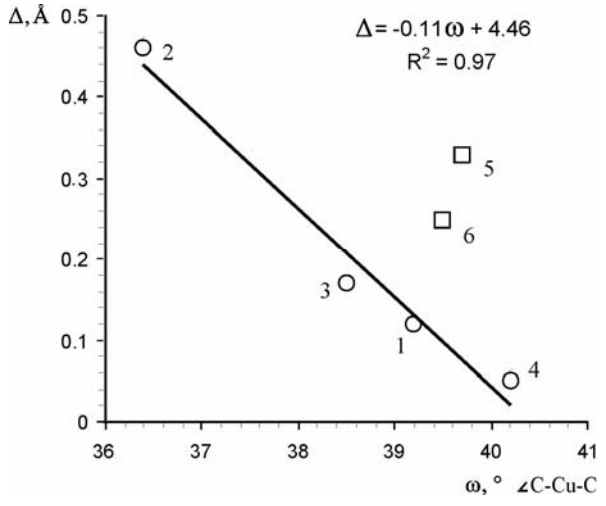

Fig. 12. The dependence of Cu atom deviation from the *rms*-plane of equatorial ligands on the C–Cu–C angle. The points for structures with *dapp* are depicted as ○ and for structures with *ahmta* as □. The trendline is calculated only for structures **1–4**

It should be noted that in comparison to recently obtained CuCl π-complexes with *ahmta* chloride [23], these structures show a stronger interaction of the ligand with Cu(I). The Cu–N3 distance in **5** is equal to 2.052(3) Å and Cu–N1 in **6** – 2.066(3) Å. They are shorter than the same contacts between the copper(I) and nitrogen atoms of the *ahtma* moiety (2.142(3)–2.241(3) Å) in the respective copper(I) chloride structures, which should be attributed to the ionic character of **5** and **6**. The existence of the [Cu(benzene)]$AlCl_4$ [30] π-complex confirms this conclusion. Thus, the ionic character of complexes **1–6** provides effective Cu(I)–(C=C) interactions and enables the sufficient stability of this type of the Cu(I) compound.

References

[1] AAKERÖY C.B., Acta Cryst., B53 (1997), 569.
[2] LU J.Y., Coord. Chem. Rev., 246 (2003), 327.
[3] PODESTA T.J., ORPEN A.G., CrystEngComm, 4 (2002), 336.
[4] DESIRAJU G.R., Angew. Chem., Int. Ed. Engl., 34 (1995), 2311.
[5] KOBKO N., PARASKEVAS L., DEL RIO E., DANNENBERG J.J., J.Am. Chem. Soc., 123 (2001), 4348.
[6] SHARMA C.V.K., Cryst. Growth Des., 2 (2002), 465.
[7] ZHANG J., XIONG R.-G., CHEN X.-T., XUE Z., PENG S.M., YOU X.-Z., Organometallics, 21 (2002), 235.
[8] SALOMON R. G., KOCHI J. K., J. Am. Chem. Soc., 95 (1973), 1889.
[9] LANG H., KÖHLER K., ZSOLNAI L., Chem. Ber., 128 (1995), 519.
[10] OLBRICH F., BEHRENS U., GRÖGER G., WEISS E.J., Organomet. Chem., 448 (1993), C10.
[11] NEUROCK M., ZHANG X., OLKEN M., JONES M., HICKMAN D., CALVERLEY T., GULOTTY R., J. Phys. Chem. B, 105 (2001), 1562.
[12] DÍAZ-REQUEJO M.M., NICASIO M.C., PÉREZ P.J., Organometallics, 17 (1998), 3051.
[13] HUANG H.Y., PADIN J., YANG R.T., J. Phys. Chem. B, 103 (1999), 326.
[14] SULLIVAN R.M., LIU H., SMITH S., HANSON J.C., OSTERHOUT D., CIRAOLO M., GREY C.P., MARTIN J.D., J. Am. Chem. Soc. 125 (2003), 11065.
[15] SHKURENKO A.A., DAVYDOV V.N., MYS'KIV M.G., Russ. J. Coord. Chem., 29 (2003), 445.
[16] GORESHNIK E.A., MYS'KIV M.G., Russ. J. Coord. Chem., 29 (2003), 871.
[17] MYS'KIV M.G., OLIJNYK V.V., ZAVALIJ P.YU., FUNDAMENSKIY V.S., PAK SEK BON., Metallorgan. Khimiya, 2 (1989), 1225.
[18] OLIJNYK V.V., MYS'KIV M.G., MAZUS M.D., ZAVALIJ P.YU., PAK SEK BON., J. Struct. Khim., 33 (1992), 121.
[19] OLIJNYK V.V., GLOWIAK T., MYS'KIV M.G., Koord. Khimiya, 25 (1990), 790.
[20] OLIJNYK V.V., MYS'KIV M.G., AKSELRUD L.G., Koord. Khimiya, 22 (1996), 71.
[21] GORESHNIK E.A., SCHOLLMEYER D., MYS'KIV M.G., Z. Anorg. Allgem. Chemie, 629 (2003), 2040.
[22] GORESHNIK E.A., SCHOLLMEYER D., MYS'KIV M.G., Acta Cryst., C61 (2005), m127.
[23] KINZHIBALO V.V., MYS'KIV M.G., DAVYDOV V.N., Russ. J. Coord. Chem., 28 (2002), 867.
[24] MELNYK O.P., MYS'KIV M.G., DAVYDOV V.N., Russ. J. Coord. Chem., 29 (2003), 363.
[25] SHKURENKO O., KINZYBALO V., LIS T., CIUNIK Z., MYS'KIV M., Abstract-book of the 14th Winter School on Coordination Chemistry, Wrocław, 2004, p. 69.
[26] MYKHALICHKO B.M., MYS'KIV M.G., Ukr. Patent UA 25450A, Bull., No. 6 (1998).
[27] OLIJNYK V., GLOWIAK T., MYS'KIV M., J. Chem. Crystallogr., 25 (1995), 621.
[28] NASKAR J.P., CHOWDHURY S., DREW M.G.B., DATTA D., New J. Chem., 26 (2002), 170.
[29] OLIJNYK V., Koord. Khimiya, 22 (1996), 550.
[30] TURNER R.W., AMMA E.L., J. Amer. Chem. Soc., 88 (1966), 1877.

Received 11 March 2004
Revised 13 May 2005

Materials Science-Poland, Vol. 23, No. 3, 2005

Metal complexes of pyrroline-N-oxide dioxime

A. B. BURDUKOV[1*], E. V. MOKINA[1], YU. G. SHVEDENKOV[1], V. A. REZNIKOV[2], G. I. ROSCHUPKINA[2], G. V. ROMANENKO[3]

[1]Nikolaev Institute of Inorganic Chemistry of SB RAS, Lavrent'ev av. 3, 630090 Novosibirsk, Russia

[2]Novosibrisk Institute of Organic Chemistry of SB RAS, Lavrent'ev av. 7, 630090 Novosibirsk, Russia

[3]International Tomography Centre of SB RAS, Institutskaya st. 3A, 630090 Novosibirsk, Russia

Syntheses and structures of nickel(II) and copper(II) complexes with pyrroline N-oxide 2,3-dioxime (H_2L^R) are reported. The ligands show an N,O chelating mode unusual for conventional dioxime ligands. Copper compounds with $Cu_2(HL^R)_2L^R$ composition can be oxidized into complexes containing coordinated vinylnitroxide radicals.

Key words: *dioximes; copper; nickel; vinylnitroxides; crystal structure; magnetic properties*

1. Introduction

1,2-Dioximes are well-known chelating ligands to transition metal ions and have been under investigation for already almost a century. Most ligands in this class, however, are hydrocarbon derivatives, while heterocyclic 1,2-dioximes are studied quite poorly. We have turned our attention to the derivatives of pyrroline N-oxide H_2L^R (Scheme 1), keeping in mind that complexes of these ligands are promising precursors of coordination polymers, as known for simpler dioximates [1, 2].

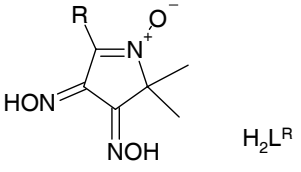

H_2L^R

Scheme 1. Pyrroline N-oxide H_2L^R

*Corresponding author, e-mail: alex@cys.che.nsk.su

On the other hand, complexes of H_2L^R dioximes are formally tautomeric with nitrosovinylhydroxylamines, which in turn can be considered as possible ancestors of the very intriguing vinylnitroxide ligands (Scheme 2). It should be noted that the only persistent vinylnitroxide known is derived from the pyrroline-N-oxide skeleton [3].

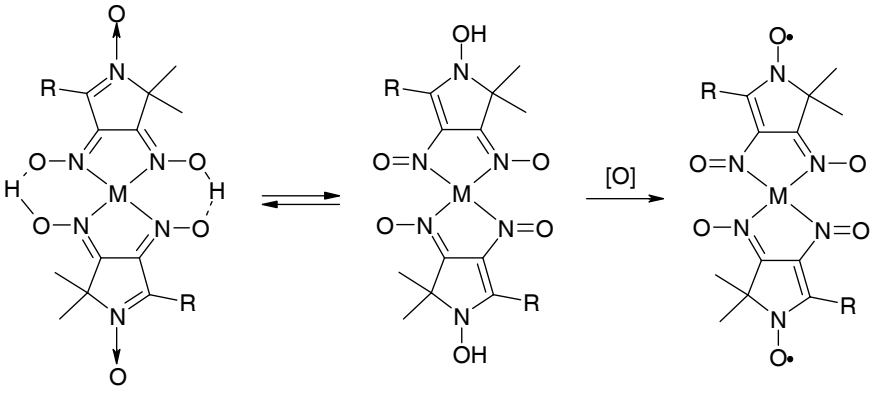

Scheme 2. Tautomerism between nitrosohydroxylamines and oxime N-oxides

In the present paper, we report the first results obtained on complexes of dioximes H_2L^R with nickel(II) and copper(II).

2. Experimental

The complexes $Cu_2(HL^{Ph})_2L^{Ph}\cdot 4H_2O\cdot EtOH$, $Cu_2(HL^{t\text{-}Bu})_2L^{t\text{-}Bu}\cdot 4H_2O$, $Ni(HL^{Ph})_2\cdot 3H_2O$ and $Ni(HL^{t\text{-}Bu})_2\cdot 2.5H_2O$ were obtained by interacting stoichiometric amounts of the reagents in a water–ethanol media (3:2), the pH of the solution being adjusted to 6 with aqueous ammonia. The complexes $CuNa(HL^{Ph})(L^{Ph})\cdot 4H_2O$, $CuNa(HL^{t\text{-}Bu})(L^{t\text{-}Bu})\cdot 5H_2O$, and $CuNa(HL^{Me})(L^{Me})\cdot 4H_2O$ were obtained similarly, at pH adjusted to 9 with a water solution of Na_2CO_3. The compounds gave satisfactory elemental analyses; the quantity of the solvent molecules may vary in different preparations, so the compounds are further denoted as solvent-free.

Intensity data for single crystals of complexes were collected on a Smart Apex (Bruker AXS) diffractometer at room temperature using graphite monochromated MoK_α radiation (λ = 0.71073 Å). Structures were solved with statistical methods (Bruker-Shelxs) and refined with full-matrix or full-matrix-block least-squares on F^2 (Bruker-Shelxl). The positions of carbon-sitting hydrogen atoms were calculated geometrically and refined isotropically as riding mode. The crystal data and some details of the diffraction experiment are given in Table 1.

The magnetochemical experiment was performed on an MPMS-5S (Quantum Design) SQUID magnetometer at temperatures from 2 K to 300 K with powder samples.

Table 1. Crystal data and X-ray diffraction experiment details for the complexes[1]

Crystal data	Compound (solvent molecules omitted)			
	$Cu_2(HL^{Ph})_2L^{Ph}$	$Ni(HL^{Ph})_2$	$CuNa(HL^{t\text{-}Bu})(L^{t\text{-}Bu})$	$CuNa(HL^{Me})(L^{Me})$
a, Å	11.516(2)	10.645(4)	9.4561(14)	12.3899(12)
b, Å	13.252(4)	10.726(4)	11.2506(17)	13.2043(13)
c, Å	16.876(5)	13.843(5)	13.545(2)	16.1493(17)
α, deg	107.065(6)	81.211(7)	102.925(2)	106.372(21)
β, deg	103.333(6)	76.894(6)	102.831(3)	107.495(16)
γ, deg	96.497(7)	74.140(7)	100.013(2)	95.185(18)
V, Å^3; *Z*	2350(3); 2	1473.7(9); 2	1331.0(3); 2	2131(2); 2
No. of reflections total/unique	10298/6708	6337/4179	5816/3819	5188/2943
GOOF	0.782	0.915	1.075	1.30
R1	0.0609	0.0488	0.0468	0.0901

[1] Triclinic crystal system, $P\bar{1}$ space group.

3. Results and discussion

Preliminary experiments on the titration of H_2L^{Me} in the presence of copper(II) ions showed that the first and second protons are lost at pH 6 and 9, correspondingly. Therefore, these values were chosen for the preparation of the complexes showing different degrees of deprotonation of the ligand. The acidity was adjusted with aqueous ammonia (pH = 6) and sodium carbonate (pH = 9). At pH = 6, nickel forms complexes with a NiL^R_2 stoichiometry (R = Ph, t-Bu). The complex with R = Ph (as $Ni(HL^{Ph})_2 \cdot EtOH \cdot 4H_2O$)

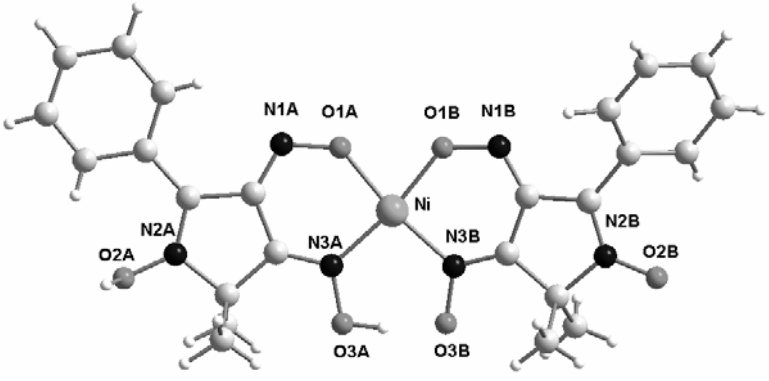

Fig. 1. The molecule of $Ni(HL^{Ph})_2$

was investigated by single crystal X-ray diffraction. The specific features of the compound are the N_2O_2 chromophore (Fig. 1), atypical of nickel dioximates [4] and the migration of

one of the oxime protons to the nitrone oxygen O2A. The latter circumstance formally converts the nitrone into hydroxylamine, however, a N–O(H) bond of 1.30 Å is too short for hydroxylamine, and strong conjugation within the heterocycle does not allow for the assignment of definite bond orders.

Unlike nickel, the copper complexes obtained at pH = 6 have a stoichiometry of $Cu_2L_3^R$. According to X-ray diffraction data for $Cu_2(HL^{Ph})_2L^{Ph}$ (as $Cu_2(HL^{Ph})_2L^{Ph}(H_2O)_5(EtOH)_2$), the complex is bi-nuclear with bridging oxime oxygens (Fig. 2). All three oxime ligands are coordinated in the N,O chelating mode. Only two oxime hydrogens were localized, which, considered together with charge balance, allows these compounds to be formulated as $Cu_2(HL^R)_2L^R$.

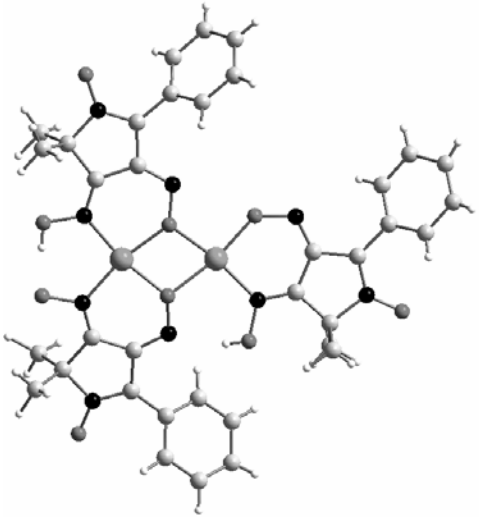

Fig. 2. $Cu_2(HL^{Ph})_2L^{Ph}$ fragment

The copper complexes obtained at pH = 9 have a common $CuNaL_2^R$ (R = Ph, t-Bu, Me) composition; our attempts to isolate similar complexes of nickel failed. According to X-ray diffraction analysis data for complexes with R = t-Bu, Me, the materials have a common CuL_2^R core, the ligands performing O,N chelating mode. One oxime hydrogen per CuL_2^R unit was localized in the $CuNaL_2^{t\text{-}Bu}$ compound (Fig. 3). This is in accordance with overall composition and results in a $CuNa(HL^R)L^R$ unit formula. CuL_2^R fragments (R = Me, t-Bu) are joined in dimers through additional axial contacts, made by copper ions to neighbouring oxime oxygens (Cu–O 2.54(3) Å, R = Me; 2.47(3) Å, R = t-Bu; Fig. 4). The supramolecular organization of $CuNa(HL^{Me})L^{Me}$ and $CuNa(HL^{t\text{-}Bu})L^{t\text{-}Bu}$ is different: in the former the dimers are isolated and sodium cations form separate tetramers, while in the latter sodium cations are coordinated by oxime oxygens (Fig. 3) and, being additionally bridged by water molecules, give rise to a 1-D coordination polymer (Fig. 5).

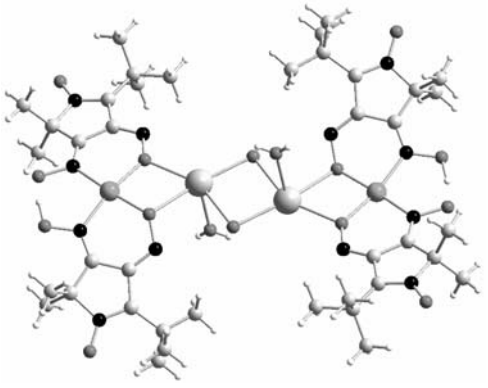

Fig. 3. Cu($HL^{t\text{-}Bu}$) $L^{t\text{-}Bu}$ units together with coordinated sodium ions and bridging water molecules

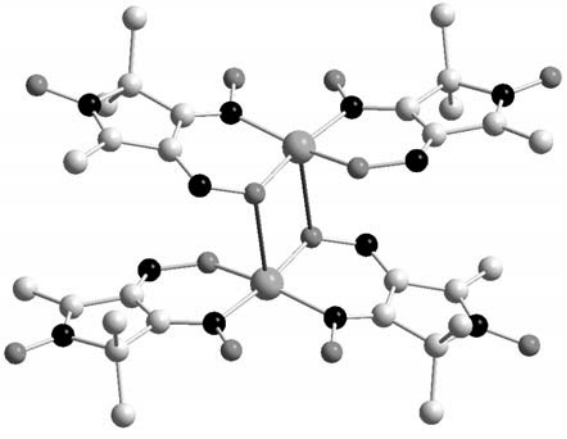

Fig. 4. Dimerization of Cu(HL^{R}) L^{R} units

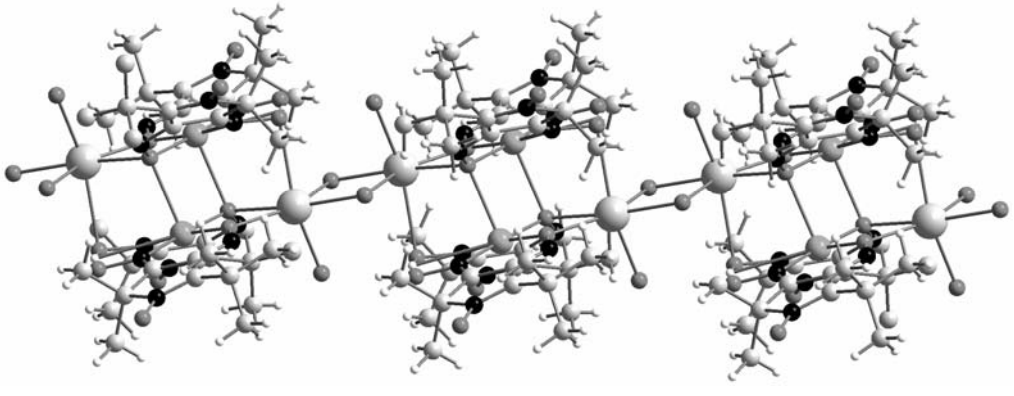

Fig. 5. Coordination polymer CuNa($HL^{t\text{-}Bu}$)($L^{t\text{-}Bu}$)·5H_2O, water of crystallization is omitted for clarity

The common feature of all the structurally characterized complexes is the unusual N,O coordination of dioxime, which is very atypical of other known dioximes. The ease of the second deprotonation step of H_2L^R is also noteworthy, which, combined with the tendency to additional coordination demonstrated in $CuNa(HL^{t\text{-}Bu})L^{t\text{-}Bu}$, makes these complexes promising as linking units between metal ions and opens the possibility for building coordination polymers.

Finally, the presence of "residual" protons makes these complexes potentially liable to oxidation and the formation of corresponding paramagnetic vynilnitroxide-containing species. We have succeeded in oxidating $Cu_2(HL^R)_2L^R$ (R = Ph, t-Bu) compounds: when solutions of these complexes in toluene are treated with PbO_2 (or *m*-nitroperoxobenzoic acid), they demonstrate a change in colour, from brown to deep-blue. The resulting solutions are stable for approximately an hour at ambient conditions; the solvent can be removed by an air stream, avoiding product decomposition provided that the temperature is below 0 ºC. The blue resin obtained can be solidified by grinding at 77 K followed by evacuation, the resulting dark-blue solids being stable at –15 ºC for several months at least.

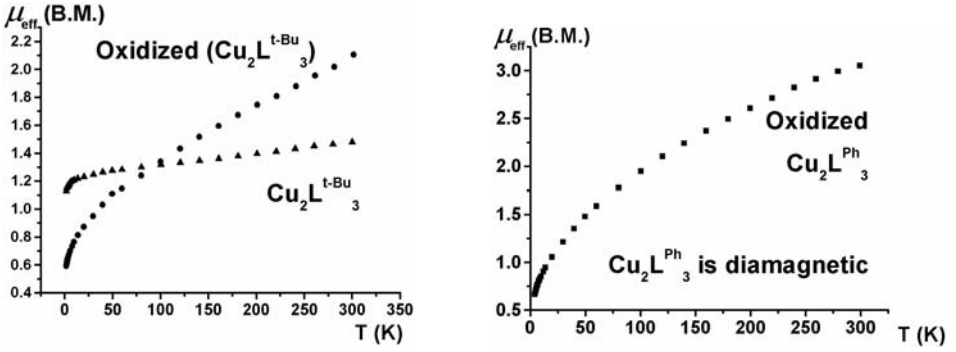

Fig. 6. Magnetic properties of the $Cu_2(HL^R)_2L^R$ complexes and their oxidation products

Figure 6 presents the temperature dependences of magnetic moment for $Cu_2(HL^{t\text{-}Bu})_2L^{t\text{-}Bu}$ ($Cu_2(HL^{Ph})_2L^{Ph}$ is diamagnetic) and their oxidation products. The data show an increment in magnetic moment for the oxidized compounds (approximately 1 B.M. for $Cu_2(HL^{t\text{-}Bu})_2L^{t\text{-}Bu}$ and 3 B.M. for $Cu_2(HL^{Ph})_2L^{Ph}$ at 300K). The magnetic behaviour of the starting complexes is determined by strong antiferromagnetic exchange interactions between the copper(II) ions propagated through the oxygen bridges, this phenomenon being well-documented in literature [5]. This antiferromagnetic exchange is expected to be generally preserved in the oxidation products. On the other hand, the nitroxide spin π-orbital, if nitroxide arises, is antisymmetrical with respect to the plane of the complex, while the copper(II) magnetic orbital, which is of a $d_{x^2-y^2}$ nature, is symmetrical with respect to this plane. Taking into account that the spin of vinylnitroxide must be strongly delocalised over the molecule [3] and therefore interact strongly with the spin of copper, one should expect a very strong exchange of fer-

romagnetic nature in this case. Qualitatively, this is in accordance with the increase in magnetic moment. Unfortunately, the inaccessibility of the high-temperature limit precludes an estimation of the number of spins per formula unit, and the lack of structural information prevents a more detailed interpretation of the magnetic data, therefore further studies are needed. The only doubtless conclusion is that the oxidation of $Cu_2(HL^R)_2L^R$ results in the formation of new paramagnetic centres, which we believe to be persistent vinylnitroxide radicals. This is an important result, since normally vinylnitroxides are transient species with lifetimes on the EPR scale. The crucial role of complexation should be stressed here, as the oxidation of H_2L^R results in the formation of diamagnetic furoxanes [6].

4. Conclusions

The first results obtained for copper(II) and nickel(II) complexes of pyrroline N-oxide dioximes show that these compounds are structurally quite different from common dioximates, the ligands performing the N,O chelating mode instead of the usual N,N one. The ability of these complexes to easily undergo deprotonation makes them promising candidates for the design of coordination polymers. Finally, copper dioximates with a $Cu_2(HL^R)_2L^R$ composition are the precursors of complexes with persistent vinylnitroxides stabilized by complexation.

References

[1] LLORET F., RUIZ R., JULVE M., FAUS J., JOURNAUX Y., CASTRO I., VERDAUGER M., Chem.Mater., 4 (1992), 1150.

[2] LLORET F., RUIZ R., CERVERA B., CASTRO I., JULVE M., FAUS J., REAL J.A., SAPIÑA F., JOURNAUX Y., COLIN J.CH., VERDAUGER M., J. Chem. Soc., Chem.Commun. (1994), 2615.

[3] REZNIKOV V.A., OVCHARENKO I.V., PERVUKHINA N.V., IKORSKII V.N., GRAND A.,OVCHARENKO V.I., Chem. Commun., 1999, 539.

[4] ALLEN F.H., KENNARD O., *Cambridge structural database ver. 5.20*, Chemical Design Automation News, 8 (1993), 31.

[5] HATFIELD W.E., [in:] Willett R.D (Ed.), *Magneto-Structural Correlations in Exchange Coupled Systems*, Reidel Publ. Comp., 1985. p. 555.

[6] ROSCHUPKINA G.I., *Interaction of chloro-substituted enaminoketones, β-oxonitrones and β-diketones with nucleophilic reagents*, Ph.D. Thesis, Novosibirsk, 2004.

Received 16 December 2004
Revised 21 March 2005

Materials Science-Poland, Vol. 23, No. 3, 2005

Polynuclear chain complexes of ruthenium(II, III) pivalate dimers linked by 2,5-dimethyl-*N,N′*-dicyanobenzoquinonediimine, 1,4-benzoquinone and 1,4-naphthoquinone*

D. YOSHIOKA[2], M. HANDA[1**], M. MIKURIYA[2], I. HIROMITSU[1], K. KASUGA[1]

[1]Department of Material Science, Interdisciplinary Faculty of Science and Engineering, Shimane University, 1060 Nishikawatsu, Matsue 690-8504, Japan

[2]Department of Chemistry and Open Research Center for Coordination Molecule-based Devices, School of Science and Technology, Kwansei Gakuin University, 2-1 Gakuen, Sanda 669-1337, Japan

Reactions of the ruthenium(II, III) pivalate dimer with 2,5-dimethyl-*N,N′*-dicyanobenzoquinonediimine (2,5-dmdcnqi), 1,4-benzoquinone (1,4-bq), and 1,4-naphthoquinone (1,4-nq) produce polynuclear chain complexes ($[Ru_2(O_2CCMe_3)_4(L)]_nX_n$, where L = 2,5-dmdcnqi, 1,4-bq, or 1,4-nq, and X = BF_4^- or PF_6^-). It has been shown that weak antiferromagnetic interaction (J = –0.15 cm^{-1}) operates between Ru(II, III) dimers in the 2,5-dmdcnqui complex.

Key words: *Ru(II, III) dimer; dicyanobenzoquinonediimine; p-quinones ; polymer complexes*

1. Introduction

In metal carboxylate dimers ($[Ru_2(O_2CR)_4]^{m+}$, m = 0–2) with a lantern-like structure ruthenium(II, II or II, III) dimers are quite unique, because they are paramagnetic with two or three unpaired electrons accommodated in their degenerated π^* and δ^* orbitals based on the metal-metal bond ($\sigma^2\pi^4\delta^2(\pi^*\delta^*)^4$ for Ru(II, II) or $\sigma^2\pi^4\delta^2(\pi^*\delta^*)^3$ for Ru(II, III) electronic configurations), although they have a large zero-field splitting (D = ca. 300 cm^{-1} for Ru(II, II) and ca. 60 cm^{-1} for Ru(II, III) [1–5]. Recently, there

*The paper presented at the 14th Winter School on Coordination Chemistry, Karpacz, Poland, 6–10 December, 2004.

**Corresponding author, e-mail: handam@riko.shimane-u.ac.jp

have been many efforts to use these dimers as building blocks in combination with bridging ligands to produce new magnetic materials [6–13]. We have studied polynuclear and oligonuclear compounds of ruthenium(II, II or II, III) carboxylate dimers ($[Ru_2(O_2CR)_4]^{+/0}$), linked by nitronylnitroxide radicals [14–20] and *N,N'*-didentate ligands such as pyrazine and 4,4′-bipyridine [21, 22]. Beside these linkage ligands, the electron acceptors 7,7,8,8-tetracyanoquinodimethane (tcnq) and 9,10-anthraquinone (9,10-aq) have also been employed in combination with ruthenium(II, III) pivalate dimers to produce the tetranuclear complexes $[\{Ru_2(O_2CCMe_3)_4(H_2O)\}_2(L)](BF_4)_2$ (**1**: L = tcnq, and **2**: L = 9,10-aq) [23, 24], of which the "dimer-of-dimers" structures were crystallographically determined for **1**. It has also been confirmed that tcnq and 9,10-aq work as neutral linkage ligands and mediate weak magnetic interactions between dimetal units in the tetranuclear complexes **1** and **2**.

In this study, we used 2,5-dimethyl-*N,N'*-dicyanobenzoquinonediimine (2,5-dmdcnqi), 1,4-benzoquinone (1,4-bq), and 1,4-naphthoquinone (1,4-nq) (Scheme 1a) for the reaction with the ruthenium(II, III) pivalate dimer (Scheme 1b) in benzene. The obtained compounds were found to be polynuclear chain complexes, described as $[Ru_2(O_2CCMe_3)_4(L)]_nX_n$, where L = 2,5-dmdcnqi, 1,4-bq, or 1,4-nq, and X = BF_4^- or PF_6^-.

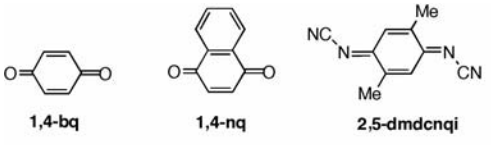

a) employed linkage ligands

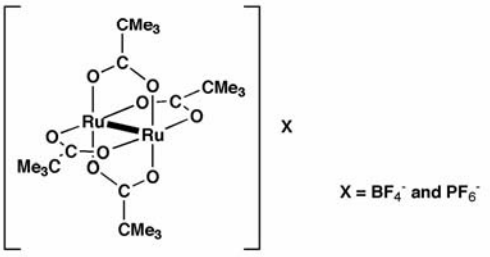

b) ruthenium(II,III) pivalate dimers

Scheme 1

2. Experimental

Preparations. The tetrafluoroborate and hexafluorophosphate salts, $[Ru_2(O_2CCMe_3)_4(H_2O)_2]X$ (X = BF_4^- or PF_6^-) and 2,5-dmdcnqi were prepared according to methods reported in literature [25, 26]. The *p*-quinones 1,4-bq and 1,4-nq were used as supplied by Wako Chemicals.

$[Ru_2(O_2CCMe_3)_4(2,5\text{-dmdcnqi})]_n(BF_4)_n \cdot 2.5nH_2O$ (3). 50 mg (0.069 mmol) of $[Ru_2(O_2CCMe_3)_4(H_2O)_2]BF_4$ was put into a Schlenk tube and heated to 60 °C under vacuum for one hour in order to remove the axial water molecules, and then dissolved in benzene (5 cm^3) under argon. A benzene solution (10 cm^3) of 2,5-dmdcnqi (25 mg, 0.136 mmol) was subsequently added to the tube and stirred overnight with the water-removed tetrafluoroborate salt at room temperature under argon. The resultant precipitate was collected by filtration, washed with benzene, and dried under vacuum to give a brown powder. The yield was 42 mg (67% based on $[Ru_2(O_2CCMe_3)_4(H_2O)]BF_4$). Anal. Found C, 38.83; H, 5.01; N, 6.39. Calcd. for $C_{30}H_{49}BF_4N_4O_{10.5}Ru_2$: C, 39.05; H, 5.35; N, 6.07. IR (KBr) ν(CN) 2174, 2110, $\nu_{as}(CO_2)$ 1481, $\nu_s(CO_2)$ 1419, $\nu(BF_4^-)$ 1080 cm^{-1}.

$[Ru_2(O_2CCMe_3)_4(1,4\text{-bq})]_n(PF_6)_n$ (4). This compound was obtained as a brown powder from a reaction of the anhydrous hexafluorophosphate salt, which was obtained by heating $[Ru_2(O_2CCMe_3)_4(H_2O)_2]PF_4$ (30 mg, 0.038 mmol) to 120 °C under vacuum, with 1,4-bq (4.5 mg, 0.042 mmol) in benzene using the same method as for **3**. The yield was 19 mg (58% based on $[Ru_2(O_2CCMe_3)_4(H_2O)_2]PF_6$). Anal. Found C, 36.20; H, 4.51. Calcd. for $C_{26}H_{40}F_6O_{10}PRu_2$: C, 36.33; H, 4.69. IR (KBr) ν(CO) 1657, 1600, $\nu_{as}(CO_2)$ 1485, $\nu_s(CO_2)$ 1420, $\nu(PF_6^-)$ 844 cm^{-1}.

$[Ru_2(O_2CCMe_3)_4(1,4\text{-nq})]_n(PF_6)_n \cdot 3nH_2O$ (5). This compound was obtained as a reddish-brown powder by treating $[Ru_2(O_2CCMe_3)_4(H_2O)_2]PF_6$ (30 mg, 0.038 mmol) with 1,4-nq (7 mg, 0.044 mmol) in the same way as **4**. The yield was 17 mg (46% based on $[Ru_2(O_2CCMe_3)_4(H_2O)_2]PF_6$). Anal. Found C, 37.09; H, 4.64. Calcd. for $C_{30}H_{48}F_6O_{13}PRu_2$: C, 37.39; H, 5.02. IR (KBr) ν(CO) 1662, 1642, $\nu_{as}(CO_2)$ 1484, $\nu_s(CO_2)$ 1420, $\nu(PF_6^-)$ 850 cm^{-1}.

Measurements. Elemental analyses for carbon, hydrogen, and nitrogen were carried out using a Perkin-Elmer Series II, CHN/O Analyzer. Infrared spectra (KBr pellets) and electronic spectra were measured with JASCO IR-700 and Shimadzu UV-3100 spectrometers, respectively. Magnetic susceptibilities were measured on a Quantum Design MPMS-5S SQUID susceptometer, operating at a magnetic field of 0.5T over the temperature range of 4.5–300 K. Susceptibilities were corrected for the diamagnetism of constituent atoms using Pascal's constant [27]. Effective magnetic moments were calculated from the equation: $\mu_{eff} = 2.828(\chi T)^{1/2}$, where χ is the magnetic susceptibility per Ru(II, III) dimer unit.

3. Results and discussion

Elemental analyses of the complexes obtained showed the stoichiometry of $[Ru_2(O_2CCMe_3)_4]^+$:L = 1:1, which is consistent with that for the polynuclear chain

structure of $[Ru_2(O_2CCMe_3)_4(L)]_nX_n$ (L = 2,5-dmdcnqi and X = BF_4^- for complex **3**; L = 1,4-bq and X = PF_6^- for complex **4**; L = 1,4-nq and X = PF_6^- for complex **5**). These complexes are not stable in air because they easily replace their axial ligands with atmospheric water molecules, although **3** is relatively stable compared to **4** and **5**. It is noteworthy that the complex formation did not occur for the reactions of the tetrafluoroborate salt $[Ru_2(O_2CCMe_3)_4(H_2O)_2]BF_4$ with 1,4-bq and 1,4-nq. It is unclear why the complex formation occurred in the case of 9,10-aq and gave the tetranuclear complex $[\{Ru_2(O_2CCMe_3)_4(H_2O)\}_2(9,10\text{-aq})](BF_4)_2$ (**2**).

In the IR spectra of the powder samples (KBr pellets) of complexes **3–5** there are two strong bands for each complex: at 1419 and 1481 cm^{-1} for **3**, 1420 and 1485 cm^{-1} for **4**, and 1420 and 1484 cm^{-1} for **5**. They are assigned to carbonyl stretching modes of the carboxylato group in the Ru(II, III) dimeric core, because the parent dimer complexes $[Ru_2(O_2CCMe_3)_4(H_2O)_2]X$ (X = BF_4^- or PF_6^-) show bands at 1420 and 1490 cm^{-1} [18, 22, 24]. The other carbonyl stretching bands, observed at 1600 and 1657 cm^{-1} for **4,** and at 1642 and 1662 cm^{-1} for **5,** originate from the linkage *p*-quinones 1,4-bq and 1,4-nq [28]. The bands based on the CN group of 2,5-dmdcnqi appear at 2216 and 2104 cm^{-1} for **3** [29, 30]. The bands at 1080 for **3**, 844 for **4**, and 850 cm^{-1} for **5** are due to the counter ions BF_4^- and PF_6^- [31]. These IR-spectral results strongly support the formation of the polynuclear chain complexes $[Ru_2(O_2CCMe_3)_4(L)]X$, where L = 2,5-dmdcnqi, 1,4-bq, or 1,4-nq, and X = BF_4^- or PF_6^-.

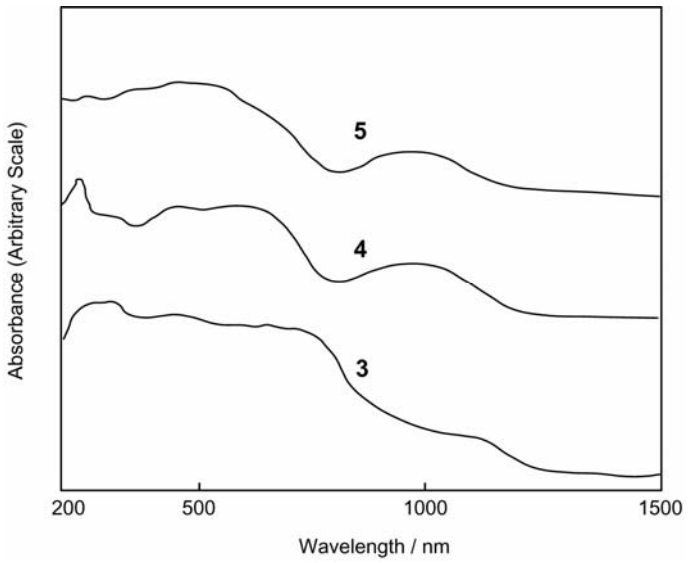

Fig. 1. Reflectance spectra of **3**, **4** and **5**

Diffuse reflectance spectra of **3**–**5** are displayed in Fig. 1. All of the complexes have absorption bands ascribed as the $\delta(Ru_2) \rightarrow \delta^*(Ru_2)$ transition within the Ru(II, III) dimeric core around 1000 nm, though the band of **3** appears as a shoulder, due to the intensive band in the visible region (below 800 nm) assigned to the $\delta^*/\pi^*(Ru_2) \rightarrow \sigma^*(Ru–O)$ transition and

considered to be red-shifted to this region by the stronger σ-donation of 2,5-dmdcnqi [22]; the parent complex, $[Ru_2(O_2CCMe_3)_4(H_2O)_2]BF_4$, shows a corresponding band at 545 nm in addition to the $\delta(Ru_2)\rightarrow\delta^*(Ru_2)$ transition band at 990 nm [22].

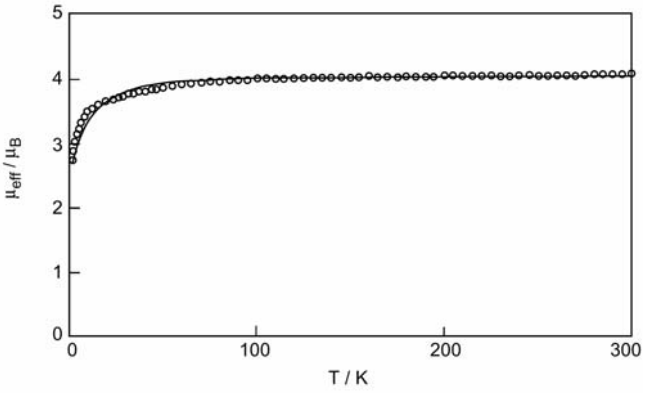

Fig. 2. Temperature dependence of the effective magnetic moment of **3**. The solid line was calculated for the parameters described in the text

Magnetic-susceptibility data could be obtained only for complex **3,** because of the relative instability of complexes **4** and **5**, which decomposed before being measured. The temperature dependence of the magnetic moment of **3** is displayed in Fig. 2. The moment at room temperature (300 K) is $4.10\mu_B$, which is slightly larger than the spin-only value calculated for the three unpaired electrons within the Ru(II, III) dimeric core ($3.87\mu_B$) and slightly lower than that of the parent complex $[Ru_2(O_2CCMe_3)_4(H_2O)_2]BF_4$ ($4.31\mu_B$ at 300 K) [18]. The moment decreases slowly when temperature falls from 300 K to 10 K, and then drops relatively rapidly until 4.5 K (the lower end of the measured temperatures). This behaviour is considered to originate from the antiferromagnetic interaction between Ru(II, III) dimers, as well as from the zero-field splitting within the dimeric core; no drop in the low temperature range (below ca. 10 K) was found for $[Ru_2(O_2CCMe_3)_4(H_2O)_2]BF_4$ [32]. The model illustrated in Scheme 2 was applied in order to analyze the magnetic behaviour, using a molecular-field approximation for the interaction between Ru(II, III) dimers (z, the number of neighboring spin centers, is set to 2 in approximation) [3,18,22,27,33]. As shown by the solid line in Fig. 2, the temperature-dependent profile could be roughly reproduced with $J = -0.15 cm^{-1}$, $D = 20\ cm^{-1}$ (the parameter for zero-field splitting), and $g = 2.1$ (the g factor). The calculated line somewhat disagrees with the experimental values at low temperatures (T below ca. 50 K), implying that an improved model that includes parameters for interactions other than those in Scheme 2 may be needed to complete the analysis, which may be possible when the crystal structure is given for **3**. It is obvious that a weak antiferromagnetic interaction exists between the Ru(II, III) dimmers, because the drop in the moment below 10 K cannot be reproduced without the J value ($-0.15\ cm^{-1}$). The value of J for **3** is the same as that for the tcnq-bridged

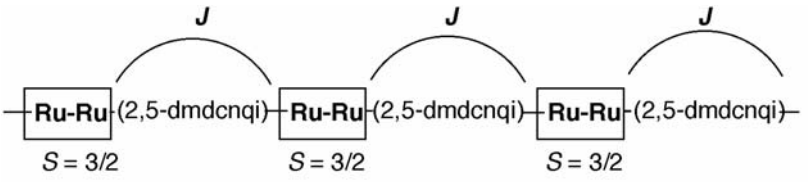

Scheme 2

tetranuclear complex **1** ($J = -0.15$ cm^{-1}) [23]. The value of D for **3** (20 cm^{-1}) is relatively small, but considered not to be unusual – similarly small values have been observed for complexes of ruthenium(II, III) carboxylate dimers [20, 34].

4. Conclusions

Polynuclear chain complexes $[Ru_2(O_2CCMe_3)_4(L)]X$ (L = 2,5-dmdcnqi, 1,4-bq, or 1,4-nq; X = BF_4^- or PF_6^-) were obtained by reactions in benzene between ruthenium (II, III) pivalate dimers and the corresponding linkage ligands with an electron-accepting nature. Complexes with 1,4-bq and 1,4-nq were unstable in air, but the complex with 2,5-dmdcnqi was stable enough to be employed in magnetic measurement. It was found that the magnetic interaction between Ru(II, III) dimers through the linkage ligands is weakly antiferromagnetic ($J = -0.15$ cm^{-1}).

Acknowledgement

The present work was partially supported by Grants-in-Aid for Scientific Research No. 14540516 and 16550062 from the Ministry of Education, Culture, Sports, Science and Technology.

References

[1] COTTON F.A., WALTON R.A., *Multiple Bonds between Metal Atoms*, 2nd Ed., Oxford University Press, New York, 1993, p. 399.
[2] AQUINO M.A.S., Coord. Chem. Rev., 170 (1998), 141.
[3] TELSER J., DRAGO R.S., Inorg. Chem., 23 (1984), 3114.
[4] COTTON F.A., MISKOWSKI V.M., ZHONG B., J. Am. Chem. Soc., 111 (1989), 6177.
[5] ESTIU G., CUKIERNIK F.D., MALDIVI P., POIZAT O., Inorg. Chem., 38 (1999), 3030.
[6] AQUINO M.A.S., Coord. Chem. Rev., 248 (2004), 1025.
[7] CUKIERNIK F.D., GIROUD-GODQUIN A.-M., MALDIVI P., MARCHON J.-C., Inorg. Chim. Acta, 215 (1994), 203.
[8] BECK E.J., DRYSDALE K.D., THOMPSON L.K., LI L., MURPHY C.A., AQUINO M.A.S., Inorg. Chim. Acta, 279 (1998), 121.
[9] WESEMANN J.L., CHISHOLM M.H., Inorg. Chem., 36 (1997), 3258.
[10] MIYASAKA H., CAMPOS-FERNÁNDEZ C.S., CLÉRAC R., DUNBAR K.R., Angew. Chem. Int. Ed., 39 (2000), 3831.
[11] MIYASAKA H., CLÉRAC R., CAMPOS-FERNÁNDEZ C.S., DUNBER K.R., J. Chem. Soc. Dalton Trans., (2001), 858.

[12] LIA Y., SHUM W.W., MILLER J.S., J. Am. Chem. Soc., 124 (2002), 9336.
[13] YOSHIOKA D., MIKURIYA M., HANDA M., Chem. Lett., 24 (2002) 1044.
[14] HANDA M., SAYAMA Y., MIKURIYA M., NUKADA R., HIROMITSU I., KASUGA K., Chem. Lett. (1996), 201.
[15] HANDA M., SAYAMA Y., MIKURIYA M., NUKADA R., HIROMITSU I., KASUGA K., Bull. Chem. Soc. Jpn., 71 (1998), 119.
[16] SAYAMA Y., HANDA M., MIKURIYA M., HIROMITSU I., KASUGA K., Chem. Lett. (1998), 777.
[17] SAYAMA Y., HANDA M., MIKURIYA M., HIROMITSU I., KASUGA K., Chem. Lett. (1999), 453.
[18] SAYAMA Y., HANDA M., MIKURIYA M., HIROMITSU I., KASUGA K., Bull. Chem. Soc. Jpn., 73 (2000), 2499.
[19] HANDA M., SAYAMA Y., MIKURIYA M., HIROMITSU I., KASUGA K., Mater. Sci., 21 (2003), 199.
[20] SAYAMA Y., HANDA M., MIKURIYA M., HIROMITSU I., KASUGA K., Bull. Chem. Soc. Jpn., 76 (2003), 769.
[21] HANDA M., YOSHIOKA D., MIKURIYA M., HIROMITSU I., KASUGA K., Mol. Cryst. Liq. Cryst., 376 (2002), 257.
[22] YOSHIOKA D., MIKURIYA M., HANDA M., Bull. Chem. Soc. Jpn., 77 (2004), 2205.
[23] HANDA M., YOSHIOKA D., SAYAMA Y., SHIOMI K., MIKURIYA M., HIROMITSU I., KASUGA K., Chem. Lett. (1999), 1033.
[24] YOSHIOKA D., HANDA M., AZUMA H., MIKURIYA M., HIROMITSU I., KASUGA K., Mol. Cryst. Liq. Cryst., 342 (2000), 133.
[25] BARRAL M.C., JIMÉNEZ-APARICIO R., PRIEGO J.L., ROYER E.C., GUTIÉNEZ-PUEBLA E., RUIZ-VALERO C., Polyhedron, 11 (1992), 2209.
[26] DRYSDALE K.D., BECK E.J., CAMERON T.S., ROBERTSON K.N., AQUINO M.A.S., Inorg. Chim. Acta, 256 (1997), 243.
[27] O'CONNOR C.J., Prog. Inorg. Chem., 29 (1982), 203.
[28] BERGER S., RIEKER A., *Identification and Determination of Quinones*, [in:] S. Patai (Ed.), *The Chemistry of Quinonoid Compounds*, Wiley, London, 1974, p. 163.
[29] MIYASAKA H., CAMPOS-FERNÁNDEZ C.S., CALÁN-MASCARÓS J.R., DUBER K.R., Inorg. Chem., 39 (2000), 5870.
[30] SCHIAVO S.L., BRUNO G., ZANELLO P., LASCHI F., PIRAINO P., Inorg. Chem., 36 (1997), 1004.
[31] NAKAMOTO K., *Infrared and Raman Spectra of Inorganic and Coordination Compounds*, 4th Ed., Wiley, New York, 1986.
[32] SAYAMA Y., HANDA M., MIKURIYA M., NUKADA R., HIROMITSU I., KASUGA K., [in:] *Coordnation Chemistry at the Turn of the Century*, Slovak. Tech. Univ. Press, Bratislava, 1999, p. 447.
[33] TELSER J., DRAGO R.S., Inorg. Chem., 24 (1985), 4765.
[34] JIMÉNEZ-APARICIO R., URBAMOS F.A., ARRIETA J.M., Inorg. Chem., 40 (2001), 613.

Received 16 December 2004
Revised 21 March 2005

Materials Science-Poland, Vol. 23, No. 3, 2005

Synthesis and structural characterization of a series of transition metal complexes with a tetradentate Schiff-base ligand derived from salicylaldehyde and 2-(2-aminoethylamino)ethanol*

M. MIKURIYA**, K. MATSUNAMI

Department of Chemistry and Open Research Center for Coordination Molecule-based Devices, School of Science and Technology, Kwansei Gakuin University, 2-1 Gakuen, Sanda 669-1337, Japan

A series of transition metal complexes with 1-[(2-hydroxyethyl)amino]-2-(salicylideneamino)ethane (H_2hase), [V(Hhase)$_2$]Cl (**1**), [VO_2(Hhase)] (**2**), [Cr(Hhase)$_2$]Cl (**3**), [Mn(Hhase)$_2$]Cl (**4**), [Fe(Hhase)$_2$]Cl (**5**), [Co(Hhase)$_2$]Cl (**6**), [Co(Hhase)$_2$]Br (**7**), [Co(Hhase)$_2$]I (**8**), [Co(Hhase)$_2$]NO_3 (**9**), [Co(Hhase)$_2$]NCS (**10**), [Co(Hhase)$_2$]ClO_4 (**11**), and [Co(Hhase)$_2$]$CH_3CO_2 \cdot H_2O$ (**12**), have been synthesized by template reactions of salicylaldehyde and 2-(2-aminoethylamino)ethanol with metal salts and characterized by infrared and electronic spectra and magnetic moments. The molecular structures of these complexes were determined by single-crystal X-ray structure analysis. All complexes, except for **2**, are mononuclear with an octahedral metal(III) ion, and the two Hhase ligands act as a meridional tridentate chelate forming hydrogen bonds with the counter anion. The two Hhase ligands are arranged so that the imino-nitrogen atoms are *trans,* while the phenoxo-oxygen atoms and the amino-nitrogen atoms are *cis*. Complex **2** comprises two vanadium (V) atoms with dioxo-bridges. A similar template reaction with copper(II) afforded [Cu(salen)] (H_2salen = *N*,*N*′-bis (salicylidene)ethylendiamine) (**13**) in a low yield.

Key words: *Schiff-base; first transition metal complex*

1. Introduction

There has been a considerable interest in the coordination chemistry of Schiff-base ligands, because of their feasibleness to make various kinds of metal complexes [1, 2]. This has resulted in a vast number of reports on Schiff-base metal complexes. Especially, salen-type tetradentate ligands (H_2salen = *N*,*N*′-bis(salicylidene)ethylendiamine) have been known since 1933 [3], their complexes became a standard system in

---

*The paper presented at the 14th Winter School on Coordination Chemistry, Karpacz, Poland, 6–10 December, 2004.

**Corresponding author, e-mail: junpei@ksc.kwansei.ac.jp

coordination chemistry, and their application as inorganic-organic composite materials was examined. We have been engaged in the chemistry of metal Schiff-base compounds with bridging groups [4–14]. Among Schiff-base-ligands, 1-[(2-hydroxyethyl)amino]-2-(salicylideneamino)ethane (H_2hase) is a unique ligand, which has a phenolic atom and alcoholic oxygen atom as potential bridging groups [9].

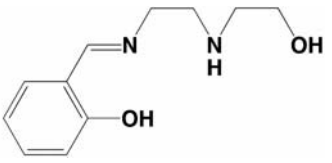

H_2hase

Although complexes of Schiff-base ligands have been reported for a number of transition metals, only a few crystal structures of metal complexes with 1-[(2-hydroxyethyl)amino]-2-(salicylideneamino)ethane have been reported. In the case of the manganese(III) complex, $[Mn(Hhase)_2]Br$, the two Hhase ligands coordinate to the metal atom meridionally, forming intramolecular hydrogen bonds with the counter anion [9]. This intramolecular hydrogen bonding could be interesting for potential inorganic-organic composite materials, because it may contribute to the stability of the metal complex and some functionalities such as anion-binding. Nonetheless, there are still few examples of metal complexes having intramolecular hydrogen bonds. In order to obtain more information on the coordination chemistry of this ligand, we have undertaken a systematic effort to prepare and structurally characterize the complexes formed by the Schiff-base ligand and first row transition metals, because the intra-hydrogen-bonding system is the case for the manganese(III) ion and no other such metal complexes are known to form for other metal ions. Herein we report our findings on vanadium(III), chromium(III), manganese(III), iron(III), and cobalt(III) complexes with the Schiff-base ligand H_2hase.

2. Experimental

Syntheses of the complexes. All reagents and solvents were purchased from commercial sources and used as received. All syntheses were performed under aerobic condition, except where specifically mentioned.

$[V(Hhase)_2]Cl$ (1). The manipulation for the preparation of this compound was carried out under Ar using standard Schlenk techniques. To an ethanol (10 ml) solution containing 2-(2-aminoethylamino)ethanol (120 mg, 1.2 mmol) and salicylaldehyde (103 mg, 0.84 mmol), vanadium(III) chloride (32 mg, 0.20 mmol) was added while stirring. The solution was placed at room temperature for three days. Purple plates were deposited and collected by filtration and dried *in vacuo* over P_2O_5: Yield 33 mg (33% on the basis of vanadium(III) chloride used). Found: C, 52.58; H, 5.99;

N, 11.35%. Calcd. for $C_{22}H_{30}ClN_4O_4V$: C, 52.75; H, 6.04; N, 11.19%. IR(hexachloro-1,3-butadiene, cm^{-1}): ν(OH) 3460 (sh), 3336; ν(NH) 3130, 3058; ν(C=N) 1613. μ_{eff}(288 K), μ_B 2.71. Λ_M (MeOH), $S \cdot mol^{-1} \cdot cm^2$ 120 (lit, range for 1:1 electrolytes [15], 80–115 $S \cdot mol^{-1} \cdot cm^2$). Diffuse reflectance spectrum: λ_{max}, nm 357, 525 sh. Electronic spectrum in MeOH λ_{max}, nm (ε, $dm^3 \cdot mol^{-1} \cdot cm^{-1}$) 312 (6030), 357 (7170), 395 sh (4660).

[VO_2(Hhase)] (2). To an ethanol (10 ml) solution of 2-(2-aminoethylamino)ethanol (128 mg, 1.2 mmol) and salicylaldehyde (103 mg, 0.64 mmol), vanadium(IV) oxydichloride (32 mg, 0.24 mmol) was added while stirring. The mixture was then filtered to remove any material that did not dissolve. After the filtrate was allowed to stand for one day at room temperature in air, pale yellow crystals appeared, which were filtered and dried in vacuo over P_2O_5: yield, 26 mg (42% on the basis of vanadium(IV) oxydichloride used). Found: C, 45.63; H, 5.18; N, 9.75%. Calcd. for $C_{11}H_{15}N_2O_4V$: C, 45.53; H, 5.21; N, 9.65%. IR(hexachloro-1,3-butadiene, cm^{-1}) ν(OH) 3334 (br); ν(NH) 3200 (s); ν(C=N) 1643 (s)). μ_{eff} (288 K), μ_B diamagnetic. Λ_M (MeOH), $S \cdot mol^{-1} \cdot cm^2$ 20. Diffuse reflectance spectrum: λ_{max}, nm 261, 351. Electronic spectrum in MeOH λ_{max}, nm (ε, $dm^3 \cdot mol^{-1} \cdot cm^{-1}$) 253 (10 700), 315 (3680), 480sh (800).

[Cr(Hhase)$_2$]Cl (3). 2-(2-Aminoethylamino)ethanol (122 mg, 1.2 mmol) and salicylaldehyde (103 mg, 0.84 mmol) were dissolved in ethanol (10 ml), then chromium(III) chloride hexahydrate (28 mg, 0.11 mmol) was added while stirring. After the mixture was allowed to stand for ten days at room temperature, dark-brown crystals appeared, which were filtered and dried *in vacuo* over P_2O_5: yield, 28 mg (51% on the basis of chromium(III) chloride hexahydrate used). Found: C, 52.32; H, 6.08; N, 10.91%. Calcd. for $C_{22}H_{30}ClCrN_4O_4$: C, 52.64; H, 6.02; N, 11.16%. IR(hexachloro-1,3-butadiene, cm^{-1}) ν(OH) 3420 (sh), 3336 (br); ν(NH) 3130 (s), 3058 (s); ν(C=N) 1613 (s). μ_{eff} (288 K), μ_B 3.65. Λ_M (MeOH), $S \cdot mol^{-1} \cdot cm^2$ 75. Diffuse reflectance spectrum: λ_{max}, nm 266, 417, 500 (sh), 625 (sh). Electronic spectrum in MeOH λ_{max}, nm (ε, $dm^3 \cdot mol^{-1} \cdot cm^{-1}$) 273 (18800), 397 (3570), 500sh (229).

[Mn(Hhase)$_2$]Cl (4). 2-(2-Aminoethylamino)ethanol (122 mg, 1.2 mmol) and salicylaldehyde (103 mg, 0.84 mmol) were dissolved in ethanol (10 ml), then manganese(II) chloride tetrahydrate (43 mg, 0.22 mmol) was added while stirring. The solution was allowed to stand for three days to give dark brown crystals, which were collected by filtration and dried *in vacuo* over P_2O_5: yield, 56 mg (51% on the basis of manganese(II) chloride tetrahydrate used). Found: C, 52.34; H, 6.21; N, 11.10%. Calcd. for $C_{22}H_{30}ClMnN_4O_4$: C, 52.36; H, 5.99; N, 11.24%. IR(hexachloro-1,3-butadiene, cm^{-1}) ν(OH) 3420 (sh), 3356 (br); ν(NH) 3176 (s), 3032 (s); ν(C=N) 1616 (s). μ_{eff} (288 K), μ_B 5.12. Λ_M (MeOH), $S \cdot mol^{-1} \cdot cm^2$ 83. Diffuse reflectance spectrum: λ_{max}, nm 277, 403, 525sh, 1350. Electronic spectrum in MeOH λ_{max}, nm (ε, $dm^3 \cdot mol^{-1} \cdot cm^{-1}$) 241 (21900), 300 (9780), 390 (2910), 580 (234).

[Fe(Hhase)$_2$]Cl (5). 2-(2-Aminoethylamino)ethanol (122 mg, 1.2 mmol) and salicylaldehyde (103 mg, 0.84 mmol) were dissolved in ethanol (10 ml), then iron(III)

chloride hexahydrate (33 mg, 0.12 mmol) was added while stirring. The solution was allowed to stand for three days to give dark brown crystals, which were collected by filtration and dried *in vacu*o over P_2O_5: yield, 45 mg (73% on the basis of iron(III) chloride hexahydrate used). Found: C, 52.18; H, 5.99, N, 11.38%. Calcd. for $C_{22}H_{30}FeN_4O_4Cl$: C, 52.24; H, 5.98; N, 11.08%. IR(hexachloro-1,3-butadiene, cm^{-1}) ν(OH) 3440 (sh), 3340 (br); ν(NH) 3114 (s), 3058 (s); ν(C=N) 1622 (s). μ_{eff} (288 K), μ_B 5.68. Λ_M (MeOH), $S \cdot mol^{-1} \cdot cm^2$, 86. Diffuse reflectance spectrum: λ_{max}, nm 325, 537, 634. Electronic spectrum in MeOH λ_{max}, nm (ε, $dm^3 \cdot mol^{-1} \cdot cm^{-1}$) 260 (26100), 321 (8740), 501 (1840).

[Co(Hhase)$_2$]Cl (6). 2-(2-Aminoethylamino)ethanol (158 mg, 1.5 mmol) and salicylaldehyde (124 mg, 1.0 mmol) were dissolved in ethanol (10 ml), then cobalt(II) chloride hexahydrate (37 mg, 0.16 mmol) was added while stirring. The solution was left to stand for three days at room temperature to give dark brown crystals, which were collected by filtration and dried in vacuo over P_2O_5: yield, 41 mg (50% on the basis of cobalt(II) chloride hexahydrate used). Found: C, 52.14; H, 6.02; N, 11.06%. Calcd. for $C_{22}H_{30}ClCoN_4O_4$: C, 51.93; H, 5.94; N, 11.01%. IR(hexachloro-1,3 -butadiene, cm^{-1}) ν(OH) 3440 (sh), 3338 (br); ν(NH) 3112 (s), 3042 (s); ν(C=N) 1640 (s).μ_{eff} (288 K), μ_B diamagnetic. Λ_M (MeOH), $S \cdot mol^{-1} \cdot cm^2$ 79. Diffuse reflectance spectrum: λ_{max}, nm 306, 394, 484, 641, 1200. Electronic spectrum in MeOH λ_{max}, nm (ε, $dm^3 \cdot mol^{-1} \cdot cm^{-1}$) 246 (52800), 300 (8810), 385 (5380), 475 (881), 640 (95).

[Co(Hhase)$_2$]Br (7). The complex was prepared in the same way as Co(Hhase)$_2$]Cl, except that cobalt(II) bromide hexahydrate was used instead of cobalt(II) chloride hexahydrate: yield, 46 mg (69% on the basis of cobalt(II) bromide hexahydrate used). Found: C, 47.97; H, 5.49; N, 10.13%. Calcd. for $C_{22}H_{30}BrCoN_4O_4$: C, 47.75; H, 5.46; N, 10.13%. IR(hexachloro-1,3-butadiene, cm^{-1}) ν(OH) 3460 (sh), 3358 (br); ν(NH) 3114 (s), 3058 (s); ν(C=N) 1640 (s). μ_{eff} (288 K), μ_B diamagnetic. Λ_M (MeOH), $S \cdot mol^{-1} \cdot cm^2$ 88. Diffuse reflectance spectrum: λ_{max}, nm 307, 400, 490, 646. Electronic spectrum in MeOH λ_{max}, nm (ε, $dm^3 \cdot mol^{-1} \cdot cm^{-1}$) 246 (40700), 300 (7890), 385 (4360), 475 (868), 639 (87).

[Co(Hhase)$_2$]I (8). The complex was prepared in the same way as [Co(Hhase)$_2$]Cl, except that cobalt(II) iodide hexahydrate was used instead of cobalt(II) chloride hexahydrate: yield, 44 mg (67% on the basis of cobalt(II) iodide hexahydrate used). Found: C, 44.02; H, 5.04; N, 9.33%. Calcd. for $C_{22}H_{30}CoIN_4O_4$: C, 44.26; H, 5.10; N, 9.30%. IR(hexachloro-1,3-butadiene, cm^{-1}) ν(OH) 3390 (br); ν(NH) 3104 (s); ν(C=N) 1636 (s). μ_{eff} (288 K), μ_B diamagnetic. Λ_M (MeOH), $S \cdot mol^{-1} \cdot cm^2$ 94. Diffuse reflectance spectrum: λ_{max}, nm 303, 396, 481, 642. Electronic spectrum in MeOH λ_{max}, nm (ε, $dm^3 \cdot mol^{-1} \cdot cm^{-1}$) 235 (41700), 305 (7350), 385 (4570), 470 (833), 641 (100).

[Co(Hhase)$_2$]NO$_3$ (9). The complex was prepared in the same way as [Co(Hhase)$_2$]Cl, except that cobalt(II) nitrate hexahydrate was used instead of cobalt(II) chloride hexahy-

drate: yield, 17 mg (24% on the basis of cobalt(II) nitrate hexahydrate used). Found: C, 49.44; H, 5.83; N, 13.22%. Calcd. for $C_{22}H_{30}CoN_5O_7$: C, 49.35; H, 5.65; N, 13.08%. IR(hexachloro-1,3-butadiene, cm^{-1}) ν(OH) 3396 (br); ν(NH) 3190 (s), 3046 (s); ν(C=N) 1639 (s). μ_{eff} (288 K), μ_B diamagnetic. Λ_M (MeOH), $S \cdot mol^{-1} \cdot cm^2$ 96. Diffuse reflectance spectrum: λ_{max}, nm 304, 397, 482, 645. Electronic spectrum in MeOH λ_{max}, nm (ε, $dm^3 \cdot mol^{-1} \cdot cm^{-1}$) 246 (49200), 300 (8890), 385 (4860), 475 (961), 642 (99).

[Co(Hhase)$_2$]NCS (10). The complex was prepared in the same way as [Co(Hhase)$_2$]Cl, except that cobalt(II) thiocyanate was used instead of cobalt(II) chloride hexahydrate: yield, 76 mg (65% on the basis of cobalt(II) thiocyanate used). Found: C, 51.69; H, 5.64; N, 13.30%. Calcd. for $C_{23}H_{30}CoN_5O_4S$: C, 51.97; H, 5.69; N, 13.18%. IR(hexachloro-1,3-butadiene, cm^{-1}) ν(OH) 3352 (br); ν(NH) 3212 (s), 3158 (s); ν(C=N) 1643 (s). μ_{eff} (288 K), μ_B diamagnetic. Λ_M (MeOH), $S \cdot mol^{-1} \cdot cm^2$ 90. Diffuse reflectance spectrum: λ_{max}, nm 305, 392, 478, 645. Electronic spectrum in MeOH λ_{max}, nm (ε, $dm^3 \cdot mol^{-1} \cdot cm^{-1}$) 246 (40100), 300 (7140), 385 (4370), 475 (761), 642 (90).

[Co(Hhase)$_2$]ClO$_4$ (11). The complex was prepared in the same way as [Co(Hhase)$_2$]Cl, except that cobalt(II) perchlorate hexahydrate was used instead of cobalt(II) chloride hexahydrate: yield, 35 mg (51% on the basis of cobalt(II) perchlorate hexahydrate used). Found: C, 46.10; H, 5.66; N, 9.80%. Calcd. for $C_{22}H_{30}ClCoN_4O_{12}$: C, 46.12; H, 5.28; N, 9.78%. IR(hexachloro-1,3-butadiene, cm^{-1}) ν(OH) 3510 (br); ν(NH) 3234 (s); ν(C=N) 1633 (s). μ_{eff} (288 K), μ_B diamagnetic. Λ_M (MeOH), $S \cdot mol^{-1} \cdot cm^2$ 119. Diffuse reflectance spectrum: λ_{max}, nm 304, 396, 479, 639. Electronic spectrum in MeOH λ_{max}, nm (ε, $dm^3 \cdot mol^{-1} \cdot cm^{-1}$) 251 (38900), 305 (4700), 386 (3810), 480 (473), 645 (85).

[Co(Hhase)$_2$]CH$_3$CO$_2$·H$_2$O (12). The complex was prepared in the same way as [Co(Hhase)$_2$]Cl, except that cobalt(II) acetate tetrahydrate was used instead of cobalt(II) chloride hexahydrate: yield, 28 mg (34% on the basis of cobalt(II) acetate tetrahydrate used). Found: C, 52.36; H, 6.41; N, 10.18%. Calcd. for $C_{24}H_{35}CoN_5O_7$: C, 52.25; H, 6.26; N, 10.45%. μ_{eff} (288 K), μ_B diamagnetic. Λ_M (MeOH), $S \cdot mol^{-1} \cdot cm^2$ 67. Diffuse reflectance spectrum: λ_{max}, nm 307, 389, 475, 627. Electronic spectrum in MeOH λ_{max}, nm (ε, $dm^3 \cdot mol^{-1} \cdot cm^{-1}$) 246 (44000), 305 (7860), 384 (4500), 470 (879), 639 (93).

[Cu(salen)] (13). 2-(2-Aminoethylamino)ethanol (100 mg, 0.96 mmol) and salicylaldehyde (90 mg, 0.74 mmol) were dissolved in ethanol (5 ml), then copper(II) chloride dihydrate (32 mg, 0.19 mmol) was added while stirring. After adding 50 mg (0.85 mmol) of triethylamine, the resulting solution was allowed to stand for two weeks to give dark violet crystals, which were collected by filtration and dried *in vacuo* over P_2O_5: yield, 8 mg (13% on the basis of copper(II) chloride dihydrate used). IR(hexachloro-1,3-butadiene, cm^{-1}) ν(C=N) 1646, 1628.

Measurements. Carbon, hydrogen, and nitrogen analyses were carried out using a Perkin-Elmer 2400 Series II CHNS/O Analyzer. Infrared spectra were recorded with a JASCO Infrared Spectrometer model IR700 in the 4000–400 cm^{-1} region on a hexachloro-1,3-butadiene mull. Electronic conductivities were measured on a Horiba conductivity meter DS-14. Electronic spectra were measured with a Shimadzu UV-vis –NIR Recording Spectrophotometer Model UV-3100. Room-temperature magnetic moments were determined with a Sherwood MSB-AUTO magnetic susceptibility balance. Susceptibilities were corrected for the diamagnetism of the constituent atoms using Pascal's constants [16]. The effective magnetic moments were calculated from the equation $\mu_{\text{eff}} = 2.828\sqrt{\chi_{\text{M}}T}$, where χ_{M} is the molar magnetic susceptibility.

X-Ray crystal structure analysis. Unit-cell parameters and intensities were measured on an Enraf–Nonius CAD4 diffractometer using graphite-monochromated Mo-K_α radiation at 25±1 °C. Unit-cell parameters were determined by least-squares refinement based on 25 reflections with $20° \le 2\theta \le 30°$.

Table 1. Crystal data of the complexes

Complex	$[V(Hhase)_2]Cl$ (**1**)	$[VO_2(Hhase)]$ (**2**)	$[Cr(Hhase)_2]Cl$ (**3**)
Formula	$C_{22}H_{30}VN_4O_4Cl$	$C_{11}H_{15}VN_2O_4$	$C_{22}H_{30}CrN_4O_4Cl$
F.W.	500.90	290.19	501.95
Crystal system	monoclinic	monoclinic	monoclinic
Space group	$P2_1/n$	$P2_1/n$	$P2_1/n$
a, Å	9.885(6)	11.239(5)	9.918(6)
b, Å	24.97(1)	6.830(2)	24.81(1)
c, Å	10.514(6)	16.052(8)	10.445(7)
β, °	115.63(3)	105.20(2)	116.08(3)
V, $Å^3$	2339(2)	1189(1)	2309(2)
Z	4	4	4
D_m, $g·cm^{-3}$	1.40	1.43	1.44
D_c, $g·cm^{-3}$	1.42	1.44	1.44
μMo-K_α, cm^{-1}	5.59	8.062	6.336
Crystal size, mm	0.35×0.30×0.20	0.43×0.23×0.20	0.40×0.35×0.15
$F(000)$	1048	600	1052
2θ range, °	1.0–48.0	1.0–50.0	1.0–48.0
Total No. of observed reflections	3765	2305	3731
No. of observations ($I \ge 3\sigma$)	1384	1111	1752
Total No. of variables	289	163	289
$h;k;l$ range	–11/11; 0/28; 0/12	–13/13; 0/8; 0/19	–11/11; 0/28; 0/12
Largest diff. peak, $eÅ^{-3}$	0.299	0.615	0.291
R	0.047	0.059	0.048
R_w	0.052	0.068	0.055

Table 1 (continued)

Complex	[Mn(Hhase)$_2$]Cl (**4**)	[Fe(Hhase)$_2$]Cl (**5**)
Formula	$C_{22}H_{30}MnN_4O_4Cl$	$C_{22}H_{30}FeN_4O_4Cl$
F.W.	504.90	505.80
Crystal system	monoclinic	monoclinic
Space group	$P2_1/n$	$P2_1/n$
a, Å	9.880(3)	9.857(3)
b, Å	25.299(3)	24.936(3)
c, Å	10.437(3)	10.470(3)
β, °	116.59(1)	115.71(1)
V, Å^3	2232.9(9)	2318(1)
Z	4	4
D_m, g·cm^{-3}	1.43	1.46
D_c, g·cm^{-3}	1.44	1.45
μMo-K$_\alpha$, cm^{-1}	6.931	7.999
Crystal size, mm	0.30×0.24×0.21	0.40×0.25×0.17
F(000)	1056	1060
2θ range, °	1.0–48.0	1.0–46.0
Total No. of observed reflections	3757	3315
No. of observations ($I \geq 3\sigma$)	2412	2420
Total No. of variables	289	289
h;k;l range	–11/11; 0/29; 0/11	–10/10; 0/29; 0/11
Largest diff. peak, eÅ^{-3}	0.488	0.273
R	0.037	0.031
R_w	0.040	0.033

Complex	[Co(Hhase)$_2$]Cl (**6**)	[Co(Hhase)$_2$]Br (**7**)	[Co(Hhase)$_2$]I (**8**)
Formula	$C_{22}H_{30}CoN_4O_4Cl$	$C_{22}H_{30}CoN_4O_4Br$	$C_{22}H_{30}CoN_4O_4I$
1	2	3	4
F.W.	508.89	553.34	600.34
Crystal system	monoclinic	monoclinic	monoclinic
Space group	$P2_1/n$	$P2_1/n$	$P2_1/n$
a, Å	9.828(3)	9.806(2)	9.788(2)
b, Å	24.913(3)	25.070(3)	24.344(3)
c, Å	10.427(3)	10.486(3)	11.080(3)
β, °	115.89(1)	115.041(9)	111.11(1)
V, Å^3	2297(1)	2335.6(9)	2463(1)
Z	4	4	4
D_m, g·cm^{-3}	1.50	1.63	1.62
D_c, g·cm^{-3}	1.49	1.60	1.62
μMo-K$_\alpha$, cm^{-1}	8.968	24.63	19.67
Crystal size, mm	0.37×0.25×0.19	0.43×0.18×0.17	0.45×0.21×0.19
F(000)	1072	1136	1208
2θ range, °	1.0–47.0	1.0–48.0	1.0–48.0
Total No. of observed reflections	3471	3764	3973

Table 1 (continued)

1	2	3	4
No. of observations ($I \geq 3\sigma$)	2420	2258	2812
Total No. of variables	289	289	289
$h;k;l$ range	−11/11; 0/27; 0/11	−11/11; 0/28; 0/11	−11/11; 0/27; 0/12
Largest diff. peak, eÅ^{-3}	0.256	0.353	0.614
R	0.030	0.034	0.039
R_w	0.033	0.037	0.043

Complex	$[Co(Hhase)_2]NO_3$ (**9**)	$[Co(Hhase)_2]NCS$ (**10**)	$[Co(Hhase)_2]ClO_4$ (**11**)
Formula	$C_{22}H_{30}CoN_5O_8$	$C_{23}H_{30}CoN_5O_4S$	$C_{22}H_{30}CoN_4O_8Cl$
F.W.	551.44	531.52	572.89
Crystal system	$P2_1/n$	$P2_1/n$	$P2_1/n$
Space group	monoclinic	monoclinic	monoclinic
a, Å	9.757(5)	9.798(4)	9.725(2)
b, Å	25.656(6)	22.402(5)	23.590(3)
c, Å	10.532(5)	11.485(4)	11.665(3)
β, °	114.55(2)	108.11(2)	110.98(1)
V, Å^3	2397(1)	2396(1)	2498(1)
Z	4	4	4
D_m, g·cm^{-3}	1.52	1.46	1.53
D_c, g·cm^{-3}	1.53	1.47	1.52
μMo-K$_\alpha$, cm^{-1}	7.628	8.354	8.136
Crystal size, mm	0.35×0.28×0.24	0.50×0.33×0.27	0.51×0.50×0.25
F(000)	1120	1112	1192
2θ range, °	1.0–48.0	1.0–50.0	1.0–48.0
Total No. of observed reflections	3859	4337	4019
No. of observations ($I \geq 3\sigma$)	2043	2258	2812
Total No. of variables	316	289	289
$h;k;l$ range	−11/11; 0/29; 0/12	−11/11; 0/26; 0/13	−11/11; 0/27; 0/13
Largest diff. peak, eÅ^{-3}	0.357	0.353	0.614
R	0.038	0.034	0.039
R_w	0.040	0.037	0.043

Complex	$[Co(Hhase)_2]CH_3CO_2 \cdot H_2O$ (**12**)	[Cu(salen)] (**13**)
Formula	$C_{24}H_{35}CoN_5O_7$	$C_{16}H_{14}CuN_2O_2$
1	2	3
F.W.	550.50	329.85
Crystal system	monoclinic	monoclinic
Space group	$P2_1/n$	$C2/c$
a, Å	9.658(2)	26.64(1)
b, Å	23.827(4)	6.969(5)
c, Å	11.459(3)	14.699(6)
β, °	104.59(1)	97.49(2)

Table 1 (continued)

1	2	3
V, Å^3	2552(1)	2705(2)
Z	4	8
D_m, g·cm^{-3}	1.45	1.63
D_c, g·cm^{-3}	1.43	1.62
μMo-K$_\alpha$, cm^{-1}	8.436	18.80
Crystal size, mm	0.40×0.40×0.20	0.40×0.35×0.21
F(000)	1156	1248
2θ range, °	1.0–48.0	1.0–49.0
Total No. of observed reflections	4113	2463
No. of observations ($I \geq 3\sigma$)	2403	3188
Total No. of variables	316	190
h;k;l range	–11/11; 0/23; 0/17	–31/31; 0/8; 0/17
Largest diff. peak, eÅ^{-3}	0.357	0.484
R	0.038	0.041
R_w	0.040	0.054

The crystal data and details of data collection are given in Table 1. Intensity data were corrected for Lorentz-polarization effects, but not for absorption. The structures were solved by direct methods and refined by the full-matrix least-squares methods. All non-hydrogen atoms were refined with anisotropic thermal parameters. Hydrogen atoms were inserted at their calculated positions and fixed. The final discrepancy factors, $R = \Sigma||F_o| - |F_c||$, $\Sigma|F_o|$ and $R_w = [w\ (|F_o| - |F_c|)^2 / \Sigma w|F_o|^2]^{1/2}$, are listed in Table 1. The weighting scheme, $w = 1/[\sigma^2(|F_o|) + (0.02|F_o|)^2 + 1.0]$, was employed. All calculations were carried out on a VAX station 4000 90A computer using the MolEN program package [17].

3. Results and discussion

The template reaction of an excess amount of 2-(2-aminoethylamino)ethanol and salicylaldehyde in the presence of an appropriate metal chloride in ethanol yielded octahedral trivalent metal complexes with 1-[(2-hydroxyethyl)amino]-2-(salicylideneamino)ethane, [M(Hhase)$_2$]Cl (M = V (**1**), Cr (**3**), Mn (**4**), and Fe (**5**)). In the case of cobalt, the reaction with cobalt(II) salt gave similar octahedral cations, [Co(Hhase)$_2$]$^+$, of which a variety of salts (**6–12**) were isolated as crystalline solids. When H$_2$hase was reacted with vanadyl chloride in ethanol, pale yellow plates of [VO$_2$(Hhase)] (**2**) could be isolated. On the other hand, reaction mixture solutions did not yield any precipitate in the cases of nickel(II) and copper(II) except for [Cu(salen)].

The X-ray crystallography of **1** reveals that the complex consists of a six-coordinate V(III) ion, which has a distorted octahedron with two phenoxo-oxygen atoms,

two imino-nitrogen atoms, and two amino-nitrogen atoms of the two Hhase ligands. An ORTEP drawing of the complex with an atom-labelling scheme is shown in Fig. 1. Selected bond lengths and angles are listed in Table. 2. None of the Schiff-base ligands are fully deprotonated and the Hhase ligand acts a meridional tridentate chelate forming a fused 6-5 chelate ring. The two Hhase ligands are arranged so that the imino-nitrogen atoms are *trans,* while the phenoxo-oxygen atoms and the amino-nitrogen atoms are *cis*. The V–O1 and V–O3 distances are 2.002 (7) and 1.861 (7) Å, respectively. The V–N2 (2.257 (9) Å) and V–N4 (2.110 (8) Å) distances are noticeably longer than the V–N1 (2.066 (6) Å) and V–N3 (2.069 (6) Å) distances. The elongation of *trans* V–N bonds relative to V–O can be ascribed to the *trans* influence of the V-phenoxo bonds. Neither of the alcohol groups of the two Hhase ligands are coordinated to the central metal atom, but positioned *cis* to each other, forming hydrogen bonds with the chloride ion, as suggested by the distances O2···Cl – 3.30 (1), O4···Cl – 3.57 (1), O4′···Cl – 3.452 (8), N2···Cl – 3.135 (8), and N4···Cl – 3.566 (8) Å. The effective magnetic moment of **1** is 2.71μ_B at room temperature. This is close to the spin-only value (2.82μ_B) for a d^2 ion.

Table 2. Selected bond distances (Å) and angles (°) of $[M(Hhase)_2]Cl$

Bond	$[V(Hhase)_2]Cl$ (**1**)	$[Cr(Hhase)_2]Cl$ (**3**)	$[Mn(Hhase)_2]Cl$ (**4**)	$[Fe(Hhase)_2]$ Cl (**5**)	$[Co(Hhase)_2]$ Cl (**6**)
M–O1	2.002(7)	1.933(7)	1.894(3)	1.895(3)	1.896(3)
M–O3	1.861(7)	1.936(7)	2.040(3)	1.902(3)	1.897(2)
M–N1	2.066(6)	2.026(6)	2.001(3)	2.012(2)	1.901(2)
M–N3	2.069(6)	2.009(6)	2.028(4)	2.000(2)	1.903(2)
M–N2	2.257(9)	2.173(8)	2.103(3)	2.115(3)	2.008(3)
M–N4	2.110(8)	2.150(8)	2.334(4)	2.139(3)	2.027(3)
O1–M–N1	83.0(3)	90.0(3)	90.2(1)	90.5(1)	93.6(1)
O3–M–N3	82.7(3)	90.1(3)	88.1(1)	90.6(1)	93.8(1)
N1–M–N2	84.7(3)	81.8(3)	82.1(1)	81.2(1)	84.8(1)
N3–M–N4	84.8(3)	81.8(3)	79.0(1)	81.4(1)	84.7(1)
O1–M–N2	166.9(3)	171.3(2)	172.2(1)	171.6(1)	177.2(1)
O3–M–N4	165.9(3)	171.8(2)	170.0(1)	171.6(1)	178.3(1)
O1–M–O3	99.9(3)	92.8(3)	94.4(1)	94.1(1)	90.4(1)
N1–M–N3	175.6(3)	175.6(3)	174.4(1)	175.1(1)	177.9(1)
N2–M–N4	87.7(3)	92.0(3)	91.6(1)	91.4(1)	93.7(1)

Contrary to the mononuclear nature of **1**, the X-ray crystal analysis of **2** shows the structure to be a dinuclear V(V) cluster. As shown in Fig. 2, an ORTEP diagram of **2** demonstrates that each V(V) ion is six-coordinate with three oxo groups. The first of these (V–O3) is a typical V=O distance of 1.618(8) Å. The second and third oxo groups are involved in the bridges between V and V′, with distances of 1.673(8) and 2.463(7) Å for the V–O4 and V–O4′ bonds, respectively. The remaining three coordination sites are occupied by the phenoxo-oxygen (V–O1 1.919(7) Å), imino-nitrogen

(V–N1 2.151(8) Å), and amino-nitrogen (V–N2 2.164(8) Å) atoms of the Hhase ligand, with the alcohol group remaining uncoordinated. A similar structure of the dinuclear complex prepared by a different method has been reported previously [18]. The complex is diamagnetic, being consistent with the d^0 configuration of V(V).

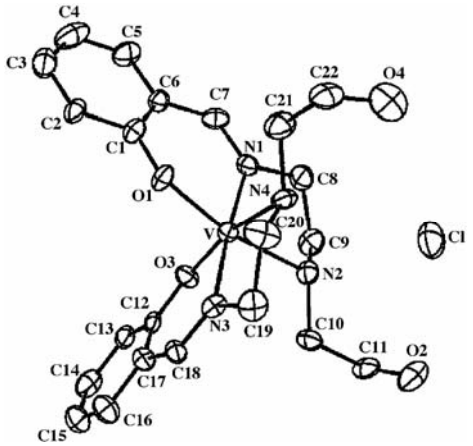

Fig. 1. ORTEP drawing of the structure of $[V(Hhase)_2]Cl$ (**1**), showing the 35% probability thermal ellipsoids and atom labeling scheme

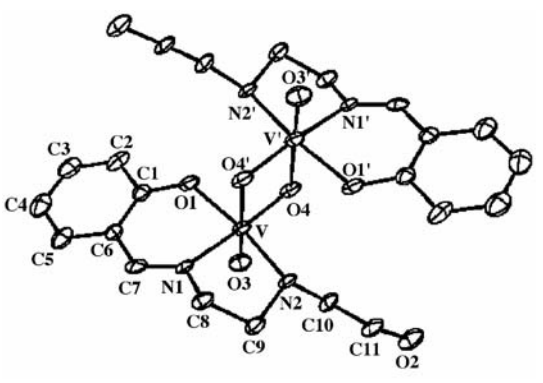

Fig. 2. ORTEP drawing of the structure of $[VO_2(Hhase)]$ (**2**), showing the 35% probability thermal ellipsoids and atom labeling scheme

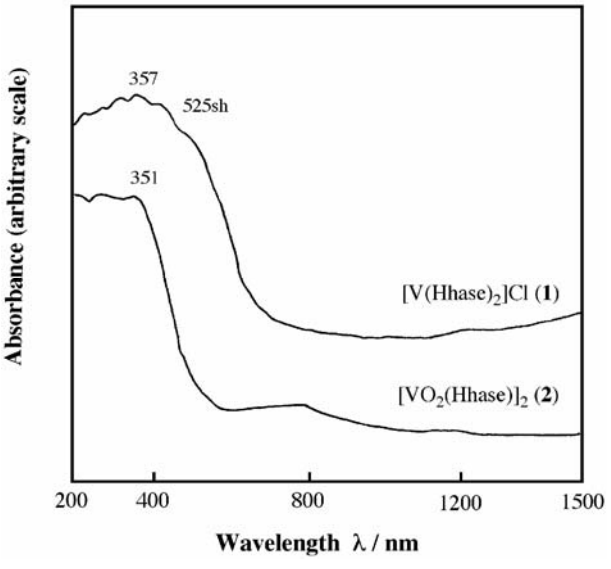

Fig. 3. Diffuse reflectance spectra of $[V(Hhase)_2]$ (**1**) and $[VO_2(Hhase)]$ (**2**)

The diffuse reflectance spectrum of **2** is shown in Fig. 3 together with that of **1**. In the UV region, the high-intensity band observed around 350 nm in both complexes may be due to a ligand-to-metal charge transfer (LMCT) transition, while the other

bands, at still higher energies, can be due to ligand-internal transitions. Contrary to the spectra of **2**, which lacks d-d bands due to the d^0 configuration of V(V), the reflectance spectra of **1** show d-d bands around 525 nm. The d-d bands, however, were hidden by a charge transfer band around 357 nm when the spectrum of **1** was measured in methanol.

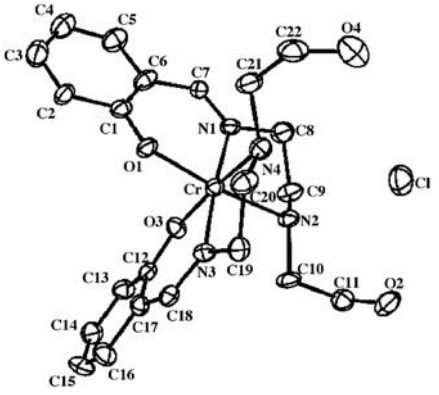

Fig. 4. ORTEP drawing of the structure of $[Cr(Hhase)_2]Cl$ (**3**), showing the 35% probability thermal ellipsoids and atom labeling scheme

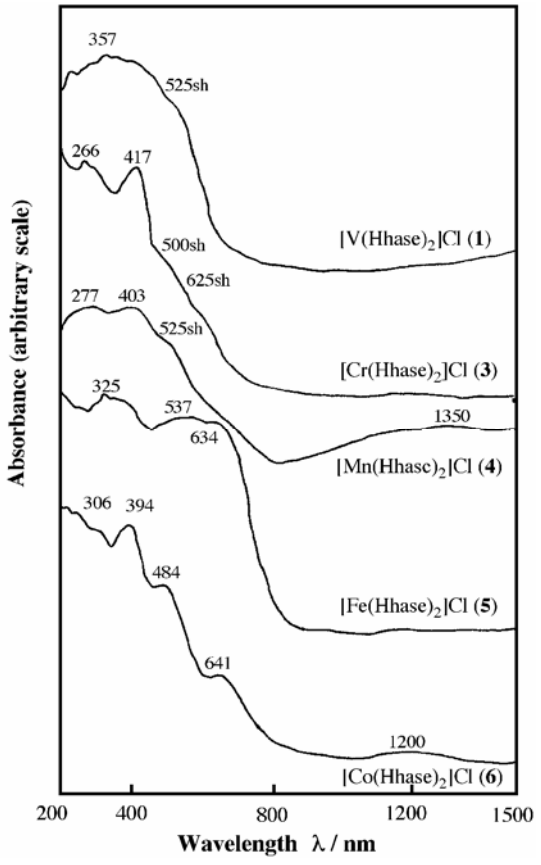

Fig. 5. Diffuse reflectance spectra of $[M(Hhase)_2]Cl$

A perspective view of the crystal structure of **3** is shown in Fig. 4. The molecular structure of the chromium(III) complex is similar to that of the vanadium(III) complex **1**, showing a more octahedral arrangement around the metal ion. The corresponding Cr–O and Cr–N bonds have similar bond lengths: Cr–O1 – 1.933 (7) Å, Cr–O3 – 1.936(7) Å; Cr–N1 – 2.026(6) Å, Cr–N3 – 2.009(6) Å; Cr–N2 – 2.137(8) Å, Cr–N4 – 2.150(8) Å. This structural feature may reflect the d^3 configuration of Cr(III). The magnetic moment of **3** is $3.65\mu_B$ at room temperature, corresponding the spin-only value $3.87\mu_B$. Both 2-hydroxyethylamino groups of the two Hhase ligands are positioned *cis* with respect to each other, forming hydrogen bonds with the chloride ion, as suggested by the distances O2···Cl – 3.188(9), O4···Cl – 3.54(1), O4′···Cl – 3.322(7), N2···Cl – 3.145(8), and N4···Cl – 3.476(7) Å. The reflectance spectrum of **4** is illustrated in Fig. 5. The shoulder bands around 500 and 625 nm may be assigned to d–d transitions. The intense band at 417 nm and more intense bands around 266 nm may be assigned as a LMCT transition and ligand-internal transitions, respectively.

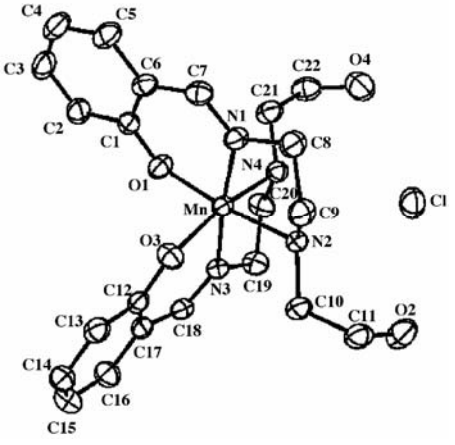

Fig. 6. ORTEP drawing of the structure of $[Mn(Hhase)_2]Cl$ (**4**), showing the 35% probability thermal ellipsoids and atom labeling scheme

The manganese(III) complex **4** is isomorphous with **1** and **3**, and the molecular structure of **4** is similar to those of **1** and **3** (Fig. 6). The most significant difference in **4** is the expected tetragonal Jahn–Teller distortion of the manganese(III) octahedron. The Mn–O1 and Mn–O3 bond distances are 1.894(3) and 2.040(3) Å, respectively, for the phenoxo oxygen. The lengths of the Mn–N bonds range from 2.001(3) for Mn–N1 to 2.334(4) Å for Mn–N4 (Mn–N3 – 2.028(4) Å, Mn–N2 – 2.103(4) Å). These differences in bond lengths are attributed to a Jahn–Teller distortion along the O3-Mn–N4 axis, arising from the d^4 configuration of the manganese centre. This structure is almost the same as that found in $[Mn(Hhase)_2]Br$ [9]. The intramolecular hydrogen bonds O2···Cl, O4···Cl, O4′···Cl, N2···Cl, and N4···Cl have the lengths of 3.175(4), 3.653(5), 3.330(3), 3.190(4), and 3.470(4) Å, respectively. The magnetic moment of **4** is $5.12\mu_B$ at room temperature, which is consistent with a d^4 high-spin system (the spin-only value is $4.90\mu_B$). The reflectance spectrum of **4** is shown in Fig. 5. The lowest energy band at 1350 nm is assigned to d-d transitions. The shoulder around 525

nm and a stronger band at 403 nm may be assigned to the LMCT transition from p_π orbitals on the phenoxo oxygen to the half-filled Mn(III) d_π^* and d_σ^* orbitals, respectively [19]. The iron(III) complex **5** is isomorphous with **1**, **3**, and **4**, and the molecular structure of **5** is similar to those of **1**, **3**, and **4**. In contrast to **4**, the corresponding Fe–O and Fe–N bonds have similar bond lengths: Fe–O1 – 1.895(3), Fe–O3 – 1.902(3) Å; Fe–N1 – 2.012(2), Fe–N3 – 2.000(2) Å; Fe–N2 – 2.115(3), Fe–N4 – 2.139(3) Å (Fig. 7). This may reflect the high–spin d^5 electronic configuration. There are intramolecular hydrogen bonds between the chloride ion and the alcohol group or amino group of the Hhase ligands, as suggested by the distances O2···Cl – 3.186(4), O4···Cl – 3.493(4), O4′···Cl – 3.391(3), N2···Cl – 3.175(3), and N4···Cl – 3.463(3) Å. In the reflectance spectrum of **5** (Fig. 5), the relatively intense bands around 537 and 325 nm can be assigned to transitions from the p_π orbital on the phenoxo oxygen to the half–filled d_π* and d_σ* orbitals on the iron(III) ion, respectively, whereas d–d transitions should be very weak and difficult to detect for iron(III) due to the high–spin state of the d^5 ion [20]. The magnetic moment of **5** at room temperature(5.68μ_B) is consistent with a d^5 high–spin system (the spin-only value is 5.90μ_B).

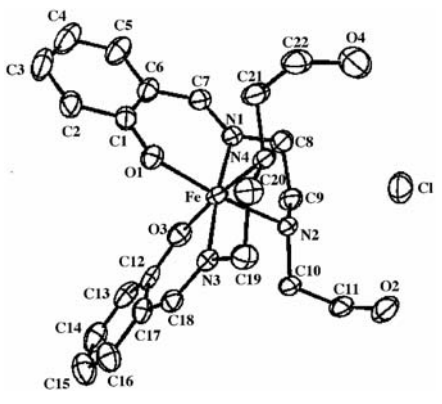

Fig. 7. ORTEP drawing of the structure of [Fe(Hhase)$_2$]Cl (**5**), showing the 35% probability thermal ellipsoids and atom labeling scheme

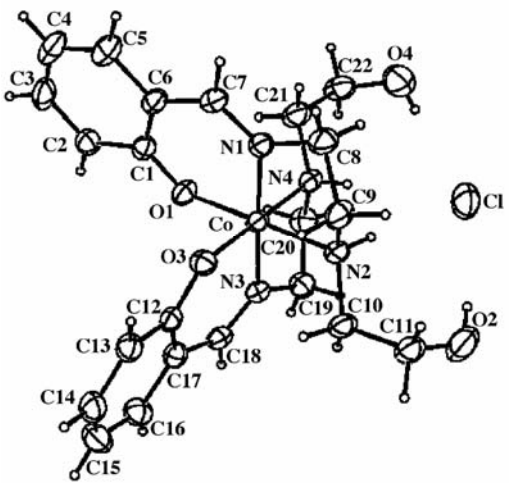

Fig. 8. ORTEP drawing of the structure of [Co(Hhase)$_2$]Cl (**6**), showing the 35% probability thermal ellipsoids and atom labeling scheme

The cobalt(III) complex **6** is also isomorphous with **1**, **3**, **4**, and **5**. As shown in Fig. 8, the molecular structure of **6** is similar to those of **1**, **3**, **4**, and **5**. Among the present [M(Hhase)$_2$]Cl complexes (M = V, Cr, Mn, Fe, Co), the coordination environment around the cobalt(III) ion is closest to a regular octahedral arrangement: Co–O1 – 1.896(3) Å, Co–O3 – 1.897(2) Å; Co–N1 – 1.901(2) Å, Co–N3 – 1.903(2) Å; Co–N2 – 2.008(3) Å, Co–N4 – 2.027(3) Å. This may arise from a large crystal field stabilization energy, which is due to the low–spin d^6 electron configuration of the

Co(III) centre. There are intramolecular hydrogen bonds between the chloride ion and the alcohol group or amino group of the Hhase ligands, as suggested by the distances O2···Cl – 3.174(4), O4···Cl – 3.503(4), O4′···Cl – 3.381(3), N2···Cl – 3.160(3), and N4···Cl – 3.462(3) Å. Complex **6** is diamagnetic as suggested from the low–spin d^6 configuration. The reflectance spectrum of **6** is shown in Fig. 5. The lower energy bands at 641 and 484 nm can be assigned to d–d transitions. The relatively intense band at 394 nm may be assigned to the LMCT transition from the p_π orbital on the phenoxo oxygen to the Co(III) d^*_σ orbitals, while the other bands, at still higher energies, can be due to ligand–internal transitions. Interestingly, the counter anion bound to the $[Co(Hhase)_2]^-$ moiety via hydrogen bonds can be changed to Br^- (**7**), I^- (**8**), NO_3^- (**9**), NCS^- (**10**), ClO_4^- (**11**), or $CH_3CO_2^-$ (**12**) by using a variety of cobalt(II) salts. All of the crystal structures of **6–12** are isomorphous with each other (Figs. 9–14). Selected bond lengths and angles are listed in Table 3.

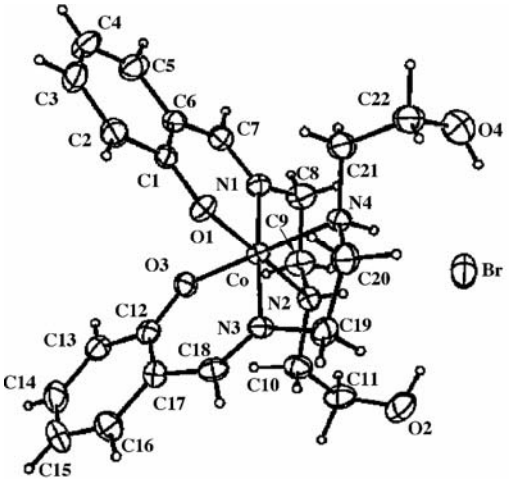

Fig. 9. ORTEP drawing of the structure of $[Co(Hhase)_2]Br$ (**7**), showing the 35% probability thermal ellipsoids and atom labeling scheme

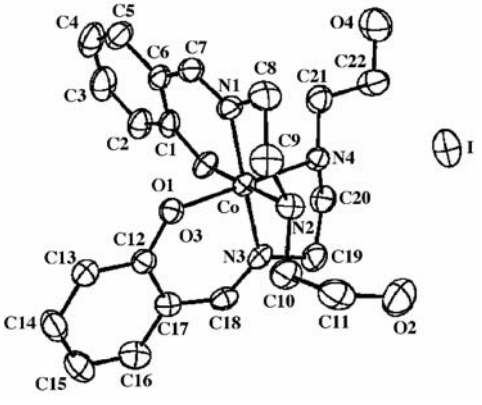

Fig. 10. ORTEP drawing of the structure of $[Co(Hhase)_2]I$ (**8**), showing the 35% probability thermal ellipsoids and atom labeling scheme

Bond lengths and angles around the cobalt ion do not differ significantly from those in **6** and exhibit an octahedral arrangement: Co–O1 – 1.893(4) Å, Co–O3 – 1.898(4) Å, Co–N1 – 1.901(4) Å, Co–N3 – 1.902(4) Å, Co–N2 – 2.002(5) Å, and Co–N4 – 2.030(4) Å for **7**; Co–O1 – 1.879(5) Å, Co–O3 – 1.896(5) Å, Co–N1 – 1.909(5) Å, Co–N3 – 1.902(5) Å, Co–N2 – 2.008(5) Å, and Co–N4 2.011(5) Å for **8**; Co–O1 – 1.892(3) Å, Co–O3 – 1.899(3) Å, Co–N1 – 1.911(3) Å, Co–N3 – 1.910(3) Å, Co–N2 – 2.010(4) Å, and Co–N4 – 2.033(4) Å for **9**; Co–O1 – 1.882(5) Å, Co–O3 – 1.897(5) Å, Co–N1 – 1.900(5) Å, Co–N3 – 1.904(5) Å, Co–N2 – 2.003(6) Å, and Co–N4 2.009(6) Å for **10**; Co–O1 – 1.872(6) Å, Co–O3 – 1.891(5) Å, Co–N1 – 1.899(5) Å, Co–N3 – 1.901(5) Å, Co–N2 – 2.006(7), and Co–N4 – 2.017(7) Å for

11; Co–O1 – 1.896(4) Å, Co–O3 – 1.880(4) Å, Co–N1 – 1.902(4) Å, Co–N3 – 1.893(3) Å, Co–N2 – 2.006(4) Å, andCo–N4 – 1.996(4) Å for **12**.

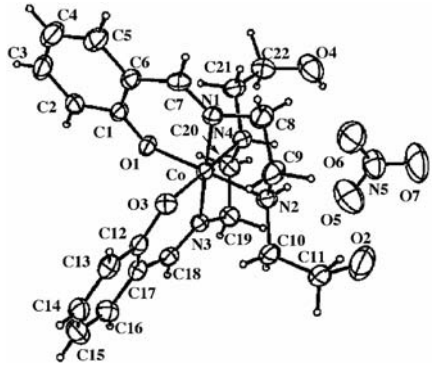

Fig. 11. ORTEP drawing of the structure of $[Co(Hhase)_2]NO_3$ (**9**), showing the 35% probability thermal ellipsoids and atom labeling scheme

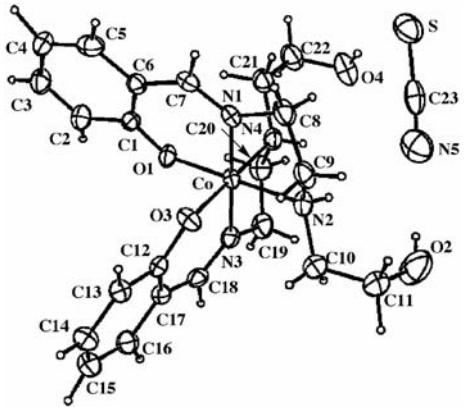

Fig. 12. ORTEP drawing of the structure of $[Co(Hhase)_2]NCS$ (**10**), showing the 35% probability thermal ellipsoids and atom labeling scheme

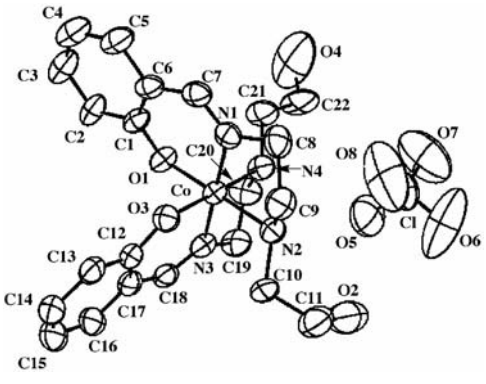

Fig. 13. ORTEP drawing of the structure of $[Co(Hhase)_2]ClO_4$ (**11**), showing the 35% probability thermal ellipsoids and atom labeling scheme

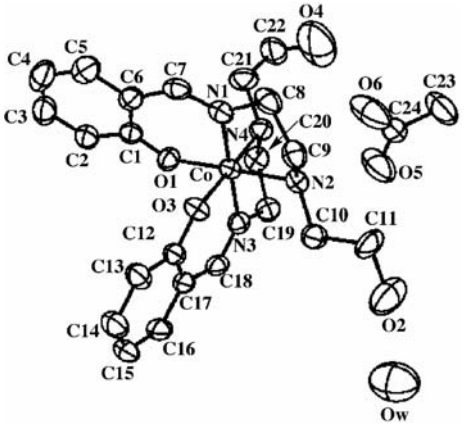

Fig. 14. ORTEP drawing of the structure of $[Co(Hhase)_2]CH_3CO_2 \cdot H_2O$ (**12**), showing the 35% probability thermal ellipsoids and atom labeling scheme

There are intramolecular hydrogen bonds between the counter anion or water molecule (in the case of **12**) and the alcohol group or amino group of the Hhase ligands, and the bond lengths are significantly different depending on the size of the counter anion, as suggested by the distances O2···Br – 3.303(5), O4···Br – 3.573(6), O4′···Br – 3.570(4), N2···Br – 3.342(4), and N4···Br – 3.611(4) Å for **7**; O2···I – 3.457(7), N2···I – 3.565(5), and N4···I – 3.719(5) Å for **8**; O2···O5 – 2.871(8), N2···O6 – 3.009(6), and N4···O6 – 3.285(7) Å for **9**; O2···N5 – 2.85(1), O4···S

Table 3. Selected bond distances (Å) and angles (°) of $[Co(Hhase)_2]X$

Bond	X						
	–Cl (**6**)	–Br (**7**)	–I (**8**)	$-NO_3$ (**9**)	–NCS (**10**)	$-ClO_4$ (**11**)	$-CH_3CO_2 \cdot H_2O$ (**12**)
Co–O1	1.896(3)	1.893(4)	1.879(5)	1.892(3)	1.882(5)	1.872(6)	1.896(4)
Co–O3	1.897(2)	1.898(4)	1.896(5)	1.899(3)	1.897(5)	1.891(5)	1.880(4)
Co–N1	1.910(2)	1.901(4)	1.909(5)	1.911(3)	1.900(5)	1.899(5)	1.902(4)
Co–N3	1.903(2)	1.902(4)	1.902(5)	1.910(3)	1.904(5)	1.901(5)	1.893(3)
Co–N2	2.008(3)	2.002(5)	2.008(5)	2.010(4)	2.003(6)	2.006(7)	2.006(4)
Co–N4	2.027(3)	2.030(4)	2.011(5)	2.033(4)	2.009(6)	2.017(7)	1.996(4)
O1–Co–N1	93.6(1)	93.8(2)	93.6(2)	93.5(1)	93.9(2)	94.2(2)	94.7(2)
O3–Co–N3	93.8(1)	93.5(2)	94.5(2)	93.4(1)	94.3(2)	94.5(3)	94.3(2)
N1–Co–N2	84.8(1)	84.9(2)	85.3(2)	85.2(2)	85.3(2)	85.4(3)	85.4(2)
N3–Co–N4	84.7(1)	85.1(2)	84.5(2)	84.9(1)	85.3(2)	84.8(3)	85.6(2)
O1–Co–O3	90.3(1)	90.6(2)	90.9(2)	90.3(1)	91.6(2)	90.7(2)	90.5(2)
N1–Co–N3	177.9(1)	178.2(2)	178.7(2)	178.7(1)	178.4(2)	179.1(3)	178.8(2)
N2–Co–N4	93.7(1)	94.2(2)	92.0(2)	93.6(2)	92.8(2)	92.6(3)	92.8(2)

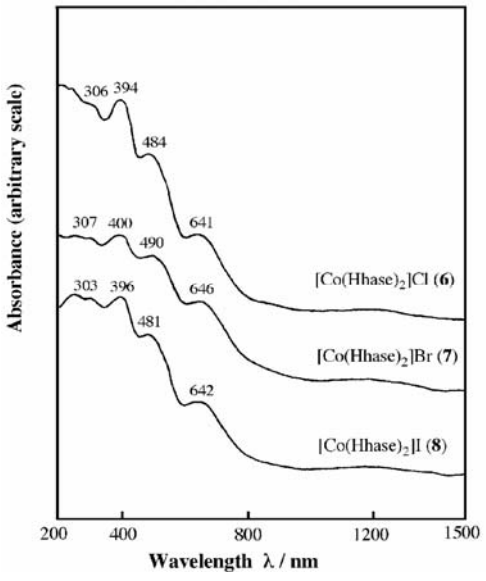

Fig. 15. Diffuse reflectance spectra of $[Co(Hhase)_2]X$ (X = Cl, Br, I)

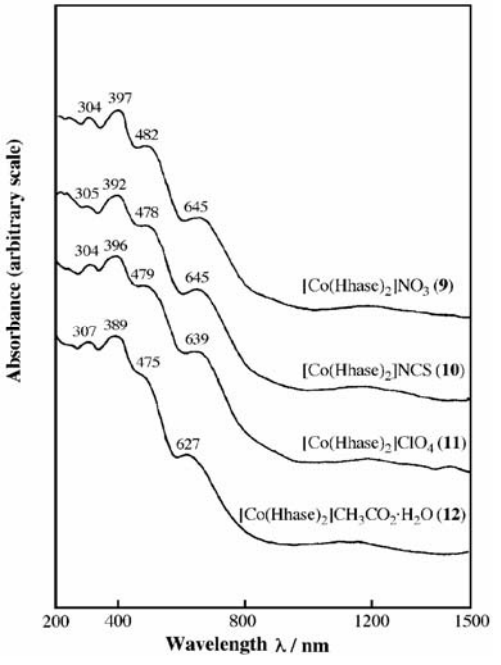

Fig. 16. Diffuse reflectance spectra of $[Co(Hhase)_2]X$ (X = NO_3, NCS, ClO_4, $CH_3CO_2 \cdot H_2O$)

– 3.265(6), and N2···N5 – 3.07(1) Å for **10**; O2···O4′ – 2.69(1) Å and O2···O5 – 3.15(2) Å for **11**; O2···OW – 2.79(1), N2···O5 – 2.874(8), and N4···O5 – 3.252(7) Å for **12**. As can be expected from the almost same structures around the metal centres,

the UV–vis spectral features of **7–12** are very similar to that of **6** (Figs. 15 and 16) and all of these cobalt(III) complexes are diamagnetic.

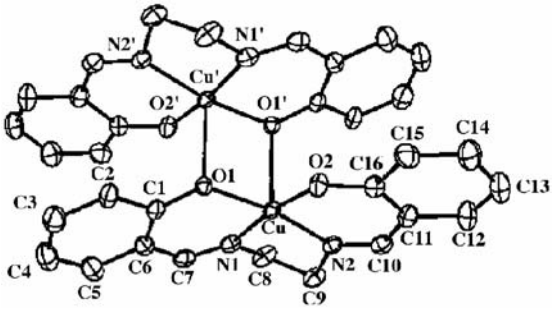

Fig. 17. ORTEP drawing of the structure of [Cu(salen)] (**13**), showing the 35% probability thermal ellipsoids and atom labeling scheme

In the case of the reaction of H_2hase with nickel(II) and copper(II) salts, we could not receive any precipitation materials. This may be due to difficulties in the oxidation of the metal centre for nickel(II) and copper(II) ions, because an oxidation state of three is necessary for the formation of the $[M(Hhase)_2]X$ complexes. We could barely isolate small amounts of crystals of **13** in the reaction with copper(II) chloride dihydrate in ethanol. The X-ray crystal structure analysis of **13**, however, revealed that the complex is a dinuclear copper(II) complex of salen [Cu(salen)], as shown in Fig. 17 – this is a well-known structure of [Cu(salen)] [21]. The formation of the salen ligand suggests that an elimination reaction of the hydroxyethyl group of 2-(2-aminoethylamino)ethanol occurs during the template reaction with salicylaldehyde in the presence of the copper(II) ion [5]. Triethylamine, which was not used in the other cases, may have induced the elimination reaction during the formation of the metal complex.

4. Conclusions

Reactions of excess amounts of the Schiff-base ligand 1-[(2-hydroxyethyl)amino]-2-(salicylideneamino)ethane(H_2hase) with an appropriate metal chloride in ethanol yielded octahedral the trivalent metal complexes $[M(Hhase)_2]Cl$ (M = V (**1**), Cr (**3**), Mn (**4**), Fe (**5**), Co(**6**)). In the case of cobalt compounds, cobalt(III) complexes incorporating different counter anions – $[Co(Hhase)_2]X$ (X = Br (**7**), I (**8**), NO_3 (**9**), NCS (**10**), ClO_4 (**11**), and CH_3CO_2 (**12**)) – can be obtained easily. These counter anions have hydrogen bonds between the *cis*-oriented 2-hydroxyethylamino groups of the two Hhase ligands. The stabilization due to these hydrogen bonds, in addition to the presence (or even the lack) of a crystal field stabilization energy in trivalent metal ions, provided a series of metal complexes with Hhase.

Acknowledgements

The present work was partially supported by the "Open Research Center" Project for Private Universities: matching fund subsidy and Grants-in-Aid for Scientific Research No. 16550062 from the Ministry of Education, Culture, Sports, Science and Technology.

References

[1] CALLIGARIS M., RANDACCIO L., *Comprehensive Coordination Chemistry*, G. Wilkinson, R.D. Gillard, J.A. McCleverty (Eds.), Pergamon Press, Oxford, 1987, Chap. 20.1.

[2] HERNANDEZ-MOLINA R., MEDEROS A., *Comprehensive Coordination Chemistry II*, J.A. McCleverty, T.J. Meyer (Eds.), Elsevier, Oxford, 2004, Chap. 1.19.

[3] PFEIFFER P., BREITH E., LUBBE E., TSUMAKI T., Liebigs Ann. Chem., 503 (1933), 84.

[4] MIKURIYA M., KIDA S., MURASE I., Chem. Lett. 1988, 35; MIKURIYA M., YAMATO Y.TOKII T., Inorg. Chim. Acta, 181 (1991), 1; MIKURIYA M., YAMATO Y., TOKII T., Chem. Lett. (1991), 1429; MIKURIYA M., SASAKI T., ANJIKI A., IKENOUE S., TOKII T., Bull. Chem. Soc. Jpn., 65 (1992), 334; MIKURIYA M., YAMATO Y., TOKII T., Bull. Chem. Soc. Jpn., 65 (1992), 1466; MIKURIYA M., YAMATO Y., TOKII T., Bull. Chem. Soc. Jpn., 65 (1992), 2624; MIKURIYA M., YAMATO Y., TOKII T., Chem. Lett. (1992), 1571.

[5] MIKURIYA M., KAWASAKI Y., TOKII T.T, YANAI S., KAWAMORI A., Inorg. Chim. Acta, 156 (1989), 21; MIKURIYA M., FUJII T., KAMISAWA S., KAWASAKI Y., TOKII T., OSHIO H., Chem. Lett., (1990), 1181; MIKURIYA M., FUJII T., TOKII T., KAWAMORI A., Bull. Chem. Soc. Jpn., 66 (1993), 1675; MIKURIYA M., NAKADERA K., TOKII T., Inorg. Chim. Acta, 194 (1992), 129.

[6] MIKURIYA M., SHIGEMATSU S., KAWANO K., TOKII T., OSHIO H., Chem. Lett. (1990), 729; MIKURIYA M., KAKUTA Y., KAWANO K., TOKII T., Chem. Lett. (1991), 2031; MIKURIYA M., JIE D., KAKUTA Y., TOKII T., Bull. Chem. Soc. Jpn., 66 (1993), 1132; MIKURIYA M., KAKUTA Y., NUKADA R., KOTERA T., TOKII T., Bull. Chem. Soc., Jpn., 74 (2001), 1425.

[7] MIKURIYA M., MAJIMA K., YAMATO Y., Chem. Lett. (1992), 1929; MIKURIYA M., NAGAO N., KONDO K., Chem. Lett. (2000), 516; MIKURIYA M., MINOWA K., Inorg. Chem. Commun., 3 (2000), 227; MIKURIYA M., MINOWA K., LIM J.-W., Bull. Chem. Soc. Jpn., 74 (2001), 331; MIKURIYA M., MINOWA K., NAGAO N., Bull. Chem. Soc. Jpn., 74 (2001), 871; MIKURIYA M., MINOWA K., NAGAO N., Inorg. Chem. Commun., 4 (2001), 441; MIKURIYA M., MINOWA K., NUKADA R., Bull. Chem. Soc., Jpn., 75 (2002), 2595.

[8] MIKURIYA M., NAKADERA K., KOTERA T., Chem. Lett. (1993), 637; MIKURIYA M., NAKADERA K., KOTERA T., TOKII T., MORI W., Bull. Chem. Soc. Jpn., 68 (1995), 3077; MIKURIYA M., NAKADERA K., Chem.Lett. (1995), 213; MIKURIYA M., NAKADERA K., KOTERA T., Bull. Chem. Soc. Jpn., 69, (1996), 399; MIKURIYA M., FUKUYA M., Bull. Chem. Soc. Jpn., 69 (1996), 679; MIKURIYA M., TASHIMA S., Polyhedron, 17 (1998), 207; MIKURIYA M., FUKUYA M., Chem. Lett. (1998), 421; MIKURIYA M., IKEMI S., LIM J.-W., Bull. Chem. Soc. Jpn., 74 (2001) 88; MIKURIYA M., IKEMI S., YAO S., Chem. Lett. (2000), 538; MIKURIYA M., NAKADERA K., LIM J.-W., Synth. React. Inorg. Met.-Org. Chem., 32 (2002), 117.

[9] MIKURIYA M., TAKEBAYASHI H., MATSUNAMI K., Bull. Chem. Soc. Jpn., 67 (1994), 3128.

[10] MIKURIYA M., HASHIMOTO Y., KAWAMORI A., Chem. Lett. (1995), 1095.

[11] MIKURIYA M., YAMAZAKI Y., Chem. Lett. (1995), 373.

[12] MIKURIYA, M., HATANO Y., ASATO E., Chem. Lett. (1996), 849; MIKURIYA M., HATANO Y., ASATO E., Bull. Chem. Soc. Jpn., 70 (1997), 2495; MIKURIYA M., FUKUMOTO H., KAKO T., Inorg. Chem. Commun., 1 (1998), 225.

[13] MIKURIYA M., IKENOUE S., NUKADA R., LIM J.-W., Bull. Chem. Soc., Jpn., 74 (2001), 101.

[14] MIKURIYA M., NUKADA R., TOKAMI W., HASHIMOTO Y., FUJII T., Bull. Chem. Soc. Jpn., 69 (1996), 1573.

[15] GEARY W.J., Coord. Chem. Rev., 7 (1971), 81.
[16] SELWOOD P.W., *Magnetochemistry*, Interscience Publ., New York, 1956, pp. 78, 91.
[17] FAIR C.K., *MolEN Structure Determination System*, Delft Instruments, Delft, 1990.
[18] LI X., LAH M.S., PECORARO V.L., Inorg. Chem. 27 (1988), 4657.
[19] NEVES A., NASCIMENTO O.R., HORNER M., BATISTA A.A., Inorg. Chem. 31 (1992) 4749.
[20] AINSCOUGH E.W., BRODIE M., PLOWMAN J.E., BROWN K.L., ADDISON A.W., GAINSFORD A.R., Inorg. Chem., 19 (1980), 3655.
[21] BAKER E.N., HALL D., MCKINNON A.J., WATERS T.N., Chem. Commun. (1967), 134; BHADBHADE M.M., SRINIVAS D., Inorg. Chem., 32 (1993), 5458.

Received 16 March 2005

Materials Science-Poland, Vol. 23, No. 3, 2005

The synthesis of hydrosodalite and its use in mortar technology

V. SASNAUSKAS, D. PALUBINSKAITĖ*

Faculty of Chemical Technology, Kaunas University of Technology,
Radvilėnų str. 19, 50254 Kaunas, Lithuania

Conditions for the low-temperature hydrothermal synthesis of zeolites from AlF_3 production waste – technogenic silica gel polluted with admixtures of fluorides – were analysed. It was determined that an AlF_3 admixture encourages the formation of hydrosodalite. When using technogenic silica gel, crystal zeolite – hydrosodalite was synthesised. The reaction was conducted under hydrothermal conditions and atmospheric pressure (90 °C for 0.5, 1, and 2 hours). The best molar ratio of the components Na_2O, Al_2O_3, SiO_2, H_2O was 2 : 0,02 : 1 : 10. Lignosulphonic plasticiser (LST) was modified with synthesised hydrosodalite. The binding duration of cement paste of normal consistence with modified LST plasticiser decreased up to 40/395 min. (at 0.25% content of admixture) and 80/150 min. (0.75%) as compared to that of unmodified mortar, for which the binding duration was 65/475 min. (0.25%) and 105/150 min. (0.75%). A larger compression strength was obtained for cement grout with modified LST plasticiser after 3, 7, and 28 days of hardening – 12.61; 21.52; 25.49 MPa (at 0.25% content of the addition) as compared to that off mortar with non-modified LST plasticiser – 6.04; 9.63; 22.69 MPa.

Key words: *hydrosodalite; lignosulphonic plasticiser; mortar*

1. Introduction

Hydrosodalite belongs to the group of zeolites, widely spread natural minerals. In comparison to natural zeolites, however, the synthetic ones are better suitable for research and better meet the requirements of industry due to their purity and homogeneity. Natural zeolites are practically not used for these purposes. As a rule, they are polluted with extraneous minerals, and it is difficult to prepare adsorbent granules of corresponding sizes, since it is impossible to control the diameter of the pores within natural zeolites. On the other hand, in agriculture natural zeolites are widely applied to improve soil structure [1–3].

*Corresponding author e-mail: danute.palubinskaite@ktu.lt

Synthetic zeolites are obtained by heating suspensions of alkaline alumosilicate mixtures composed of SiO_2, Al_2O_3, alkali and water. They may be synthesised from amorphous or crystalline materials, alumosilicate gels of alkaline metals, and from clays. The initial formation of zeolite structure occurs only in the presence of water. Under hydrothermal conditions in alkaline alumosilicate suspensions (R_2O–SiO_2 –Al_2O_3–H_2O) and at a certain temperature, the crystallization of zeolites depends not only on the ratios and concentrations of components but also on their nature and state, the conditions of preparation, mixing, the initiation of crystallization, and other properties of the reagents forming the initial alumosilicate mixtures [4, 5]. The reactants for the synthesis of zeolites are gels or solid amorphous substances. The reactions proceed at high pH values, since hydroxides of alkaline metals or other strong bases are used, at low temperatures and autoclave pressures of saturated water vapour.

The properties of zeolites and possibilities for their application have been examined in numerous branches of science and, in fact, all fields of chemical technology. They are efficient catalysts in many organic and inorganic chemistry reactions. Zeolites are also used for cleaning harmful atmospheric pollutants. Upon harmonizing the cleaning and drying processes in one-phase gaseous adsorptive processes, the treatment of emitted gas is simplified. By heating zeolites within a certain interval of temperatures it is possible to remove (reversibly) the constitutional water while not destroying the frame. Channels and cavities appear within the structure, therefore zeolites are used as molecular sieves and filters in adsorptive processes [6–8].

The synthesis of low-temperature zeolites is presented in the paper. In this synthesis it is possible to use technogenic AlF_3 production waste aggressive to the environment instead of reagent silica gel. Amorphous SiO_2 is the basis of such a raw material. In the Kėdainiai chemical plant Lifosa, several thousand tons accumulate each year.

Lignosulphonates (LST) are most widely used as hydrophilic-plasticifying admixtures in mortar technology. Their presence in cement-water suspensions predetermines the slowdown of the hardening of the mineral-binding agents in the initial period of hydration. In order to decrease the slowing impact of technical lignosulphonates on cement hydration, they are modified. As a rule, this plasticifying admixture is used in fat mortar or concrete mixtures, i.e. in mixtures with a large content of binding agents [9–11].

The principle of activity of zeolites as molecular sieves was applied to modify the LST plasticiser. This paper analyses the impact of modified LST plasticisers on the water content in cement paste of normal consistence, duration of cement paste binding, technological qualities of mortar, and the density and strength of hardened mortar.

The aim of this paper is to investigate the possibilities and conditions of synthesising zeolites from AlF_3 production waste of Lifosa, which is polluted with admixtures of fluoride compounds. After performing the synthesis of synthetic zeolite – hydrosodalite, there exists a possibility of using it for to modify technical lignosulfonatic (LST) plasticisers.

2. Experimental

AlF_3 production waste was used as the source of SiO_2 and Al^{3+}. By chemical analysis, the following content of AlF_3 waste-silicagel was determined:

I) H_2O, 70.24%; SiO_2, 93.6%; Al_2O_3, 2.88%; Fe_2O_3, 1.78%; CaO, 1.49%; F, 0.25%.

II) H_2O, 73.46%; SiO_2, 93.10%; Al_2O_3, 2.11%; CaO, 1.68%; Fe_2O_3, 2.10%; F, 1.01%.

Solutions of NaOH were also applied as well as portland cement CEM I 42.5; plasticiser LST, plasticiser LST modified with hydrosodalite; sand (coarseness module MS = 2.11, apparent density ρ_p = 1.540 kg/m^3).

X-ray diffraction analyses have been conducted using a DRON-6 diffractometer. The investigation was carried out with the 2Θ angle range of 4–60, with Ni-filtered CuK_α radiation. Thermographic analyses were conducted with a differential scanning calorimeter Du-Pont 990. The maximum temperature was 1000 °C, and the temperature increase velocity was 10 °/min. IR spectrograms were recorded with a specord M-80 (C. Zeiss Jena), and the source of light was a Ni-Cr electrode.

The hydrothermal crystallization of sodium-bearing zeolites was carried out using alkali alumosilicate mixtures. A calculated amount of technogenic silica gel was added to caustic soda dissolved in the required amount of water. Low-temperature (90 °C) crystallization occurred in glass vessels resistant to alkali put into thermostats. The obtained suspension was poured into the vessel and mixed (60 r/min). The crystallization lasted for 1, 2 or 3 hours. Upon the end of crystallization the precipitates were filtered. Apart from the main product, the admixture of sodium fluoride (NaF) formed up, which was washed away with distilled water. The obtained products of synthesis were dried at the temperature of 100 °C.

3. Results and discussion

3.1. Synthesis of hydrosodalite

It is more economical to synthesize hydrosodalite from technogenic raw materials than to synthesize it from reagents. Different contents of sodium oxide (0.5, 1, 2, and 3 mol) were used to determine the best conditions of crystallization. A constant amount of silica gel was used. In the technogenical silica gel, the fluorine content was 12 mol.

In accordance with X-ray diffraction analysis in the specimen whose initial mixtures contained 0,5 mol sodium oxide, non-reacting amorphous SiO_2 was predominant after 3 hours of crystallization, irrespective of the amount of water used. In the specimen where Na_2O content amounted to 2 or 3 mol, hydrosodalite crystallized after one hour; water amount did not have a major impact on the synthesis of the product. When using 1 mol Na_2O and 20 or 30 mol water, non-reacting amorphous SiO_2 was predominant in the products of the reaction. Upon reducing water content down to 10

mol, however, hydrosodalite (Fig. 1) crystallized. The peaks typical of hydrosodalite were: 0.365; 0.628; 0.256; 0.290; 0.210; 0.175; 0.158 nm. This can be explained by the conditions of hydrosodalite crystallization.

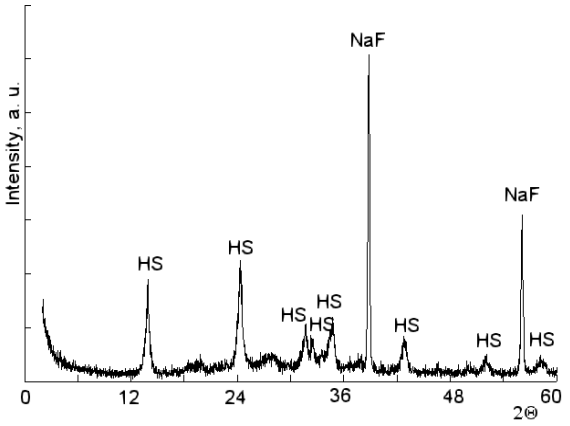

Fig. 1. The X–ray pattern of the specimen synthesised at 90 °C for 1 hour. The initial molar ratio of $Na_2O : Al_2O_3 : SiO_2 : H_2O$ was 2 : 0.02 : 1 : 10. The hydrosodalite (HS) and sodium fluoride admixture formed up

Table 1. The synthesis of low-temperature hydrosodalite by using AlF_3 production waste

No.	Molar ratio $Na_2O : Al_2O_3 : SiO_2 : H_2O$	Conditions of synthesis		Product of synthesis
		t, °C	τ, h	
1	1 : 0.026 : 1 : 30	90	1	amorph.
2	2 : 0.026 : 1 : 30	90	1	HS
3	1 : 0.026 : 1 : 30	90	2	amorph.
4	2 : 0.026 : 1 : 30	90	2	HS
5	1 : 0.026 : 1 : 20	90	1	amorph
6	2 : 0.026 : 1 : 20	90	1	HS
7	1 : 0.026 : 1 : 20	90	2	amorph
8	2 : 0.026 : 1 : 20	90	2	HS
9	1 : 0.026 : 1 : 10	90	1	HS
10	2 : 0.026 : 1 : 10	90	1	HS
11	1 : 0.026 : 1 : 10	90	2	HS
12	2 : 0.026 : 1 : 10	90	2	HS
13	2 : 0.026 : 1 : 10	90	1	HS
14	2 : 0.026 : 1 : 30	90	0.5	HS
15	2 : 0.018 : 1 : 10	90	1	HS

With 2 and 3 moles of Na_2O, hydrosodalite formed up when using different amounts of water (10, 20, and 30 moles). The results are given in Table 1.

The effect of fluorides is explained by the fact that when the components containing an active admixture of fluorides having a mineralising effect, react within the system of sodium alumosilicagel, HF associates with water (H_2O+ HF = H_3O^+ + F^-) and hydrogen bonds are formed: H_2F_2, H–F… H–F (for ions : HF_2, F^-… H – F), and complexes of fluorine silicates form up in the alkali medium [5]. Similar results (Table 1 No. 15) were obtained when using a silica gel of (II) composition for synthesis.

The obtained synthetic zeolites were investigated by IR spectroscopy. Based on this research method it is possible to decide about the structure of the zeolite (X-ray characteristics are insufficient), the way water molecules are associated with cations, oxygen ions, and other hydroxyl groups.

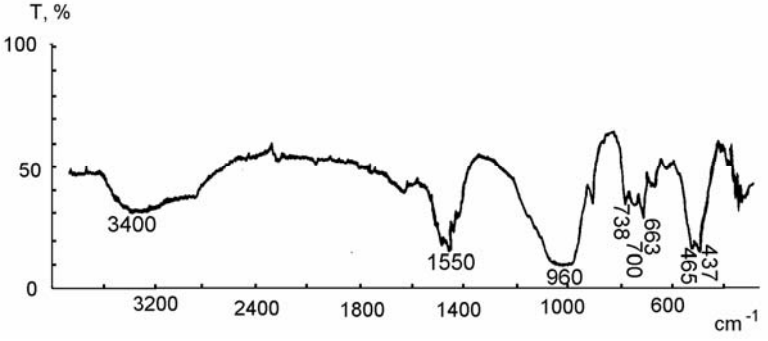

Fig. 2. IR spectra of the specimen synthesised at 90 °C for 2 hours.
The initial molar ratio of Na_2O : Al_2O_3 : SiO : H_2O was 3 : 0.026 : 1 : 30

IR spectra testify the predominance of hydrosodalite in the products of the reaction. The absorption bands characteristic of hydrosodalite are: 960 cm^{-1} within the ranges of asymmetrical stretching vibrations, 738, 700, and 663 cm^{-1} within the ranges of symmetric stretching vibrations, and 465 and 437 cm^{-1} Si(Al) within the ranges of O deformation fluctuations.

Absorption bands located in the 3400 cm^{-1} area are observed in the IR spectra, which can be ascribed to the vibrations of OH hydroxyl groups interconnected by hydrogen bonds. Absorption bands in the 1550 cm^{-1} range show deformation fluctuations of simple water molecules. No isolated OH groups connected with hydrogen bonds were detected in hydrosodalite since the absorption band at 3700 cm^{-1} has not been observed (Fig. 2).

The obtained products of synthesis were analysed thermographically. As a rule, the emission of water from zeolites ends between 300 and 400 °C. The exothermal point, fixed at 667 °C, reflects the transformation of dehydrated zeolite into anhydrous alumosilicate (Fig. 3). After a partial dehydration, water molecules shift to positions where they are more firmly bound with the (Si, Al, O) frame [4]. DTA curves and other physical and chemical methods confirm the predominance of hydrosodalite with an NaF admixture in the products of the reactions.

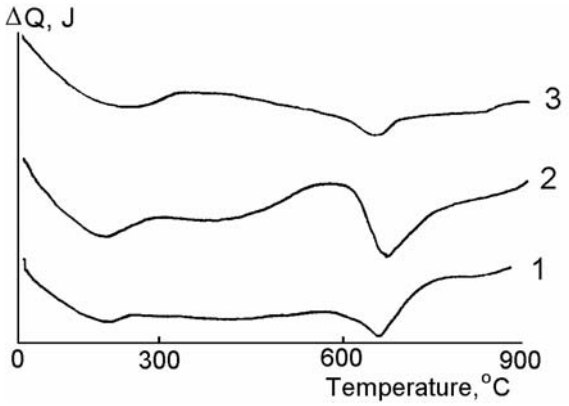

Fig. 3. Thermograms of specimen synthesised at 90 °C. Initial substances: technogenical silica gel and NaOH. The initial molar ratio of $Na_2O : Al_2O_3 : SiO_2 : H_2O$ 1 – 2 : 0,026 : 1 : 20; τ = 2 h; 2 – 2 : 0,026 : 1 : 30; τ = 3 h; 3 – 2 : 0,026 : 1 : 30; τ = 1 h

3.2. Modification of the LST plastifying admixture with synthesized hydrosodalite

In this part of the research, we have analysed the efficiency of the LST plastifying admixture modified with synthetic hydrosodalite on the hydration processes of cement paste and mortar. An anhydrous non-modified admixture of lignosulfonic plasticiser was used. In comparison to cement mortar with unmodified LST plasticiser, the duration of binding of cement mortar modified with LST plasticiser of normal density becomes shorter (Table 2).

The lignosulphonates introduced into cement mortar change the rate and intensity of hydration of cement clinker minerals as well as the crystalline structures of newly formed elements. Also, they influence the temporal and final strength of cement stone. The ability of dispergation and drawing air by lignosulphonates depends on the surface tension at the liquid–air interface. The surface tension of water solutions of lignosulphonates depends on their molecular mass and cation valence. Hence, bearing in mind these regularities, it is feasible to change the lignosulphonate properties that determine their polymolecular structure and valence.

The modification of lignosulfonic plasticiser was performed in three ways under normal conditions: by filtering LST plasticiser via a respective layer of synthesized hydrosodalite, by filtering plasticiser via a hydrosodalite layer in a vacuum filter, or by mixing hydrosodalite with plasticiser and, after a certain time, separating the hydrous solution of plasticiser by decanting. The synthesized hydrosodalite adsorbed reducing substances when large molecules or sugary substances were present in the lignosulfonic plasticiser (hydrogen, organic acids, and related compounds). Owing to this, the slowing effect of technical lignosulfonates on the hydration processes of cement minerals decreased.

Table 2. Initial and final durations of binding of normal density cement paste

No.	Additives	The amount of additive, %	W/C	The duration of binding, min	
				Initial	Final
1	Without additives	–	25.0	240	330
2	LST unmodified	0.25	22.1	65	475
		0.75	21.7	105	150
3	LST mod. self flowing	0.25	22.1	45	420
		0.75	21.7	100	150
4	LST mod. vacuum filtering	0.25	22.1	50	415
		0.75	21.7	90	150
5	LST mod. adsorption	0.25	22.1	40	395
		0.75	21.7	80	150
6	Plastiment BV 60	0.25	23.1	30	340
		0.75	21.9	75	290

The effect of unmodified and modified LST plasticisers on the duration of cement paste binding beginning and binding end was investigated; for the sake of comparison, the binding durations with commercial plastifying admixtures applied in mortar technology (from the companies Sika and MC Bauchemie) were determined. The amount of plasticiser was 0.25% (calculating dry substances), 0.75% from cement mass. The results are presented in Table 2.

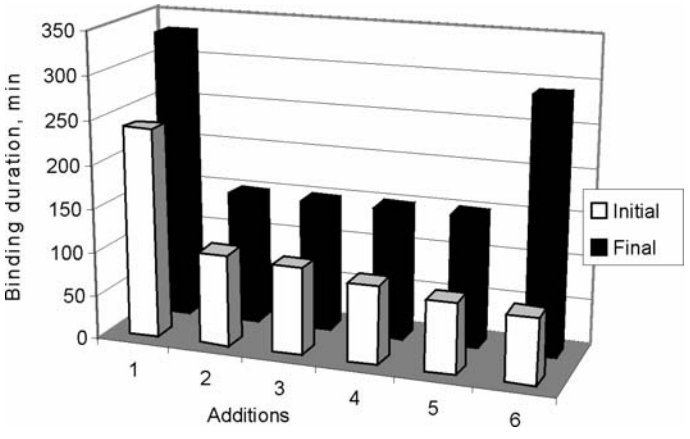

Fig. 4. Binding durations of cement slurry of normal consistence. Different admixtures were used (0.75 % from cement mass): 1 – without admixtures; 2 – LST unmodified; 3 – LST modified by discharge; 4 – LST modified by vacuum dessication; 5 – LST modified by adsorption; 6 – plastiment BV 60

When modified LST plasticiser was used, the binding duration of Portland cement decreased (Fig. 4). Consequently, the slowing effect of modified LST plasticiser on the hydration process of cement paste and mortar is lower than that of non-modified lignosulfonatic plasticiser at the same admixture content.

The strength qualities were determined, i.e. densities and compression strengths after 3, 7, and 28 days of mortar hardening with unmodified and modified LST plasticifying admixtures (Fig. 5).

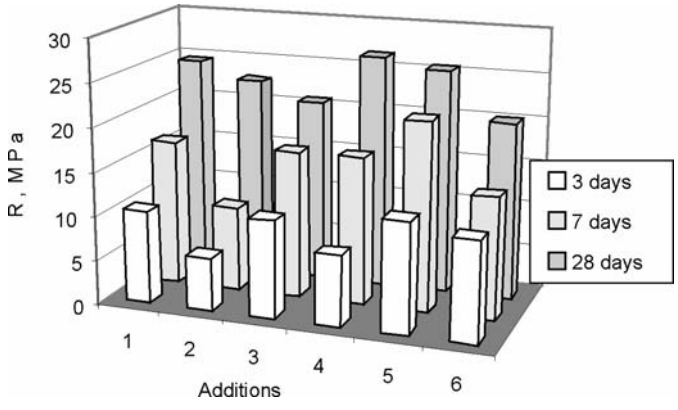

Fig. 5. Strength characteristics of normal consistence cement grout. Various admixtures were used (0.25 % from cement mass): 1 – without admixtures; 2 – LST unmodified; 3 – LST modified by discharge; 4 – LST modified by vacuum dessication; 5 – LST modified by adsorption; 6 – plastiment BV 60

The compression strength of mortar specimens after 3, 7, and 28 days of hardening, with LST plasticiser, when its content accounts for 0.2% of the cement mass, was larger than for specimen with unmodified LST plasticiser (Fig. 5). The strength characteristics of mortar specimens with modified LST plasticiser as compared specimens with plasticifying Plastiment BV 60 and Muraplast NN (FM) admixtures are similar. Therefore, research findings allow us to draw the conclusion that the zeolite way of modifying lignosulfonatic mortar plasticisers is perspective.

4. Conclusions

AlF_3 admixture stimulates the formation of hydrosodalite. When using technogenic silica gel, crystal zeolite – hydrosodalite has been synthesized. The reaction was performed under atmospheric pressure at the temperature of 90 °C for 0.5, 1 and 2 h. The molar ratio of $Na_2O : Al_2O_3 : SiO_2 : H_2O$ was (1–3): 0.026: 1 : (10–30). The best molar ratio was 2 : 0.02 : 1 : 10.

LST plasticiser was modified with synthesized hydrosodalite. The binding duration of normal consistence cement paste with modified LST plasticiser decreased up to 40/395 min. (at 0.25% content of admixture) and 80/150 min. (0.75%), as compared to cement paste with unmodified LST plasticiser, for which binding durations were 65/475 min. (0.25%) and 105/150 min. (0.75%).

Higher compression strengths for mortar with modified LST plasticiser after 3, 7, and 28 days of hardening were obtained: 12.61, 21.52, 25.49 MPa (at 0.25% content of admixture), as compared to those of mortar with unmodified LST plasticiser (the compression strengths of these were: 6.04, 9.63, 22.69 MPa).

References

[1] ALLEN E.R., MING D.W., HOSSNER L.R., HENNINGER D.L., GALINDO C., Agronomy J., 87 (1995), 1052.
[2] MING D.W., ALLEN E.R., Rev. Mineral Geochem., 45 (2001), 619.
[3] BREK D., *Molecular Sieve Zeolites*, Mir, Moscow, 1976, pp. 257–383 (in Russian).
[4] KENDRICK E., MORRIS R., DANN S., Solid State Chemistry Solid State Phenomena, 90 (2003), 57.
[5] KENDRICK E., DANN S., J. Solid State Chem., 177 (2004), 1513.
[6] KOPAC T., KAYMAKCI E., KOPAC M., Chem. Eng. Commun., 164 (1998), 99.
[7] OUKI S.K., KAVANNAGH M., Waste Manage Res., 15 (1997), 383.
[8] MIRSKII J.W., DOROCHINSKII A.Z., *Synthetical Zeolites and Their Application in Oilfield*, Mir, Moscow, 1967 (in Russian).
[9] EMERITUS A.W., Construction and Building Materials, 15, 323 (2001).
[10] SKRIPKIŪNAS G., Building and Architecture 10 (1998), 9 (in Lithuanian).
[11] JONKUS V., JASIŠKIENĖ E., Concrete and Ferroconcrete, Nowadays and Future 21, 59 (1999) (in Lithuanian).

Received 14 October 2004
Revised 6 January 2005

Materials Science-Poland, Vol. 23, No. 3, 2005

Multilayer Al_2O_3/Mo composites

H. MATYSIAK[1*], Ł. CIUPIŃSKI[2], A. OLSZYNA[1], K. J. KURZYDŁOWSKI[1]

[1]Faculty of Materials Science and Engineering, Warsaw University of Technology, ul. Wołoska 141, 02-507 Warsaw, Poland

[2]Functional Materials Research Center, Warsaw University of Technology, ul. Wołoska 141, 02-507 Warsaw, Poland

The present study was concerned with multilayer composites of the .../Al_2O_3/Al_2O_3 + *x* vol. % Mo/Al_2O_3 type produced by tape casting. Molybdenum content in individual layers of the composites varied from 4 to 28 vol. %. The densities, porosities, Young moduli, bending strengths, and fracture toughnessess of the composites were measured. The residual stress in the layers was analysed by FEM. Investigations of the composite microstructures revealed: α-Al_2O_3, Mo, and Mo_2C. After sintering, the composites had a high relative density (the porosity P_c did not exceed 10%). As the volumetric content of molybdenum increased, the densities of the composites increased, whereas their Young moduli E decreased. The highest values of the bending strength σ_b (819 MPa), stress intensity factor K_{IC} (7.75MPa·m$^{1/2}$), and cracking energy γ (102 J/m^2) were obtained in the composite with the 14 vol. % molybdenum content. The strength σ_b and fracture toughness of this composite were more than two times higher than those of Al_2O_3, and the cracking energy – six times. These values can be partly explained in terms of the compressive residual stress in the composite layers.

Key words: *tape casting; fracture toughness; residual stress*

1. Introduction

Multilayer composites are materials composed of a number of layers with properties varying from one layer to another in a way depending on their phase composition. In current practice, the component layers can be ceramic, metallic or polymeric, and their thickness may range from nanometers to millimetres [1]. Multi-layered composites are produced using various techniques, such as CVD, PVD, plasma spraying, electrophoresis, powder sintering, and tape casting. They exhibit increased mechanical strength and strain to failure, as well as improved fracture toughness. This is in general due to the interactions of the crack with the transition layers and residual stress fields existing within the material. More specifically, the following mechanisms

* Corresponding author, e-mail: huba@inmat.pw.edu.pl

have been identified to contribute to the increased fracture toughness of multilayer composites [2–23]:

- crack deflection due to lower cracking energy, lower strength, or a decreased rigidity in composites – a weak layer or a weak interlayer,
- crack deflection due to compressive or tensile residual stresses in the individual layers of the composite,
- phase transformation hardening, occurring in composites that, in layers of a certain type, contain a metastable form of zirconium oxide,
- crack bridging mechanisms, occurring in ceramic/metal composites.

From the above discussion, it can be concluded that residual stress is one of the important factors influencing the strength of multi-layered composites. Residual stress in metal-ceramic composites is of technological origin. The sintering process, which is a common technique used for the fabrication of multilayer ceramic composites, may be divided into three basic steps: heating, annealing, and cooling. Annealing generates stresses in the composite layers, because of the differences in the sintering kinetics of the individual components. These stresses can result in the material cracking at high temperatures or induce preferred centres of crack initiation during the cooling operation. During the cooling stage, residual stresses are generated due to differences in the linear thermal expansion coefficient α between components.

The increase of fracture toughness due to residual stress is principally related to the crack deflection effect. Developing cracks deflect from their energetically preferred propagation direction by compressive stress in the microstructure. This mechanism increases the effective crack path and cracking energy, thereby increasing the fracture toughness of the composite [8–10, 14–21]. Its relevance obviously depends on the value and spatial distribution of residual compressive stresses.

The aim of the study was to develop multiplayer Al_2O_3/Mo composites with increased fracture toughness. Moreover, the selected composite production technique was tape casting, which is relatively inexpensive and can be used to fabricate large components. The technological routes used here allow the production of ceramic/metal composites with volume fractions of the metal ranging from 4 to 28% of the volume, without visible sedimentation of Mo particles in spite of the large difference in the densities of the components.

2. Experimental

The composites were produced using AKP-50 α-Al_2O_3 powder from Sumitomo Chemical Co. Ltd., and MO006020 Mo powder from Goodfellow Advanced Materials. Test specimens were prepared by the tape casting method [27]. The procedure used here consisted of the following steps:

- Preparation of the cast composition containing the powder (Al_2O_3 or Al_2O_3 + x % Mo), binder (PVB resin), softener (dibutyl phthalate), solvent (ethanol and TRI), and flux (linseed oil) via mixing in a RETSCH agate mill for t = 4 h.

• Casting of a foil, which was subsequently dried and cut according to the assumed shape of specimens. The as-cast foil thickness was g = 1 mm and the casting rate V = 0.5 m/min. The foil was dried at room temperature.

• Arranging the foils in packets in a die and subsequent lamination under uniaxial pressing using a TM4 hydraulic press (p = 10 MPa).

• Isostatic consolidation in an autoclave under pressure (p = 120 MPa).

• Sintering in a Lenton-Thermal furnace at T = 1473 K in an N_2 atmosphere for t = 1 h (a), in a Baltzers furnace in vacuum ($p = 10^{-4}$ Pa) at T = 1973 K for t = 1.5 h (b).

The densities and porosities of the specimens were determined by the Archimedes method using a Radwag WPS balance. The qualitative characterisation of the microstructures was based on light microscopy images (Nikon Epiphot) at magnifications ranging from 100 to 1000×. The Young moduli (E) were determined by the ultrasonic method using an UR19A refractometer. The bending strengths of the composites were measured with an Instron 1114 strength machine in the three-point bending mode using 6×4×50 mm bars (10 samples from each type of composite). The support spacing used was L = 40 mm. Specimens were loaded at a rate of 1 mm/min until failure, and the failure force was measured. A similar three-point bending setup was used to determine the stress intensity factors. Test specimens (8 bars 6×4×50 mm from each type of composite) were notched, in their mid-length, to a depth of a = 1.1 mm. The notching was made stepwise, using a 0.2 mm diamond saw down to a depth of 0.9 mm and then a 0.025 mm diamond saw. The support spacing used this time was L = 15 mm.

The cracking energy was calculated from the relationship $\gamma = K_{IC}^2/2E$, where K_{IC} is the stress intensity factor. The distribution and magnitude of the residual stress occurring in the composites as a result of cooling were modelled using Ansys 5.7 software. For the purpose of modelling, a representative volume was selected in the way schematically shown in Fig. 1. The modelled representative composite volume contained 2 complete and 2 halves of composite layers. An initial thickness of the layers of 1 mm was assumed, which corresponds to the thickness of the as-cast foil.

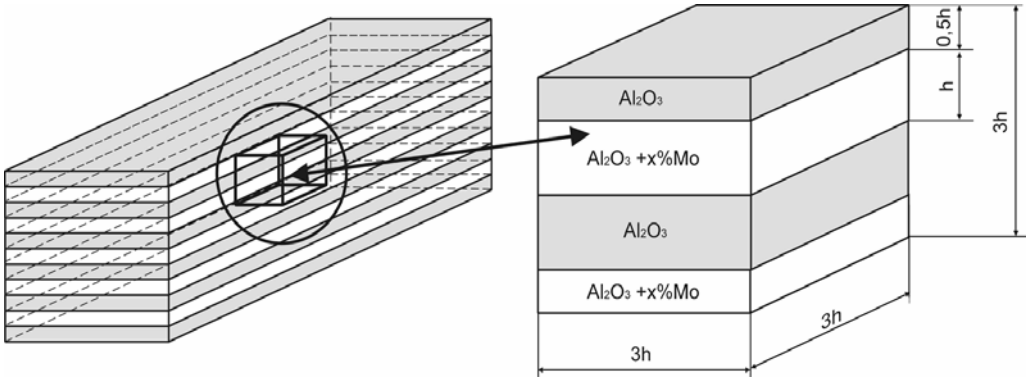

Fig. 1. Geometrical model of the layered composite structure adopted in the FEM analysis of residual stress

In the analysis, the materials of the individual layers (α-Al_2O_3 layers and the Al_2O_3 + x % Mo composite layers) were modelled as perfectly elastic. In this case, their macroscopic behaviours can be described by the Young moduli E and Poisson ratios. The Young moduli of alumina and Mo as a function of temperature are shown in Fig. 2a. Additionally, the Poisson ratio for corundum was assumed to be invariant with temperature and equal to 0.23. Variations of α for alumina and molybdenum are shown in Fig. 2b.

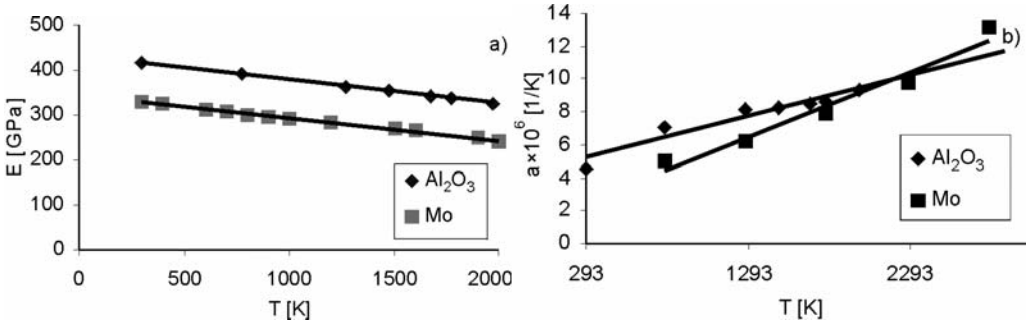

Fig. 2. The variations of the Young moduli (a) and linear thermal expansion coefficients α (b) in corundum and molybdenum as functions of temperature [25, 26]

For the generation of the FE mesh, a 20 nodes "cubic" structural element (Solid 95) was employed. Figure 3 shows the assumed geometry of the model and the mesh of finite elements. The straight line P shown in the figure denotes the path along which the stress distributions were analysed.

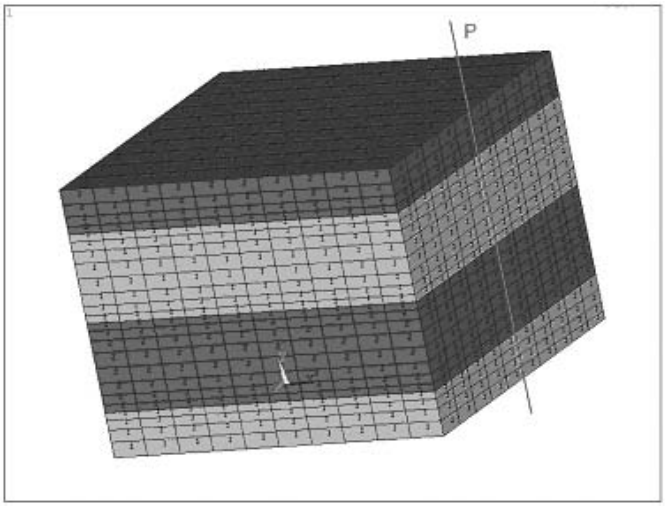

Fig. 3. Geometry of the model and the mesh of finite elements. Line P shown in the figure denotes the path along which the stress distributions were analysed

Two different boundary conditions were assumed in the modelling:

Model 1:

- symmetric with respect to the planes $\{X,Y,Z\} = 0$,
- the displacements u_x, u_y, and u_z of the nodes positioned in the planes $X = 3h$, $Y = 3h$, and $Z = 3h$, respectively, along the respective directions normal to these planes, are coupled.

Model 2:

- symmetric with respect to the planes $\{X,Y,Z\} = 0$,
- only the displacements u_x and u_y of the nodes positioned in the planes $X = 3h$ and $Y = 3h$, respectively, along the directions normal to these plane, are coupled.

It was assumed that the internal stress is generated when the composites are cooled from the sintering temperature T_S (1973 K) to room temperature T_r (293 K), as a result of differences in the linear expansion coefficients α of their components. Accordingly, as the load imposed on the models, a temperature drop of 1680 K was used. Figure 2b shows the values of the linear expansion coefficients of the individual components of the layered composites. Since no experimental data were available as to the coefficient α for Al_2O_3 + *x* % Mo composite layers, these values were calculated based on the rule of mixtures.

3. Results and discussion

Figures 4a–e show examples of the structures of the examined multilayer composites. Microscopic observations revealed that the molybdenum particles were uniformly distributed throughout the volumes of the composites. In the composites with molybdenum content up to 14 vol. %, the individual layers and the interlayer boundaries did not contain defects generated during the fabrication process, whereas in specimens with 21 and 28 vol. % of molybdenum, the composite microstructures contained numerous cracks formed during fabrication. These cracks developed in the Al_2O_3 layers, but no transverse cracks were observed within the composite layers. There were also delaminating cracks, which propagated along interlayer boundaries.

Table 1 lists selected properties of the fabricated multilayer Al_2O_3/Mo composites. The sintered composites had a fairly good relative density (the porosity P_c did not exceed 10%). With increasing volumetric content of molybdenum, the density d increases linearly, whereas the Young modulus E decreases in similar way. This suggests that the studied structure can be assumed to vary primarily in the content of Mo. The highest values of the bending strength σ_b (819MPa), the stress intensity factor K_{IC} (7.75 MPa·m$^{1/2}$), and the cracking energy γ(102 J/m^2) were observed in the composite with 14 vol. % of molybdenum in the individual layers. The mechanical strength σ_b and fracture toughness of this composite are more than twice higher than for Al_2O_3, and the cracking energy more than 6 times higher.

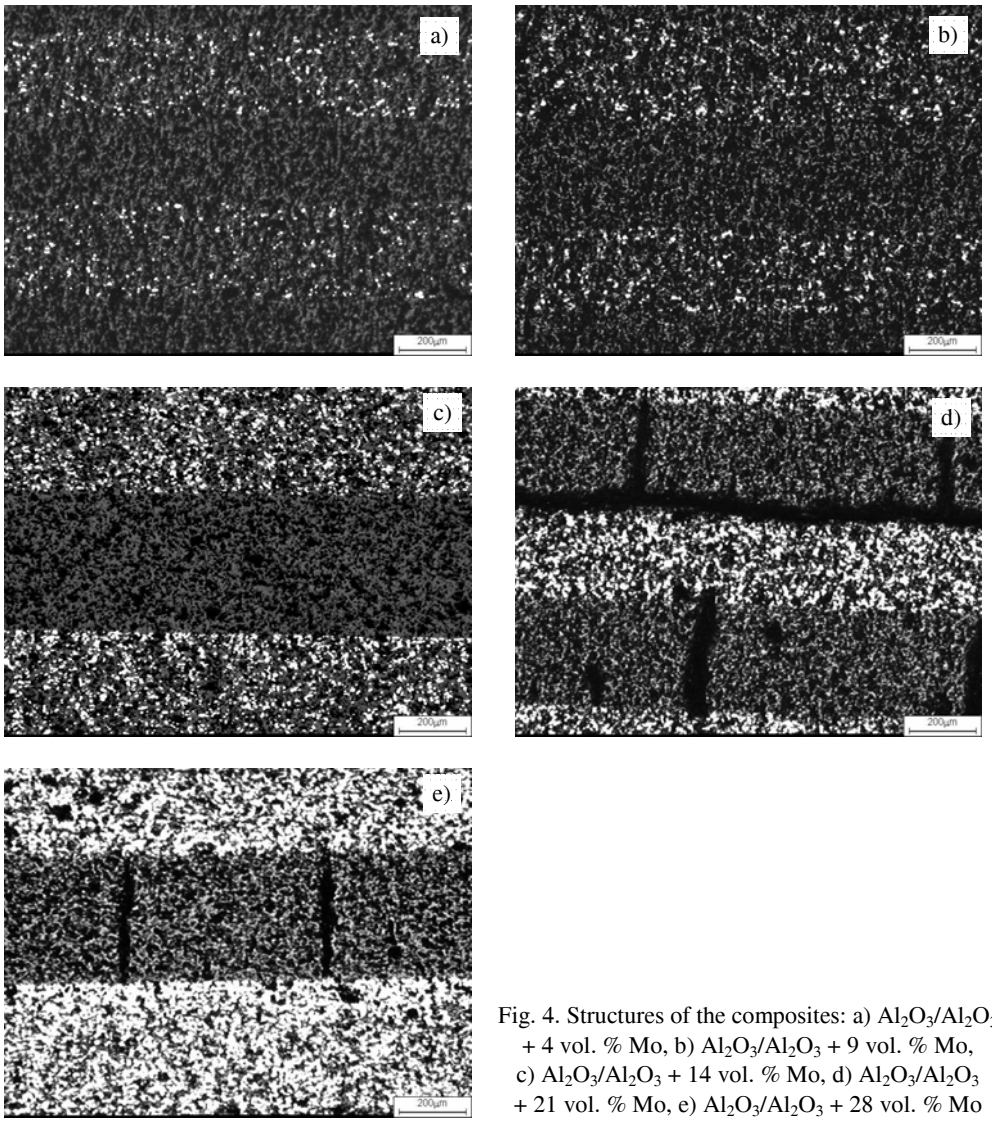

Fig. 4. Structures of the composites: a) Al_2O_3/Al_2O_3 + 4 vol. % Mo, b) Al_2O_3/Al_2O_3 + 9 vol. % Mo, c) Al_2O_3/Al_2O_3 + 14 vol. % Mo, d) Al_2O_3/Al_2O_3 + 21 vol. % Mo, e) Al_2O_3/Al_2O_3 + 28 vol. % Mo

Table 1. Mechanical properties (density d, porosity P_c, Young modulus E, bending strength σ_b, fracture toughness K_{IC}, cracking energy γ) of the Al_2O_3/Al_2O_3 + x vol. % Mo composites

x % vol. Mo	d [g/cm^3]	P_c [%]	E [GPa]	σ_b [MPa]	K_{IC} [MPa·m$^{1/2}$]	γ [J/m^2]
0	3.98	0	400	380	3.5	15
4	3.86	6	336±14	420±80	4.7±0.4	33±5
9	3.85	10	313±4	590±70	6.0±0.7	59±14
14	4.22	4	297±4	820±30	7.8±0.66	102±15
21	4.39	4	287±8	560±50	6.5±0.9	74±19
28	4.59	3	276±7	350±30	6.0±0.7	67±16

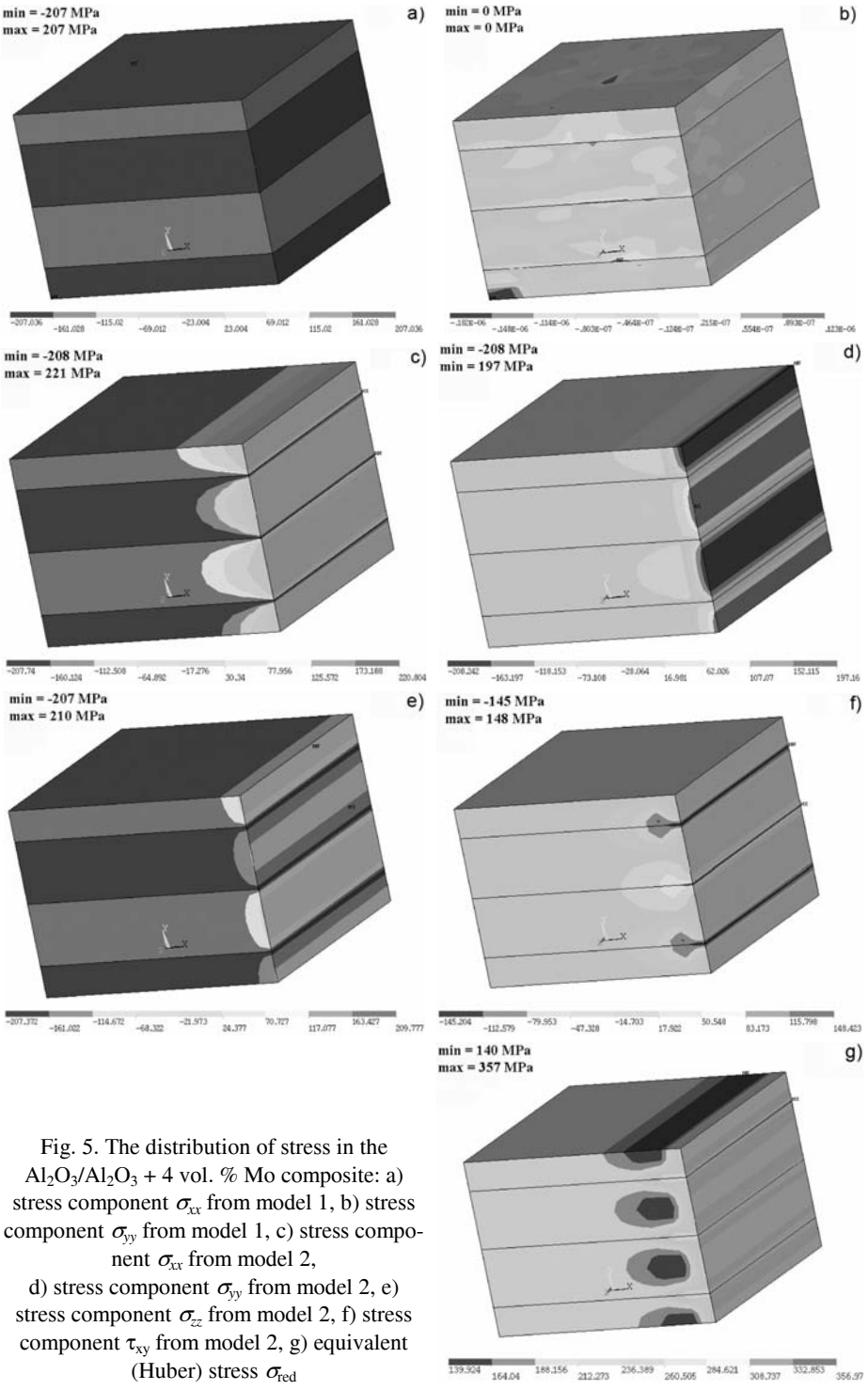

Fig. 5. The distribution of stress in the Al_2O_3/Al_2O_3 + 4 vol. % Mo composite: a) stress component σ_{xx} from model 1, b) stress component σ_{yy} from model 1, c) stress component σ_{xx} from model 2, d) stress component σ_{yy} from model 2, e) stress component σ_{zz} from model 2, f) stress component τ_{xy} from model 2, g) equivalent (Huber) stress σ_{red}

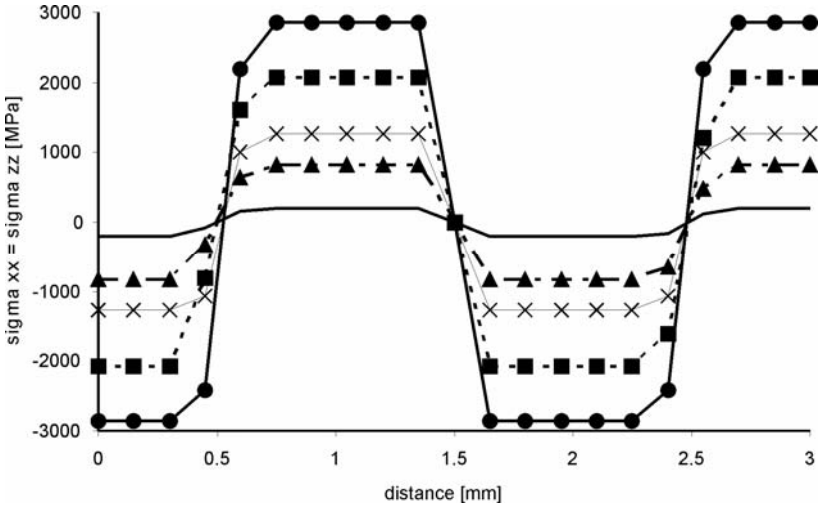

Fig. 6. Variation of the residual stress tensor component $\sigma_{xx} = \sigma_{zz}$ as a function of the distance along the line P in multilayer $Al_2O_3/Al_2O_3 + x$ vol. % Mo composites (Model 2): – $x = 4$, ▲ – $x = 9$, × – $x = 14$, ■ – $x = 21$, ● – $x = 28$

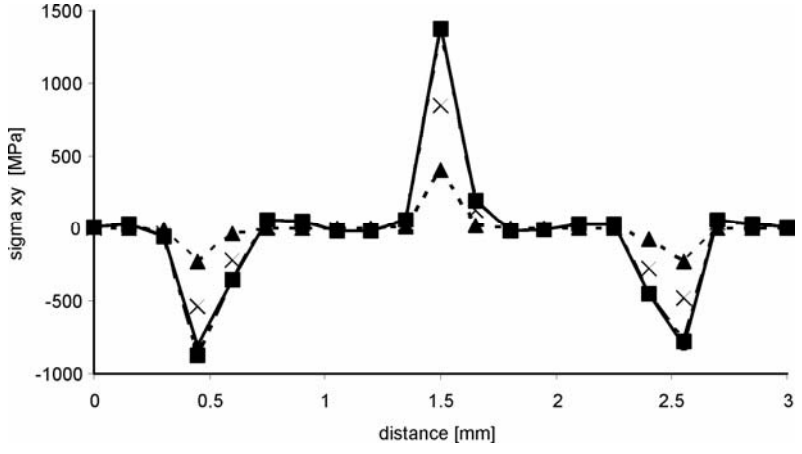

Fig. 7. Variations of the components σ_{xy}, σ_{xz}, and σ_{yz} of the residual stress tensor as a function of the distance along the line P in multi-layer $Al_2O_3/Al_2O_3 + x$ vol. % Mo composites: – $x = 4$, ▲ – $x = 9$, × – $x = 14$, ■ – $x = 21$

Figures 5–7 show the results of the analysis of residual stresses, performed using the Finite Elements Method. Since the characters of the stress distributions are identical for all the analysed models of the composite structures, only the results obtained for the Al_2O_3/Al_2O_3 + 4 vol. % Mo composite are shown. The description given is based on the numerical results of all modelled cases.

Model 1. The distributions and values of the stress tensor components σ_{xx} and σ_{zz} (the stresses whose mutually perpendicular directions lie in the plane of the interlayer

boundary) are identical. In Al_2O_3 layers, these stress components are tensile, whereas in Al_2O_3 + x vol. % Mo composite layers they are compressive. The magnitudes of these stresses increase with increasing molybdenum content in the layers. At the interlayer boundary, the magnitude of stress abruptly changes in a step-wise manner. The stress component σ_{yy} (acting in the direction perpendicular to the interlayer boundary plane) is zero, irrespective of the molybdenum content in the composite layer.

Model 2. The effect of a free surface due to the removal of the condition on the displacements u_z of the nodes positioned in the plane $Z = 3h$ essentially changes the distributions of stress tensor components. The components σ_{xx} and σ_{zz} are equal to zero, and, as the distance from this surface towards the interior of the material increases, the stress magnitudes increase and reach their maximum values (tension in the Al_2O_3 layers and compression in the composite layer) equal to those adopted in model 2. It should be noted, however, that in the immediate vicinity of the entire interlayer boundary the components σ_{xx} and σ_{zz} reach their maximum values. The stress σ_{yy}, on the other hand, reaches its maximum value in the plane of the free surface and then decreases to zero in the interior just as is the case of model 2.

Another consequence of the presence of the free surface is the shear stress σ_{xy} (σ_{xz} and σ_{yz} are zero). The largest stress σ_{xy} is generated at the interlayer boundary. In terms of the von Mises–Huber criterion, the most stressed components of multilayer composites are the interlayer boundaries.

The geometry of the composite structure model considered here appears to be sufficient for an analysis of the residual stress. The character of the distributions of stress tensor components obtained from this analysis are consistent with the qualitative analysis of the material properties of the composite constituents.

The calculated average values considerably exceed the tensile strength of alumina (except in the composite with the lowest molybdenum content). The transverse and delaminating cracks in Al_2O_3 layers, however, are observed only in composites with 21 and 28 vol. % molybdenum content.

This can be attributed to the assumption that the Al_2O_3 + x vol. % Mo composite layers are uniform and purely elastic in the early stages of sintering. On the other hand, the stress distributions calculated here give better insight into the mechanics of multi-layered composites.

4. Conclusions

The tape casting technique used in the present experiment permitted the fabrication of ceramic/metal composites with a wide range of metal volumetric content (4 to 28 vol. % Mo) and porosity (1 to 10%). The densities of the composites did not exceed 5.5 g/cm^3, i.e. 138% of the density of alumina.

The best properties were obtained for the composite with 14 vol. % of Mo. The fracture toughness of this composite was twice that of Al_2O_3. This was accompanied by a six-fold increase of the cracking energy and bending strength.

The proposed FEM model of two-fold layered composites is useful for the qualitative analysis of residual stress arising during cooling from the fabrication temperature. Quantitative analyses of stress require that it be modified to take into account the visco-elastic behaviour during the early stages of cooling.

Aknowledgements

This work was supported by the State Committee for Scientific Research (grant No. 4T08D00223).

References

[1] CAHN R.W., HAASEN P., KRAMER E.J., *Materials Science and Technology. Structure and Properties of Ceramics*, Vol. 11, CH, Weinheim, 1994.
[2] MARSHALL D.B., RATTO J.J., LANG F.F., J. Am. Cer. Soc., 74 (1991), 2979.
[3] KOVAR D., THOULESS M.D., HALLORAN J.W., J. Am. Cer. Soc., 81 (1998), 1004.
[4] HUANG Y., CAI S., GUO H., WANG C., XIE Z., *The Biomimetric Structure Design and Preparation of Si_3N_4 Matrix Composites with High Toughness*, 9th Cimtec-World Ceramics Congress 2000, pp. 881–888.
[5] ZENG Y., JIANG D., Fabrication and properties of laminated Al_2O_3/TiC composites, Cer. Int., 27 (2002), 597.
[6] MING L.Y., WEI P., SHUGIN L., JIAN CH., RUIGANG W., JIANQUING LI, Cer. Int., 28 (2002), 223.
[7] DREWNY E.N., MOON R.J., BOWMAN K.J., TRUMBLE K.P., BREMM J., Scripta Materialia, 41 (1999), 749.
[8] CAI P.Z., GREEN D.J., MESSING G.L., J. Am. Cer. Soc., 80 (1997), 1929.
[9] CAI P.Z., GREEN D.J., MESSING G.L., J. Am. Cer. Soc., 80 (1997), 1940.
[10] GREEN D.J., CAI P.Z., MESSING G.L., J. European Cer. Soc., 19 (1999), 2511.
[11] FOLSOM C.A., ZOK F.W., LANGE F.F., J. Am. Cer. Soc., 77 (1994), 689.
[12] OECHSNER M., HILLMAN C., LANGE F.F., J. Am. Cer. Soc., 79 (1996), 1834.
[13] WANG H., XIAOZHI H., J. Am. Cer. Soc., 79 (1994), 553.
[14] SERGO V., LIPKIN D.M., DE PORTU G., CLARKE D.R., J. Am. Cer. Soc., 80 (1997), 1633.
[15] LAKSHMINARAYANAN R., SHETTY D.K., CUTLER R.A., J. Am. Cer. Soc., 79 (1996), 79.
[16] MARSHALL D.B., MORGAN P.E.D., HOUSLEY R.M., J. Am. Cer. Soc., 80 (1997), 1677.
[17] CUTLER W.A., ZOK F.W., LANGE F.F., J. Am. Cer. Soc., 80, (1997), 3029.
[18] MOON R.J., BOWMAN K.J., TRUMBLE K.P., RODEL J., Acta Mater., 49 (2001), 995.
[19] LUCCHINI E., SBAIZERO O., J. European Cer. Soc., 15 (1995), 975.
[20] CAI P.Z., GREEN D.J., MESSING G.L., J. European Cer. Soc., 5 (1998), 2025.
[21] ZHANG G-J., YUE X-M., WATANABE T., J. European Cer. Soc., 19 (1999), 2111.
[22] JIMENEZ-MELENDO M., GUTIERERREZ-MORA F., DOMINGUEZ-RODRIGUEZ A., Acta Mater., 48 (2000), 4715.
[23] HWU K.L., DERBY B., Acta Mater., 47 (1999), 545.
[24] CHENG Z., MECHOLSKY J.J., J. Am. Cer. Soc., 76 (1993), 1258.
[25] http://michelle.ucsd.edu/lib/props/panos/moa.html.
[26] MUNRO R.G., J. Am. Cer. Soc., 80 (1997), 1919.
[27] MISTLER R.E., TWINAME E.R., *Tape Casting: Theory and Practice*, American Ceramic Society, Westerville, OH, 2000.

Received 3 December 2004
Revised 5 August 2005

Materials Science-Poland, Vol. 23, No. 3, 2005

The effect of the reactive milling of graphite with boron nitride, tin and antimony on lithium insertion

DANIEL WASZAK[1], ELŻBIETA FRĄCKOWIAK[2*]

[1]Central Laboratory of Batteries and Cells, Forteczna 12, 61-362 Poznań, Poland

[2]Institute of Chemistry and Technical Electrochemistry,
Poznań University of Technology, Piotrowo 3, 60-965 Poznań, Poland

Boron-, tin-, and antimony-based graphite composites were studied as potential materials for negative electrodes in lithium-ion batteries. The materials were prepared by the reactive milling of mixtures of graphite (90 wt. %) with boron nitride (10 wt. %), tin (10 wt. %), or antimony (10 wt. %). Milling was performed for 2 h, 4 h, 6 h, or 8 h. The composites were characterized by X-ray diffraction and nitrogen adsorption at 77 K (BET). A gradual development of surface area during milling was observed as well as the appearance of amorphous forms. The galvanostatic characteristics of lithium insertion–deinsertion for these new composite materials were investigated. Graphite-tin composites exhibit the best reversible capacity. Modification by milling leads to a significant particle size reduction, good association of the metallic phase with graphite crystal grains, and consequently to an increase of the reversible capacity. A significant enhancement of the irreversible capacity for the composites is also observed due to the development of specific surface area.

Key words: *lithium-ion cell; graphite; milling; anodic material*

1. Introduction

Graphite remains the most often used anode material for lithium-ion accumulators. Li-ion cells with graphite anodes are characterized by long durability (over 1000 cycles), high stable voltage (>3 V), a lack of hysteresis (i.e., the divergence between the polarization of lithium insertion and deinsertion). The maximum reversible capacity for lithium intercalation into graphite is 372 mAh/g (the 1st stage of the intercalation compound Li_xC_6, where $x = 1$) and is related to the graphitic crystal structure [1–3]. The irreversible capacity, i.e. the amount of lithium consumed in the formation of solid electrolyte interphase (SEI) during the first cycle is very low, ca. 50 mAh/g. The

*Corresponding author, e-mail: fracko@fct.put.poznan.pl

great interest for graphite as the Li-ion anode is also caused by moderate price of both natural and synthetic graphite. Due to all these useful characteristics, a lot of research has been devoted to the further modification of graphite in order to increase the reversible capacity through the insertion and deposition of heteroatoms, metals, and other treatments.

Among various modifications of graphitic materials for Li-ion cells, structural changes through mechanical treatment [4–6], incorporation of heteroatoms [7–12], and a carbon surface coating by pyrolytic carbon, metals [11–16] have already been proposed.

Even if it is assumed that doping with heteroatoms, e.g. boron [8], is beneficial for the process of lithium ion intercalation into graphites, practical results show some discrepancies [10]. When a shell of BC_x covers the graphite surface, its properties should be significantly improved, because B incorporated into the structure of a carbonaceous material reduces its reactivity through changes in charge distribution in the crystallographic plane, especially on the edges [7]. This hinders the processes of surface chemical degradation [9], which directly affects the prolongation of electrode lifetime during cycling. The expected improvement of lithium storage capability for boronated carbons seems to be due to the electron deficiency of boron, which has only three valence electrons. This electron acceptor character of boronated carbon can increase Li–C binding energy. On the other hand, when boron occurs in the form of boron carbide, the irreversible capacity rises, because this compound does not take part in the process of lithium storage [7].

One of alternatives for graphite anodes are materials made of the metal–carbon composites having high capacities in the process of forming intermetallic compounds with lithium, e.g. tin $Li_{22}Sn_5$ and antimony Li_3Sb [7, 11–14]. Unfortunately, apart from the capacity, which can be three times higher than that of graphite, their greatest disadvantage is a poor cycle life, usually not exceeding a few cycles. This is due to the fact that during the creation of compounds with lithium, the system volume increases more than three times, and during the reverse process it returns to the starting volume, thus causing mechanical stress, particle fracture, and a loosening of the electrical contact between them.

In the present work, attempts were performed to incorporate boron atoms into graphite structure, using high-energy ball-milling. Trials were also undertaken to combine the positive features of graphite with such metals as Sn and Sb by forming graphite–metal composites through milling.

2. Experimental

Graphite–boron composites were synthesized by high-energy ball milling using a shaker-type ball mill Retsch MM 200. Graphite UF2 of high purity from Kropfmühl (Germany) was used. Mixtures of graphite 90 wt. % and boron nitride 10 wt. % were put into the mill reactor together with the grinding balls. The weight ratio of the grind-

ing balls to the milled material was 5:1. Both the reactor and grinding balls were made of zirconium oxide. The milling was conducted in an inert argon atmosphere. Mixtures of graphite and BN were milled for 2, 4, 6, and 8 hours and the obtained materials were designated as 10B2h, 10B4h, 10B6h, and 10B8h, respectively. Sn–graphite and Sb–graphite composites were obtained and labelled analogously (Sn–graphite composites: 10Sn2h, 10Sn4h, 10Sn6h, and 10Sn8h, and Sb–graphite composites: 10Sb2h, 10Sb4h, 10Sb6h, and 10Sb8h).

Physicochemical characterization of the obtained materials was conducted using X-ray diffraction (XRD) and nitrogen adsorption at 77 K (BET). XRD measurements were done using a Phillips PW 1710 diffractometer with FeK_α radiation, whereas for nitrogen adsorption an ASAP 2010 (Micromeritics) analyser was used.

Galvanostatic characteristics were determined using Atlas-Sollich galvanostats 9835 in two-electrode Swagelok cells. The anodes in the half-cells were round pellets cut out from copper foil covered with a mixture of the examined composite: binder (10 wt. % of PVdF) and acetylene black (5 wt. %). The counter electrode (and simultaneously the reference electrode) was metallic lithium. The electrolyte was a 1 M solution of $LiPF_6$ in a 1:1 mixture of ethylene carbonate and diethyl carbonate. The half-cells were cycled between 0 V and 2 V using a constant current density of 10 mA per gram of active material.

3. Results and discussion

The results of all physicochemical and electrochemical tests for the composites are collected in Table 1.

Table 1. Physicochemical and electrochemical results for the milled composites

Sample	BET surface area [m^2/g]	Irreversible capacity (x)	Reversible capacity (x)
Graphite	14	0.28	1.00
10B2h	162	1.20	0.85
10B4h	212	1.36	0.96
10B6h	304	2.00	0.92
10B8h	-	2.19	0.91
10Sn2h	153	1.39	1.19
10Sn4h	241	1.83	1.27
10Sn6h	322	2.20	1.31
10Sn8h	324	2.21	1.36
10Sb2h	153	1.44	1.14
10Sb4h	233	1.93	1.17
10Sb6h	280	2.34	1.22
10Sb8h	301	2.39	1.34

For $x = 1$, the first stage of the intercalation compound Li_xC_6 is formed.

Milling causes a significant development of surface area evidenced by adsorption isotherms. Both surface area and the ratio of micropores to the total porosity of materials rise. Figure 1 presents typical adsorption isotherms for selected composites of graphite with B, Sn, and Sb milled for 2 h, 6 h, or 8 h.

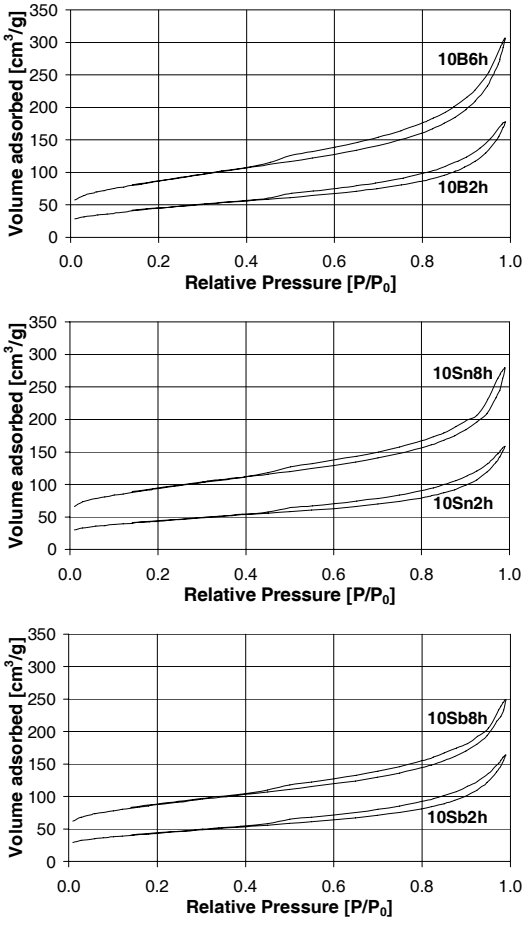

Fig. 1. Nitrogen adsorption isotherms for the graphitic composites 10B2h and 10B6h, 10Sn2h and 10Sn8h, and 10Sb2h and 10Sb8h

As can be seen, even two hours of milling results in a surface area increase by an order of magnitude compared to pure graphite (Table 1). A longer milling causes even greater surface development, however not so distinct. This effect is observed for all the milled materials being connected with the applied modification technique. High-energy milling not only links the mixture components into a composite material, but also causes grinding of particles and an increase in the surface area. The materials undergo structure degradation and become amorphous. Another effect of milling is the increasing number of active sites and dangling bonds [16].

A strong degradation of the crystal structure after milling is clearly evidenced by the XRD patterns as a broadening and disappearing of certain signals. Selected XRD patterns are shown in Fig. 2.

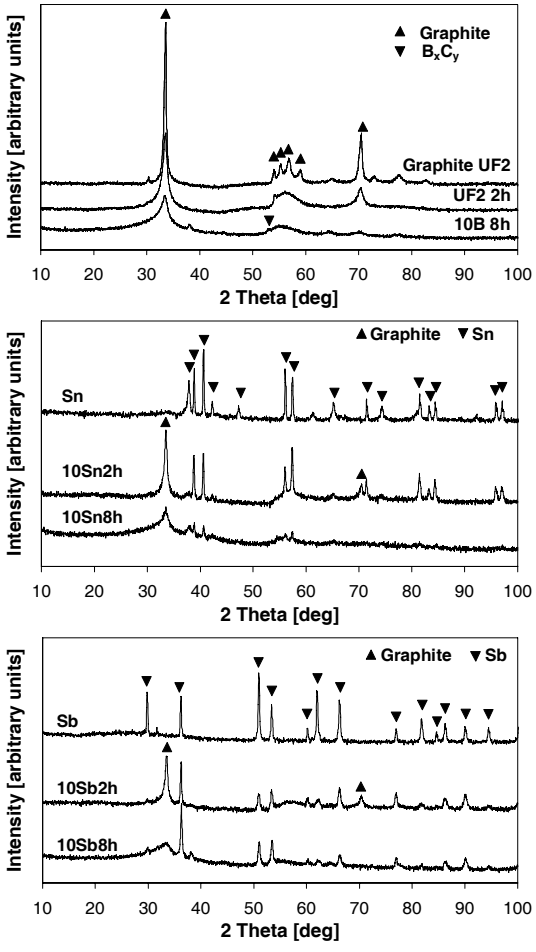

Fig. 2. Selected XRD patterns for the following pairs of composite materials: graphite and 10B8h, 10Sn2h and 10Sn8h, and 10Sb2h and 10Sb8h

In the case of 10Sn and 10Sb there are no signs of XRD peaks from any intermediate compounds of mixture components that could be formed during milling. On the other hand, in the case of 10B8h there is a signal in the XRD pattern that might be ascribed to the intermediate phase of some compound of carbon and boron (B_xC_y). However, such an assumption should be supported by further examinations with a longer milling time. In the hypothesis that boron forms a compound with carbon, the residual nitrogen from boron nitride can eventually create nitrogen functionalities with carbon.

Physicochemical results are fully confirmed by the data from galvanostatic experiments, which were done in half-cells with metallic lithium as both the counter and reference electrode (Fig. 3). For comparison, the galvanostatic intercalation–deintercalation process with a pure UF2 graphite sample is also presented. For all composites an increase of irreversible capacities can be seen, which is due to the development of surface and the creation of a large number of active sites, such as crystal structure defects and dangling bonds. Larger hysteresis in the charge–discharge curves indicates that the structure has been disordered to a large extent and that graphitic regions coexist with amorphous ones. It also proves that different sites of various Li–C bonding exist in composites where the deinsertion process involves higher energies.

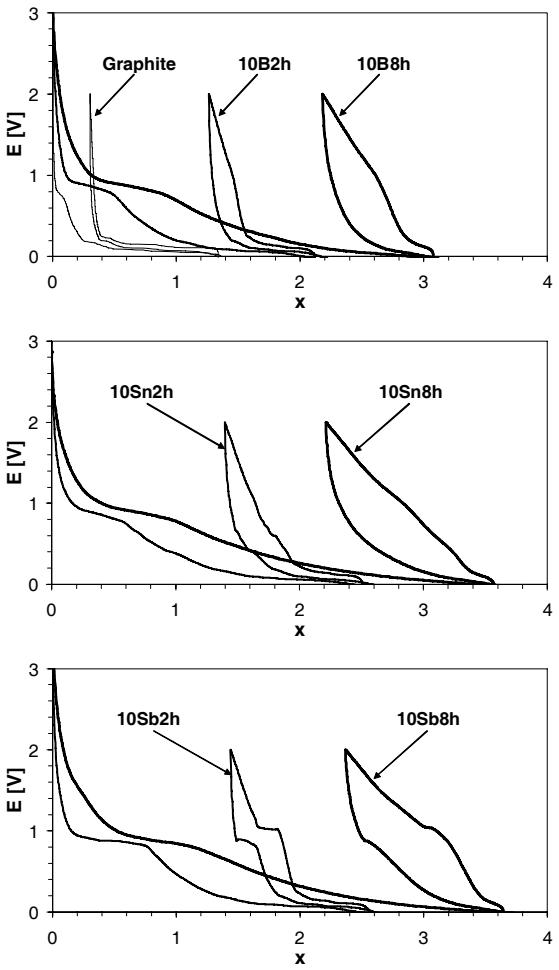

Fig. 3. Galvanostatic curves of lithium insertion–deinsertion
for graphite and the following composite materials:
10B2h and 10B8h, 10Sn2h and 10Sn8h, and 10Sb2h and 10Sb8h

Three small plateaus are visible in the discharge curve of 10Sn2h in the range of 0.55–0.85 V vs. Li/Li^+ (Fig. 4). They are connected with lithium ion deinsertion from the intermetallic compound Li_xSn_y. It is noteworthy that these plateaus are very reproducible and observed in repeated experiments. Upon grinding, tin becomes more amorphous, which is the reason why the plateaus disappear in the composite 10Sn8h.

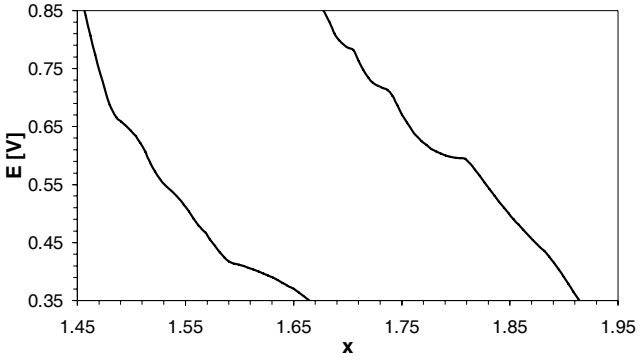

Fig. 4. Plateaus in the composite 10Sn2h
(left: lithium insertion; right: lithium deinsertion)

The situation is similar in the case of antimony–graphite composites. For the sample 10Sb2h, a distinct plateau at 1.03 V vs Li/Li^+ is seen on the discharge curve (Fig. 5). The plateau vanishes upon milling and is markedly smaller in sample 10Sb8h (Fig. 3).

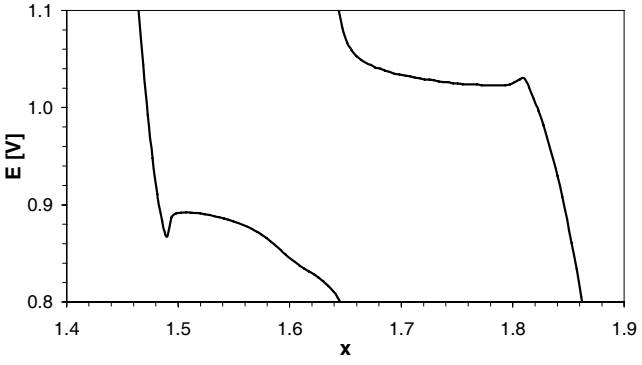

Fig. 5. Plateaus in the composite 10Sb2h
(left: lithium insertion; right: lithium deinsertion)

The galvanostatic curves obtained for composites milled with boron nitride are different in character. Materials 10B2h and 10B8h do not exhibit any plateaus beside those of graphite (in the range of 0–0.3 V), which proves that neither boron nitride nor B_xC_y compound, created during prolonged milling, do not take part in the process of lithium storage.

4. Conclusions

The positive effect of boron on Li insertion in graphite, described in literature, has not been confirmed in the present work, in which graphite was milled with boron nitride. Nevertheless, the technique of milling can be suitable for obtaining mixtures of graphite with other boron compounds.

Milling of graphite with tin and antimony gave positive results. Upon milling, reversible lithium insertion capacity rises; unfortunately, irreversible capacities and charge–discharge hysteresis are also increased. Modification of the mixture composition as well as milling conditions, such as the environment, milling energy, or ratio of millers to the milled material, can bring about a significant improvement in the material characteristics in terms of reversible capacities without negative effects.

Further improvement of electrochemical performance of graphitic composites with incorporated heteroatoms should be connected with the suppression of volume change during lithium intercalation–deintercalation, and with good electronic conductivity of the composite as well as a limited surface area and number of active sites.

Acknowledgements

Financial support from the State Committee for Scientific Research of Poland (KBN, grant No. 4 T10A 045 22) is gratefully acknowledged.

References

[1] GUÉRARD D., HÉROLD A., Carbon, 13 (1975), 337.
[2] VINCENT C.A., SCROSATI B., *Modern Batteries*, Wiley, New York, 1997.
[3] *Lithium Ion Batteries – Fundamentals and Performance*, M.Wakihara, O.Yamamoto (Eds.), Wiley, New York, 1998.
[4] DISMA F., AYMARD L., DUPONT L., TARASCON J-M., J. Electrochem. Soc., 143 (1996), 3959.
[5] CHEVALLIER F., AYMARD L., TARASCON J-M., J. Electrochem. Soc., 148 (2001), A1216.
[6] AZAIS P., DUCLAUX L., FAUGERE A.-M., BÉGUIN F., Appl. Phys. Lett., 81 (2002), 775.
[7] WU Y.P., RAHM E., HOLZE R., Electrochim. Acta, 47 (2002), 3491.
[8] SHIRASAKI T., DERRÉ A., GUÉRIN K., FLANDROIS S., Carbon, 37 (1999), 1961.
[9] MA X., WANG Q., CHEN L.-Q., CERMIGNANI W., SCHOBERT H.H., PANTANO C.G., Carbon, 35 (1997), 1517.
[10] MACHNIKOWSKI J., FRACKOWIAK E., KIERZEK K., WASZAK D., BENOIT R., BÉGUIN F., J. Phys. Chem. Solids, 65 (2004), 153.
[11] FLANDROIS S., SIMON B., Carbon, 37 (1999), 165.
[12] WU Y.P., RAHM E., HOLZE R., J. Power Sourc., 114 (2003), 228.
[13] LIU Y., XIE J.Y., YANG J., J. Power Sourc., 119–121 (2003) 572.
[14] DAILLY A., GHANBAJA J., WILLMANN P., BILLAUD D., Electrochim. Acta, 48 (2003), 977.
[15] CHEVALLIER F., LETELLIER M., MORCRETTE M., TARASCON J-M., FRACKOWIAK E., ROUZAUD J-N., BÉGUIN F., Electrochem. Solid State Lett., 6 (2003), A225.
[16] BÉGUIN F., CHEVALLIER F., VIX C., SAADALLAH S., ROUZAUD J-N., FRACKOWIAK E., J. Phys. Chem. Solids, 65 (2004), 211.

Received 3 December 2004
Revised 5 August 2005

Materials Science-Poland, Vol. 23, No. 3, 2005

Evaluation of metal–mould interfacial heat transfer during the solidification of aluminium –4.5% copper alloy castings cast in CO_2–sand moulds

S.N. KULKARNI[1*], K. RADHAKRISHNA[2]

[1]Department of Mechanics, Adhiyamaan College of Engineering, Hosur-635 1009, India

[2]Department of Mechanics, B.M.S.College of Engineering, Bangalore-19, India

In this study, two methods were employed to measure the heat transfer coefficient h at the metal –mould interface during casting. The first method measured the size of the gap formed between the metal and mould during the casting process and estimated the value of h based on the gap size. The second method measured the temperature at certain locations of the metal and mould, and derived h at the gap by using a reverse method. A procedure is also developed to use temperature measurement data in order to obtain h as a function of casting temperature near the interference. This data is very useful for the mathematical modelling of solidification for casting. In the present study, the casting material is an Al–4.5% Cu alloy and the mould material is CO_2 sand. The results of measurements show that h is not constant, but varies with time and temperature during casting. With the measurement of gap size, h is very large in the beginning and keeps dropping afterwards. As the gap is fully developed, h approaches a constant value between 130 and 40 W/(m^2·°C). By the inverse method, along with temperature measurement, the value of h increases in the beginning stage, reaches a peak value of approximately 710 W/(m^2·°C), and then drops rapidly approximately to the solidification temperature, and rises again until the end of solidification. After that, h keeps dropping until the end of casting.

Key words: *CO_2–sand mould; interfacial heat transfer; heat transfer coefficient; gap size.*

1. Introduction

In recent years, the development of digital computer technology and applied numerical methods has provided a powerful means for simulating casting solidification. One of the main interests of the casting process is to produce parts near net shape and with complex geometry, for instance with internal cavities. Shape casting consists of two stages, the first of which is mould filling – the mould cavity is filled with liquid

*Corresponding author, e-mail: suneelkumarkulkarni@rediffmail.com

metal; the second is cooling, which continues until the part has solidified. Controlling both stages is of major importance for obtaining sound parts with the required geometry and mechanical properties. As computer-aided design and manufacture experience increasing use in industry, computer modelling of the cooling stage in casting processes appears to be of great interest since it enables the microstructure, final shape, residual stresses, and defects to be predicted.

Since molten casting metal is poured into the mould cavity, it is initially in the liquid state with a high fluidity. It quickly becomes very viscous, in the early stage of solidification, and later completely solidifies. During this process, a gap is formed between the casting metal and the mould. This gap forms due to the following reasons. First of all, the thermal expansion coefficients of the casting metal and mould are different. Second, some of the air initially in the mould cavity cannot escape through the mould and is trapped between the metal and the mould. Third, the binder in the mould materials and the coatings on the inner surface of the mould may evaporate or burn due to high temperature, which contributes as an additional source of gases between the metal and mould. These combined factors affect the size of the gap formed.

As the gap is formed, it presents a resistance to heat transfer from the casting metal to the mould. This is due to the fact that heat can be transferred through the gases in the gap. The heat flux is much smaller compared to the conductive heat transfer in a metal, or even in the mould. It is generally believed that the resistance to heat transfer at the gap increases with the size of the gap. The resistance to heat transfer at the interface will naturally be reflected in the solidification of the casting metal. It is thus very desirable to know the magnitude of this resistance to heat transfer, which is represented by an interfacial heat transfer coefficient. Especially for the mathematical modelling of solidification phenomena in casting, which is gaining much popularity in recent years, it is very critical to have accurate data concerning the amount of heat transfer at the interface in order to build an accurate and reliable solidification model.

The effect of accurately assessing interfacial heat transfer on the accuracy of the thermal analysis of casting has been demonstrated by several previous studies. Zeng and Pehlke have not been able to obtain accurate cooling curves for copper alloy [1] and grey cast iron [2] castings until they made accurate measurements on the gap formed in a sand casting of cylindrical shape. Issac et al. tried to predict the solidification time for casting with a metallic mould. They made an assumption concerning the interfacial gap. The prediction was 24% off from the measured data. They then designed an apparatus to measure the interfacial gap in a metallic mould and used that data for prediction. The accuracy was within 5% of the measured solidification time [3, 4].

Hou and Pehlke tried to calculate the solidification pattern for a casting of a particular shape. They initially used an assumed value to account for the interfacial heat transfer and failed to obtain an accurate prediction either for sand casting [5] or for casting with a metallic mould [6]. Then they proceeded to measure the interfacial gap in cylindrical casting [7]. When they applied the measured data to the predictions, they managed to obtain predictions within 1% of the measurements. All these studies

demonstrate how important an accurate assessment of interfacial heat transfer is on the accuracy and reliability of solidification analysis.

Reviewing literature, it can be found that there are basically two methods to measure the interfacial heat transfer coefficient. One is to measure the size of the gap formed between the casting metal and the mould and convert this gap size to an appropriate heat transfer coefficient. The other is to conduct temperature measurements in the casting and mould and convert the mould at several designated locations, and use the inverse method to derive the interfacial heat transfer coefficient.

Using the first method, as early as in 1920, researchers noticed that both the casting metal and mould moved during casting. It was not until 1973, however, that Engler proposed a reliable method to simultaneously measure the amount of movement of the casting metal and mould. In the eighties, Winter and Pehlke systematically measured the variation of the air gap and volume shrinkage for various alloys in a cylindrically shaped casting by using Engler's method. The casting alloys they measured included copper alloys, various cast irons, and aluminium alloys. In the same period, Issac et al. made use of self-designed equipment to measure the size of the gap in a casting with metallic mould. Results showed that the formation of the gap was related not only to the mould material, but also to the shape of the casting and the location of the measurement.

The second method is to derive the interfacial heat transfer coefficient h by using the inverse method. Ho and Pehlke [9–11] studied the mechanisms of heat transfer phenomena at the interface and adapted the inversed method to calculate s. The same method was employed by Hao [12] to study the solidification of cast iron.

Nishida et al. [13] measured the sizes of gaps formed in cylindrical and flat castings. They also used two calculation methods to calculate the variation of h: finite difference method (FDM) simulation and heat flow approximation calculations. Their results showed that the movements of the mould wall and casting alloy depended largely on the shape and location of the casting. They also evaluated the relationship between the size of the gap and h.

More recently, Lukens, Hou, and Pehlke [14] measured the size of the air gap for a cylindrical casting placed horizontally, and showed that the size of the gap was affected by gravity, hydrostatic pressure exerted by the rise, and by the mould material. They found that the casting sections near the bottom formed larger gaps. The movement of the mould wall was smaller if the mould was rigid, and, therefore, a smaller gap was formed.

Chiesa [15] measured the temperature variation of molten metal during the solidification of casting. Comparing with a theoretical model, he obtained h under various coating conditions. His results also demonstrated that interfacial heat transfer resistance existed even in the filling period when the metal was still in the liquid state. Kumar [16] found that the heat flux was actually an exponential function of time. Kulkarni and Radhakrishna [17] studied the thermal behaviour of hollow cylindrical castings for aluminium base alloys using the FEM technique.

The purpose of this study is to employ the two methods, namely gap size measurement and temperature measurement with the inverse method, to estimate the heat transfer coefficient h at the metal–mould interface for a hollow cylindrical casting of Al–4.5% Cu alloy cast in a CO_2–sand mould. The results obtained from the two methods were then compared and evaluated. To make the data useful for the mathematical modelling of solidification phenomena in casting, a procedure is also developed to obtain the relation between h and the casting temperature near the interface.

2. Experimental

2.1. Measurements of gap size

It is generally believed that heat transfer resistance at the interface originates from imperfect contact or even separation of the casting and mould. This means a gap is formed between the casting and the mould during casting. The main reason for the formation of a gap is the difference between the thermal expansion coefficients of the casting and mould. When the gap is formed, it is filled by a mixture of air and mould gases. Heat transfer in this stage proceeds mainly by the conduction of the air–gas mixture, since convection and radiation effects can be neglected. Therefore, if the size of the gap formed and the thermal conductivity of the air–gas mixture can be established, the interfacial heat transfer coefficient can then be estimated simply from $h = k/x$, where k is the thermal conductivity of the air–gas mixture and x is the size of the gap.

The main step in this method is measuring the size of the gap formed. In this study, two very sensitive displacement gauges are used to measure the movements of the casting and mould. When the casting is filled, the mould is heated and starts to expand. As heat is extracted from the casting to the mould, the casting solidifies and shrinks, while the mould keeps being heated and expands. The difference of the two movements is defined as the size of the gap formed. Since the displacement gauges can reflect the two movements, the size of the gap can be measured.

2.2. Inverse method

For the analysis of a heat transfer problem, an appropriate set of equations is first determined to describe the heat transfer behaviour. With the boundary conditions, initial conditions, and thermo-physical properties of the materials being known, it is possible to obtain the temperature and variation of the whole system. However, if one of the thermo-physical properties of the materials is not known, but temperature information can be obtained, then it is possible to calculate this unknown property by a reverse scheme, which is the basic idea of the inverse method.

To make use of the inverse method for determining h, temperature measurements need to be made. In order to make the analysis of the inversed method easier, a one-dimensional heat transfer system is devised. It serves as the boundary conditions and as the calibration point. Naturally, more temperature measurements make the analysis more accurate. A brief description of the inverse method for analysing the temperature data of h follows.

The metal–mould heat transfer coefficient is determined basically by solving Fourier's heat conduction equation. The one-dimensional heat conduction equation is:

$$\frac{\partial}{\partial x}\left(k\frac{\partial T}{\partial t}\right)=\rho c\frac{\partial T}{\partial t}$$

where k, ρ, and c are the thermal conductivity, density, and specific heat, respectively. The initial and boundary conditions are as follows:

- Initial condition

$$T(x,0)=T_i(x) \text{ at } t=0$$

- Boundary conditions

$$T(0,t)=T_{B1}(t) \text{ at } x=0$$

$$T(1,t)=T_{B2}(t) \text{ at } x=L$$

Where $T_i(x)$, $T_{B1}(t)$, and $T_{B2}(t)$ are obtained by actual measurements. The configuration of the one-dimensional system is shown in Fig. 1.

Fig. 1. Configuration of the one-dimensional system

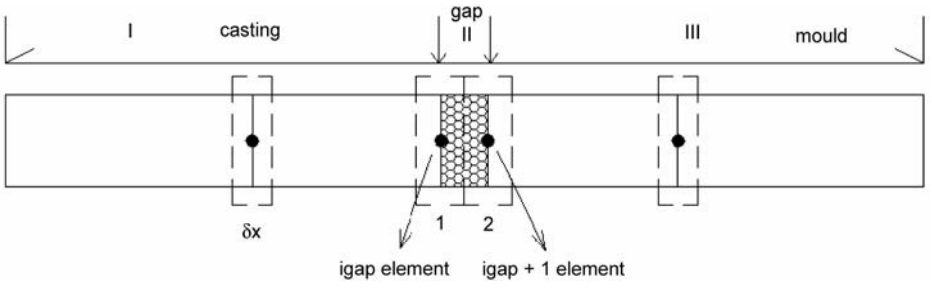

Fig. 2. Regions I, II, and III considered in the model

Notice that the equations are applied to solve the temperature distribution of regions I and III, where gaps do not exist. Region II, where the air gap exits, is treated as two elements. One includes the gap and casting, the other includes the gap and mould, as shown in Fig. 2.

In this study, the principle of enthalpy conservation is used to calculate the temperature history of the system. By the finite difference method, the system can be treated as two parts, regions I and III, and region II.

For regions I and III

$$\rho c \delta x \frac{T_i - TN_i}{\delta t} = k \frac{TN_{i-1} - TN_i}{\delta x} - k \frac{TN_i - TN_{i+1}}{\delta x} \tag{1}$$

from which it follows that

$$T_i = TN_i + \frac{k \delta t}{\rho c \delta x^2} (TN_{i-1} - 2TN_i + TN_{i+1}) \tag{2}$$

For an element in region II (denoted by the index i_{gap}),

$$\rho c \frac{\delta x}{2} \frac{T_{i\text{gap}} - TN_{i\text{gap}+1}}{\delta t} = k \frac{TN_{i\text{gap}-1} - TN_{i\text{gap}}}{\delta x} - h(TN_{i\text{gap}} - TNS) \tag{3}$$

which gives

$$T_{i\text{gap}} = TN_{i\text{gap}+1} + \frac{2k \delta t}{\rho c \delta x^2} (TN_{i\text{gap}-1} - TN_{i\text{gap}}) + \frac{2h \delta t}{\rho c \delta x} (TN_{i\text{gap}+1} - TN_{i\text{gap}}) \tag{4}$$

For the element with the index $i_{\text{gap}+1}$ of region II,

$$\rho c \frac{\delta x}{2} \frac{T_{i\text{gap}+1} - TN_{i\text{gap}+1}}{\delta t} = h(TN_{i\text{gap}} - TN_{i\text{gap}+1}) - k \frac{TN_{i\text{gap}+1} - TN_{i\text{gap}+2}}{\delta x} \tag{5}$$

and

$$T_{i\text{gap}+1} = TN_{i\text{gap}+1} + \frac{2k \delta t}{\rho c \delta x_2} (TN_{i\text{gap}+2} - TN_{i\text{gap}+1}) + \frac{2h \delta t}{\rho c \delta x} (TN_{i\text{gap}} - TN_{i\text{gap}+1}) \tag{6}$$

where: T_i – temperature at the i-th node, TN_i – temperature of the previous time step at the i-th node, δt – time increment, δx – dimension of an element, i_{gap}, $i_{\text{gap}+1}$ – nodes at which the air gap exits, h – heat transfer coefficient of the air gap.

To calculate the temperature history of the casting and mould, some thermal physical properties were needed. The data necessary to calculate the heat transfer coefficient n is given in Table 1.

To calculate the heat transfer coefficient h the temperature distribution was estimated by first minimizing the function

$$F(h) = \sum_{m=1}^{M} \sum_{i=1}^{I} (T_{\eta+1,m} - Y_{\eta+i,m})^2 \tag{7}$$

Table 1. Thermal physical properties of the casting and mould

Properties	Al–4.5% Cu alloy [18]	CO_2–sand mould [17]
Thermal conductivity k, W/(m·s·K)	192	152
Density, kg/m^3	2380	1580
Heat capacity, W/(g·K)	1086	1045
Latent heat, kJ/kg	395.041	

The value of h was obtained when the sum of the squares of the experimental temperature deviations from the estimated temperatures was minimized. The terms $T_{\eta+1,m}$ and $Y_{\eta+1,m}$ are the measured and calculated temperatures. The meanings of the subscripts η, m, and i are the starting time, time, and location, respectively. The value of m was set to 1 in this study, which means there was only one verifying point. The heat transfer coefficient was calculated as a function of integer times recorded time interval, and the superscript I was used to determine the time range for the value of h at a given time.

The minimal value of $F(h)$ could be calculated by setting the partial derivative to zero:

$$\frac{\partial F(h)}{\partial h} = 0 \tag{8}$$

when calculating h_{j+1} it was assumed that $h_{j+2} = h_{j+3} = \ldots = h_{j+r} = h_{j+1}$ (r was the index value after which h was the "undetermined h" of the future domain). Equation 8 was approximated by an explicit FDM as follows

$$\sum_{i=1}^{I} (T_{\eta+1},_m - Y_{\eta+i},_m) \frac{\partial T_{\eta+i}}{\partial h_{j+1}} = 0 \tag{9}$$

Using the Taylor series expansion

$$T_{\eta+1}^{1} = T_{\eta+1}^{1-1} + \left(\frac{\partial T_{\eta+1}}{\partial T_{j+1}} \right)^{\mathrm{I}-1} \left(h_{j+1}^{1} - h_{j+1}^{\mathrm{I}-1} \right) \tag{10}$$

$$\delta h_{j+1}^{1} = h_{j+1}^{1} - h_{j+1}^{\mathrm{I}-1} \tag{11}$$

The superscript 1 denotes the first iteration step, the initial value of h when $I = 0$ and, generally speaking, h_1^0 was set to 1 and h_{j+1}^0 was set to converse value of h_j.

The sensitivity coefficient ϕ was defined as:

$$\phi_{n+1}^{n-1} = \left(\frac{\partial T_{\eta+1}}{\partial T_{j+1}} \right)^{I-1} = \frac{T_{\eta+1}[(1+\in).h_{j+1}^{I-1}] - T_{\eta+i}(h_{j+1}^{I-1})}{\in .h_{j+1}^{I-1}}$$

where $\in$ is a very small value, always set as 0.001. In the *I*-th iteration:

$$T_{\eta+1}^{1} = T_{\eta+1}^{I-1} + \phi_{\eta+i}^{I-1} \delta h_{j+1}^{1} \tag{12}$$

Replacing $T_{\eta+1}^{1}$ in Eq. (9) by Eq. (11) we have

$$\sum_{i=1}^{I} \left(T_{\eta+1}^{I-1} + \phi_{\eta+i}^{I-1} \delta h_{j+1}^{1} - i \right) \phi_{\eta+i}^{I-1} = 0 \tag{13}$$

and the procedure was not repeated for a new coefficient value until

$$\frac{\delta h_{j+1}^{1}}{h_{j+1}^{1}} \leq 0.001$$

The calculation of the heat transfer coefficient as a function of time was continued until the end of the desired period.

2.3. Experimental procedures

CO_2–sand moulds were used in the present work. Sodium silicate (Na_2CO_3) of 4% by weight was mixed with silica sand and used for making the moulds. The moulds were hardened using CO_2 gas. The dimensions of the moulds were selected to establish a good interference. Figure 3 shows a schematic sketch of the CO_2 sand mould used in the present investigation. The particle size of the silica sand was 50 mesh. Moulds were prepared with a regular hand moulding technique for the different configurations (Table 2). CO_2 gas was then passed through the mould at a pressure of 2 kg/cm^2. In this study, the gap size and temperature measurements are conducted in the same casting. The casting was hollow and cylindrical in shape. To make sure that the heat transfer in the casting is one-dimensional, heat-insulating material was placed on the two sides and bottom of the casting mould. Two thermocouples were then inserted in the mould cavity, one at the centre and the other near the mould surface. Another three thermocouples were inserted in the mould, one near the inner surface, one near the centre, and the other near the outer surface.

In the other half of the casting, two ceramic tubes for displacement measurement were inserted. One was in the cavity near the inner mould surface and the other was in the mould near the inner mould surface. The two ceramic tubes and four thermocouples were carefully placed at the same level. The dimensions of the casting, the placement of the ceramic tubes for displacement measurement, and thermocouples are illustrated in Figs. 4–6. Special care must be taken to make sure that the ceramic tubes move along with the casting and mould, so that the readings from the optical displacement gauge scan actually reflect the expansion–shrinkage of the casting and mould. The apparatus set up for gap size measurement is shown in Fig. 7.

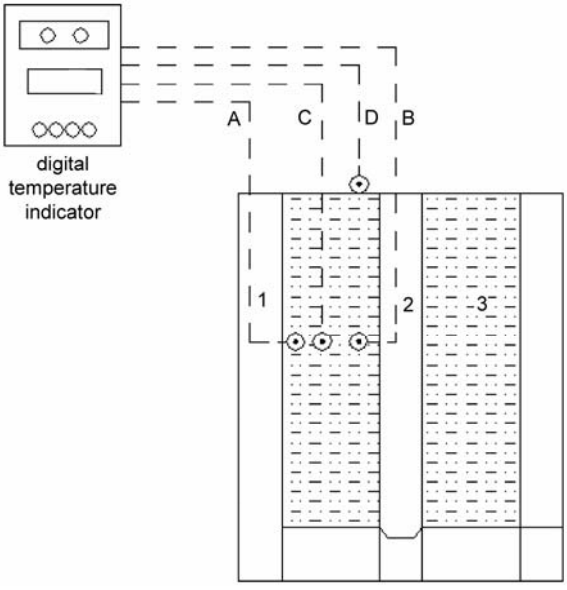

Fig. 3. Experimental setup and thermocouple locations: A – thermocouple placed at the molten metal–mould interface, B – thermocouple placed at the molten metal–core interface, C – thermocouple placed at the centre of the molten metal, D – thermocouple placed at the surface of the molten metal; 1 – CO_2–sand mould, 2 – CO_2–sand core, 3 – molten metal

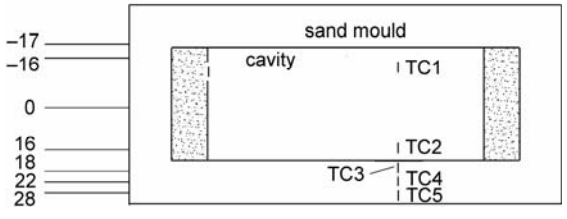

Fig. 4. Locations of the thermocouples and ceramic tubes for displacement measurements

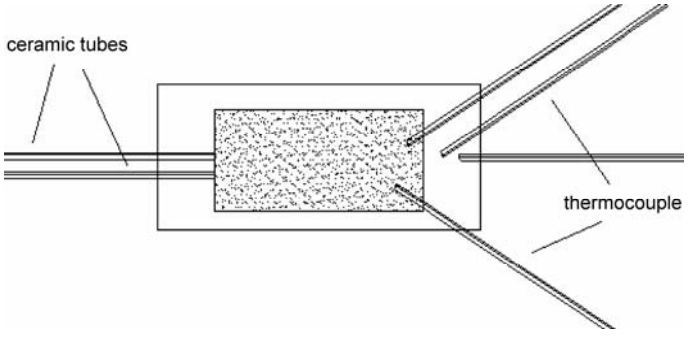

Fig. 5. Top view showing how the thermocouples and ceramic tubes were placed for displacement measurements

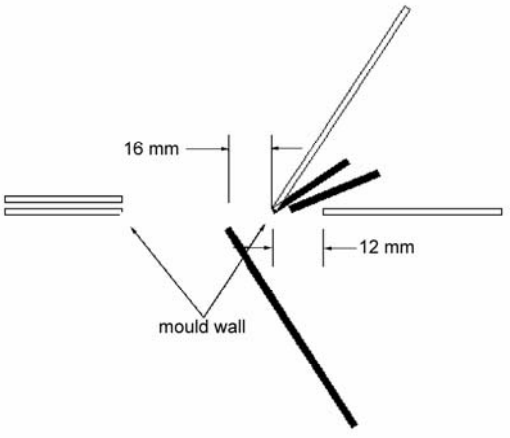

Fig. 6. Isoparametric view showing how the thermocouples and ceramic tubes were placed for displacement measurements

Table 2. Dimensions of hollow, cylindrical castings[1]

Sl.No	OD D, mm	ID d, mm	Thickness t, mm	Height of casting h, mm
1	75	25	25	250
2	125	25 50>	50 37.5	250
3	175	25 50 75	75 62.5 50	250

[1]OD – outside diameter of casting, ID – core or inner diameter of casting, t – thickness of casting.

Alloy Al–4.5% Cu (commercial) was used. Details of its chemical composition are given in Table 3.

Table 3. Details of the chemical composition of the alloy

Composition (%)										
Si	Fe	Cu	Mn	Mg	Zn	Ni	Pb	Sn	Ti	Al
0.343	0.602	4.36	0.683	0.480	0.038	0.006	0.007	0.005	0.013	Remainder

As molten Al–4.5% Cu alloy was poured into the mould cavity with a constant flow rate of approximately 5m/s, heat-insulating material was quickly placed on top. The pouring temperature was about 750 °C. The thermal histories of the five thermocouples were then recorded for the whole period of filling, solidification, and subsequent cooling with a high-speed data acquisition system. The displacements of

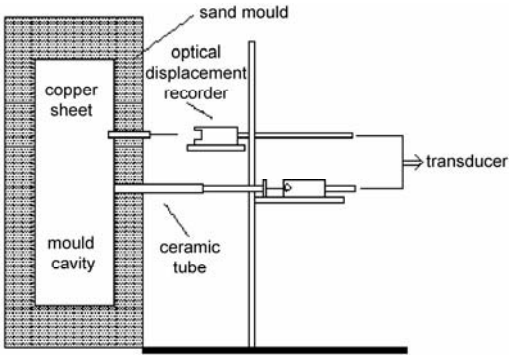

Fig. 7. Apparatus setup for gap size measurements

the casting and mould were also detected by the displacement gauges and recorded through a transducer during the same period.

3. Results and discussion

3.1. Heat transfer coefficients obtained from gap size measurement

The amount of movement of the casting and mould measured during the whole casting period is shown in Fig. 8. The difference between the two movements is believed to be the gap formed at the interface. As can be seen from the figure, when molten metal is first poured into the cavity, both metal and mould expand outward. This is due to the outward movement of the mould when it is heated up by the metal.

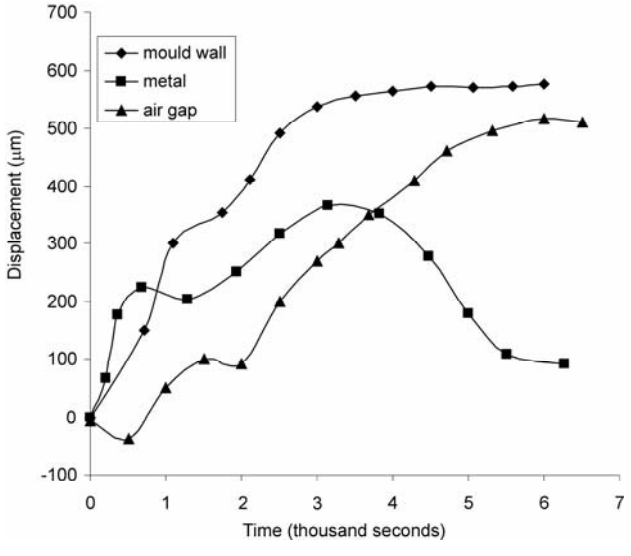

Fig. 8. The displacements of the casting and mould, as well as the corresponding gap size during the whole casting period for a CO_2–sand mould 25 mm thick (75 mm OD, 25 mm ID)

At this time, molten metal is still flexible and moves outward along with the mould. At approximately 340 s, the movement of metal starts to slow down while the mould still moves at the same pace. This is the instant when gap starts to form. At approximately 1240 s, the outward movement of the metal stops and starts to move inward while the mould keeps moving outward. This is believed to be caused by the shrinking of the solidifying metal. At this point, the size of the gap abruptly increases. The rate of increase of the gap slows down when the mould stops expanding, at approximately 1675 s. The metal, however, keeps shrinking until the end of the recording.

To convert the gap size to the interfacial heat transfer coefficient, data for the thermal conductivity of the air–mould gas mixture is needed. Ho made the assumption [10] that the thermal conductivity of the air–mould gas mixture in the gap is equal to that of stagnant air in the atmosphere. Under this assumption, the thermal conductivity of the gap can be expressed as follows:

$$k = 10533\times10^{-5} + 10563\times10^{-7}T \quad [\mathrm{W/(m\cdot s\cdot K)}]$$

where T is the gas temperature in the gap in kelvins, Nishida, however, used another expression to estimate the thermal conductivity of the gas mixture in the gap [13]:

$$k = 1.38733\times10^{-4}T \quad [\mathrm{W/(m\cdot s\cdot K)}]$$

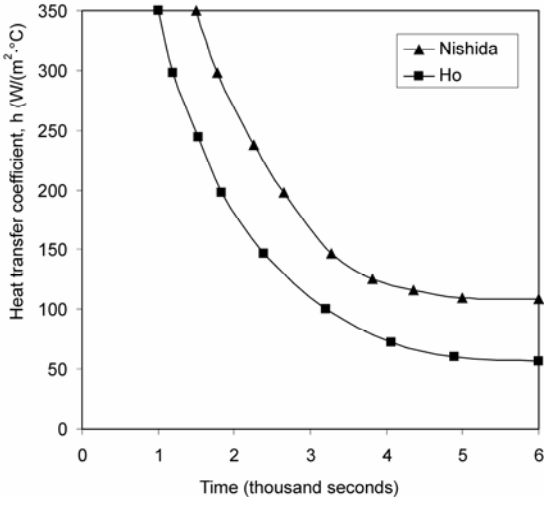

Fig. 9. The interfacial heat transfer coefficient obtained from thermal conductivity data by Ho and Nishida

In this study, both Ho's and Nishida's data were used to estimate the interfacial heat transfer coefficient, and the result is shown in Fig. 9. It can be seen from the figure that the value of h obtained from Nishida's thermal conductivity is always higher than that of Ho's data.

3.2. Heat transfer coefficient obtained from temperature measurement and the inverse method

The temperatures five thermocouples during the whole period are shown in Figs. 10, 11. From these figures it can be seen that the temperature histories of two thermocouples in the casting (#1 metal and #2 metal surface) are almost identical. Therefore, when analysing the temperature data with the inverse method, the temperature readings of T.C. #1 and #3 (metal–mould interface) were used as the boundary conditions. The temperature readings of T.C. #1 to #3 were used to set up the initial conditions, while that of T.C. #3 was used as the verifying condition.

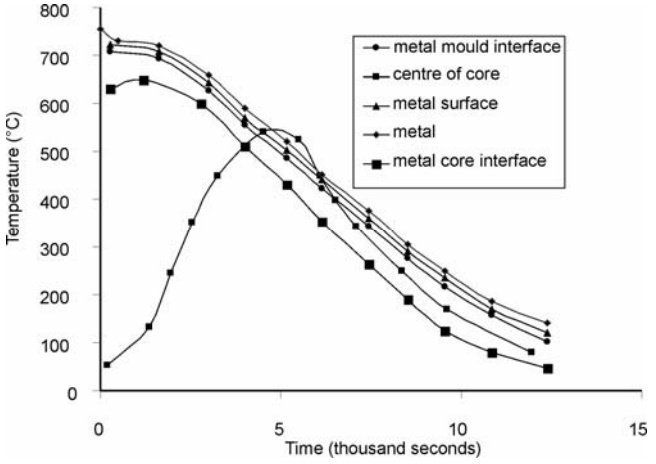

Fig. 10. The thermal histories of the five thermocouples in the 25 mm thick CO_2–sand mould (75 mm OD, 25 mm ID)

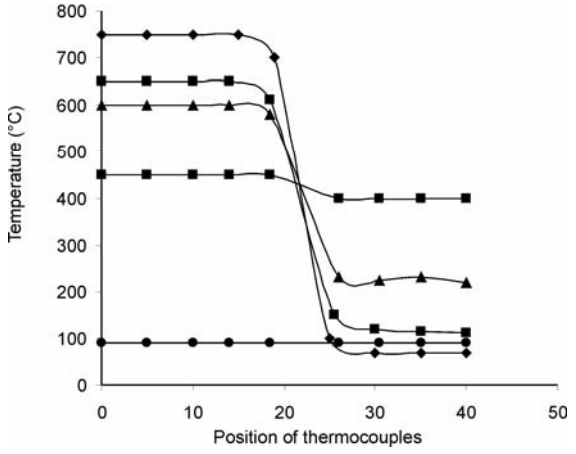

Fig. 11. Temperature distributions in the casting and mould for certain instants of casting operations, obtained from temperature measurements for a 25 mm thick CO_2–sand mould (75 mm OD, 25 mm ID)

The obtained interfacial heat transfer coefficient is shown in Fig. 12. The figure shows that h starts from a finite value and gradually increases to about 710 W/(m^2·°C), and then more sharply decreases to approximately 590 W/(m^2·°C). As h reaches its peak value, the heat flux reaches a maximum across the interface. Then the metal temperature drops more rapidly and the metal shrinks more and forms a larger gap, resulting in a smaller h. After that, h increases to about 670 W/(m^2·°C) and keeps dropping until the end of casting.

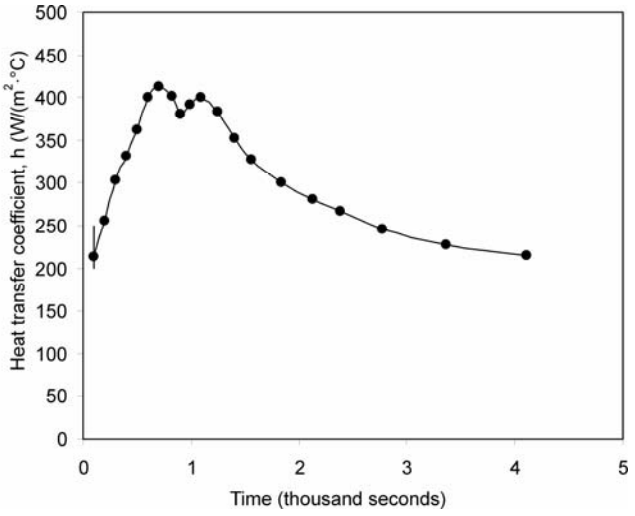

Fig. 12. The interfacial heat transfer coefficient obtained from temperature measurements for a 25 mm thick CO_2–sand mould (75 mm OD, 25 mm ID)

It is noted, however, that the data for h are useful only when its relation to the metal temperature near the interface is known. During the analysis of the temperature data by the inverse method, the temperatures of the casting metal and the mould very near the interface were obtained. The data is shown in Fig. 13. Combining the data in Figs. 11, 12, the interfacial heat transfer coefficient, as a function of metal temperature very near the interface, can be obtained, as shown in Fig. 14.

With the metal temperature very near the interface known, it is also possible to convert the gap size and h as functions of time obtained from the gap size measurement to functions of metal temperature. The results are shown in Figs. 15, 16. From Fig. 14, it can be seen that no gap is formed between the casting metal and the mould until the solidification temperature is approximately 590 °C. At that temperature a gap starts to form. The gap does not grow, however, and maintains a size of about 70 μm until the end of solidification, at approximately 550 °C and then starts to grow quickly. No gap is formed before the formation of the solidification phase, because the liquid–solid mixture in this stage still maintains good contact with the mould wall.

The moment solidification starts, however, the strength of the solid shell increases. The shell is strong enough to resist the hydrostatic pressure of the molten metal, which tends to push the metal shell outward. It is not until the end of solidification

that the metal is completely separated from the mould. Correspondingly, in Fig. 14, the interfacial heat transfer coefficient is rather high before the solidification temperature and drops significantly at the solidification temperature.

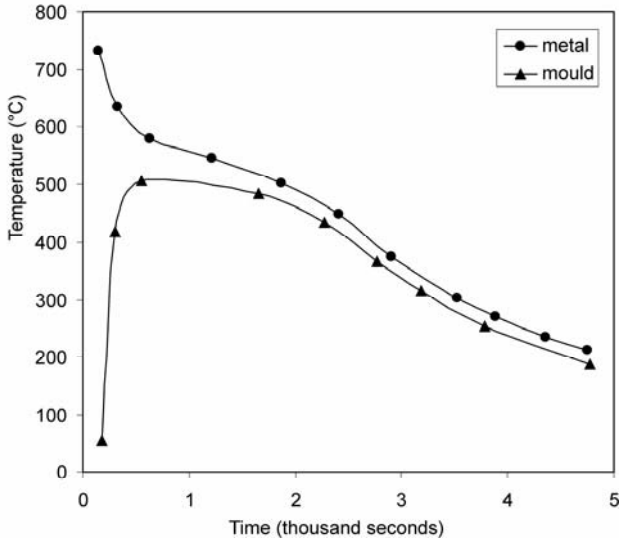

Fig. 13. Temperature of the casting metal and mould very near the interface during the entire casting period, obtained from the inverse method for a 25 mm thick CO_2–sand mould (75 mm OD, 25 mm ID)

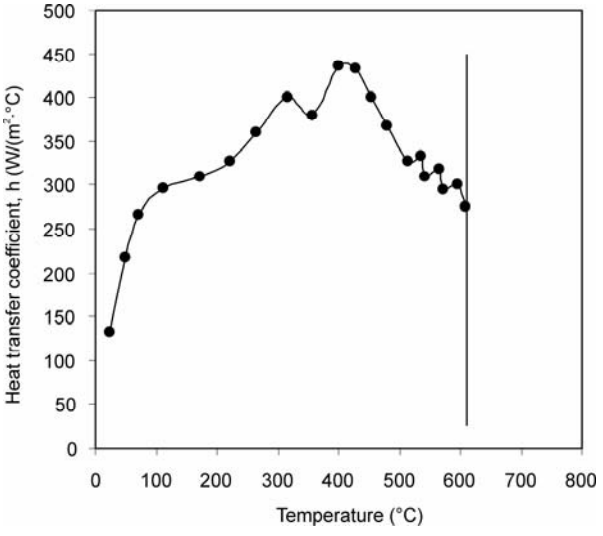

Fig. 14. The interfacial heat transfer coefficient as a function of metal temperature very near the interface, obtained from temperature measurements and the inverse method for a 25 mm thick CO_2–sand mould (75 mm OD, 25 mm ID)

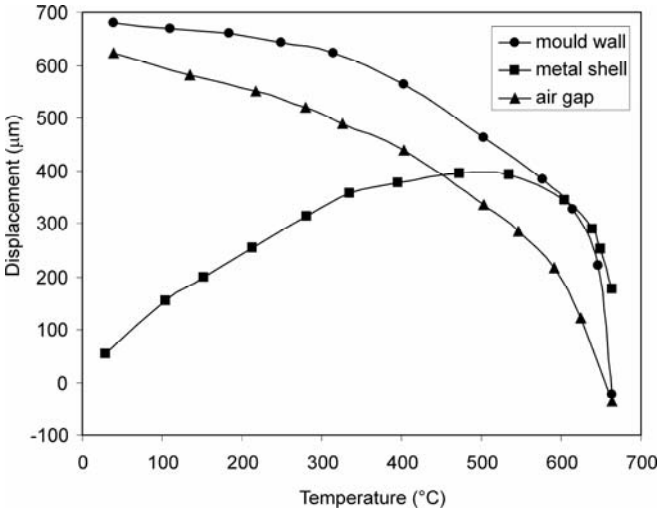

Fig. 15. The displacements of the casting and mould, as well as the corresponding gap size, as functions of the metal temperature very near the interface, for a 25 mm thick CO_2–sand mould (75mm OD, 25 mm ID)

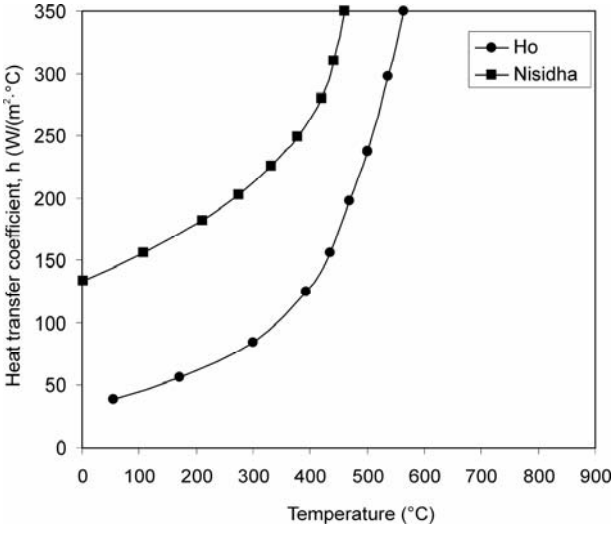

Fig. 16. The interfacial heat transfer coefficient as functions of metal temperature very near the interface, obtained from Nishida's and Ho's thermal conductivity values, for a 25 mm thick CO_2–sand mould (75mm OD, 25 mm ID)

The value of *h*, however seems to increase again to a higher value, still smaller than the peak value. The source of this phenomena is unknown. It may be due to reversal heat transfer from the core. It is speculated that, when cooling first starts, the core forms a solid network and resists the hydrostatic pressure of the inner molten

metal from pushing it outward. The network is still porous enough, however, for the melt to penetrate through it until the end of solidification, when a complete solid shell is formed.

Then the value of h drops again and keeps dropping as the gap grows. At a higher temperature above the solidification temperature, the value of h obtained from temperature measurements and the inverse method maintains a certain value – even somewhat lower that the peak value, while the gap size method shows a very high value. The former is believed to be more reliable than the latter since very high values result from a very small gap size. At this stage, it is not reasonable to assume that the relation of $h = k/x$ still holds.

An increase of h during the beginning stage can result from the imperfect contact of the molten metal and the mould when the metal is first poured into the casting. Due to the roughness of the mould, it takes a certain time for the molten metal to wet the mould and establish a close contact.

4. Conclusions

Two methods were employed to measure the heat transfer coefficient at the metal –mould interface during the casting of Al–4.5% Cu alloy in a CO_2–sand mould. One was to measure the size of the gap formed between the casting metal and the mould and using the relation $h = k/x$, where k is the thermal conductivity of the air–mould gas mixture in the gap and x is the size of the gap. The other method was to take temperature measurements at certain locations of the casting and mould and, by using the inverse method, to obtain the value of h. The results of measurements and observations can be summarized as follows:

- The determination of h through the measurement of gap size greatly depends on the assumed thermal conductivity of the gas mixture in the gap.
- The relation $h = k/x$ is not appropriate for the beginning stage of the casting, when molten metal is poured into the mould cavity.
- The value of h derived from temperature measurements and the inverse method is about ten times higher than that obtained from gap size measurements and Ho's and Nishida's values of k.
- With temperature measurements and the inverse method, h starts at about 210 W/(m^2·°C), increases to 710 W/(m^2·°C) at the solidification temperature, abruptly drops to about 590 W/(m^2·°C), and then increases again to about 670 W/(m^2·°C) at the end of solidification. After that, h keeps dropping until the end of casting.

References

[1] ZENG X.C., PEHLKE R.D., AFS Trans. (1984), 479.
[2] ZENG X.C., PEHLKE R.D., AFS Trans. (1985), 275.

[3] ISSAC J., REDDY G.P., SHARMA G.K., AFS Trans. (1985), 29.
[4] ISSAC J., REDDY G.P., SHARMA G.K., AFS Trans. (1985), 123.
[5] HOU T.X., PEHLKE R.D., AFS Trans. (1986), 477.
[6] HOU T.X., PEHLKE R.D., AFS Trans. (1988), 151.
[7] HOU T.X, PEHLKE R.D., AFS Trans. (1988), 129.
[8] ENGLER S., BOENISCH D. , KOHLER B., AFS Cast Metals Research J. (1973), 20.
[9] HO K., PEHLKE R.D., AFS Trans. (1983), 689.
[10] HO K., PEHLKE R.D., AFS Trans. (1987), 587.
[11] HO K., PEHLKE R.D., Metall. Trans., 16B (1985), 585.
[12] HAO S.W., ZHANG Z.Q., CHEN J.Y., LIU P.C., AFS Trans. (1987), 601.
[13] NISHIDA Y., DROSTE W., ENGLER S., Metall. Trans. B., 17B (1986), 833.
[14] LUKENS M.C., HOU T.X, PEHLKE R.D., AFS Trans. (1990), 63.
[15] CHIESA F., AFS Trans. (1990), 193.
[16] KUMAR T.S.P., PRABHU K.N., Metall. Trans., 22B (1991), 717.
[17] KULKARNI S.N., RADHAKRISHNA K., Int. J. Cast Metals Research, 17 (2004), 57.
[18] *ASM Metals Handbook*, 9th Edn. Vol. 15 (1998), ASM Int, Materials Park, OH.

Received 11 February 2005
Revised 5 March 2005

Materials Science-Poland, Vol. 23, No. 3, 2005

Microstructure and mechanical properties of nickel deformed by hydrostatic extrusion

M. KULCZYK[1, 3*], W. PACHLA[1], A. MAZUR[1], R. DIDUSZKO[2], H. GARBACZ[3], M. LEWANDOWSKA[3], W. ŁOJKOWSKI[1], K. J. KURZYDŁOWSKI[3]

[1]Institute of High Pressure Physics, Polish Academy of Sciences, ul. Sokołowska 29/37, 01-142 Warsaw, Poland

[2]Institute of Electronic Materials Technology, ul. Wołczyńska 133, 01-919 Warsaw, Poland

[3]Warsaw University of Technology, Faculty of Materials Science and Engineering, ul. Wołoska 141, 02-507 Warsaw, Poland

The goal of the present work is to demonstrate that a bulk, ultra-fine grained microstructure can be obtained by the hydrostatic extrusion process of a 99.5% technical purity of nickel. Deformation with the total true strain of 3.8 was performed at room temperature to a wire 3 mm in diameter. Microstructure was characterized by light microscopy, TEM, XRD and mechanical properties. Hydrostatic extrusion was shown to be an effective method of severe plastic deformation, which allows ultra-fine grained structures to be obtained within the deformed material. After cumulative hydrostatic extrusion, the yield stress tripled, reaching a maximum of 812 MPa with a moderate elongation of 13%. A mean subgrain size of 200 nm was observed, with a considerable diversity in the size of individual grains. For the final passes of hydrostatic extrusion, a slight decrease in the mechanical properties was observed, accompanied with an increase in crystallite size. This is explained in terms of thermal softening processes activated by the heat generated during hydrostatic extrusion.

Key words: *severe plastic deformation; hydrostatic extrusion; ultra-fine grains; nanocrystalline structure; grain refinement*

1. Introduction

Severe plastic deformation (SPD) is commonly applied to generate nanostructures in metals. By SPD methods the mean grain size is usually reduced to 100–500 nm (ultra-fine grained structures, UFG), and even below 100 nm (nanocrystalline structures, NC). This results in substantial strength increase, accompanied by a reduction

*Corresponding author, e-mail: mariusz@unipress.waw.pl

in toughness. In some cases, however, the SPD technique has allowed very promising combinations of high strength and ductility to be achieved [1, 2].

Up to now, the main SPD techniques having been studied for bulk metals are: high pressure torsion (HPT) [3, 4–6], equal-channel angular pressing (ECAP) [3, 7, 8], multiple rolling [9, 10], and cyclic extrusion-compression (CEC) [11]. The majority of the metals investigated by these methods were ductile metals, such as copper and aluminium and its alloys [2]. Somewhat harder materials, such as Fe [12], Ni [20], or Al–Ti [13] and Al–Fe–Ni [14] alloys, were usually processed by the powder consolidation of nanopowders. Powder methods, however, often result in low ductility of the final products [1]. Recently, the hydrostatic extrusion (HE) method has been used for obtaining NC structures in metals [15, 16]. The HE process has been used to generate NC structures in aluminium, aluminium alloys, and titanium [15, 16].

NC nickel has been processed into thin films by electro-deposition techniques [17, 18]. The development of an effective fabrication method that allows bulk, large volumes of NC nickel to be obtained may be an alternative for the consolidation of nanopowders [2, 3]. Only few literature data on ultra-fine grained UFG nickel, processed by HPT (grains ~100 nm) [19] and ECAP combined with rolling (grains ~ 300 nm) [3], have been reported up to now. On the other hand, nickel characterized by high strength and good ductility can find immediate application in micro-electromechanical systems (MEMS) [20–25].

In the present paper, the effect of cumulative HE on the microstructure and mechanical properties of nickel of 99.5% technical purity are presented and discussed.

2. Experimental

Nickel of technical purity 99.5% in the shape of a forged rod was used for machining the billet for hydrostatic extrusion in the form of a cylinder with OD = 20 mm and length 50 mm. Cumulative (multi-pass) HE was run in seven consecutive passes, with a total true strain 3.8, the strain rates varying between 2.3 s^{-1} and 1.18×10^{2} s^{-1}, and the extrusion pressure ranging between 500 MPa and 1400 MPa. The final diameter of the extruded wire was 3 mm. The macrostructure of the initial material and after the first three passes of HE was evaluated by light microscopy (METAVAL Zeiss). Specimen for light microscopy were polished and chemically etched with the solution containing HNO_3 (85 cm^3), HCOOH (18 cm^3), H_2O (17 cm^3). The microstructure of the final wire was investigated by transmission electron microscope (Philips EM-300), and the texture and crystallite size were investigated by X-ray diffraction using CuK_α radiation (Siemens D500). All structural investigations were made on the transverse cross sections of the extruded wires. The ultimate tensile strength, yield stress, and elongations were evaluated at room temperature from tensile (MTS-810) and compression (QTEST/10 -MTS) tests under a 2×10^{-3} s^{-1} strain rate. Microhardness and microhardness distribution tests were also measured (Zwick-HV0.2/15).

3. Results and discussion

The initial material shows a mean grain size of ~200 μm (Fig. 1a), and the material contains annealing twins. The macrostructure after three passes of HE with the total strain $\varphi = 2.77$ is shown in Fig. 1b. Apparently, the macrostructure undergoes drastic refinement and shows substantial disturbance, confirming the large degree of deformation (almost 95% reduction).

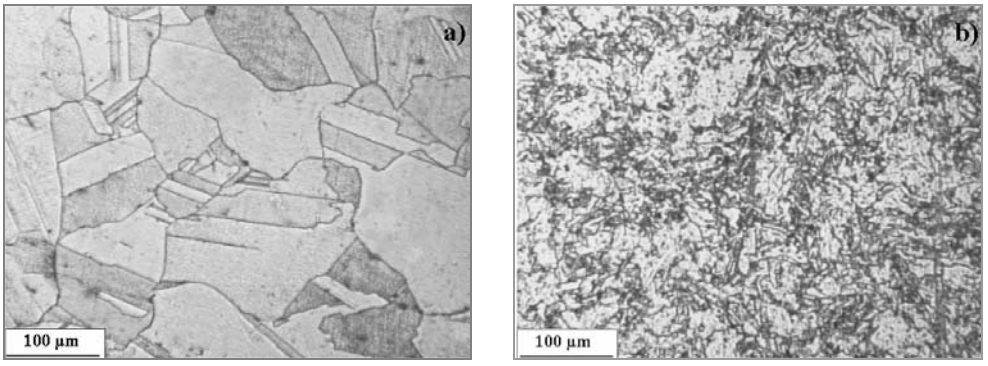

Fig. 1. Light microscopy images of nickel 99.5%:
a) the initial state (before HE), b) after three consecutive hydrostatic extrusion passes (true strain $\varphi = 2.77$)

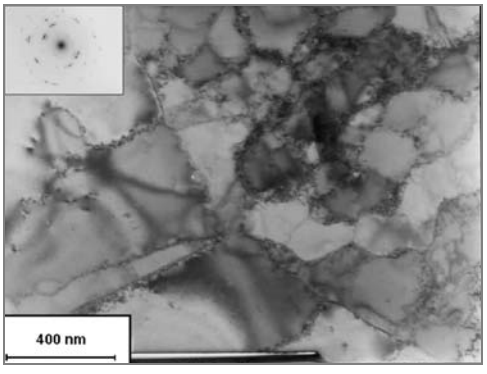

Fig. 2. TEM image of the microstructure of nickel 99.5% after seven consecutive hydrostatic extrusion passes (true strain $\varphi = 3.8$)

Figure 2 shows a TEM image of nickel after seven consecutive extrusion passes (true strain $\varphi = 3.8$). Subgrains with an approximate mean size ~200 nm are observed. The mean diameter of grains is reduced by ~1000 times, starting from 200 μm down to ultra-fine subgrain structure. X-ray diffraction patterns have thereby revealed low misorientation angles between individual subgrains. The observed microstructure is non-uniform (inhomogeneous) and subgrain sizes vary substantially. For structural applications, it is even better to generate an inhomogeneous substructure, substantially differing in grain size [1]. As has been reported, such a mixed substructure leads

to the optimum combination between strength and ductility. Therefore, the highly inhomogeneous substructure obtained in the present work (Fig. 2) can be advantageous from the point of view of future applications. Up to now, such mixed structures have been obtained in copper [26, 27], with micrometer size grain content ~25 vol. %, and in zinc [28] and aluminium alloys [29]. According to previous investigations, nanograins are crucial for obtaining high strength and micrometer sized grains stabilize the plastic deformation process in metals [1, 26, 27].

To evaluate the ultra-fine grained structure behaviour within deformed nickel, XRD scans on the transverse cross sections of the extruded wires were made. Already after the first extrusion pass (φ = 1.38), the substantial refinement of crystallite domains in all selected crystallographic orientations was observed (Fig. 3). Further extrusion passes led to much smaller crystallite decrease, with an evident increase (approximately 30% in the <111> direction) in the last extrusion pass (φ = 3.8).

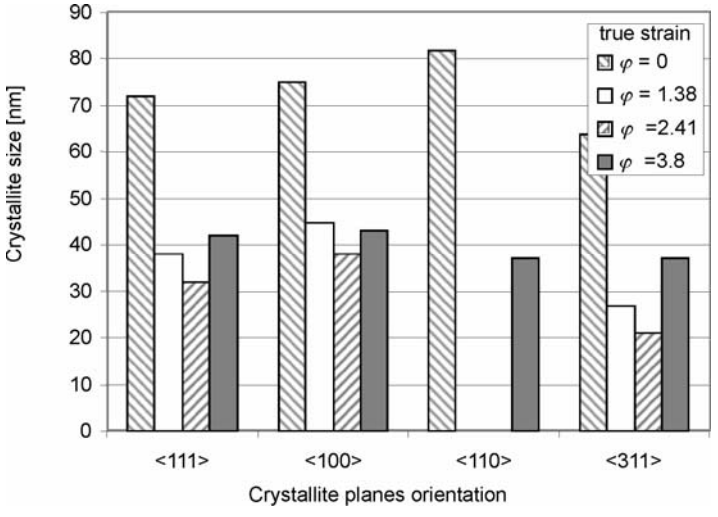

Fig. 3. Crystallite sizes in hydrostatically extruded nickel 99.5% for four crystallite planes orientations, evaluated from X-ray diffraction patterns

The texture in nickel after consecutive extrusion passes was also evaluated in a quantitative way. Table 1 shows the volume content of crystallites in a given orientation. In comparison to isotropic material, <110> crystallite orientation dominates in the initial state, which can be attributed to rod forging. After the first extrusion pass (φ = 1.38) a domination of <111> begins, which continues to increase with subsequent passes. This is a typical texture of the axis-symmetrical deformation processes of wire drawing [30]. After the fourth pass (φ = 2.98), the contribution of <111> crystallites starts to decrease and a new orientation, <311>, emerges. This is accompanied by an increase in crystallite sizes, resulting from the result of heat generated during high-speed severe extrusion [31], which plays a more meaningful role for thinner wires during the last extrusion passes. Thin wires with a high surface-to-volume ratio

are more susceptible to recovery and recrystallization activated by temperature increase due to friction and the work of deformation. Microstructure recovery leads to a decrease in strength and an increase in the ductility of the material.

Table 1. Volume content of coherent domains in nickel 99.5% after consecutive hydrostatic extrusion passes

Crystallographic direction	Isotropic Ni	Initial material	Number of extrusion passes					
			1 (φ^1 = 1.38)	2 (φ = 2.41)	3 (φ = 2.77)	4 (φ = 2.98)	5 (φ = 3.21)	7 (φ = 3.8)
<111>	0.16	0.156	0.863	0.803	0.819	0.782	0.743	0.701
<200>	0.12	0.083	0.064	0.142	0.116	0.107	0.100	0.067
<220>	0.24	0.285	0.000	0.005	0.004	0.009	0.011	0.016
<311>	0.48	0.477	0.074	0.051	0.062	0.103	0.147	0.216

[1] φ – true strain.

Microhardness measurements have confirmed the recovery processes (Fig. 4). A maximum microhardness of 2.27 GPa has been measured after the fourth pass with φ = 2.98, (an increase of 1.7 times compared to the initial material). The yield stress also reaches a maximum for a true strain of φ = 2.98. At this stage, the yield stress has tripled, reaching 812 MPa. Although the largest increase in microhardness and strength was measured after the first extrusion pass (φ = 1.38), it is attributed to the highest reduction applied for that pass. The final yield stress (after 7 extrusion passes, φ = 3.8) reached 783 MPa, i.e. 2.8 times larger than for the initial material. The respective increase in ultimate tensile strength was 2.5. This was accompanied by a drop in elongation of 40–13%.

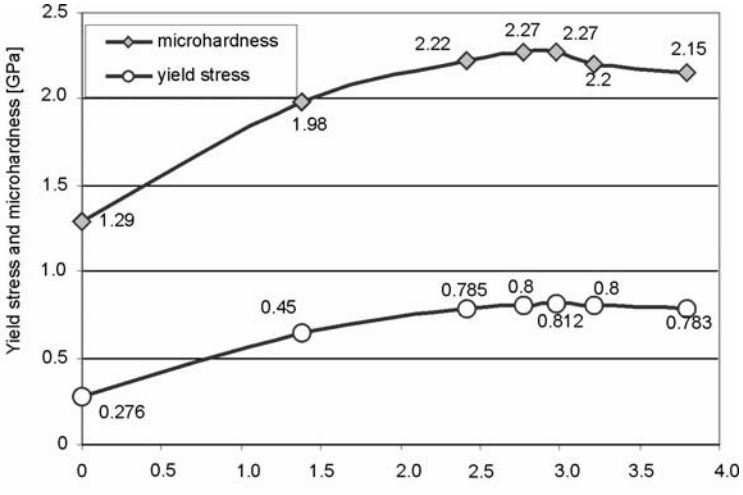

Fig. 4. Microhardness (HV0.2) and yield stress of nickel 99.5% after consecutive hydrostatic extrusion passes

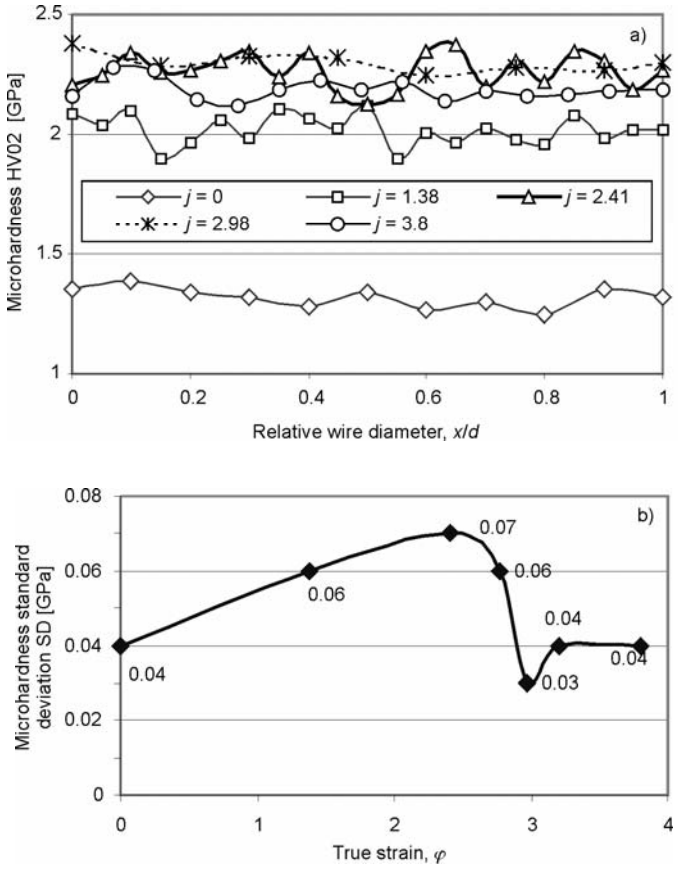

Fig. 5. Microhardness distribution at the transverse cross sections of nickel 99.5% wires (a), and the standard deviation (*SD*) of microhardness plotted against the true strain in hydrostatic extrusion (b)

The transformations of the microstructures in extruded nickel are well seen on the microhardness distribution graphs measured across the extruded wires (Fig. 5a). The initial, relatively stable distribution of microhardness shows higher oscillations in the intermediate range of extrusions, and recovers its high uniformity for the fourth pass ($\varphi = 2.98$) of the extrusion. With further deformation, disordering begins again and progressively increases up to the seventh pass ($\varphi = 3.8$). The standard deviations, *SD*, of microhardness are plotted as functions of true strain in Figure 5(b). The initial material is characterized by lower variations in microhardness, confirming its homogeneity. With an increasing number of HE passes, homogeneity decreases (*SD* increases), and at a certain true strain suddenly drops. After the fourth pass, $\varphi = 2.98$ (wire diameter 4.5 mm), *SD* is lowest, which suggests a highest homogeneity of microstructure. Further passes result in an increase of *SD*, indicating that the microstructure changes (homogeneity decreases again).

Table 2. Comparison between the mechanical properties of nickel after ECAP, rolling, and annealing [3] and nickel after cumulative hydrostatic extrusion (present work)

Material history	Ultimate tensile strength, UTS [MPa]	Yield stress 0.2% YS [MPa]	Elongation to fracture ε [%]
8 passes of ECAP[1] + cold rolling + annealing 200 °C/1h	890	835	11.7
7 passes of hydrostatic extrusion	820	783	13.0

[1]ECAP – equal channel angular pressing.

In Ref. [3], an ultra-fine grained microstructure in nickel has been generated by the combination of two methods, ECAP and rolling, followed by final heat treatment. In Table 2, the results of the complex, thermomechanical procedure of Ref. [3] are compared with the results of the present research, in which the HE process alone (without final heat treatment) has allowed similar mechanical properties to be achieved with the same level of elongation.

4. Conclusions

Nickel of 99.5% purity has been hydrostatically extruded with a cumulative strain of 3.8. Remarkable microstructure refinement by three orders of magnitude (initial grains of 200 μm to final subgrains of 200 nm) was observed. The transformation in microstructure was accompanied by a substantial increase in mechanical properties (~3 times in yield stress and over 1.7 times in microhardness). After the final passes of extrusion, a coarsening of the microstructure was observed, accompanied by a decrease in yield stress and microhardness. This can be attributed to the recovery processes activated by thermal effects generated during high speed (~1.2×10^2 s^{-1}) hydrostatic extrusion. Moderate ductility (ε~13%) in extruded wires can be attributed to the mixed (non-uniform) character of the microstructure obtained after extrusion (a wide variety in subgrain sizes and defect content). Using cumulative hydrostatic extrusion, 99.5% nickel with high strength (above 0.8 GPa), high hardness (above 3 GPa), and moderate ductility (13%) has been obtained, whch brings closer the potential application of this material in, for example, MEMS systems.

Acknowledgements

Authors thank Mr. K. Wojciechowski from Institute of High Pressure Physics, Polish Academy of Sciences, for his assistance in performing hydrostatic extrusion tests.

References

[1] VALIEV R., Nature, 3 (2004), 511.
[2] VALIEV R.Z., ISLAMGALIEV R.K., ALEXANDROV I.V., Progr. Mater. Sci., 45 (2000), 103.

[3] KRASILNIKOV N., ŁOJKOWSKI W., PAKIEŁA Z., VALIEV R., Solid State Phenomena, 94 (2003), 51.
[4] IVANISENKO YU., VALIEV R.Z., FECHT H.-J., Mater. Sci. Eng. A, 390 (2005), 159.
[5] ZHILYAEV A.P., NURISLAMOVA G.V., KIM B.-K., BARO M.D., SZPUNAR J.A., LANGDON T.G., Acta Mater., 51 (2003), 753.
[6] JIANG H., ZHU Y.T., BUTT D.P., ALEXANDROV I.V., LOWE T.C., Mater. Sci. Eng., A290 (2000), 128.
[7] STOLYAROV V.V., ZHU Y.T., LOWE T.C., VALIEV R.Z., Mater. Sci. Eng., A303 (2001), 82.
[8] STOLYAROV V.V., LAPOVOK R., BRODOVA I.G., THOMSON P.F., Mater. Sci. Eng., A357 (2003), 159.
[9] GIGUERE A., HAI N.H., DEMPSEY N., GIVORD D., J. Magn. Magn. Mater., 242–245 (2002), 581.
[10] SAGEL A., SIEBER H., FECHT H. J., PEREPEZKO J. H., Phil. Mag. Lett., 77 (1998), 109.
[11] RICHERT M., LIU Q., HANSEN N., Mater. Sci. Eng., A260 (1999), 275.
[12] TAKAKI S., KAWASAKI K., KIURA Y., J. Mater. Proces. Technol., 117 (2001), 359.
[13] GUOXIAN L., ZHIMIN L., ERDE W., J. Mater. Process. Technol., 55 (1995), 37.
[14] GUOXIAN L., MENG Q., LI Z., WANG E., Nanostructured Materials, 5 (1995), 673.
[15] LEWANDOWSKA M., GARBACZ H., PACHLA W., MAZUR A., KURZYDŁOWSKI K.J., Solid State Phenomena, 101–102 (2005), 65.
[16] LEWANDOWSKA M., GARBACZ H., PACHLA W., MAZUR A., KURZYDŁOWSKI K. J., Mater. Sci.-Poland, 23 (2005), 279.
[17] WANG N., WANG Z., AUST K., ERB U., Mater. Sci. Eng., A237 (1997), 150.
[18] XIAO C., MIRSHAMS R.A., WHANG S.H., YIN W.M., Mater. Sci. Eng., A301 (2001), 35.
[19] KORZNIKOW V., PAKIEŁA Z., KURZYDŁOWSKI K.J., Acta Phys. Polon. A, 102 (2002), 265.
[20] VALIEV R.Z., MISHRAL R.S., GROZAL J., MUKHERJEE A.K., Scripta Mater., 34 (1996), 1443.
[21] HEMKER K.J., LAST H., Mater. Sci. Eng., A319–321 (2001), 882.
[22] BUCHHEIN T.E., LAVAN D.A, MICHAEL J.R., CHRISTENSON T.R., LEITH S.D., Metall. Mat. Trans., A, 32A (2002), 539.
[23] ROBERTSON A., ERB U., PALOMBO G., Nanostruct. Mater., 12 (1999), 1035.
[24] YOUNG D.J., MRS Bulletin, April (2001), 331.
[25] DE BOER M.P., MAYER T.M., MRS Bulletin, April (2001), 302.
[26] WANG Y., CHEN M., ZHOU F., MA E., Nature, 419 (2002), 912.
[27] MUGHRABI H., HÖPPEL H.W., KAUTZ M., VALIEV R.Z., Z. Metallkunde, 94 (2003),1079.
[28] ZHANG X., WANG H., SCATTERGOOX R.O., NARAYAN I., KOCH C.C., SERGUEEVA A.V., MUKHERJEE A.K., Acta Mater., 50 (2002), 4823.
[29] PARK Y.S., CHUNG K.H., KIM N.J., LAVERNIA E.J., Mater. Sci. Eng., A374 (2004), 211.
[30] COULOMB P., *Les textures dans les métaux de réseau cubique*, Dunod, Paris, 1972 (Polish translation: *Tekstura w metalach o sieci regularnej*, PWN, Warszawa, 1977).
[31] WIŚNIEWSKI T.S., PACHLA W., KUKLA D., MAZUR A., KURZYDLOWSKI K.J.K., QIRT 2004, 7th Int. Conf. on Quantitative Infrared Thermography, Rhode-St-Genèse, Belgium, July 5–8, 2004.

Received 22 March 2005